Ground State Properties and Field Induced Phases in Quasi One-Dimensional Quantum Magnets

Von der Fakultät für Elektrotechnik, Informationstechnik, Physik
der Technischen Universität Carolo-Wilhelmina
zu Braunschweig
zur Erlangung des Grades einer
Doktorin der Naturwissenschaften
(Dr.rer.nat.)
genehmigte

D i s s e r t a t i o n

von

Britta Willenberg

aus Braunschweig

1. Referent: Prof. Dr. Stefan Süllow
2. Referent: Prof. Dr. Michael Lang

eingereicht am: 11.09.2013
mündliche Prüfung (Disputation) am: 09.12.2013

Druckjahr 2014

Vorabveröffentlichungen der Dissertation

Teilergebnisse aus dieser Arbeit wurden mit Genehmigung der Fakultät für Elektrotechnik, Informationstechnik, Physik, vertreten durch den Mentor der Arbeit, in folgenden Beiträgen vorab veröffentlicht:

Publikationen:

B. Willenberg, M. Schäpers, K.C. Rule, S. Süllow, M. Reehuis, H. Ryll, B. Klemke, K. Kiefer, W. Schottenhamel, B. Büchner, B. Ouladdiaf, M. Uhlarz, R. Beyer, J. Wosnitza, and A. U. B. Wolter, Magnetic Frustration in a Quantum Spin Chain: The Case of Linarite $PbCuSO_4(OH)_2$, Phys. Rev. Lett. 108, 117202 (2012).

M. Schäpers, A.U.B: Wolter, S.-L. Drechsler, S. Nishimoto, M. Abdel-Hafiez, W. Schottenhamel, B. Büchner, J. Richter, B. Ouladdiaf, M. Uhlarz, R. Beyer, Y. Skourski, J. Wosnitza, K.C. Rule, H. Ryll, B. Klemke, K. Kiefer, M. Reehuis, B. Willenberg, S. Süllow, Thermodynamic Properties of the Frustrated Spin-chain Compound Linarite $PbCuSO_4(OH)_2$, arXiv:1305.6731 (2013).

Tagungsbeiträge:

B. Willenberg, M. Schäpers, K.C. Rule, S. Süllow, M. Reehuis, H. Ryll, B. Klemke, K. Kiefer, B. Ouladdiaf, and A. U. B. Wolter: The magnetic ground state of the frustrated spin chain linarite. (Vortrag) Frühjahrstagung der DPG 2012, Berlin

B. Willenberg, M. Schäpers, K.C. Rule, B. Klemke, H. Ryll, K. Kiefer, S. Süllow, and A. U. B. Wolter, Magnetocaloric effect measurements of the frustrated spin chain linarite. (Poster) International Conference on Highly Frustrated Magnetism 2012, Hamilton, Kanada

B. Willenberg, M. Schäpers, K.C. Rule, M. Reehuis, B. Ouladdiaf, A.U.B. Wolter, H. Ryll, B. Klemke, K. Kiefer, and S. Süllow, Magnetic Frustration in a Quantum Spin Chain: The Case of Linarite. (Poster), Frühjahrstagung der DPG 2013, Regensburg

B. Willenberg, H. Ryll, K. Kiefer, D. A. Tennant, K. C. Rule, F. Groitl, K. Rolfs, and S. Süllow, Magnetocaloric effect measurements on the alternating spin chain system copper nitrate. (Poster) International Conference on Strongly Correlated Electron Systems 2013, Tokio, Japan

Kurzfassung

In der vorliegenden Arbeit wurden verschiedene quasi-eindimensionale Kupferoxidsysteme mit Hilfe von Neutronenstreuung und thermodynamischen Methoden, wie Magnetisierung, Wärmekapazität und Messungen des magnetokalorischen Effekts, untersucht.

Die magnetischen Eigenschaften in diesen Verbindungen werden von den Cu^{2+}-Ionen dominiert, welche einen Spin $S = \frac{1}{2}$ tragen. Der magnetische Austausch wird durch die Sauerstoffionen vermittelt und kann mit dem Mechanismus des Superaustausches beschrieben werden. Die Bestimmung des Charakters der an der magnetischen Kopplung beteiligten Orbitale im Superaustausch ist zum Verständnis der magnetischen Eigenschaften des Materials wichtig. Mit Hilfe von Neutronendiffraktion mit polarisierten Neutronen kann eben der Charakter dieser Orbitale ermittelt werden, was am Beispiel von Azurit ($Cu_3(CO_3)_2(OH)_2$), in welchem die Kupferatome in einer sogenannten Diamantstruktur angeordnet sind, gezeigt wird.

Die Verbindung Kupfernitrat ($Cu(NO_3)_2 \cdot 2.5D_2O$), welches als System alternierender Heisenberg Ketten beschrieben werden kann, ist ein Beispiel eines Systems, in dem eine Energielücke den Grundzustand (Singulett) von den Triplettzuständen trennt. Durch ein extern anglegtes Magnetfeld führt die Zeeman-Aufspaltung zu einem Schließen der Lücke. Kupfernitrat wurde ausführlich untersucht, indem sowohl Neutronendiffraktion und thermodynamische Techniken angewandt wurden. Im Verlauf all dieser Messungen wurden Probleme mit der Thermalisierung der Proben sichtbar. Mit Messungen des magnetokalorischen Effekts konnte dieses Problem schließlich umgangen werden, indem kleine Proben verwendet wurden und das Magnetfeld sehr langsam verändert wurde. Das magnetische Phasendiagramm für Magnetfelder parallel zur kristallographischen b-Achse wurde im Detail mit dieser Methode bestimmt. Das Phasendiagram zeigt eine kuppelförmige Phasengrenze einer feldinduzierten, langreichweitig geordneten Phase für Temperaturen unterhalb von 166 mK und Feldern zwischen 2,8 T und 4,3 T, welche im Zusammenhang mit einer Bose-Einstein-Kondensation von Triplonen diskutiert wird. Weiterhin wurden besondere Merkmale in den Daten der Messungen des magnetokalorischen Effekts als Übergänge in eine Luttinger-Flüssigkeit interpretiert. Simulationen, welche der Methode der exakten Diagonalisierung zu Grund liegen, konnten die experimentellen Daten beschreiben und vervollständigen.

In dem Material Linarit ($PbCuSO_4(OH)_2$), welches als quasi-eindimensionale Kette beschrieben werden kann, führen konkurrierende nächste-Nachbar-Wechselwirkungen/übernächste-Nachbar-Wechselwirkungen zu Frustration. Bei 2,8 K zeigt das System im Nullfeld einen Phasenübergang erster Ordnung in einen langreichweitig geordneten Zustand. Magnetisierungsmessungen und Messungen des magnetokalorischen Effekts wurden verwendet, um das magnetische Phasendiagramm für Magnetfelder, die entlang der Kettenrichtung angelegt werden, und Temperaturen bis hinunter zu 250 mK zu bestimmen. Vier verschiedene Phasen wurden beobachtet, in denen die Spinstrukturen mit Hilfe von Neutronendiffraktion bestimmt wurden. Im Grundzustand wurde eine spiralförmige Struktur gefunden. Für Magnetfelder, die größer als 2,5 T sind, wurde ein komplexer spin-flop-Prozess in zwei Schritten beobachtet. Bei diesem geht die Spinstruktur schließlich in eine kollineare Struktur über, bei der die Spins in der ac-Ebene liegen. In einer Region im Phasendiagram, welche bei höheren Temperaturen liegt, wurde eine außergewöhnliche sinusmodulierte Phase gefunden. Hier verschiebt sich der Propagationsvektor mit dem Magnetfeld. Diese Phase wurde im Sinne einer Spindichtewelle interpretiert, welche mit Dichtewellen von „gebundenen 3-Magnonen“ beschrieben werden kann. Ähnlich wie bei der Verbindung $LiCuVO_4$, bei der die Möglichkeit des Auftretens einer spin-nematischen Phase diskutiert wird, könnte Linarit eine triatische Phase zeigen.

Da die interessantesten Phänomene in den untersuchten Verbindungen erst bei sehr tiefen Temperaturen auftreten, wurde eine Messoption zum Messen der Wärmekapazität und des magnetokalorischen Effekts im Rahmen dieser Arbeit gebaut. Der magnetokalorische Effekt konnte bis zu Temperaturen von etwa 100 mK gemessen werden, was am Beispiel von Kupfernitrat demonstriert wurde. Die Wärmekapazität ist

bis 300 mK mit einer sehr hohen Genauigkeit messbar, was nötig war um den Phasenübergang von Linarit im Nullfeld zu studieren. Als eine komplementäre Methode wurden hier außerdem Neutronendiffraktionsmessungen durchgeführt, wofür eine sehr gute Temperaturstabilität von Nöten war. Aus diesem Grund wurde ein neuer Probenstab gebaut, welcher beispielsweise im Zusammenhang mit einem standardmäßig in der Neutronenstreuung verwendeten „Orange Cryostat“ benutzt werden kann.

Abstract

In this thesis different quasi one-dimensional copper oxide systems were investigated by means of neutron scattering and thermodynamic experiments such as magnetization, heat capacity, and magnetocaloric effect measurements.
The magnetic properties in these compounds are dominated by the Cu^{2+} ions, which carry spin $S = \frac{1}{2}$. The magnetic exchange is mediated by the oxygen ions and can be described within the mechanism of superexchange. The determination of the character of the orbital participating in the magnetic exchange is important for the understanding of the magnetic properties of a material. By means of neutron diffraction with polarized neutrons the character of these orbitals can be obtained, which is demonstrated for the compound azurite ($Cu_3(CO_3)_2(OH)_2$), where the copper atoms are arranged in a so called diamond structure.
The compound copper nitrate ($Cu(NO_3)_2 \cdot 2.5D_2O$) can be described as an alternating Heisenberg chain system. It is an example of a system, in which an energy gap between the ground state (singlet) and the triplet states is present. In an external applied magnetic field Zeeman splitting leads to a closing of the gap. Copper nitrate was investigated extensively using both neutron diffraction and thermodynamic techniques. In all measurements problems with the thermalization of the samples were noticed. Finally, by using magnetocaloric effect measurements the problem could be handled by means of the use of small samples and very slow sweep rates of the magnetic field. The magnetic phase diagram for magnetic fields applied parallel to the crystallographic b axis was mapped out in much detail using this technique. The phase diagram shows a dome-shaped phase boundary of a field induced long-range ordered state for temperatures below 166 mK and fields between 2.8 T and 4.3 T, which is discussed in terms of a Bose-Einstein condensation of triplons. Furthermore, features in the magnetocaloric effect data at temperatures up to 220 mK were interpreted as crossovers into a Luttinger liquid regime. Simulations using the method of exact diagonalization could be used to describe and complement the experimental data.
In the compound linarite ($PbCuSO_4(OH)_2$), which can be described as a quasi-one-dimensional chain, the nearest neighbor interactions compete with the next nearest neighbor interactions leading to frustration. At 2.8 K the system shows a first order phase transition into a long-range ordered state in zero field. Magnetization as well as magnetocaloric effect measurements were used to map out the phase diagram for magnetic fields applied along the chain direction and temperatures down to 250 mK. Four different magnetic phases were detected. By means of neutron diffraction the spin structures in these phases were determined. In the ground state a helical spin arrangement was found. For applied magnetic fields larger than 2.5 T a complex spin-flop process was observed, which is realized in two steps and results in a collinear spin arrangement with spins lying in the *ac* plane. In the high temperature region an extraordinary sine wave modulated spin structure was found. Here, the wave vector is shifting with the magnetic field. This phase was interpreted in terms of a spin density wave phase, which can be described with density waves of bound three-magnons. Similar to the compound $LiCuVO_4$, where the appearance of a spin-nematic phase is discussed, linarite could show a spin-triatic phase.
As the most interesting phenomena in these compounds occur at very low temperatures, an option for measuring the heat capacity and magnetocaloric effect has been built within the framework of this thesis. The magnetocaloric effect could be measured at temperatures down to ∼100 mK, which was demonstrated for copper nitrate. The heat capacity is mensurable down to 300 mK with high accuracy, which was necessary to study the phase transition of linarite at zero field. As a complementary method the behavior was also investigated with neutron diffraction, where a very good temperature stability was required. For this purpose, a new sample stick has been built, which can be used for example in a standard “Orange Cryostat” for neutron scattering experiments.

Contents

1 Introduction

Magnetism is pervasive in our everyday life. We are constantly surrounded by the Earth's magnetic field. Many technological devices are based upon magnetism. From the early development of electric motors, research into magnetism has lead to such applications as data storage in computers or medical devices such as Magnetic Resonance Imaging. Still, there is much about magnetic materials that we do not understand, and which may one day lead to further great technological achievements. For these purposes research into novel magnetic materials with unusual properties is of high importance. In particular, investigating quantum magnets may reveal information about the mechanisms which lead to novel magnetic phenomena.

Low dimensional quantum spin systems open up a fascinating field of study for both experimentalists and theorists owing to their rich and varied magnetic properties. In particular one-dimensional (1D) systems are of great interest due to the difference in physics as compared to 3D systems and the relative simplicity of microscopic models to describe such systems [1, 2]. Moreover, in such materials various intriguing types of excitations appear such as spinon or multimagnon excitations as well as exotic field induced phases like multipolar ones. While long range magnetic order is suppressed due to quantum fluctuations in 1D quantum magnets even at zero temperature, real materials typically show weak residual three-dimensional magnetic exchange, which often leads to a long-range ordered ground state at very low temperatures. Rich magnetic phase diagrams are observed for these *quasi* one-dimensional systems containing among others multiferroic phases in frustrated chain systems or Bose-Einstein condensation of triplons in dimerized systems.

Interest in low dimensional quantum spin systems began with theoretical considerations since low dimensional spin systems can be described within simple models, which are relatively easy to calculate (in fact, sometimes they are even analytically solvable). In 1931 Bethe was able to determine the quantum mechanical ground state of an antiferromagnetic spin chain exactly using the approach which is now known as *Bethe ansatz* [3]. Not only has the simplicity of the models attracted further interest subsequently, but also the novel physics emerging in this research field. In one dimension the Fermi liquid theory fails, as no individual motion of the electrons is possible. The excitations become collective. Furthermore, the excitations are separated into two: one which carries the charge (holon) and the other which carries the spin (spinon). These spinons are fermions with spin $S = \frac{1}{2}$ in contrast to higher dimensional systems where the excitations (magnons) carry spin $S = 1$. In this situation, to describe the properties of one-dimensional systems with a gapless excitation spectrum the Luttinger liquid theory was developed, which corresponds to the Fermi liquid theory for higher dimensions [4–6]. The Luttinger liquid theory is not only applicable to spin chains embedded in bulk materials, but it can also be adapted to quantum wires such as carbon nanotubes [7, 8].

When in 1986 high T_c-superconductivity was discovered in the doped layered copper oxide system $Ba_xLa_{5-x}Cu_5O_{5(3-y)}$ [9], the interest in low dimensional systems rose enormously. Particularly,

when Anderson suggested that resonating valence bound (RVB) states might play a role in this type of superconductivity [10], the search of materials showing RVB states began. An RVB state is a superposition of different pairings of spins forming fluctuating singlet states. The ground state of this phase is predicted to be a quantum spin liquid, in which the spins fluctuate even when the temperature goes to zero [11, 12]. These systems exhibit characteristic properties of one-dimensional magnets such as spin $S = \frac{1}{2}$ excitations and spin charge separation.

Candidates showing spin liquid behavior are for example two-dimensional spin $S = \frac{1}{2}$ systems whose moments are sitting on triangular or kagomé (cornersharing triangles) lattices and couple antiferromagnetically. Due to the antiferromagnetic nearest neighbor coupling and the triangular geometry the system cannot simultaneously satisfy all of its nearest neighbor interactions so that the system is called *frustrated*. Experimental evidence of fractional spin excitations in 2D-systems were first observed in the kagomé compound herbertsmithite [13].

Aside from those experimental realizations of frustrated quasi two-dimensional systems, also frustrated quasi one-dimensional systems stand in the focus of research activities, as they can be described with a simpler model and show other fascinating features. Further, one-dimensional systems play a role in present day research, as they offer a testing ground for basic concepts such as Luttinger liquids and Bose-Einstein condensation of triplons. Thus, in the following I will review the basic properties of the various systems in one-dimension, which can be classified by different types of frustrated or nonfrustrated microscopic models.

The simplest model of a one-dimensional system is the **uniform antiferromagnetic Heisenberg chain** (Fig. 1.1 a)). It is described by only one nearest neighbor exchange constant J_1, which couples the spins within the chain antiferromagnetically. In this Heisenberg chain, the spins can point in any direction, in contrast to XY-chains and Ising chains, which are due to anisotropy planar or unidirectional, respectively.

Depending on the value of the spin quantum number, different characteristics concerning the excitation spectra are expected. For integer spins Haldane conjectured a spin gap [14, 15] to the excited states. The first experimental verification of the so called *Haldane gap* was found for the spin $S = 1$ system $CsNiCl_3$ [16, 17]. In contrast, for half-integer spins the excitations are gapless. A consequence of the gapless ground state in combination with the one-dimensionality was found for the quasi 1D uniform spin $S = \frac{1}{2}$ chain compound $KCuF_3$ via inelastic neutron measurements. The data showed

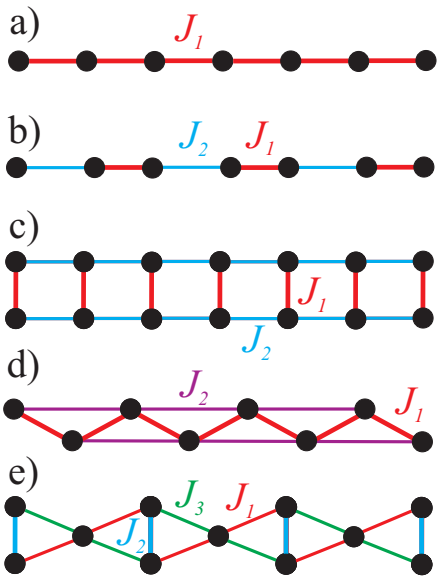

Fig. 1.1: Schematic pictures of a uniform chain a), an alternating chain b), a ladder system c), zigzag-chain as an example of a *nn afm-nnn afm*-chain d), and a diamond chain e).

that the dynamics form an excitation continuum (*two-spinon continuum*), which indicates that the system behaves like a Luttinger liquid [18, 19]. Other experimental realizations of a uniform spin $S = \frac{1}{2}$ chain system are for instance the compounds Sr_2CuO_3, $CuSe_2O_5$, $K_2CuP_2O_7$, $Ba_2Cu(PO_4)_2$, and $Sr_2Cu(PO_4)_2$ [20–26].

The simple 1D chain model may be modified by introducing a second exchange constant $J_2 \neq J_1$ so that the spins are coupled within the chain antiferromagnetically via $J_1 - J_2 - J_1 - J_2 - ....$ The excitation spectrum of the spin $S = \frac{1}{2}$ system for this model is gapped. This type of chain is called **alternating antiferromagnetic chain** (Fig. 1.1 b)). In this case, the spins are dimerized forming singlets in the ground state, which are separated by an energy gap Δ from the excited triplet states. The dimerization can be realized as a result of crystal structure features which have alternating exchange paths along the chain so that the two exchange constants alternate. This kind of dimerization was found for instance in the systems $(VO)_2P_2O_7$, $Pb_2V_3O_9$, and $Cu(NO_3)_2 \cdot 2.5\ H_2O$ (copper nitrate) [27–29]. A dimerization can also arise from a spin Peierls transition. Here, a prominent example is $CuGeO_3$, which can be described as a uniform antiferromagnetic spin $S = \frac{1}{2}$ chain at temperatures above a critical temperature $T_{SP} \sim 14\,\mathrm{K}$ [30]. Below T_{SP} the chain becomes dimerized by a structural deformation in which pairs of copper ions move closer to each other causing the formation of spin dimers.

The family of dimerized one-dimensional systems also includes the so called **ladder systems** (Fig. 1.1 c). These systems have dominant exchange interactions J_1 forming dimers which can be regarded as the rungs of a ladder, while smaller interchain interactions J_2 form the legs of the ladder. For even leg ladders with spin $S = \frac{1}{2}$ an energy gap separates the singlet ground state from the triplet excited states similar to the alternating chains. Contrary, for odd leg ladders a gapless excitation spectrum is predicted. Experimental realizations of a two-leg ladder model include for instance $(C_5H_{12}N)_2CuBr_4$ and $(C_5H_{12}N)_2CuCl_4$ [31–33].

Due to the similarities between the alternating antiferromagnetic chain and the even leg ladder compounds concerning the energy gap, they are expected to behave similarly in applied magnetic fields. When applying a magnetic field Zeeman splitting of the triplet states occurs, which closes the gap at a certain critical field H_c. This point is characterized as a quantum critical point, which is a transition from one quantum ground state to another at zero temperature. The gapless regime can be described with Luttinger-liquid theory like the uniform spin $S = \frac{1}{2}$ chain. The Luttinger liquid behavior was experimentally observed by inelastic neutron scattering measurements in the gapless regime of the ladder system $(C_5H_{12}N)_2CuBr_4$. Here, a two-spinon continuum similar to that observed in $KCuF_3$ was found [34]. Further, heat capacity and magnetocaloric effect measurements show clear features at the crossover into the Luttinger liquid regime [35].

For weak interchain/interladder J' interactions however 3D long-range ordering is expected at low enough temperatures. This long-range ordering may be characterized by a **Bose-Einstein condensation of triplons** (BEC), which can be treated as hard core bosons. The Bose-Einstein condensation was extensively studied for the 3D interacting dimer compound $TlCuCl_3$ [36–38], the 2D system $BaCuSi_2O_6$ [39, 40], as well as the quasi one-dimensional spin $S = 1$ chain $NiCl_2$-

$4SC(NH_2)_2$ [41]. Further, the ladder system $(C_5H_{12}N)_2CuBr_4$ was discussed in the context of BEC [42]. This system is the only system so far where a detailed phase diagram was determined containing both Luttinger liquid regime and long-range ordered phase, which may be interpreted as Bose-Einstein phase. Here, the dimensional crossover between a Luttinger liquid and a Bose-Einstein condensation could be studied. Another promising candidate showing both the Bose-Einstein condensation as well as the Luttinger liquid regime is the alternating spin chain system copper nitrate. Several bulk measurements were performed on copper nitrate in the 1970s, which focus on the determination of the exchange constants and magnetic spin structure. However, a detailed phase diagram with the investigation of a possible Luttinger phase is lacking, which was the motivation of the magnetocaloric effect measurements on copper nitrate presented in this thesis.

Going one step further and adding next nearest neighbor interactions to the model of the uniform spin chain, the interactions can compete with each other leading to **frustration**. Systems with competing interactions include chains with nearest and next nearest interactions both antiferromagnetic (*nn afm-nnn afm*) or chains with spins coupled ferromagnetically to the nearest neighbor spin and antiferromagnetically to the next nearest neighbor spin (*nn fm-nnn afm*). Several different ground states are predicted for these chains depending on the ratio $\alpha = J_2/J_1$, where J_1 is the nearest neighbor interaction and J_2 the next nearest interaction. According to theory, for the spin $S = \frac{1}{2}$ ***nn afm-nnn afm* chain** the ground state remains gapless up to a critical value of $\alpha = 0.2411$ [43], while for larger α-ratios a gapped dimerized ground state is predicted [44]. Competing antiferromagnetic interactions were found in the compounds $(N_2H_5)CuCl_3$ and $Cu(ampy)Br_2$, which can be described with α-ratios of 4 and 0.2, respectively [45–47]. These compounds form zigzag-chains, which are schematically drawn in Fig. 1.1 d). Based on theoretical studies various interesting features are expected in magnetic fields like cusp singularities and $\frac{1}{3}$-plateaus in the magnetization [48] or a field-induced vector chiral order, which is the quantum counterpart of the classical helical spin order [49].

For the ***nn fm-nnn afm* chain** the ground state is expected to be ferromagnetic for $0 > \alpha > -0.25$, while for $\alpha < -0.25$ the ground state is helical in the classical limit $S \to \infty$. Considering a chain with spins $S = \frac{1}{2}$ and anisotropy, various ground states are predicted including vector chirality, dimer phases, and Luttinger liquid phases [50]. Weak interchain interactions, which are present in real materials, lead in all known systems to a long-range ordered helical ground state when $\alpha < -0.25$. For some compounds it was observed that the twist of the spins in the helical spin arrangement induces *multiferroicity*. For applied magnetic fields several exotic phases are expected such as multipolar Luttinger liquid phases [51, 52]. These can be described by a condensation of two-magnon bound states (nematic phase), three-magnon bound states (triatic phase) or four-magnon bound states (quartic phase). Several compounds were found to belong to the class of *nn fm-nnn afm* chain systems, among these are $LiCuVO_4$, $LiCu_2O_2$, as well as $PbCuSO_4(OH)_2$ known as linarite [53–57].

The compounds $LiCuVO_4$ and $LiCu_2O_2$ were extensively studied in the past. Rich magnetic

phase diagrams were observed containing phases with helical spin arrangements as well as several phases with collinear spin structures. Unfortunately, the phases close to the saturation field could not be analyzed in detail due to their large magnitude. For linarite, which has a saturation field of only 10 T, paradoxically only a few studies exist. For this reason several thermodynamic measurements were performed within the framework of this thesis in order to determine the ground state properties and the magnetic phase diagram. Furthermore, neutron diffraction was used to investigate the different phases on a microscopic scale.

Quasi one-dimensional systems also include the so called **diamond chains**, which consist of two spins forming the backbone of the diamond arranged in a chain like structure together with one spin (the monomer) sitting between them (Fig. 1.1 e)). In the most simple case, the chain can be described as a symmetric diamond chain with only two exchange constants J_1 and J_2, where J_2 couples the spins of the backbones and J_1 the backbones with the monomer spin. A more complex case is the distorted diamond chain, which is described by three exchange constants as it is depicted in Fig. 1.1 e). A good realization of a distorted diamond chain is $Cu_3(CO_3)_2(OH)_2$ (azurite), which attracted attention due to the appearance of a $\frac{1}{3}$-plateau in the magnetization [58]. Depending on the nature of the three exchange constants the diamond chain may be magnetically frustrated. If all spins are coupled antiferromagnetically, the chain is frustrated, while in the case of one coupling being ferromagnetic, it is not. The spins can couple either antiferromagnetically or ferromagnetically, which case being realized depending on minute details of the electronic structure. In the copper oxide systems, which were studied within this thesis, the magnetism arises from the Cu^{2+}-ions which carry spin $S = \frac{1}{2}$. The magnetic exchange of these localized moments is dominated by the *superexchange* mechanism, in which the exchange is mediated by oxygen ligands. This mechanism is strongly dependent of the type of involved orbitals and their geometry.

The magnetic superexchange is reviewed in chapter 2 as it is the dominant coupling mechanism of the quasi one-dimensional spin $S = \frac{1}{2}$ systems studied within this thesis. The chapter concludes with the determination of a spin density map of the natural mineral **azurite** via polarized neutron diffraction.

Chapter 3 summarizes the experimental techniques which were used to investigate the copper oxide materials linarite, copper nitrate, and azurite. These include neutron diffraction as well as thermodynamic measurements. Since many of the intriguing magnetic properties of the copper oxide systems investigated here appear only at very low temperatures, the thermodynamic measurements focus on measurements at temperatures below 1.8 K. These temperatures cannot be achieved with a simple ^{4}He-cooling system but require ^{3}He systems. For these low temperatures the demands on the performance of the measurements systems are very high and often commercial systems are not sufficient to achieve satisfactory results. Therefore, a heat capacity and magnetocaloric effect measurement option was built during the experimental work period of

this thesis.

In chapter 4 the alternating antiferromagnetic chain system **copper nitrate** is introduced. Due to the dimerization within the chain a gap is present, which closes for fields of about 2.8 T. To study this material, first of all, copper nitrate crystals were grown and characterized using x-ray diffraction and magnetization measurements down to 1.8 K. Afterwards the magnetic phase diagram was investigated by using different experimental techniques at dilution temperatures. These include elastic neutron scattering, magnetization, and magnetocaloric effect measurements. The optimal technique to define the boundaries of the field induced phase was established to be magnetocaloric effect measurements. The obtained detailed phase diagram contains a long-range ordered phase, which could possibly be a Bose-Einstein phase, as well as a Luttinger liquid regime.

In chapter 5 measurements on the frustrated chain system **linarite** are presented. These include thermodynamic measurements such as magnetization, heat capacity, and magnetocaloric effect measurements. A focus lies on the determination of the magnetic phase diagram. A rich phase diagram was found for magnetic fields applied along the crystallographic b axis. Here, it contains four different long-range ordered phases and a hysteretic region at low-temperatures. By means of neutron diffraction measurements the spin structures in these four phases were determined, which show that a complex spin flip process occurs. Furthermore, ferroelectric phase transitions were found which coincide with the magnetic phase transitions of two phases indicating that a special type of multiferroicity exists. Finally, one phase is discussed in terms of spin nematics.

The main results of this thesis are reviewed in chapter 6.

2 Magnetic Exchange Interaction in Quasi One-Dimensional Copper Oxides

One-dimensional copper oxide systems are generally formed by Cu^{2+}-ions, which are surrounded by four oxygen ions forming more or less squares. These CuO_4 units often share one or two oxygen atoms with the next unit forming a chain. In this arrangement, they can either share their edges with each other leading to so-called edge-sharing systems, or they share their corners in corner-sharing systems (Fig. 2.1). While in corner-sharing systems the angle along Cu-O-Cu bonds are 180°, the angle is nearly 90° for edge-sharing systems. This difference can lead to completely different magnetic properties since it influences the magnetic exchange interaction in these systems significantly (Goodenough-Kanamori-Anderson Rules [59–61]).

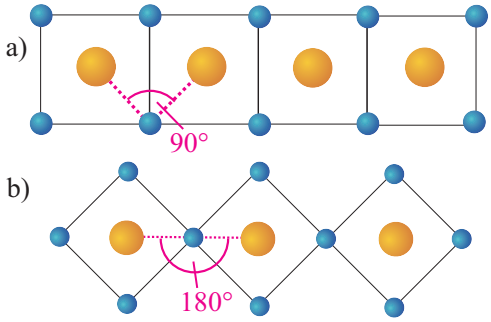

Fig. 2.1: Edge-sharing (a) and corner-sharing (b) copper oxide chains. The copper and oxygen atoms are represented by orange and blue balls, respectively. While the angle between Cu-O-Cu is 90° for the edge-sharing chain, the angle is 180° for the corner-sharing chain.

2.1 Magnetic Exchange Interaction

Magnetic exchange arises when two electrons with eigenstates $\psi_{a,b}(\boldsymbol{r}_{1,2})$ form a joint state. The joint state can be either a singlet state or a triplet state. Since the energies ϵ of the two possibilities differ from each other, one can define the exchange constant or integral J as

$$J = \frac{\epsilon_{\text{singlet}} - \epsilon_{\text{triplet}}}{2} = \int \psi_a^*(\boldsymbol{r}_1)\psi_b^*(\boldsymbol{r}_2)\hat{H}\psi_a(\boldsymbol{r}_2)\psi_b(\boldsymbol{r}_1)d\boldsymbol{r}_1 d\boldsymbol{r}_2. \tag{1}$$

Further, the spin-dependent term of the Hamiltonian can then be defined as

$$\hat{H}_{\text{spin}} = -2J\boldsymbol{S}_1 \cdot \boldsymbol{S}_2 \tag{2}$$

between spins S_1 and S_2.

For an exchange constant $J > 0$ ($J < 0$) the triplet (singlet) state is favored leading to an ferromagnetic (antiferromagnetic) configuration. In particular, for two electrons sitting on the same atom, the exchange integral is positive leading to Hund's first rule. [62]

For exchange interactions involving more than two spins the Heisenberg model with the following

Hamiltonian was developed:

$$\hat{H} = -2\sum_{i>j} J_{ij}\boldsymbol{S}_i \cdot \boldsymbol{S}_j, \tag{3}$$

where J_{ij} denotes the exchange constant between the ith and jth spin.

Magnetic exchange in localized spin systems can be either *direct* or *indirect*. The *direct* case is quite rare. A hopping process of an electron from one atom to the neighboring atom can take place when the orbitals of the two atoms strongly overlap. The hopping would lower the energy since it leads to delocalization. On the other hand it costs potential energy (Coulomb energy) whenever two electrons occupy the same site. Thus, two energetic terms need to be accounted for: The kinetic energy and the Coulomb energy. This argumentation is followed for example in the Hubbard model. The hopping can be described as an annihilation of an electron sitting on the atom i with the spin σ and the creation of an electron sitting on the atom j with spin σ. Using the creation (annihilation) operators $c^+_{i\sigma}$ ($c_{i\sigma}$) the Hamiltonian can be defined as follows:

$$\hat{H}_t = -t\sum_{i,j,\sigma} c^+_{j\sigma}c_{i\sigma} \tag{4}$$

with the transfer integral t. For this simple model only the Coulomb repulsion between electrons on the same site is accounted for. The Hamilton can be described as

$$\hat{H}_U = U\sum_i n_{i\uparrow}n_{i\downarrow} \tag{5}$$

with the repulsive energy U. The occupation-number operators $n_{i\uparrow}$ and $n_{i\downarrow}$ are defined as $n_{i\sigma} = c^+_{i\sigma}c_{i\sigma}$. The Coulomb energy is only nonzero when electrons sitting on the same site have different spins since the Pauli exclusion principle forbids that two electrons with the same spin are sitting in one orbital. The complete Hamiltonian of the Hubbard model is then described by $\hat{H} = \hat{H}_t + \hat{H}_U$. [63]

The consequence of the hopping is illustrated in Fig. 2.2. Hopping from one atom to another is only possible when one electron has spin up and the other spin down (Pauli principle). The direct exchange is therefore antiferromagnetic.

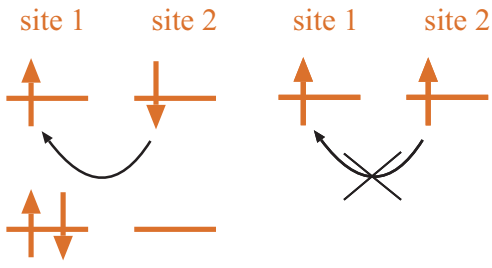

Fig. 2.2: Direct exchange: electrons are only allowed to hop to the next site when they have different spins. For electrons with the same spin state the Pauli principle forbids the hopping.

In copper oxides a magnetic interaction is not possible via a direct exchange since the copper ions

are typically not nearest neighbors and the d-orbitals of the copper atoms are too localized so that they cannot overlap. Therefore, a magnetic interaction in copper oxides is only possible with an *indirect* exchange via the nonmagnetic O^{2-} ion. This type of exchange is called *superexchange*.

2.1.1 Superexchange

Superexchange was first proposed by Kramers in 1934, who pointed out that the nonmagnetic ions perturb the wave functions of the magnetic ions spin dependently resulting in a magnetic exchange effect over long distances [64]. In 1950 Anderson developed his idea further [65]. He described the superexchange mechanism in two steps: first, a p-electron is transferred from the nonmagnetic ion to a d-orbital of the magnetic ion. In the second step, the remaining unpaired electron of the nonmagnetic ion provides the exchange coupling (direct exchange). After several refinements it turned out that the uncertainties and complexities of this mechanism increased excessively. In 1959 Anderson improved his idea by looking at the problem from a different point of view [66]. He divided the problem into two parts: First, he determined the wave function of the magnetic ions which interact only with the surrounding diamagnetic atoms. This leads to molecular orbitals. In the second part, only the interaction of the magnetic ions with each other are determined which includes already the solution of the first part.
Depending on the symmetry and the orientation of the interacting orbitals with respect to each other, ferromagnetic or antiferromagnetic coupling occurs. Over several years, Kanamori and Goodenough developed semi-empirical rules for the different cases, which are known as GKA-rules [59–61]. These rules take into account the d-orbitals which are occupied according to the ligand field theory. A summary of the rules is given by Anderson [61]: If two orbitals have the same symmetry with respect to the connection line, they are nonorthogonal to each other and can therefore overlap. The exchange is antiferromagnetic. If they do not have the same symmetry, the orbitals are orthogonal leading to weak ferromagnetic exchange.
In the following, two scenarios of superexchange are discussed to demonstrate the variety of the superexchange (see Fig. 2.3). In the case of copper oxides there is one $3d$-orbital on each copper ion which is occupied by only one electron, while on the oxygen in between all $2p$-orbitals are filled with two electrons. Which orbital of the $3d$-orbitals is occupied by only one electron is determined by the crystal field (for this example the $d_{x^2-y^2}$-orbital was chosen). Hopping from the oxygen ions to the copper ions is possible when the orbitals overlap. In this case a hopping only from the $2p$-orbital (here the p_x-orbital) which is pointing towards the $3d$-orbital of the copper ion is possible as it is shown in Fig. 2.3 a). In a 180° geometry, in which the two copper ions and the oxygen ion form a line, the exchange can be treated similarly to the direct exchange but with an additional step over the oxygen. The resulting Hamiltonian can be written in the following form [63]:

$$\hat{H} = \sum_{\sigma} \left(\epsilon_d \sum_i n_{i\sigma} + \epsilon_p n_{p\sigma} - t_{pd} \sum_i \left(c^+_{i\sigma} c_{p\sigma} + c^+_{p\sigma} c_{i\sigma} \right) \right) + U_d \sum_i n_{i\uparrow} n_{i\downarrow}, \tag{6}$$

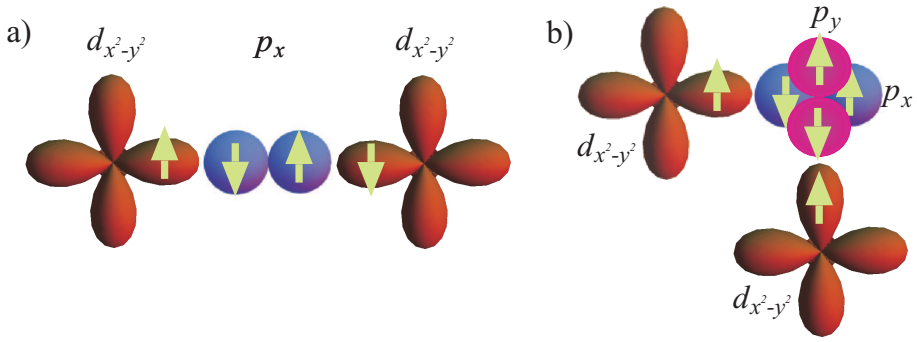

Fig. 2.3: Examples for superexchange for a) a 180° configuration leading to antiferromagnetic coupling and b) a 90° configuration leading to ferromagnetic coupling

$c^+_{i\sigma}/c_{i\sigma}$ is the creation/annihilation operator which creates/annihilates a spin in the 3d-orbital of the ith copper ion with the spin σ. Similarly, $c^+_{p\sigma}/c_{p\sigma}$ creates/annihilates a spin in the 2p-orbital of the oxygen ion just between the two copper ions. Further, the Coulomb repulsion between two electrons in the d-orbital is U_d (the Coulomb repulsion in the p-orbital is neglected in this simple model). ϵ_d and ϵ_p denote the energy of an electron in a d- or p-orbital, respectively. The hopping between a d-orbital and the p-orbital is given by t_{pd}. $n_{i\uparrow}$ and $n_{i\downarrow}$ are the occupation-number operators. The hopping process for this case is shown schematically in Fig. 2.4. The coupling is then defined to be antiferromagnetic for this case. In Anderson's picture the $d_{x^2-y^2}$-orbitals and the p_x-orbital do have the same symmetry and overlap leading to antiferromagnetic exchange. This type of exchange interaction takes place in corner-sharing copper oxide systems.

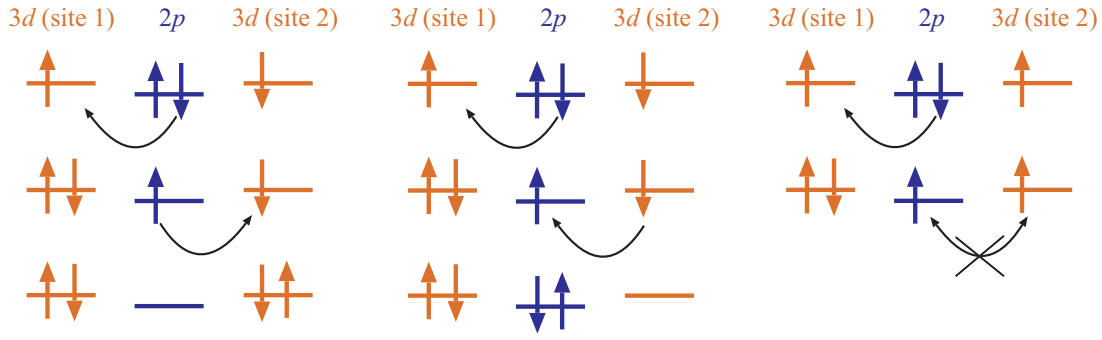

Fig. 2.4: Simple model for the 180°-superexchange: The superexchange is antiferromagnetic (left and middle sketch). For parallel spins in the two d-orbitals (right sketch) hopping from the oxygen site to one copper site is possible, but another hopping process is forbidden by the Pauli principle (compare Ref. [63]).

For edge-sharing systems the angle between Cu-O-Cu is not 180° but about 90°. In this case the 2p-orbital cannot overlap with both 3d-orbitals but instead one of the copper 3d-orbitals overlap with e.g. the 2p_x-orbital and the other with the 2p_y-orbital (Fig. 2.3 b)). Hopping between these two p-orbitals is not possible, but another coupling mechanism is present: the Hund's coupling. Because of Hund's first rule the remaining spins on both p-orbitals need to be parallel. For this

reason the 90°-coupling is ferromagnetic but weaker than the 180°-coupling described above (see Fig. 2.5).

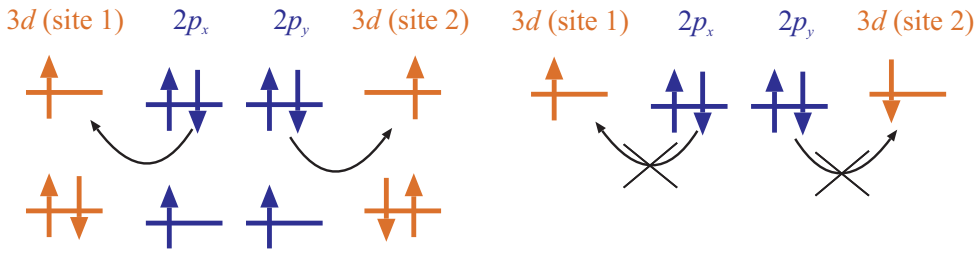

Fig. 2.5: Simple model for the 90°-superexchange, which is ferromagnetic. The remaining unpaired spins sitting at the p-orbitals need to be aligned parallel because of Hund's first rule.

When the angle is larger than 90° hopping to both p-orbitals can occur (Slater-Koster rules) resulting in a competition between antiferromagnetic and ferromagnetic exchange [63]. For angles just above 90° the exchange can already change from ferromagnetic to antiferromagnetic.
Magnetic exchange is also possible for exchange paths including two nonmagnetic ions. For example the next nearest neighbor interaction of linarite or the nearest neighbor interaction in copper nitrate is mediated over two oxygen ions (Cu-O-O-Cu).
As indicated above the sign of the interaction strongly depends on the symmetry of the orbitals and their orientation with respect to each other. Therefore, the knowledge of the symmetry of the orbitals participating in the magnetic exchange is crucial for the understanding of the exchange paths and also the magnetic properties.
An experimental method to determine the character of the orbitals participating in the magnetic exchange is neutron diffraction with polarized neutrons. This method is presented exemplary on the diamond chain system azurite in the following section.

2.2 Spin Density Map of Azurite

The spin density of azurite has been investigated by polarized single-crystal neutron diffraction. Measurements were taken on D3 at the Institute Laue-Langevin (Grenoble) below T_N =1.9 K at 1.3 K using hot neutrons with a wavelength of 0.825 Å (instrument description: see section 3.1.6).

The natural mineral azurite, $Cu_3(CO_3)_2(OH)_2$, has been proposed to represent a realization of the 1D distorted diamond chain model. In this material, the copper ions are sitting on two different sites of the monoclinic lattice (space group $P2_1$ [67] ; a = 5.011 Å, b = 5.850 Å, c = 10.353 Å, β = 92.41° [68–70]): Cu2 is sitting on site 4e forming the backbone of the diamond structure, while Cu1 is sitting on 2a in between the backbones (Fig. 2.6). All copper atoms are surrounded by

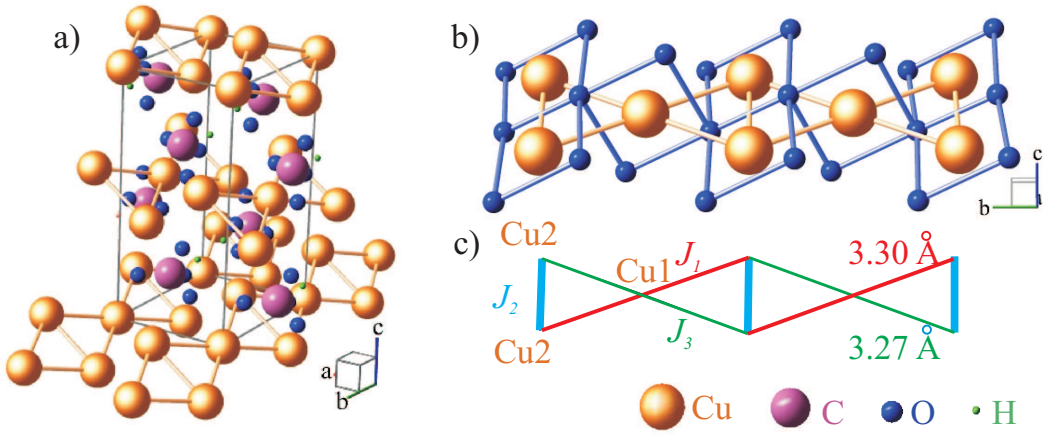

Fig. 2.6: a) unit cell of azurite, b) diamond chain along the b direction, c) exchange interactions between the magnetic ions.

four oxygen atoms forming squares, which share their edges or corners. Superexchange couples the magnetic ions, according to the most basic model assumptions, via three exchange paths. The coupling between the copper ions on the backbone is called J_2. It has a bond angle Cu2-O-Cu2 of 98°. The exchange couplings J_1, J_3 between Cu1 and Cu2 are defined in Fig. 2.6 c). The angles between Cu1-O-Cu2 are 113°, which would imply that the coupling is antiferromagnetic (GKA-Rules: the angle is much bigger than 90°).

In agreement with this conjecture Kikuchi *et al.* deduced from susceptibility measurements that all three exchange interactions should be antiferromagnetic with J_1 = 19 K, J_2 = 24 K, and J_3 = 8.6 K, which would result in a frustrated arrangement [58]. In contrast, Gu *et al.* interpreted the same data in terms of a non frustrated system where J_3 is ferromagnetic [71]. Rule *et al.* also concluded from inelastic neutron measurements that the exchange J_3 is ferromagnetic [72]. They argued that the antiferromagnetic exchange expected by the GKA-rules are only valid for $d_{x^2-y^2}$-orbitals. The ferromagnetic exchange J_3 found in this experiment could be the consequence of a d_{z^2}-character of the interacting ions. The exchange mechanism for this case was discussed by Filippetti *et al.* for CuO [73]. The configuration in which the coupling is ferromagnetic is the following: The exchange must be mediated between atoms with an angle smaller than 180° but

bigger than 90°. In the discussed system, CuO, the angle is 109°. Further, all three atoms must sit in the xy-plane. Then, only p_x or p_y have the same symmetry as the d_{z^2}-orbital leading to an overlap. Furthermore, if one of the copper ions forms a $p_x d_{z^2}$ interaction and the other a $p_y d_{z^2}$ interaction, the Hund's coupling leads to a ferromagnetic coupling. However, Jeschke *et al.* did not find any contribution of d_{z^2}-character in azurite from their DFT-calculations [74]. Rather, they found J_3 to be antiferromagnetic. Therefore, if the character of the interacting orbitals would be known, it would yield information as to whether the interaction J_3 is ferromagnetic with the previously described exchange mechanism.

It is generally accepted that the exchange between the copper atoms Cu2 in the backbone is the strongest resulting in a dimerization of the two spins of the backbone. The dimerization was observed in the magnetization curves: Here, a $\frac{1}{3}$-magnetization plateau was detected for applied magnetic fields between 11 T and 30 T (16 T and 26 T) perpendicular (parallel) to the crystallographic b axis [58] (Fig. 2.7). The plateau is assumed to reflect a dimerized state of the two Cu^{2+} ions on the backbone of the diamond unit, while the third Cu^{2+} on the monomer site is fully polarized. Below a temperature of T_N =1.9 K azurite is magnetically long-range ordered [75, 76]. Neutron diffraction shows that the magnetic unit cell is doubled in each direction (propagation vector $\boldsymbol{K} = (\frac{1}{2}, \frac{1}{2}, \frac{1}{2})$) [77]. Further, the magnetic moments of the Cu2-atoms (dimer sites) were found to be 0.26 μ_B, significantly smaller than the moment 0.68 μ_B found for the Cu1-atoms (monomer sites) [67]. This difference of the magnetic moment for the two sites could be due to quantum fluctuations and magnetic frustration in the system. Recently, in NMR experiments the nature of the spin dimers was studied in detail [78]. It was concluded that in the plateau phase there is a residual (0.1 μ_B) spin polarization measurable on these Cu sites, reflecting some triplet admixture on these singlet states. Given this context, a polarized neutron scattering study was initiated in order to resolve the issues of the magnetically active orbitals and residual spin density.

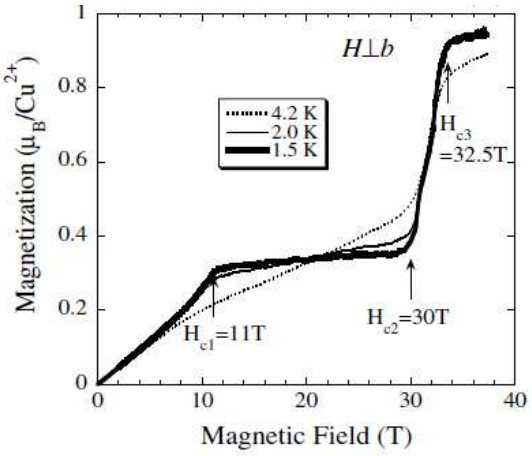

Fig. 2.7: Magnetization data of azurite from Kikuchi *et al.* [58]. The magnetic field is applied perpendicular to the b axis. The 1/3-plateau starting at 11 T indicates a strong dimer coupling of 2/3 of the Cu^{2+} ions in the diamond chain.

For the experiment on D3 a 100 mg crystal of azurite was mounted on an Al-pin and loaded into the cryomagnet such that the 9 T magnetic field was applied along the crystallographic a-axis. The applied field of 9 T was the maximum field which could be achieved with this instrument. In such a field, the monomers would not be completely polarized (ferromagnetically), but a large proportion of them would be as the applied field is close to 11 T, the field necessary to reach the plateau phase. The sample was cooled to a base temperature

of 1.3 K (below T_N) and all measurable Bragg-reflections in the monoclinic space group $P2_1/c$ were collected. Although azurite has been found to exhibit reflections pertaining to the $P2_1$ exclusion rules [67], the scattering from the $00l$ and $h0l$ where $l = 2n$ are so weak that they were not observable within the resolution of D3. Thus, it was decided to use the previously attributed, higher symmetry space group $P2_1/c$ to refine the nuclear structure. 204 Bragg peaks (120 inequivalent) were measured. From the flipping ratios $R = I^+/I^-$ of each peak the spin density is determined as it is the Fourier transform of the magnetic form factor (see section 3.1.3). Since azurite has the propagation vector $\boldsymbol{K} = (\frac{1}{2}, \frac{1}{2}, \frac{1}{2})$, the antiferromagnetic Bragg peaks are not found for the same scattering vector as the nuclear Bragg peaks. Therefore, with the given choice of Bragg peaks only the field induced moments (ferromagnetically aligned) are measured.

As the determination of the magnetic form factors by polarized neutron diffraction needs as an input the nuclear structure factor, the knowledge of the correct nuclear structure is crucial. The lattice and atomic positions are well known, but the extinction for the sample and for the wavelength used for this experiment are unknown. Therefore, the same crystal was used for both the D3 diffractometer and at the single crystal diffractometer D9, which was used to refine the nuclear structure from 873 nuclear reflections (457 inequivalent). The measurement at D9 was performed at 2.5 K in zero field. Afterwards, the nuclear Bragg peaks were refined to obtain the effect of extinction in this sample ($R_F = 100 \sum_n [|F_{obs,n} - \sqrt{\sum_k F^2_{calc,k}}|] / \sum_n F_{obs,n} = 5$).

For the refinement of the flipping-ratio data using FullProf a magnetization density $m(\boldsymbol{r}) = |\phi_l(\boldsymbol{r})|^2$ is considered for each atom where $\phi_l(\boldsymbol{r})$ is expressed in terms of a series of real spherical harmonics [79]:

$$\phi_l(\boldsymbol{r}) = O_l R_l(r) \sum_{m,p} A_l^{m,p} y_l^{m,p}(\theta, \varphi). \tag{7}$$

l indicates the azimuthal quantum number of the particular atom and O_l is an occupation factor. The real spherical harmonics $y_l^{m,p}(\theta, \varphi)$ are defined as follows:

$$y_l^{m,p}(\theta, \varphi) = \frac{1}{\sqrt{2(l + \delta_{m0})p}} \left((-1)^m Y_l^{+m}(\theta, \varphi) + p Y_l^{-m}(\theta, \varphi) \right), \tag{8}$$

with $0 \leq m \leq l$ and $p = \pm 1$. The coefficients $A_l^{m,p}$ are refineable parameters which define the occupancies of the different spherical harmonics. The radial function $R_l(r)$ is approached with the Slater-type function

$$R(r) = \frac{(2\eta)^{2n+1}}{(2n)!} r^{n-1} e^{-\eta r}, \tag{9}$$

where n is the principal quantum number and η indicates the shielding of the nuclear charge by the other electrons.

The orbital approach in Eq. (7) is only applicable if the moments for the specific atom are large enough. In the case of azurite the model can therefore be used only for the copper atoms. For the Cu1 atoms sitting on the monomer sites the magnitude of the moment is sufficient to refine all values $A_l^{m,p}$, but since the moment of the Cu2 atoms (dimer sites) is small, the coefficients

$A_l^{m,p}$ were all set to be one. Therefore, the character of the magnetically active orbital could only be refined for the copper atom Cu1. The value η was refined in such a way that it is the same for both Cu atoms. For the other atoms C, O and H a spherical approach was employed which uses also Eq. (7) but with l set to zero.
From these refinements ($R_{\text{Flip-factor}}$=100 $\times \sum |\text{Flip}_{\text{obs}} - \text{Flip}_{\text{calc}}| / \sum |\text{Flip}_{\text{obs}}|$= 2.39) the spin density map shown in Fig. 2.8 is obtained. The $d_{x^2-y^2}$-orbitals of the Cu1 ions contain a high spin density. The orbitals are pointing towards the surrounding oxygen ions suggesting that the orbitals participating in the magnetic exchange have $d_{x^2-y^2}$-character. This observation is inconsistent with the assumption deduced from the neutron scattering experiment by Rule *et al.*.

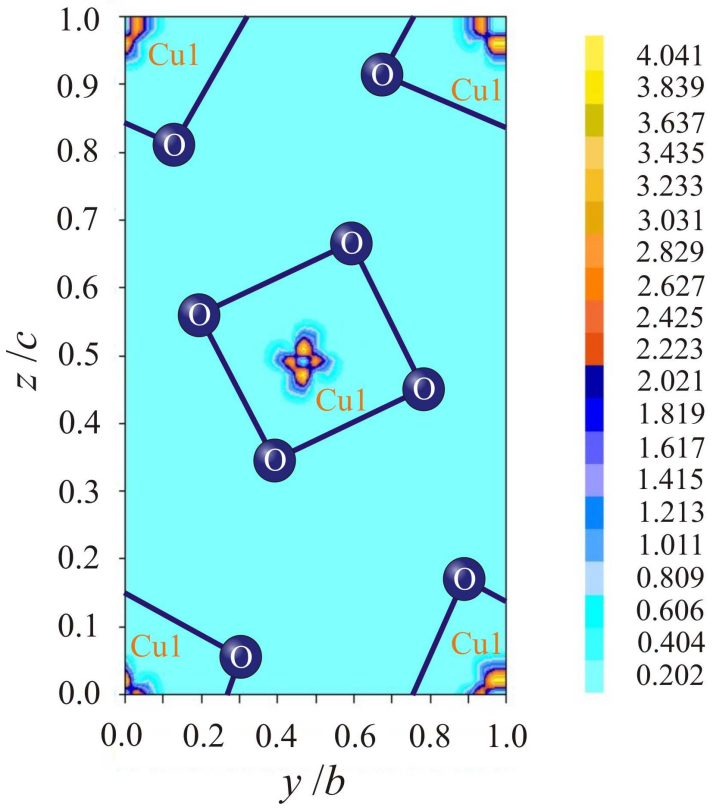

Fig. 2.8: Spin density map of azurite at $x = 0$: The $d_{x^2-y^2}$-orbitals of the Cu1-atoms are pointing towards the oxygen atoms. The surrounding oxygen atoms are added to the map as a projection onto the *bc* plane.

The magnetic moment for each atom is listed in Tab. 1. It can be seen that the Cu2 atoms (dimers) have a spin polarization of 0.07(3) μ_B along the field direction, which is consistent with the residual moment of 0.1 μ_B found in NMR-Experiments. From the magnetization data (Fig. 2.7) an average magnetic moment of 0.22 μ_B in field direction is expected for an applied magnetic field of 9 T. With the moments of Cu1 and Cu2 being 0.39(2) μ_B and 0.07(3) μ_B, respectively, an average induced moment of 0.18 μ_B is obtained. Therefore, 20 % of the moment measured in the magnetization measurements apparentely is missing in these neutron data. Since the experimental errors for the magnetic moment on carbon, oxygen, and hydrogen are larger than the fitted magnetic moments, it is hard to decide to which atom the residual moment is attached.

Atom	magnetic moment (μ_B)
Cu1	0.3879 ± 0.0743
Cu2	0.0716 ± 0.0326
C	0.0430 ± 0.1391
O1	0.0062 ± 0.0298
O2	0.0197 ± 0.0697
O3	0.0045 ± 0.0269
O4	-0.0002 ± 0.0328
H	0.0270 ± 0.0649

Tab. 1: Magnetic moments of the atoms of azurite as obtained by the refinement described in the text. The notation is the same as it was used in Ref. [67].

From the table, and taking the conclusions drawn from NMR [78], it is most probable that the oxygen atom O2 carries a small moment. O2 is the oxygen atom shared by the CuO_2 units of both Cu1 and Cu2. Adding $0.02\,\mu_B$ from the O2 ions to the average moment a magnetization of $0.19\,\mu_B$ is obtained, which is still too small, but within the error bars would fit to the $0.22\,\mu_B$ measured by magnetization.

3 Experimental Techniques

Low dimensional magnetic materials were investigated using several techniques to obtain a manifold of experimental information important for a complete understanding of the mechanisms occurring in these materials. On the one hand neutron diffraction measurements provide information on a microscopic scale. This technique is introduced in section 3.1. On the other hand bulk methods like heat capacity, magnetocaloric effect, and magnetization measurements were used to investigate the thermodynamic bulk properties (sections 3.2, 3.3, and 3.4). Furthermore, the dielectric constant was measured for the multiferroic material linarite with the experimental option described in section 3.5.

3.1 Neutron Scattering

Neutron scattering is an excellent probe for nuclear and magnetic structures as well as for excitations. Neutrons are classified in the three groups cold, thermal, and hot neutrons depending on their wavelength and energy. Thermal neutrons range in energy between 5 and 100 meV and wavelengths from 1 up to 4 Å which correspond to interatomic distances. Cold neutrons have energies between 0.1 and 10 meV, which is ideal for investigating a wide range of low energy excitations. These energies correspond to wavelengths of 3 to 10 Å. Hot neutrons have wavelengths of 0.4 to 1 Å and energies between 100 and 500 meV. [80]
Neutrons have no charge and for that reason do not interact with the electron density like x-rays but with the potential of the nuclei. Only the weak nuclear forces affect the neutrons. This implies that the penetration depth is large compared to x-ray and the sensitivity of neutron scattering to the elements is not a regular function of the atomic number (see Fig. 3.1). Thus, even light elements can be detected with a strong signal, in contrast to x-ray scattering, which has difficulty observing such elements as hydrogen. Furthermore, neutrons have a magnetic dipole moment, which interacts with unpaired electrons in magnetic ions. Therefore, neutron scattering is a powerful tool especially to investigate magnetic structures.
In a neutron scattering experiment the neutrons can transfer energy and momentum to the target obeying the conservation of energy and momentum:

$$E_i - E_f = \frac{1}{2}mv_i^2 - \frac{1}{2}mv_f^2 = \frac{1}{2m}\hbar^2\left(k_i^2 - k_f^2\right) = \hbar\omega, \tag{10}$$

$$\hbar\boldsymbol{Q} = \hbar\left(\boldsymbol{k}_i - \boldsymbol{k}_f\right), \tag{11}$$

where E_i and $\boldsymbol{k}_i$ are the initial energy and momentum and E_f and $\boldsymbol{k}_f$ the final energy and momentum of the neutron. $\boldsymbol{Q} = \boldsymbol{k}_i - \boldsymbol{k}_f$ is known as the *scattering vector*. In the case when $k_i = k_f$, the scattering is called elastic otherwise inelastic.
For analyzing a scattering process, independent of looking at nuclear or magnetic scattering, it is helpful to define three scattering cross sections (see textbooks like Ref. [80] by Squires), which are measured essentially in scattering experiments. The total cross section σ_{tot} gives the number

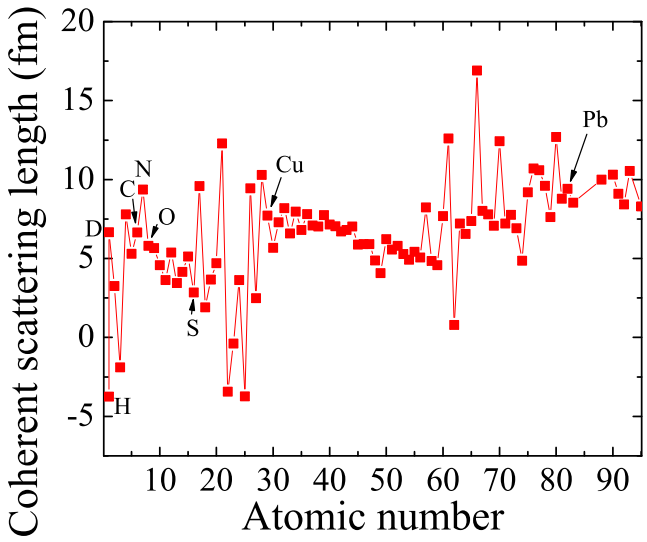

Fig. 3.1: Neutron coherent scattering lengths for different elements. The scattering lengths of the atoms are randomly distributed with respect to the electron number. That makes neutron scattering sensitive even to light elements like hydrogen. The values for the scattering length are taken from [81].

of scattered neutrons per second and flux Φ in all directions and with all energies, while the differential cross section $\frac{\mathrm{d}\sigma}{\mathrm{d}\Omega}$ takes into account only scattering into a small solid angle $\mathrm{d}\Omega$. The partial differential cross section $\frac{\mathrm{d}^2\sigma}{\mathrm{d}\Omega \mathrm{d}E_f}$ counts only the neutrons with a final energy in an energy interval between E_f and E_f+$\mathrm{d}E_f$ in a certain direction. The cross sections are related to each other as follows:

$$\sigma_{tot} = \int \frac{\mathrm{d}\sigma}{\mathrm{d}\Omega}\mathrm{d}\Omega, \tag{12}$$

$$\frac{\mathrm{d}\sigma}{d\Omega} = \int \frac{\mathrm{d}^2\sigma}{\mathrm{d}\Omega \mathrm{d}E_f}\mathrm{d}E_f. \tag{13}$$

3.1.1 Nuclear Scattering

In this chapter the most important facts about nuclear neutron scattering (see Refs. [80], [82], [83]) are summarized starting with the simplest case of a target, namely a single fixed nucleus. An incoming neutron beam with a wave vector $\boldsymbol{k}_i$ described by a plane wave $\Psi_i = e^{i\boldsymbol{k}_i \cdot \boldsymbol{r}}$ is scattered by a nucleus at the origin. Since the nuclear forces are in the range of 10^{-14} to 10^{-15} m and the neutrons have a wave length of about 10^{-10} m, the angular distribution for the scattering is spherically symmetric (s-waves). The scattered wave can therefore be described by a spherical wave $\Psi_f = -\frac{b}{r}e^{i\mathbf{k}_f \cdot \mathbf{r}}$. Here, the factor b is called the *scattering length*. For this simple case $4\pi b^2$ is equal to the total cross section. If the atom is not a strongly absorbing atom, b is independent of the wave length and the imaginary part of b is very small. Therefore, b is assumed to be real for most atoms. Since neutrons have a spin $\frac{1}{2}$, the system neutron-nucleus can have two different total spins $I + \frac{1}{2}$ and $I - \frac{1}{2}$ leading to two different values of the scattering length b^+ and b^-,

respectively.

Now, we can assume that the target consists of an assembly of fixed atoms rather than a single, isolated nucleus. In that case the scattering cross sections for a transition from state λ_i into λ_f can be evaluated by means of Fermi's golden rule, which in this case is equal to the Born approximation:

$$\left(\frac{\mathrm{d}^2\sigma}{\mathrm{d}\Omega \mathrm{d}E_f}\right)_{\lambda_i\to\lambda_f} = \frac{k_f}{k_i}\left(\frac{m}{2\pi\hbar^2}\right)^2 \left|\langle \boldsymbol{k}_f\lambda_f|V|\boldsymbol{k}_i\lambda_i\rangle\right|^2 \delta\left(E_{\lambda_i} - E_{\lambda_f} + E_i - E_f\right), \tag{14}$$

where E_i and E_f are the initial and final energy of the neutron and E_{λ_i} and E_{λ_f} the initial and final energy of the target. V corresponds to the operator of the interaction potential. Only by combining this approximation with the Fermi-pseudo-potential $V(\boldsymbol{r}) = \frac{2\pi\hbar^2}{m} b\delta(\boldsymbol{r} - \boldsymbol{R})$ from a nucleus at the position $\boldsymbol{R}$ it leads to the correct result. The matrix element in Eq. (14) can be evaluated using the Fourier transform of the pseudo-potential $V_j(\boldsymbol{Q}) = \frac{2\pi\hbar^2}{m} b_j$:

$$\langle \boldsymbol{k}_f\lambda_f|V|\boldsymbol{k}_i\lambda_i\rangle = \sum_j V_j(\boldsymbol{Q}) \left\langle \lambda_f|e^{i\boldsymbol{Q}\cdot\boldsymbol{R}_j}|\lambda\right\rangle. \tag{15}$$

The partial differential cross section is then given by:

$$\left(\frac{\mathrm{d}^2\sigma}{\mathrm{d}\Omega \mathrm{d}E_f}\right)_{\lambda_i\to\lambda_f} = \frac{k_f}{k_i}\left|\sum_j b_j \left\langle \lambda_f|e^{i\boldsymbol{Q}\cdot\boldsymbol{R}_j}|\lambda\right\rangle\right|^2 \delta\left(E_{\lambda_i} - E_{\lambda_f} + E_i - E_f\right). \tag{16}$$

To compare equation (14) with an experiment a summation over all final states λ_f and an averaging over the initial states λ_i is needed, leading to equation (17):

$$\frac{\mathrm{d}^2\sigma}{\mathrm{d}\Omega \mathrm{d}E_f} = \frac{k_f}{k_i}\frac{1}{2\pi\hbar}\sum_{j,j'} b_j b_{j'} \int_{-\infty}^{\infty} \left\langle e^{-i\boldsymbol{Q}\cdot\boldsymbol{R}_{j'}(0)} e^{i\boldsymbol{Q}\cdot\boldsymbol{R}_j(t)}\right\rangle \cdot e^{-i\omega t}\mathrm{d}t, \tag{17}$$

with the scattering vector $\boldsymbol{Q} = \boldsymbol{k}_i - \boldsymbol{k}_f$ and the position vector of the jth nucleus $\boldsymbol{R}_j$.

The scattering lengths b_j differ from each nucleus j to the other due to different isotopes or nuclear spins or both, resulting in two components of the scattering cross section, namely the *coherent* and *incoherent* scattering. Assuming that there is no correlation of the scattering lengths b_j of the different nuclei of the same element, the measured cross section is given by the average over all systems with all possible distributions of b_j. Therefore, $b_j b_{j'}$ in Eq. (17) needs to be replaced by the average $\overline{b_j b_{j'}}$ leading to the two aforementioned components of the scattering cross section:

$$\left(\frac{\mathrm{d}^2\sigma}{\mathrm{d}\Omega \mathrm{d}E_f}\right)_{coh} = \frac{\sigma_{coh}}{4\pi}\frac{k_f}{k_i}\frac{1}{2\pi\hbar}\sum_{j,j'} \int_{-\infty}^{\infty} \left\langle e^{-i\boldsymbol{Q}\cdot\boldsymbol{R}_{j'}(0)} e^{i\boldsymbol{Q}\cdot\boldsymbol{R}_j(t)}\right\rangle \cdot e^{-i\omega t}\mathrm{d}t, \tag{18}$$

$$\left(\frac{\mathrm{d}^2\sigma}{\mathrm{d}\Omega \mathrm{d}E_f}\right)_{inc} = \frac{\sigma_{inc}}{4\pi}\frac{k_f}{k_i}\frac{1}{2\pi\hbar}\sum_j \int_{-\infty}^{\infty} \left\langle e^{-i\boldsymbol{Q}\cdot\boldsymbol{R}_j(0)} e^{i\boldsymbol{Q}\cdot\boldsymbol{R}_j(t)} \right\rangle \cdot e^{-i\omega t}\mathrm{d}t, \tag{19}$$

where

$$\sigma_{coh} = 4\pi(\bar{b})^2 \;\text{ and }\; \sigma_{inc} = 4\pi(\overline{b^2} - (\bar{b})^2). \tag{20}$$

The coherent scattering is the part of the scattering which exhibits interference effects. The cause of the interference can be related to the average scattering potential, which is proportional to $\bar{b}$. Therefore, the cross section is proportional to $(\bar{b})^2$. In contrast, the incoherent scattering does not show interference since it is caused by the random distribution of the scattering lengths from the average. The scattering cross section is isotropic in this case. Thus, incoherent scattering gives in an experiment an unwanted background in the scattering spectrum. Since hydrogen is a strong incoherent scatterer, it is often substituted by the weak incoherent scatterer deuterium (see chapter 4.3.1).

Eqs. (18) and (19) can also be expressed as follows:

$$\left(\frac{\mathrm{d}^2\sigma}{\mathrm{d}\Omega \mathrm{d}E_f}\right)_{coh} = \frac{k_f}{k_i}\frac{1}{4\pi}\sigma_{coh}N' S(\boldsymbol{Q},\omega), \tag{21}$$

$$\left(\frac{\mathrm{d}^2\sigma}{\mathrm{d}\Omega \mathrm{d}E_f}\right)_{inc} = \frac{k_f}{k_i}\frac{1}{4\pi}\sigma_{inc}N' S_{inc}(\boldsymbol{Q},\omega), \tag{22}$$

where N' is the number of nuclei. $S(\boldsymbol{Q},\omega)$ and $S_{inc}(\boldsymbol{Q},\omega)$ are known as the *scattering function* and *incoherent scattering function*, respectively [80]. The scattering function is proportional to the Fourier transform of the time-dependent pair-correlation function $G(\boldsymbol{r},t)$:

$$S(\boldsymbol{Q},\omega) = \frac{1}{2\pi\hbar}\int G(\boldsymbol{r},t) e^{i(\boldsymbol{Q}\cdot\boldsymbol{r}-\omega t)}\mathrm{d}\boldsymbol{r}\mathrm{d}t. \tag{23}$$

In order to determine crystal structures from periodic lattices only the elastic coherent cross section is relevant. The basis is Eq. (18) with $\omega = 0$ and $k_i = k_f$ since it is elastic scattering. Also the thermal displacement of the atoms needs to be considered. The cross section is in that case:

$$\left(\frac{\mathrm{d}\sigma}{\mathrm{d}\Omega}\right)_{coh,el} = N\frac{(2\pi)^3}{v_0}\sum_{\boldsymbol{\tau}} \delta(\boldsymbol{Q}-\boldsymbol{\tau})|F_N(\boldsymbol{Q})|^2 \tag{24}$$

with the *nuclear unit-cell structure factor* $F_N(\boldsymbol{Q})$:

$$F_N(\boldsymbol{Q}) = \sum_{\boldsymbol{d}} \bar{b}_{\boldsymbol{d}}\, e^{i\boldsymbol{Q}\cdot\boldsymbol{d}}\, e^{-W_{\boldsymbol{d}}}, \tag{25}$$

where v_0 is the volume of the unit cell, N the number of the unit cells, $\boldsymbol{d}$ the equilibrium position of the atom j in the unit cell, and $\boldsymbol{\tau}$ a reciprocal lattice vector. The *Debye-Waller factor* $e^{-W_{\boldsymbol{d}}}$ contains the thermal displacement of the atoms about their equilibrium positions. From Eq. (24) it is clear, that scattering only occurs if the condition $\boldsymbol{Q} = \boldsymbol{\tau}$ is fulfilled. A reflection can only be

observed if the scattering vector is equal to a reciprocal lattice vector, which is known as *Bragg's law*. This condition is often expressed using the scattering angle 2θ between k_i and k_f and the d-spacing, which is the distance between a set of scattering planes in the crystal perpendicular to $\boldsymbol{\tau}$:

$$n\lambda = 2d\sin\theta. \tag{26}$$

Here, n is an integer. Eq. (24) also shows that the intensity measured in a scattering experiment is proportional to $|F_N(\boldsymbol{Q})|^2$.

3.1.2 Magnetic Scattering

The magnetic scattering occurs due to the interaction of the magnetic dipole moment of the neutron $\boldsymbol{\mu}_n = -\gamma\mu_N\boldsymbol{\sigma}$ and the magnetic field $\boldsymbol{B}$ created by the unpaired electrons of the sample, where γ is the gyromagnetic ratio, μ_N the nuclear magneton, and $\boldsymbol{\sigma}$ the Pauli spin operator for the neutron.

The magnetic field caused by the magnetic dipole moment of the electron at a point $\boldsymbol{R}$ from the electron can be expressed as:

$$\boldsymbol{B} = -\frac{\mu_0}{4\pi}\left(\nabla\times\left(\frac{-2\mu_\mathrm{B}\boldsymbol{S}\times\boldsymbol{R}}{R^3}\right) - \frac{2\mu_\mathrm{B}}{\hbar}\frac{\boldsymbol{p}_e\times\boldsymbol{R}}{R^3}\right), \tag{27}$$

where $\boldsymbol{S}$ is the spin angular momentum operator of the electron, μ_B is the Bohr magneton, and $\boldsymbol{p}_e$ the momentum of the electron.

The scattering cross section regarding the transition of the neutron spin state $\boldsymbol{\sigma}$ as well reads analog to Eq. (14)

$$\left(\frac{\mathrm{d}^2\sigma}{\mathrm{d}\Omega\mathrm{d}E_f}\right)_{\lambda_i\sigma_i\to\lambda_f\sigma_f} = \frac{k_f}{k_i}\left(\frac{m}{2\pi\hbar^2}\right)^2 |\langle\boldsymbol{k_f}\boldsymbol{\sigma_f}\lambda_f|V_m|\boldsymbol{k_i}\boldsymbol{\sigma_i}\lambda_i\rangle|^2\,\delta\left(E_{\lambda_i}-E_{\lambda_f}+E_i-E_f\right). \tag{28}$$

With the magnetic potential being $V_m = -\boldsymbol{\mu}_n\cdot\boldsymbol{B}$ the matrix element $\langle\boldsymbol{k}_f|V_m|\boldsymbol{k}_i\rangle$ in Eq. (28) can be evaluated resulting in an expression which is proportional to $\boldsymbol{\sigma}\cdot\boldsymbol{D}_\perp(\boldsymbol{Q})$ with

$$\boldsymbol{D}_\perp(\boldsymbol{Q}) = \sum_i\left(\hat{\boldsymbol{Q}}\times(\boldsymbol{S}\times\hat{\boldsymbol{Q}}) + \frac{i}{\hbar|\boldsymbol{Q}|}(\boldsymbol{p}_e\times\hat{\boldsymbol{Q}})\right)\cdot e^{i\boldsymbol{Q}\cdot\boldsymbol{r}_i} \tag{29}$$

and $\hat{\boldsymbol{Q}} = \boldsymbol{Q}/|\boldsymbol{Q}|$. Since $\boldsymbol{D}_\perp(\boldsymbol{Q})$ is the projection of $\boldsymbol{D}(\boldsymbol{Q})$ on a plane perpendicular to $\boldsymbol{Q}$ and $\boldsymbol{D}(\boldsymbol{Q})$ is proportional to the Fourier transform of the magnetization $\boldsymbol{M}(\boldsymbol{r})$, only the components of the magnetization which are perpendicular to $\boldsymbol{Q}$ contribute to the cross section. Therefore, magnetic moments which lie parallel to the scattering vector are not detectable.

To get an expression for the cross section for unpolarized neutrons, a summation of the final states must be combined with an average of the initial states similar to the process for calculating the nuclear cross section.

The final cross section for identical, localized magnetic moments $\boldsymbol{\mu} = \frac{1}{2} g \boldsymbol{S}$ at a position $\boldsymbol{R}_j$ is [82]

$$\left(\frac{\mathrm{d}^2\sigma}{\mathrm{d}\Omega \mathrm{d}E_f}\right) = \frac{k_f}{k_i}\left(\gamma r_0 \frac{g}{2} f(\boldsymbol{Q})\right)^2 \sum_{\alpha,\beta}\left(\delta_{\alpha,\beta} - \hat{Q}_\alpha \hat{Q}_\beta\right) S^{\alpha\beta}(\boldsymbol{Q},\omega), \tag{30}$$

with the magnetic scattering function

$$S^{\alpha\beta}(\boldsymbol{Q},\omega) = \frac{1}{2\pi\hbar}\int \sum_{j,j'} \left\langle S_{j'\alpha}(0) S_{j\beta}(t)\right\rangle \left\langle e^{-i\boldsymbol{Q}\cdot\boldsymbol{R}_{j'}(0)} e^{i\boldsymbol{Q}\cdot\boldsymbol{R}_j(t)}\right\rangle e^{-i\omega t}\mathrm{d}t. \tag{31}$$

The components $S_{j\alpha}$ can either be the components of the spin $\boldsymbol{S}$ in case of spin only, the components of the total angular momentum $\boldsymbol{J}$ or the components of an effective spin in case of partially quenched orbital momentum. g represents the Landé splitting factor, r_0 the classical radius of the electron, and $f(\boldsymbol{Q})$ the magnetic form factors. The magnetic scattering function, in analogy to the nuclear scattering, is the Fourier transform of the magnetic pair correlation function.

In periodic magnetic structures the magnetic moment can be described with a Fourier series

$$\boldsymbol{\mu}(\boldsymbol{R}) = \sum_{\boldsymbol{K}} \boldsymbol{S}_{\boldsymbol{K}} e^{i\boldsymbol{K}\cdot\boldsymbol{R}}, \tag{32}$$

where $\boldsymbol{K}$ is known as *propagation vector*. Its components are in units of the reciprocal lattice. The propagation vector can be either *commensurate* or *incommensurate* leading to commensurate or incommensurate magnetic structures, respectively. A structure is called commensurate (incommensurate) when the magnetic cell is (not) a simple multiple of the nuclear cell.

In the case of elastic magnetic scattering the cross section is given by

$$\left(\frac{\mathrm{d}\sigma}{\mathrm{d}\Omega}\right)_{el} = N\frac{(2\pi)^3}{v_0}\sum_{\boldsymbol{K}}\sum_{\boldsymbol{\tau}} \delta\left(\boldsymbol{Q}+\boldsymbol{K}-\boldsymbol{\tau}\right)\left|\boldsymbol{F}_{M_\perp}(\boldsymbol{\tau})\right|^2, \tag{33}$$

where $\boldsymbol{F}_{M_\perp} = \boldsymbol{Q}\times\boldsymbol{F}_M\times\boldsymbol{Q}$ is called *magnetic structure factor*. $\boldsymbol{F}_M$ is known as *magnetic unit-cell structure factor*, which is defined as follows:

$$\boldsymbol{F}_M(\boldsymbol{Q}) = \gamma r_0 \sum_{\boldsymbol{d}} \boldsymbol{S}_{\boldsymbol{K}} f_{\boldsymbol{d}}(\boldsymbol{Q}) e^{-W_d} e^{i(\boldsymbol{K}+\boldsymbol{Q})\cdot\boldsymbol{d}}. \tag{34}$$

Eq. (33) shows that magnetic Bragg peaks can be observed only at positions $\boldsymbol{Q}+\boldsymbol{K}=\boldsymbol{\tau}$, which is similar to the nuclear case except for the propagation vector $\boldsymbol{K}$. Since for each incommensurate propagation vector $\boldsymbol{K}$, the vector $-\boldsymbol{K}$ is also a propagation vector, the magnetic Bragg peaks appear symmetrically near the nuclear Bragg peaks and are called satellites to the nuclear peaks for that reason.

A special case is the case when the nuclear and the magnetic scattering occur for the same scattering vector (e.g. for ferromagnetic spin alignments). For unpolarized neutrons the squares

of the nuclear structure factor $|F_N|^2$ and the magnetic structure factors $|\boldsymbol{F}_{M_\perp}|^2$ are simply additive, but for polarized neutrons the nuclear and magnetic scattering interfere with each other. Due to the interference neutron diffraction using polarized neutrons is a sensitive tool to determine the magnetic structure factors with a high accuracy. [80, 82, 84, 85]

3.1.3 Neutron Diffraction Using Polarized Neutrons

In the case of polarized neutrons the initial and final spin states $\boldsymbol{\sigma}_{i\,\mathrm{and}\,f}$ of the neutrons need to be taken into account. The four possibilities for the initial and final spin states *spin up* $\rightarrow$ *spin up* $(++)$, *spin down* $\rightarrow$ *spin down* $(--)$, *spin up* $\rightarrow$ *spin down* $(+-)$ and *spin down* $\rightarrow$ *spin up* $(-+)$ result in four different cross sections for both nuclear and magnetic scattering. For the derivation of the nuclear cross section an averaging over the scattering length b^+ and b^- is not possible any more. Therefore, the nuclear cross section in Eq. (16) is replaced by the following expression

$$\left(\frac{\mathrm{d}^2\sigma}{\mathrm{d}\Omega\mathrm{d}E_f}\right)_{\lambda_i\rightarrow\lambda_f} = \frac{k_f}{k_i}\left|\sum_j \left\langle \boldsymbol{\sigma}_f\lambda_f \left|\widehat{b}_j e^{i\boldsymbol{Q}\cdot\boldsymbol{R}_j}\right| \boldsymbol{\sigma}_i\lambda_i\right\rangle\right|^2 \delta\left(E_{\lambda_i} - E_{\lambda_f} + E_i - E_f\right), \tag{35}$$

with $\widehat{b} = A + B\boldsymbol{\sigma}\cdot\boldsymbol{I}$ where $\boldsymbol{I}$ indicates the nuclear spin of the isotopes and A and B are constants. The analogous matrix element in Eq. (35) for magnetic scattering is proportional to $\langle\boldsymbol{\sigma}_f\lambda_f|\boldsymbol{\sigma}\cdot\boldsymbol{Q}_\perp|\boldsymbol{\sigma}_i\lambda_i\rangle$ as mentioned in the section before. Matching both nuclear and magnetic scattering together, the following expression is obtained:

$$\left(\frac{\mathrm{d}\sigma}{\mathrm{d}\Omega}\right)_{el} = N\frac{(2\pi)^3}{v_0}\sum_{\boldsymbol{\tau}}\left|\left\langle \boldsymbol{\sigma}_f\left|\widehat{F}\right|\boldsymbol{\sigma}_i\right\rangle\right|^2\delta\left(\boldsymbol{Q}-\boldsymbol{\tau}\right), \tag{36}$$

where $\widehat{F}$ is the sum of the magnetic and nuclear contributions. Therefore, the matrix element of interest for elastic scattering of polarized neutrons is $\left\langle \boldsymbol{\sigma}_f\left|\widehat{F}\right|\boldsymbol{\sigma}_i\right\rangle$. It turns out that the matrix elements for magnetically ordered crystals for the four possibilities of initial and final spin states are combinations of nuclear and magnetic structure factors

$$\begin{aligned}
\left\langle\uparrow\left|\widehat{F}\right|\uparrow\right\rangle &= \quad F_N + F_{M\perp z},\\
\left\langle\downarrow\left|\widehat{F}\right|\downarrow\right\rangle &= \quad F_N - F_{M\perp z},\\
\left\langle\downarrow\left|\widehat{F}\right|\uparrow\right\rangle &= F_{M\perp x} + iF_{M\perp y},\\
\left\langle\uparrow\left|\widehat{F}\right|\downarrow\right\rangle &= F_{M\perp x} - iF_{M\perp y}.
\end{aligned} \tag{37}$$

Here, z is the polarization direction of the neutrons.

For a scattering geometry in which $\boldsymbol{F}_M$ is parallel to z and the scattering vector $\boldsymbol{Q}$ perpendicular to z as it is shown in Fig. 3.2 both $F_{M\perp x}$ and $F_{M\perp y}$ are zero. Thus, there is no magnetic spin-flip scattering. By measuring the two intensities I^+ and I^- for the non-spin-flip scattering separately

the *flipping ratio* R is obtained:

$$R = \frac{I^+}{I^-} = \frac{\left(\frac{\mathrm{d}\sigma}{\mathrm{d}\Omega}\right)^{++}_{el}}{\left(\frac{\mathrm{d}\sigma}{\mathrm{d}\Omega}\right)^{--}_{el}} = \frac{|F_N + F_{M\perp z}|^2}{|F_N - F_{M\perp z}|^2} = \frac{F_N^* F_N + (F_N^* F_{M\perp z} + F_N F_{M\perp z}^*) + F_{M\perp z}^* F_{M\perp z}}{F_N^* F_N - (F_N^* F_{M\perp z} + F_N F_{M\perp z}^*) + F_{M\perp z}^* F_{M\perp z}}. \quad (38)$$

Due to the interference terms $F_N^* F_{M\perp z} + F_N F_{M\perp z}^*$ in Eq. (38) this method is very accurate in determining magnetic structure factors since only the flipping ratio is important and not the absolute intensity. This implies that several types of systematic errors are negligible. The high precision of the determination of the magnetic structure factors is the reason that diffraction with polarized neutrons in this geometry is used for measuring spin densities of unpaired electrons, as for instance demonstrated for azurite in Section 2.2. For this method a magnetic field is applied along z (Fig. 3.2) so that a magnetic moment along z is induced. The magnetic and nuclear scattering occurs with the same scattering vector so that both contributions can interfere with each other. The intensities for both polarizations of the incoming neutrons are measured. When the exact nuclear structure is known, the magnetic structure factor and therefore magnetic form factor $f(\boldsymbol{Q})$ as introduced in the previous section can be determined from the flipping ratios. Finally, a Fourier transformation of the magnetic form factor leads to the density of the unpaired electrons $\rho(\boldsymbol{r})$. [80, 84, 85]

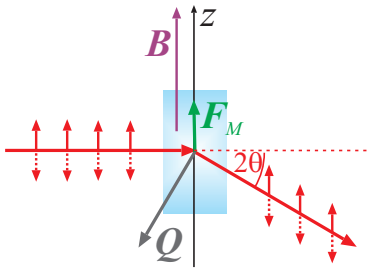

Fig. 3.2: Non-spin-flip scattering geometry: the polarization of the neutrons is parallel to the magnetization and perpendicular to the scattering vector.

3.1.4 Rotating Crystal Method

In the rotating crystal method (described in detail in textbooks like in the Refs. [80, 85]) a monochromatic beam of neutrons is directed at a single crystal. The crystal is rotated to fulfill the Bragg-condition $\boldsymbol{Q} = \boldsymbol{\tau}$ for nuclear scattering or $\boldsymbol{Q} + \boldsymbol{K} = \boldsymbol{\tau}$ for magnetic scattering.
In an experiment the δ-function in Eqs. (24) and (33) is replaced by a peak with finite width because of the mosaic spread and the instrumental resolution. Therefore, the integrated intensity of a Bragg peak is measured. That means that the scattered neutrons are counted by rotating the sample in such a way that the Bragg-condition is passed through. Therefore, the total cross section is measured in the experiment:

$$\sigma_{tot} = \int_{\text{all directions}} \left(\frac{\mathrm{d}\sigma}{\mathrm{d}\Omega}\right)_{coh,el} \mathrm{d}\Omega. \quad (39)$$

The case of a rotation of the crystal around an axis perpendicular to $\boldsymbol{k}_i$ and $\boldsymbol{k}_f$ is shown in Fig. 3.3. By varying the angle ω the vector $\boldsymbol{\tau}$ describes a circle around the origin O. When $\boldsymbol{\tau}$ crosses the Ewald's sphere, a Bragg peak is observed. The counting rate as a function of the rotating angle ω is known as *rocking curve* or *ω-scan*. From these scans the integrated intensity of a

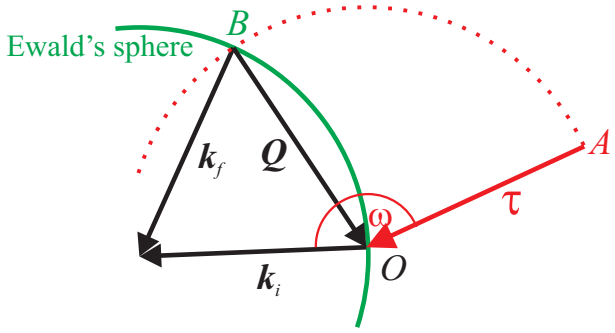

Fig. 3.3: Schematic picture of the rocking scan in the reciprocal space. The Bragg peak is observed when the point A and B coincide with each other.

nuclear Bragg peak for a flux Φ is obtained by the following relation:

$$I = \Phi \int_0^{\pi} \sigma_{tot}\, \mathrm{d}\omega = \frac{N}{v_0} \Phi \lambda^3 L(\theta) \left|F_N(\boldsymbol{\tau})\right|^2, \tag{40}$$

where N and v_0 are as before the number of unit cells and the volume of the unit cell, respectively. $L(\theta)$ is the *Lorentz factor*. For a four-circle geometry $L(\theta)$ is equal to $\frac{1}{\sin\theta}$. For geometries in which only one rotation of the crystal is possible plus the lifting of the detector by an angle ν, the additional factor $\frac{1}{\cos\nu}$ is needed. The latter case is realized when the sample is loaded for example into cryomagnets.

Eq. (40) describes also the intensity of Bragg peaks from spin dependent scattering when the nuclear structure factor $|F_N(\boldsymbol{\tau})|^2$ is replaced by the magnetic structure factor $|F_{M_\perp}(\boldsymbol{\tau})|^2$.

Taking absorption effects into account an additional factor $A(\theta)$ needs to be included in Eq. (40), which reduces the intensity by the integral

$$A(\theta) = \int_{\text{sample}} \frac{1}{V} e^{-\mu x} \mathrm{d}V. \tag{41}$$

Here, $V = v_0 N$ is the volume of the crystal, x the path length of the neutrons through the crystal, and μ is the absorption coefficient. [85]

Furthermore, extinction also reduces the detected intensity in single crystal diffraction. In contrast to absorption, it occurs only at angles which fulfill the Bragg condition and affects mainly the intensity of the strong Bragg reflections. There are two different types of extinction: primary and secondary extinction. Primary extinction is related to interference effects. It occurs within a perfect crystal, where the periodic lattice leads to a coupled system of the incident and diffracted beam. By passing through the crystal a fraction of the incident neutron beam is reflected at a lattice plane. The reflected beam is then again partly reflected at the bottom side of the next

lattice plane since the Bragg condition is still fulfilled. Due to a phase change of $\pi/2$ at each reflection the phase of double reflected beam differs by π from the incident beam, which leads to destructive interference and therefore to an attenuation of the primary beam. Secondary extinction arises for mosaic spread crystals, which can be treated as a system of misoriented perfect blocks of crystals so that interference between the blocks does not occur. If an extensive amount of the beam is reflected by the first mosaic blocks, the blocks lying deeper in the crystal are encountered by a less intense beam and reflect therefore less power. For both types of extinction effects, calculations using the dynamical theory lead to approximations of the extinction factor y, which need to be included in Eq. (40). [85–88]

3.1.5 Time-of-Flight Technique

The time-of-flight technique is used in particular at spallation sources where white neutron pulses are produced at a target and a time t_0. Due to the different wavelengths of the neutron pulse the velocities of the neutrons v differ from each other owing to de Broglie's relationship:

$$\lambda = \frac{h}{mv}, \tag{42}$$

where m is the mass of the neutron and h the Planck's constant. Therefore, neutrons with smaller wavelengths reach the sample and the detector sooner than neutrons with larger wavelength. By measuring the time $t - t_0$ it takes for the neutrons to reach the detector and by knowing the length of the flight path L the wavelength can be calculated as

$$\lambda = \frac{h(t - t_0)}{mL}. \tag{43}$$

Here, t denotes the time at which the neutrons reach the detector. Bragg's equation Eq. (26) leads then to the relation

$$d = \frac{h(t - t_0)}{mL2\sin\theta}, \tag{44}$$

which determines the d-spacing for a special scattering angle. Using detector banks the scattered neutrons for a large 2θ-range can be detected simultaneously. For single crystals a wide range in reciprocal space can be mapped out at the same time, which is a great advantage of the time-of-flight technique in contrast to the traditional way using the rotating-crystal-method for a continuous monochromatic beam. [89]

3.1.6 Neutron Scattering Instruments at Research Reactors

One possibility for producing a steady state neutron beam is by the process of nuclear fission. The fuel rods contain ^{235}U, which absorbs slow neutrons and transforms into the unstable isotope ^{236}U. During the decay of ^{236}U into smaller, stable daughter nuclei, two or three neutrons can be emitted along with energy. After slowing down the neutrons in a moderator (typically heavy water D_20), they are able to cause fission in other nuclei, which leads to a chain reaction. In contrast to nuclear power reactors, which use the emitted energy of the fission process, a research reactor uses only the emitted neutrons. These are guided from the reactor to all experiments. Furthermore, research reactors tend to have only a fraction of thermal power of nuclear power reactors. For example the reactors at the Helmholtz-Zentrum Berlin and the Institute Laue-Langevin in Grenoble (France) have a thermal power of 10 MW and 58 MW, respectively, while nuclear power reactors have a thermal power of 3000 to 4000 MW [90, 91]. With a moderator the neutrons can be cooled down to a special energy/wavelength. For cold neutrons a specialized liquid D_2 vessel at a temperature of 20 K is used, while for thermal neutrons heavy water with a temperature of 300 K is used. To obtain hot neutrons graphite is used as the moderator, which has a temperature of 2000 °C [92]. The advantage of scientific research performed at a research reactor is the provision of a continuous neutron beam. Research reactors are used for instance at BERII at the Helmholtz-Zentrum Berlin (HZB) and at the Institute Laue Langevin (ILL) in Grenoble. In the following, the instruments used in this thesis, which are located at research reactors, are described.

D10 at the Institute Laue-Langevin

The instrument D10 at the Institute Laue-Langevin in Grenoble (France) is a four-circle single crystal diffractometer. It is positioned in the guide hall using thermal neutrons. A pyrolytic graphite (PG) and a copper monochromator provide a monochromatic beam with a wavelength of 2.36 Å and 1.26 Å, respectively. The scattered neutrons are detected by a ^{3}He position sensitive detector or an analyzer in combination with a point detector. Fig. 3.4 illustrates the setup of D10. The instrument was used with two different sample environments. For zero field measurements on linarite a helium flow cryostat was used, which provides temperatures down to 1.9 K. The cryostat was mounted on a Eulerian cradle, which allows a rotation of the sample in all directions using the three angles ω, χ and ϕ. For the in field measurements of linarite a cryomagnet with a maximum field of 6 T and a minimum temperature of 1.7 K was installed. Due to the dimensions of the magnet only sample rotations around the vertical axis are possible. Further, the detector can be lifted by an angle $\nu = \pm 5°$.

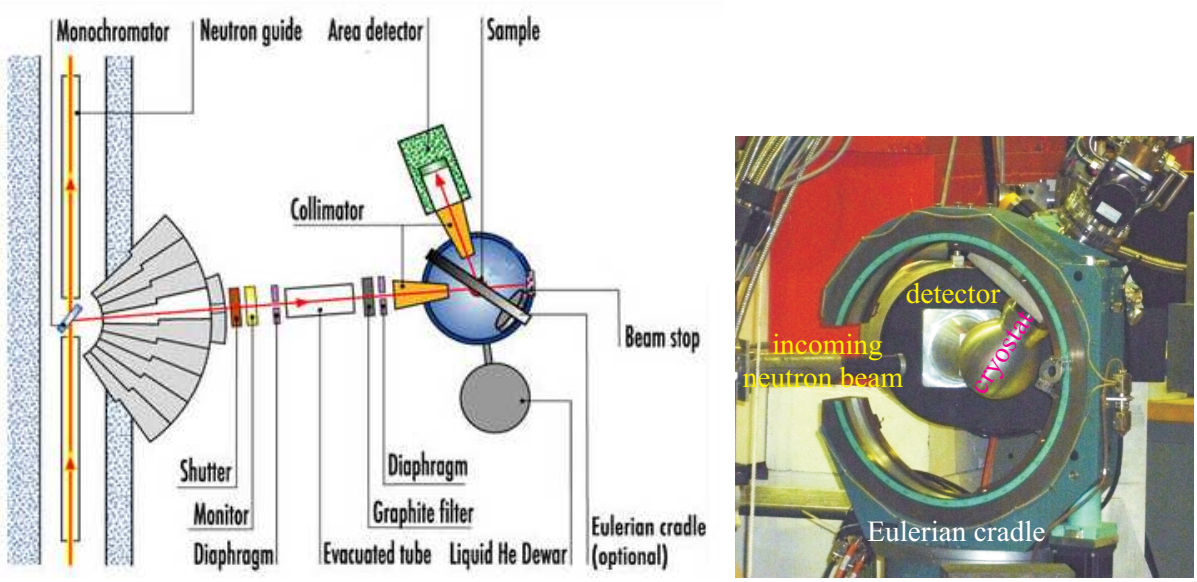

Fig. 3.4: Setup (left) and photograph (right) of the instrument D10 as it was used for the zero field measurements on linarite (the figure on the left is taken from Ref. [93]).

E4 at Helmholtz-Zentrum Berlin

For the investigation of the behavior of linarite close to the magnetic transition temperature the instrument E4 at the Helmholtz-Zentrum Berlin was used. Similar to D10 the instrument E4 uses thermal neutrons which scatter from a PG monochromator yielding a wavelength of 2.36 Å. The sample environment for this experiment consisted of a standard Orange Cryostat with a base temperature of 1.65 K and a sample stick specialized for temperature stabilities of 0.5 mK in a temperature region of 1.7 to 3.5 K. The specialized sample stick is described in the next paragraph. The cryostat was mounted on a cradle. In this set up it is possible to tilt the cryostat to about ±20° and also to rotate the cryostat with the whole sample table around its vertical axis. For the neutron detection a position sensitive detector was used.

Special Sample Stick with a Temperature Stability of ±0.5 mK

By running a standard Orange Cryostat according to the standard procedure, the sample is placed in the variable temperature insert (VTI) using exchange gas to cool down or heat up the sample. The temperature of the VTI is controlled via a needle valve regulating the helium gas flow and a heater for heating up the gas in a tube around the VTI. Therefore, the temperature is defined by a gas flow and the thermal contact via the gas in the VTI leading to a temperature stability of only $10 - 50$ mK, which is insufficient for analyzing the behavior near T_N of linarite. For that reason a new sample stick with a better temperature stability was needed. The new sample stick is designed as follows (Fig. 3.5): The bath, which is the variable temperature insert (VTI), is set on base temperature at 1.65 K. The sample has a strong thermal contact with a Cernox^{TM} 1030 temperature sensor and a 630 Ω heater. That part of the stick is located in a vacuum can with only a weak thermal link to the bath. By heating up the part which is connected

to the sample a well defined heat exchange with the bath is achieved due to the weak link, which makes it easy to control the temperature with a LakeShore LS340 temperature controller in the range of 1.7 K to 3.5 K with a temperature stability of ±0.5 mK (see Fig. 3.6).

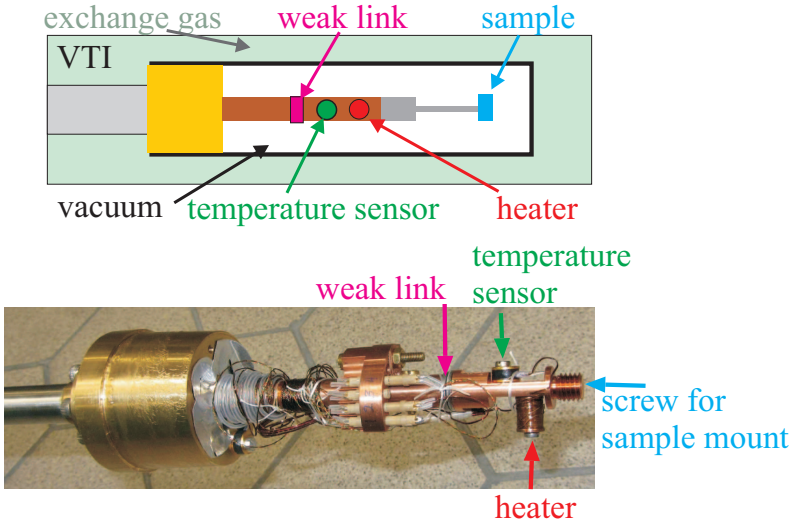

Fig. 3.5: Schematic drawing (upper figure) and photo (lower figure) of the sample stick with a temperature stability of ±0.5 mK. Description see text.

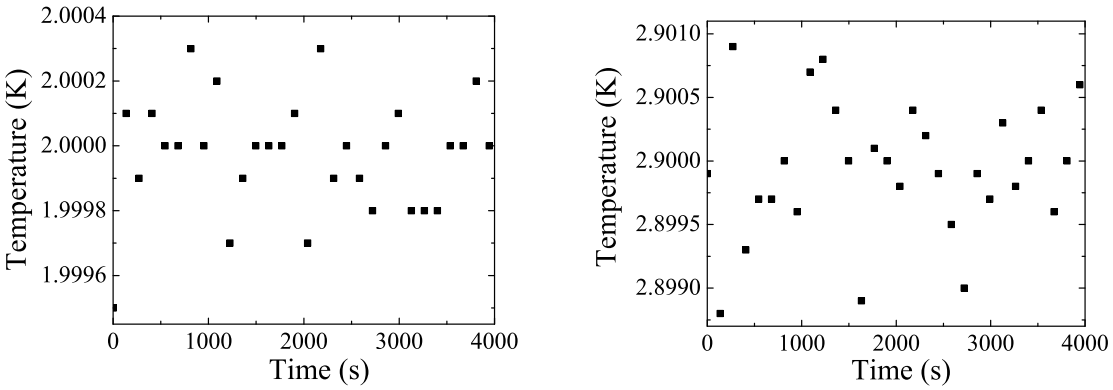

Fig. 3.6: Temperature stability for a set point of 2.0 K (left) and 2.9 K (right) during the neutron measurements.

The thermal conductivity $k(T)$ of the weak link was determined using the relation in Eq. (48). The power of the heater P was varied while the temperature of the sample and the bath was measured (Fig. 3.7). Assuming that the thermal conductivity can be described with $k(T) = k_0 T$ leading to the relation $P = \frac{1}{2} k_0 \left(T^2_{\text{sample}} - T^2_{\text{bath}} \right)$ the value k_0 is obtained by a linear fit of the plot P versus $T^2_{\text{sample}} - T^2_{\text{bath}}$. This way, a thermal conductivity $k(T) = 8.49\,\text{mW/K}^2 \cdot T$ was obtained.

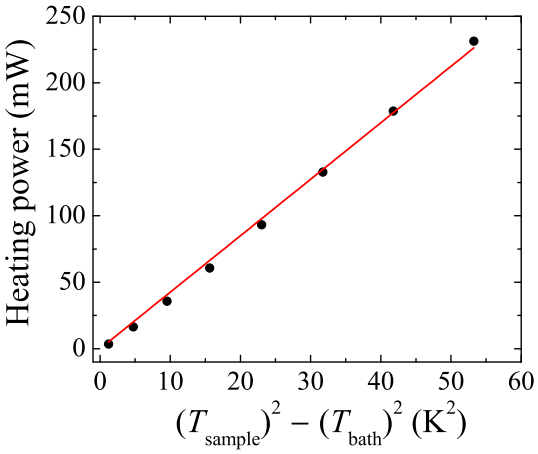

Fig. 3.7: Measurement of the thermal conductivity of the specialized sample stick via the weak link. The thermal conductivity can be described by $k(T) = 8.49\,\mathrm{mW/K^2} \cdot T$. The stick was tested in an Oxford Variox cryostat, which has a base temperature of 1.4 K. (For the experiment the stick was used in an standard Orange Cryostat with a base temperature of 1.65 K.)

E2 at the Helmholtz-Zentrum Berlin

E2 is the flat-cone diffractometer located in the reactor beam hall at HZB. The advantage of the instrument E2 is the multi detector bank which consists of four position sensitive detectors with the dimensions $300 \times 300\,\mathrm{mm}^2$ [94]. Further, the flat cone technique can be used meaning that the detectors can be lifted. Tilting angles up to 18° are possible. In this way, experimentally a wide range in reciprocal space can be mapped out easily. At E2 it can be chosen between three different thermal neutron wavelengths. The largest is obtained by means of a PG monochromator resulting in a wavelength of 2.41 Å, which was used for the experiment on copper nitrate. For this experiment a cryomagnet with a maximum field of 6 T was used with a dilution insert to reach temperatures down to 40 mK. In this configuration the sample can only be rotated around the vertical axis.

D3 at the Institute Laue-Langevin

The instrument D3 is a 2-axis hot neutron diffractometer located at the Institute Laue-Langevin. It is used for determining magnetic form factors in order to determine the spin density distribution. A hot neutron source provides neutrons, which were scattered at a Heusler Cu_2MnAl-polarizing monochromator so that the incident beam is polarized as well as monochromatic with a wavelength of 0.825 Å. The spin direction of the neutrons can be reversed by a cryogenic flipper. The sample is located in a cryomagnet with a maximum field of 9.5 T and a minimum temperature of 1.3 K. By rotating the sample stick the sample could be rotated by an angle ω. A vertical access of $-24° < \nu < +5°$ is achieved by lifting the detector. For the neutron detection a point detector is used. The measuring routine for obtaining the flipping ratio I^+/I^- of each Bragg peak consists of two steps. First, ω-scans were performed to determine the maximum of

the Bragg peak. Thereafter, the intensity of the Bragg peak maximum is measured for spin up I^+ and spin down I^- (see section 3.1.3).

3.1.7 Neutron Scattering Instruments at Spallation Sources

Neutrons for scattering experiments can also be produced by a spallation process. This process is used for example at ISIS, Rutherford Appleton Laboratory, U.K., where some of the data has been collected. Therefore, the specifics of this spallation source are described here briefly [95]. An Ion source produces H^- ions, which are focused, bunched, and accelerated in a Radio Frequency Quadrupole accelerator. Afterwards, they are further accelerated in a linear accelerator (linac) to 70 MeV. In the following the H^- ions pass through a 0.3 μm thick aluminium oxide foil, where the electrons are stripped off. The resulting protons are then accelerated to 800 MeV. Finally, an intense pulsed proton beam with a mean current of 200 μA collides with the target made from tungsten. As a result of the spallation process a neutron pulse is produced with highly energetic neutrons. These need to be slowed down for use in neutron scattering experiments. In target station 2, where some of the data presented in this thesis were obtained, this is achieved by a solid methane moderator with a temperature of about 43 K.

WISH at ISIS

The instrument WISH (Fig. 3.8) is located at the target station 2 at ISIS, Rutherford Appleton Laboratory, UK. It is a time of flight neutron scattering instrument and uses a wavelength distribution from 1.5 Å to 15 Å. A detector bank with ^{3}He position sensitive detectors covers a 2θ-range from 10° to ∼170° in-plane and ±15° out-of-plane. Thus, a d-spacing range of 0.7 Å to ∼50 Å is reached. To obtain good statistics for the observed Bragg peak the sample should be rotated in such a way that most of the wavelength spectrum can be used for that specific peak. Other peaks can be observed at the same time as well but with reduced statistics. Several sample environments can be used at WISH. A cryomagnet with a maximum magnetic field of 13.5 T and a dilution insert was used in the experiment on copper nitrate, which is described in detail in section 4.4.1.

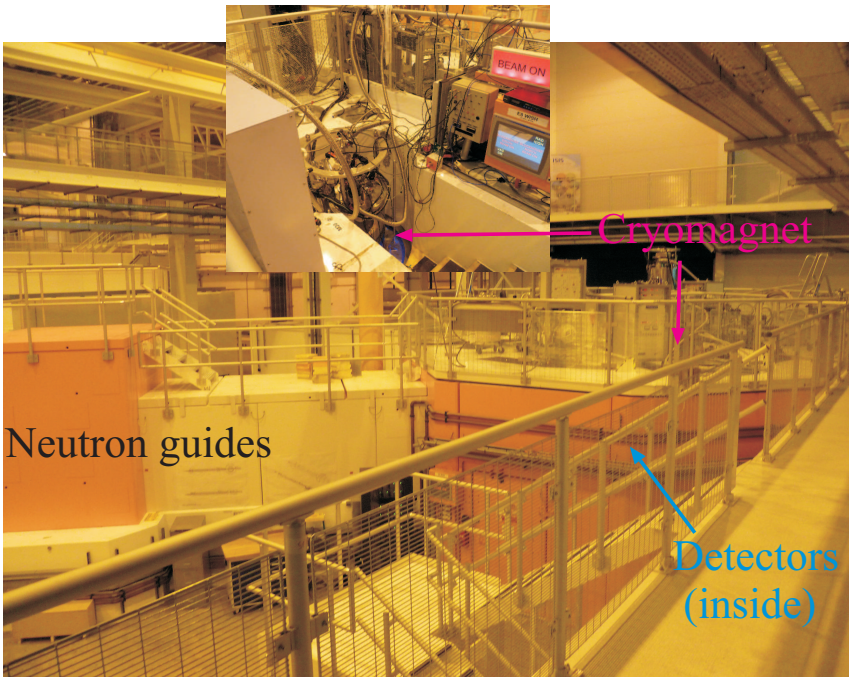

Fig. 3.8: Photograph of the WISH-instrument. The whole instrument is covered with thick concrete blocks to provide shielding from stray neutrons. The cryomagnet is placed inside the shieldings in the middle of the detector banks. Only the top of the cryomagnet is visible from the outside.

3.2 Heat Capacity

The heat capacity is defined as the heat input δQ which is necessary to increase the temperature of a material by $\mathrm{d}T$:

$$C = \frac{\delta Q}{\mathrm{d}T}. \tag{45}$$

Measuring the heat capacity of materials gives useful information about the bulk of the material e.g. information about lattice vibrations and magnetic excitations. Further, temperatures of phase transitions as well as the character of different kinds of phase transitions such as magnetic, superconducting or structural transitions can be studied. Moreover, the heat capacity is related to the entropy by the second law of thermodynamic ($\mathrm{d}S = \frac{\delta Q}{T}$) giving information about the entropy evolution [96]:

$$C = T\left(\frac{\partial S}{\partial T}\right). \tag{46}$$

There are several methods of measuring heat capacities. Two of them are introduced in the following: relaxation method and dual-slope method. Both methods can be performed with the same experimental setup.

The heat capacity option used in this thesis basically consists of a sapphire chip with a resistive heater to apply a heating power $P_h = \dot{Q}_h$ and a field calibrated Cernox temperature sensor. The chip has a well known thermal link to the bath. On the chip the sample is placed. Good thermal contact between chip and sample is achieved by using Apiezon N grease, so that the effect of this thermal contact usually can be disregarded. Taking into account the heat loss $\dot{Q}_0$ via the weak link to the bath and other types of heat losses or gains $\dot{Q}_{\mathrm{other}}$, the power balance of the system can be described by the following differential equation:

$$\dot{Q}_h = \dot{Q}_0 + \left(C_{\mathrm{sample}}(T) + C_{\mathrm{chip}}(T)\right)\dot{T} + \dot{Q}_{\mathrm{other}}, \tag{47}$$

with the heat capacity of the sample C_{sample} and the chip C_{chip}. Depending on the method, the heating power is changed differently in order to extract the heat capacity. A heat pulse is used in the relaxation method, while a steady increase/decrease of the heating power is used in the dual-slope method. Both methods will be presented in the following.

3.2.1 Relaxation Method

The relaxation method measures the time constant of the exponential decay of the sample temperature when switching on/off the heater of the calorimeter chip. From this time constant the heat capacity can be calculated as it is described for example by Bachmann *et al.* [97].

The basis of this method is Eq. (47). Further, it is assumed that the heat diffusion within the sample and chip is much faster than the diffusion along the wires to the bath. Then a one-dimensional model for the heat flow from sample to the bath via the link with the thermal

conductivity k can be used:

$$\dot{Q}_0 = \int_{T_{\text{bath}}}^{T_{\text{sample}}} k(T')\mathrm{d}T'. \tag{48}$$

As long as the temperature difference $T_{\text{sample}} - T_{\text{bath}}$ is small enough Eq. (48) can be written as:

$$\dot{Q}_0 = k(T_{\text{sample}} - T_{\text{bath}}), \tag{49}$$

with the average thermal conductivity k. Neglecting $\dot{Q}_{\text{other}}$, the power balance is then described by:

$$P_h = k(T_{\text{sample}} - T_{\text{bath}}) + (C_{\text{sample}}(T) + C_{\text{chip}}(T))\ \dot{T}_{\text{sample}}. \tag{50}$$

If the bath temperature is stable, $\frac{\mathrm{d}T_{\text{bath}}}{\mathrm{d}t} << \frac{\mathrm{d}T_{\text{sample}}}{\mathrm{d}t}$ holds so that $\frac{\mathrm{d}T_{\text{sample}}}{\mathrm{d}t}$ can be replaced by $\frac{\mathrm{d}\Delta T}{\mathrm{d}t}$ with $\Delta T = T_{\text{sample}} - T_{\text{bath}}$.

Upon switching the heater on at $t = 0$ the solution of the differential equation is

$$\Delta T(t) = \frac{P_h}{k}\left(1 - e^{-t/\tau}\right), \tag{51}$$

with the time constant $\tau = (C_{\text{sample}} + C_{\text{chip}})/k$. In analogy the solution for a switching-off process at $t = 0$ would be

$$\Delta T(t) = \Delta T_0\ e^{-t/\tau}, \tag{52}$$

where ΔT_0 indicates the temperature difference at $t = 0$. Eqs. (51) and (52) show that the time constant of the relaxation process, when switching the heater on or off, gives the heat capacity of the sample and chip at the average temperature T_{average} (i.e., average between the equilibrium sample temperatures when the heater is on and off) when the thermal conductivity k is known:

$$(C_{\text{sample}} + C_{\text{chip}}) = \tau\ k. \tag{53}$$

The thermal conductivity is obtained by measuring the constant temperature difference ΔT between sample and bath for a heating power P_h after a time much bigger than the time constant:

$$k = \frac{P_h}{\Delta T(t >> \tau)}. \tag{54}$$

In the heat capacity measurement the relaxations for both switching the heater on and off are used to determine the time constant as described by Kiefer [98]. A similar exponential decay as described by Eqs. (51) and (52) can be obtained by considering a constant bias power even if $T_{\text{sample}} - T_{\text{bath}}$ is not small in this case. By applying a bias power rather than by regulating the bath temperature, the sample temperature can be regulated faster and more accurately. For this reason a bias power was used in the measurements presented in this thesis. The temperature of the bath is kept constant. For the heat step the heating power is increased within 90 μs. A typical curve for sample temperature and heating power during a heat pulse for $T_{\text{average}} \approx 313.5$ mK is

shown in Fig. 3.9. The data were collected at the CM8T instrument at the Helmholtz-Zentrum Berlin.

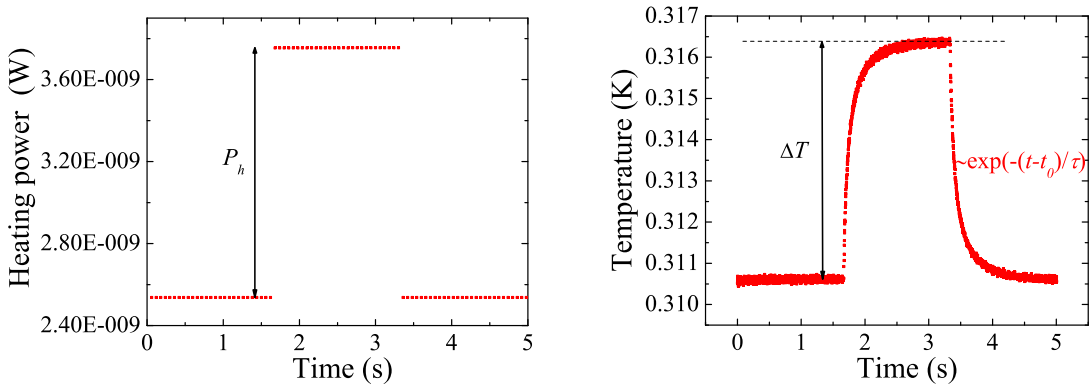

Fig. 3.9: Heating pulse (left) and temperature response of the sample (here: linarite) at $T_{\text{average}} = 313.5\,\text{mK}$ (right) with an applied bias power of $2.54{\cdot}10^{-9}\,\text{W}$.

Since the heat capacity of both sample and chip is measured, the contribution of the chip needs to be known. Therefore, a measurement with the empty chip is performed before the sample is attached. This data is subtracted from the sample measurement to obtain the heat capacity of the sample. For this measurement Apiezon N grease is already on the chip, which serves as a glue and assures a good thermal contact of the sample. This way, no additional correction is needed for the heat capacity of the Apiezon N.

In case of a poor thermal contact between the sample and the chip, a second relaxation process with a time constant τ_2 is present, arising from the internal thermal relaxation of the system chip/sample. Since the two time constants τ_2 and τ usually differ by one order of magnitude from each other, it is often not possible to fit two exponential functions to the data. An approximation was introduced by Shepherd [99] which still uses only one exponential function $f(t) = A\exp(-t/\tau)$ to fit the data. Using this fitting function the heat capacity can be approximated by

$$C \sim k\frac{A\tau}{\Delta T}, \tag{55}$$

where ΔT is the temperature difference of the heat pulse.

For investigations of phase transitions the relaxation method described above is unsuitable. Near the transition the heat step drives the temperature of the sample over the transition temperature during a single pulse. In this case the relaxation cannot be described by the simple exponential decay discussed above resulting in incorrect values of C. This problem can be avoided by using the dual-slope method described in the next section.

3.2.2 Dual-Slope Method

The dual-slope method is a variation of the relaxation method [100]. The chip with the sample is continuously heated, for instance with a quadratic increase in heating power $P_h(t) = \dot{Q}_h(t)$ from a start temperature T_s up to an end temperature T_e. Afterwards, the sample is cooled continuously with typically the same sweep rate using the heating power $P_c(t) = \dot{Q}_c(t)$. In order to achieve a cooling of the sample $P_c(t)$ is smaller than the power loss $\dot{Q}_0$ due to the thermal link to the bath. Typical cooling and heating curves for such an experiment as well as the response of the sample temperature is depicted in Fig. 3.10, where a phase transition is observable in the raw data as a very small anomaly, implying that a very good temperature resolution is necessary.

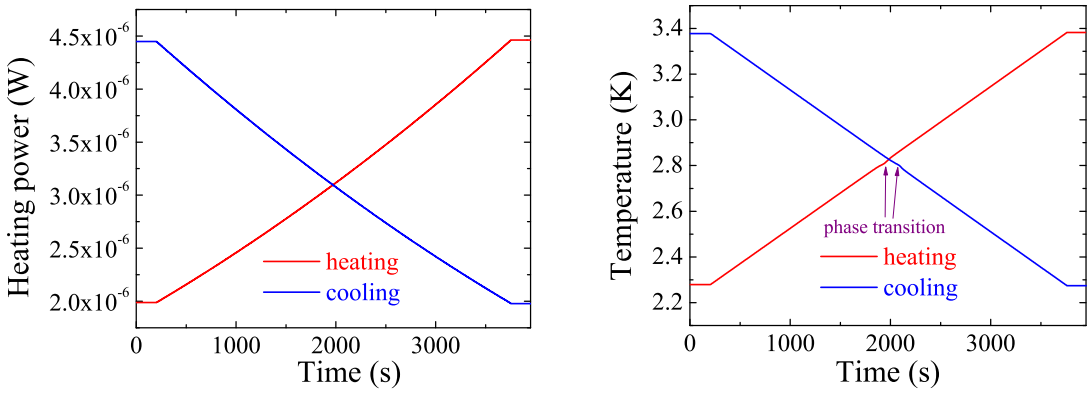

Fig. 3.10: Experimental parameters for the dual-slope method: quadratic increase/decrease of the heating power (left). Resulting temperature change of the sample (here: linarite) (right). The change in the slope of the temperature curve at 2.8 K is due to the phase magnetic transition of the sample.

The power balance for heating and cooling can be described as follows:

$$(C_{\text{sample}}(T) + C_{\text{chip}}(T))\ \dot{T}_h = \dot{Q}_h - \dot{Q}_0(T) + \dot{Q}_{\text{other}}(T), \tag{56}$$

$$(C_{\text{sample}}(T) + C_{\text{chip}}(T))\ \dot{T}_c = \dot{Q}_c - \dot{Q}_0(T) + \dot{Q}_{\text{other}}(T), \tag{57}$$

where $\dot{Q}_{\text{other}}$ again represents other heat gains or losses of any other extrinsic origin. By assuming that $\dot{Q}_0(T)$ and $\dot{Q}_{\text{other}}(T)$ are not explicitly time dependent and that the measurement is taken in thermal equilibrium, a simple subtraction of Eq. (56) and Eq. (57) leads to the relation

$$(C_{\text{sample}}(T) + C_{\text{chip}}(T)) = \frac{\dot{Q}_h - \dot{Q}_c}{\dot{T}_h - \dot{T}_c}. \tag{58}$$

With this method it is obviously not necessary to know the thermal conductance between sample and bath or any other heat gains or losses, which is one of the advantages of this method. Another great advantage is that the heat capacity is measured as a continuous function of the temperature. This is in contrast to the relaxation method, which averages the heat capacity over a temperature

interval. Therefore, the dual-slope method is most suitable for investigating phase transitions. The disadvantage is the necessity of the correction for the hysteresis in case a first order phase transition occurs.
In principle, it is also possible to calculate C from the heating *or* cooling branch only. The heat capacity is then obtained by Eq. (47) and (48). The disadvantage is that the integral of the thermal conductivity in Eq. (48) needs to be known with very high accuracy.

3.2.3 Experimental Setup

For this thesis a new experimental setup was built. As sample environment a superconducting solenoid magnet with a maximum field of 8 T (CM8T) and a ^{3}He stick from Oxford Instruments were available, which is described in more detail in the next section. The calorimeter and the electronics were constructed during this thesis following the design of Kiefer [98]. The hardware can be used for heat capacity as well as for magnetocaloric effect measurements.
The calorimeter consists of a 10 mm × 10 mm × 0.2 mm sapphire chip on which the sample is glued with Apiezon N grease (Fig. 3.11). The chip is attached by nylon cords to a copper frame (thermal bath). A resistive heater made from platinum is evaporated on the chip using the vapor deposition method. It has a resistance of about 9.1 kΩ at low temperatures. Further, a Cernox^{TM} 1010 temperature sensor is glued on the chip with GE varnish in order to determine the sample temperature. The copper frame serves as the thermal bath, whose temperature is measured with another Cernox^{TM} 1010 temperature sensor. The thermal contact between chip and bath is provided by the aforementioned nylon cords and phosphor bronze wires with a diameter of 50 μm, which are the electrical contacts to the sample sensor and the heater. Mainly the phosphor bronze wires are responsible for the thermal conductance k representing the weak thermal link.

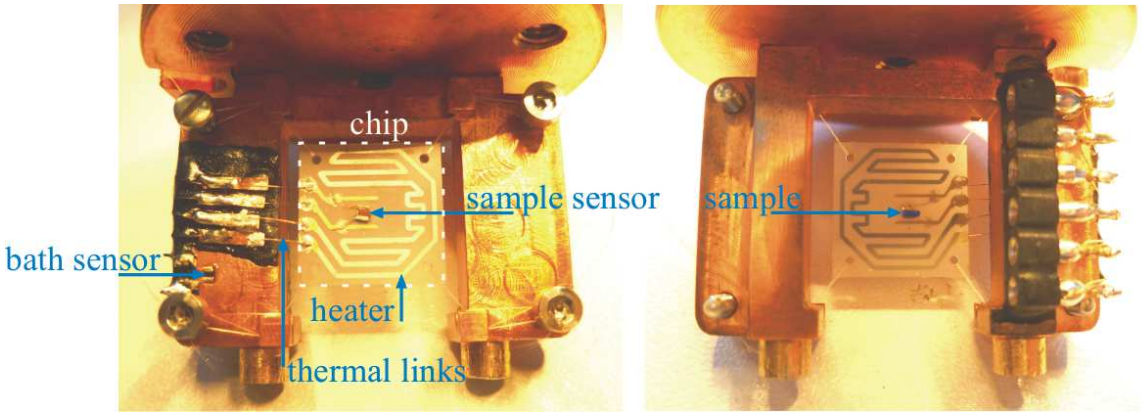

Fig. 3.11: Calorimeter for the CM8T instrument at HZB, which can be used for heat capacity as well as for magnetocaloric effect measurements, with top and bottom views.

The resistance of the sample temperature sensor is measured via an AC-resistance bridge, which is described in detail in Appendix A.1, while the bath temperature is measured using a LakeShore

LS370 resistance bridge. The calorimeter is portable and was also attached to a Kelvinox 400 dilution refrigerator in a 17 T magnet (CM17T) for magnetocaloric effect and heat capacity measurements on copper nitrate. For these measurements sample and bath temperature were both read out with a LS370 device. The disadvantage of the LS370 compared to the bridge setup is that the read out frequency of the resistance is much lower for the LakeShore bridge. To obtain reasonable values of the heat capacity by the relaxation method the time constant τ should be in the range of a minute. For smaller time constants fast electronics are required for a reasonable resolution of the temperature decay, which is only possible by using the aforementioned AC-resistance bridge. The heating power is provided by a Burster Digistant 4462 while the heating power is measured via two Keithley 2000 multimeters. A timer is used to close and reopen a relay which adds a variable parallel resistance into the electric circuit for a certain time. This way, the heating power is increased for this period producing a well defined heat pulse. The details of the heater are described in Appendix A.2.

3.2.4 Sample Environment

The heat capacity using the above described techniques can be measured at temperatures down to 300 mK using a Heliox 2^{VL} sorption pumped ^{3}He Insert from Oxford Instruments (Fig. 3.12). Low temperatures are reached by pumping on liquid ^{3}He using a closed circuit. For the cooling process, first of all, ^{3}He gas from a storage dump needs to be condensed. That is realized by means of a 1K-pot, which is a liquid ^{4}He reservoir connected to the ^{4}He bath via a pick-up tube. By pumping at the reservoir the 1K-pot is cooled down to 1.3 K (during the condensing process 1.7–1.8 K) according to the Clausius Clapeyron equation. Thermal contact between 1K-pot and ^{3}He gas leads to condensation of the gas, which is running down into the ^{3}He-pot. During the condensing process the adsorption pump, which consists of charcoal, needs to stay at 40 K in order to release stored ^{3}He gas. As soon as all ^{3}He is condensed, the adsorption pump can be cooled down with liquid helium from the bath using a second pick-up tube. The pump begins to pump at the ^{3}He reservoir, this way cooling it to a base temperatures of 297 mK. After about 25 hours at base temperature the ^{3}He gas needs to be condensed again.
The copper frame of the calorimeter is mounted on a platform which is thermally connected to the ^{3}He-pot of the sample stick. The frame can be completely disconnected and used in any other temperature insert or even in a glovebox for sample mounting. In an experiment, the frame sits inside a copper can, which serves as a radiation shield from the surrounding 4.2 K environment. Much effort was put into shielding of the wiring and thermal anchoring in order to achieve a high temperature resolution and a low base temperature. Two twisted pairs of cables made from constantan are used for measuring the bath temperature via a four point measurement. Two other pairs are used for the heater on the chip. In order to reduce the electrical noise level coaxial cables are used to measure the sample temperature. The core of a coaxial cable is hard to anchor thermally due to the dielectric insulator surrounding it. Thus, they transport more heat than the usual constantan cables, which would cause an increase of the base temperature.

Therefore, coaxial cables are used only down to the 1K-pot. Between the 1K-pot and the ^{3}He-pot constantan cables were installed. The sample stick was used in an Oxford bath cryostat with a superconducting magnet with a maximum field of 8 T.

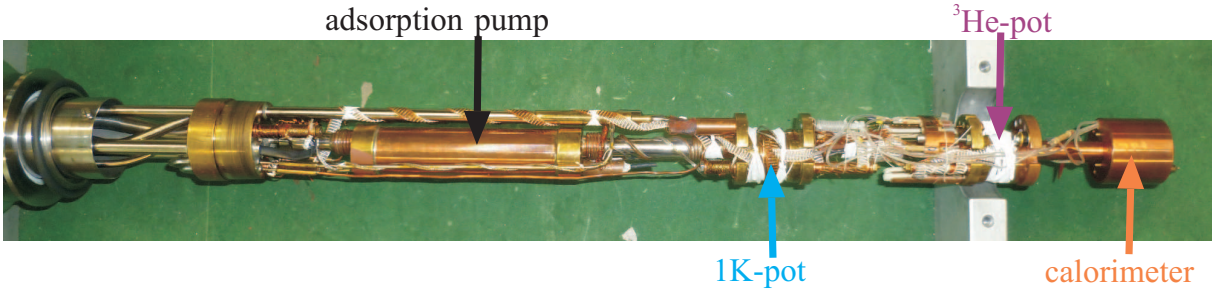

Fig. 3.12: Photograph of the ^{3}He insert from Oxford Instrument. At the ^{3}He-pot the calorimeter is attached, which is surrounded by a copper cap.

For measurements at lower temperatures a dilution refrigerator was used. A dilution refrigerator uses the complex phase diagram of ^{3}He-^{4}He-mixtures. If these He-mixtures are cooled down to temperatures below 0.87 K they separate into two phases: the ^{3}He-rich phase and the superfluid ^{4}He-rich phase. For temperatures close to zero, the ^{3}He-rich phase becomes pure ^{3}He (concentrated phase) while the other phase contains a constant concentration of ^{3}He of 6.6 % (dilute phase). In a dilution refrigerator the mixing of ^{3}He and ^{4}He occurs in the *mixing chamber*. When ^{3}He atoms pass from the concentrated phase into the dilute phase, the mixing chamber is cooled down since the enthalpy of the dilute phase is larger than the enthalpy of the concentrated phase. The diluted phase is connected with the *still*. It is a pot heated up to a temperature of about 0.7 K. Due to the higher vapor pressure of ^{3}He at that temperature, only ^{3}He atoms are recovered while pumping the still. The reduction of ^{3}He concentration of the dilute phase at the still keeps the whole refrigeration process running continuously. For more details see textbooks like Ref. [101]. For the low temperature heat capacity measurements and magnetocaloric effect measurements of copper nitrate the dilution fridge described in Ref. [102] was used.

3.3 Magnetocaloric Effect

The (adiabatic) magnetocaloric effect Θ measures the temperature change $\mathrm{d}T$ of a magnetic sample by changing the applied magnetic field $\mathrm{d}H$ for adiabatic - isobaric processes [96]:

$$\Theta = \frac{\mathrm{d}T}{\mathrm{d}H} \ . \tag{59}$$

The temperature change is due to the exchange of entropy between the phonons and the spins [62]. By increasing the magnetic field H the moments become aligned resulting in a decrease of entropy of the magnetic moments. Since the field change is adiabatic, the overall entropy of the sample remains constant, which results in an increase of the number of phonons (lattice vibrations) and therefore in an increase of the sample temperature.

Regarding the total differential of the entropy of a magnetic material

$$\mathrm{d}S = \left(\frac{\partial S}{\partial T}\right)_{H,p} \mathrm{d}T + \left(\frac{\partial S}{\partial H}\right)_{T,p} \mathrm{d}H + \left(\frac{\partial S}{\partial p}\right)_{H,T} \mathrm{d}p \ , \tag{60}$$

the magnetocaloric effect for an adiabatic ($\mathrm{d}S = 0$) - isobaric ($\mathrm{d}p = 0$) process can be formulated as

$$\frac{\mathrm{d}T}{\mathrm{d}H} = \left(\frac{\partial S}{\partial H}\right)_{T,p} \Big/ \left(\frac{\partial S}{\partial T}\right)_{H,p} = -\frac{T}{C_{H,p}} \left(\frac{\partial S}{\partial H}\right)_{T,p} = -\frac{T}{C_{H,p}} \left(\frac{\partial M}{\partial T}\right)_{H,p} \ . \tag{61}$$

For the last two steps in Eq. (61) the equation Eq. (46) and the the Maxwell relation $\left(\frac{\partial S}{\partial H}\right)_{T,p} = \left(\frac{\partial M}{\partial T}\right)_{H,p}$ were used.

To measure the magnetocaloric effect the same experimental setup can be used as for the heat capacity measurement. Due to the weak thermal link between sample and thermal bath, the experimental conditions cannot be considered as being fully adiabatic, but rather as quasi-isothermal. Thus, Θ cannot be measured by simply recording the sample temperature as it is indicated by Eq. (59). Instead the increase of the heat within the sample due to magnetocaloric effect $\mathrm{d}Q/\mathrm{d}H$ is measured [98].

The power balance of the system is described by adding to the power balance in Eq. (47) the heating power of the sample due to the changing field, $\dot{Q}_{\mathrm{sample}}$, and using the heat loss due to the thermal link in Eq. (48) ($\dot{Q}_{\mathrm{other}}$ is neglected):

$$\dot{Q}_{\mathrm{sample}} = -\dot{Q}_h + \int_{T_{\mathrm{bath}}}^{T_{\mathrm{sample}}} k(T')\mathrm{d}T' + \left(C_{\mathrm{sample}}(T) + C_{\mathrm{chip}}(T)\right) \dot{T} \ . \tag{62}$$

The heating power $\dot{Q}_h = \text{const.}$ is only used for setting the chip and sample to a constant temperature (bias power) so that it is possible to measure the magnetocaloric effect at different temperatures. This is only done for temperatures down to 300 mK, which is the lowest attainable temperature of the ^{3}He system. For measurements at lower temperatures the sample temperature is controlled via the mixing chamber of the dilution fridge.

For slow sweep rates the temperature change $\dot{T}$ is negligible resulting in:

$$\dot{Q}_{\text{sample}} = -\dot{Q}_h - \int_{T_{\text{bath}}}^{T_{\text{sample}}} k(T')\mathrm{d}T' \ . \tag{63}$$

The change of the heat increase of the sample by sweeping the magnetic field $\frac{\mathrm{d}Q_{\text{sample}}(H)}{\mathrm{d}H}$ with a sweep rate $\dot{H}$ is described by [98]:

$$\frac{\mathrm{d}Q_{\text{sample}}(H)}{\mathrm{d}H} = \frac{1}{\dot{H}} \left(-\dot{Q}_h + \int_{T_{\text{bath}}}^{T_{\text{sample}}} k(T')\mathrm{d}T' \right) \ . \tag{64}$$

Equation (64) shows that knowing the exact integral of the thermal conductance is crucial for these measurements. For the approximation of the integral an additional measurement is performed: By setting a constant heating power and measuring in the equilibrium state the temperature of the sample and the bath the integral can be approximated. Using this method the temperature of both the sample and the bath need to be measured during the field sweep.
In contrast to the measurement of the adiabatic magnetocaloric effect Θ (Eq. (59)), a direct measurement of $\mathrm{d}Q/\mathrm{d}H$ has great advantages. From these measurements the change of entropy can be calculated easily, which is equivalent to the derivative of the magnetization with respect to the temperature using Maxwell's relation mentioned above:

$$\frac{\mathrm{d}S}{\mathrm{d}H} = \frac{\mathrm{d}M}{\mathrm{d}T} = -\frac{1}{T}\frac{\mathrm{d}Q_{\text{magcal}}(H)}{\mathrm{d}H}. \tag{65}$$

Assuming that the only heating power of the sample is due to the magnetocaloric effect, the adiabatic magnetocaloric effect Θ can be calculated as follows if the heat capacity is known:

$$\frac{\mathrm{d}T}{\mathrm{d}H} = \frac{1}{(C_{\text{sample}} + C_{\text{chip}})(H)}\frac{\mathrm{d}Q_{\text{magcal}}(H)}{\mathrm{d}H}. \tag{66}$$

It should be emphasized that the magnetocaloric effect is obtained by varying the magnetic field. Especially for determining phase boundaries in a magnetic phase diagram which do not change much with the temperature, magnetocaloric effect measurements are a powerful tool. In contrast, in heat capacity measurements the changing parameter is the temperature, so that magnetocaloric effect measurements complement heat capacity measurements very well.
For the magnetocaloric effect measurements on linarite fields up to 10 T were required. Therefore, measurements using the CM8T-setup (described in this thesis) alone were not possible to fully map out the phase diagram due to the maximum field of 8 T. Instead the instrument described in Ref. [98], which features a 14 T magnet, was used for this purpose. Only for the detailed study of the transition into region II the CM8T-setup was used.

3.4 Magnetization Measurements

Magnetization measurements are crucial for studying the magnetic properties of materials. The evolution of the magnetization with field and temperature reveals the magnitude of the exchange constants, phase transitions into a long range ordered phase, or even changes of the spin structure of long range ordered states. Several different techniques have been established depending on the requirements such as temperature range, field range, sample size, and accuracy. Two different techniques were used during this thesis. They are introduced in the following.

3.4.1 Vibrating Sample Magnetometer

For magnetization measurements at temperatures down to 1.8 K a PPMS (Physical Property Measurement System) with VSM (Vibrating Sample Magnetometer) option from Quantum Design was used. The vibrating sample magnetometer is a DC-magnetometer which resolves magnetization changes of less than 10^{-6} emu [103]. The PPMS provides applied magnetic fields up to 14 T.

For the measurements the sample is oscillated sinusoidally with a frequency f of 40 Hz and an oscillating amplitude A of 1 mm to 3 mm in pick-up coils. The changing flux as a result of the sample movement induces the voltage $U_{ind} = -\frac{\mathrm{d}\Phi}{\mathrm{d}t}$ in the coils from which the magnetic moment M of the sample can be obtained [103]:

$$U_{ind} = 2\pi f C M A \sin(2\pi f t), \tag{67}$$

where C is a constant specific for the instrument and t is the time. The fixed frequency allows the use of lock-in techniques, which results in the high resolution. On the other hand, heat input due to mechanical friction prevents the use of this technique in ^{3}He or dilution fridges.

3.4.2 Cantilever Magnetometer

The magnetization data at temperatures down to 100 mK were obtained by using the in-house built cantilever magnetometer at the Laboratory for Magnetic Measurements at the HZB (LaMMB) [33], which works like a Faraday force magnetometer.

The sample is mounted with Apiezon N on a silicon cantilever ($\sim 5\,\mu$m thickness) which is shown in Fig. 3.13. By mounting a magnetic sample with a moment $\boldsymbol{M}$ on the cantilever and placing it within a gradient coil and an additional field coil, it will bend due to the static magnetic field as well as the magnetic field gradient. Two components contribute to the bending of the cantilever: on the one hand, the torque contribution $\boldsymbol{\tau}_T = \boldsymbol{M} \times \boldsymbol{B}$ stemming from the magnetic moment perpendicular to the applied field, and on the other hand, the torque $\boldsymbol{\tau_F} = \boldsymbol{L} \times \boldsymbol{F}_F$ stemming from the force on the magnetic moment from the magnetic field gradient in the gradient coils ($\boldsymbol{F} = \boldsymbol{M} \cdot \nabla \boldsymbol{B}$).

For an applied gradient field $\frac{\partial B_z}{\partial z}$ and a static magnetic field B_z along the z-direction as it is

shown in Fig. 3.13, only a torque τ_x in x direction can cause a bending. The torque originating from the gradient field $\tau_{F,x}$ is given by

$$\tau_{F,x} = L_y M_z \frac{\partial B_z}{\partial z}, \tag{68}$$

while the torque $\tau_{T,x}$ stemming from the static field is given by

$$\tau_{T,x} = M_y B_z, \tag{69}$$

where L is defined as in Fig. 3.13.

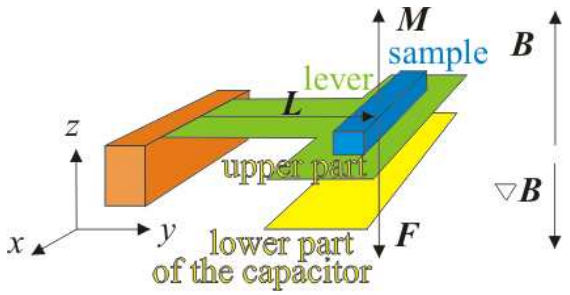

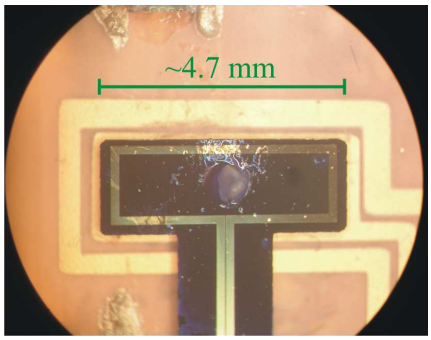

Fig. 3.13: left: Schematic drawing of the cantilever magnetometer for measurements of the magnetic moment parallel to the applied magnetic field (from Ref. [98]). right: Photo of the cantilever with a linarite sample on top (from Ref. [33]).

The component of the magnetic moment which is mostly of interest is the component along the field direction (here: M_z). It is obtained by performing measurements at two different gradient fields. The torque contribution $\tau_{T,x}$ remains the same for a changing gradient field and therefore it can be eliminated.

The cantilever is coated with gold on the underpart, this way providing the upper part of a plate capacitor while below the cantilever a fixed gold plate serves as the lower part of the capacitor. For this capacitor the distance between the two plates is about 0.17 mm. The capacitance is measured by means of an Andeen Hagerling 2500A Capacitance Bridge. If the cantilever bends due to the torque $\boldsymbol{\tau}$, a change in capacitance $\Delta C = C - C_0$ will occur (C_0 is the capacitance without $\boldsymbol{\tau}$).

A current loop made from gold is on top of the cantilever, which produces a well defined moment $M_{z,cal}$ so that the device can be calibrated in-situ and M_z can be measured quantitatively.

With the field coil it is possible to perform magnetization measurements in applied magnetic fields up to 17 T. The maximum gradient of the gradient coil is 9 T/m. A dilution refrigerator allows measurements at temperatures down to 100 mK.

With the same measurement routine the torque contribution $\tau_{T,x}$ and therefore M_y can be extracted from the measurements with both gradient fields.

3.5 Measurements of Ferroelectric Phase Transitions

For the measurements of ferroelectric phase transitions in linarite an in-house built measurement option shown in Fig. 3.14 was used. The sample is located in between the two copper plates of a plate capacitor in such a way that the upper plate does not have contact with the sample. In this configuration possible thermal expansions or contributions of the magnetostriction to the signal can be avoided. An AC-capacity bridge Andeen Hagerling 2500A is used to measure the capacitance C. For an ideal capacitor C is proportional to the dielectric constant ϵ:

$$C = \epsilon\epsilon_0 \frac{A}{d}, \tag{70}$$

where A is the area of the plates, d the distance between them, and ϵ_0 is the vacuum permittivity. For a ferroelectric material, below a certain temperature T_C a polarization P is present even in the absence of an external electric field. Therefore, for temperatures close to T_C the dielectric constant becomes infinite since a small field is sufficient to change the polarization substantially [104]. Thus, in an experiment a peak in the dielectric constant is expected at T_C, which appears as a peak in the capacitance C. Note that due to the fact that the capacitor is not ideal the phase transitions were defined via the peak in the capacitance. Thus, quantitative values of the dielectric constant were not determined.

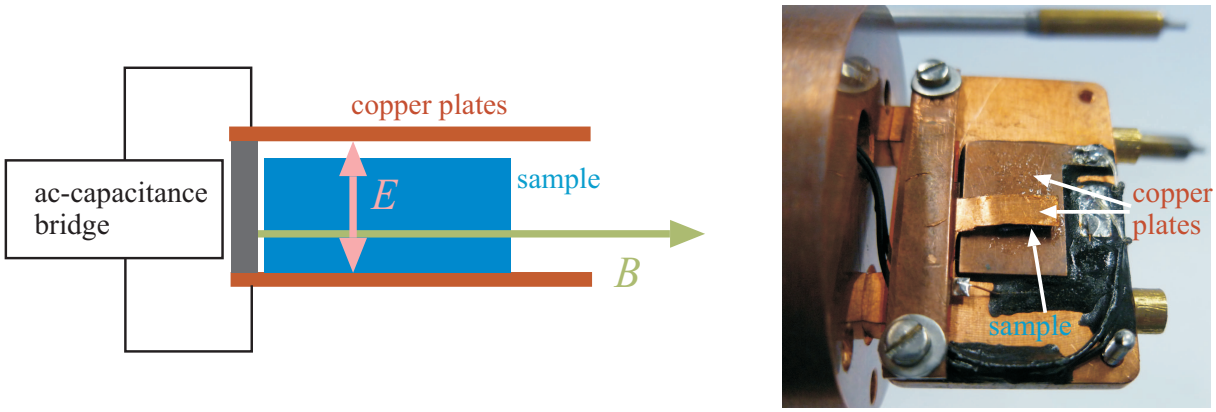

Fig. 3.14: Schematic drawing and photograph of the option to measure the ferroelectric phase transitions in linarite.

For the measurements on linarite the option shown in Fig. 3.14 was attached to the ^{3}He-stick described in section 3.2.4 and loaded into a cryomagnet with a maximum field of 8 T.

4 Alternating Antiferromagnetic Chain: Copper Nitrate

In order to investigate low dimensional quantum systems it is required to use the techniques and instruments described in the previous chapter at very low temperatures since only then the most interesting phenomena become emergent in these systems. This in turn poses a challenge to the experimentalist, which becomes especially apparent if studying the alternating antiferromagnetic spin chain copper nitrate. This compound is an example of a dimerized spin $S = \frac{1}{2}$ system which is supposed to undergo a Bose-Einstein condensation of triplons in applied magnetic fields of a few Tesla and temperatures below $\sim$160 mK.

The concept of Bose-Einstein condensation of triplons is introduced in the following section. Section 4.2 summarizes the properties of copper nitrate, focusing on the magnetic properties that are already known from the literature. In the next section the single crystal growth and sample characterization is described (section 4.3). Further, in section 4.4 new neutron diffraction, magnetization, and magnetocaloric effect measurements are described, allowing to construct a detailed magnetic phase diagram for copper nitrate. The results are discussed in section 4.5 and compared to the theoretical model. Finally, section 4.6 summarizes the findings.

4.1 Bose-Einstein Condensation of Triplons

Dimerized spin $S = \frac{1}{2}$ systems are in the focus of many recent studies owing to the occurrence of exotic field induced phenomena like the Bose-Einstein condensation of triplons. The idea of a Bose-Einstein condensation (BEC) was introduced in 1925 as Einstein concluded from Bose-Einstein statistics that at low enough temperature atoms can form a collective ground state [105]. In other words: They condense in the lowest energy state. The phenomenon of a BEC was first observed for fluid ^{4}He at the transition into the superfluid phase at 2.18 K. Later, Eric A. Cornell, Wolfgang Ketterle, and Carl E. Wieman were able create a BEC of a diluted gas of alkali atoms at temperatures in the nanokelvin region [105], which was honored with the Nobel prize in 2001. The concept of BEC can also be applied to bosonic excitations in solids, such as in gapped dimerized spin $S = \frac{1}{2}$ systems for which the Hamiltonian possesses at least an axial symmetry [106]. In these systems pairs of spins are coupled antiferromagnetically with a coupling constant $J_1 < 0$ forming singlets with total spin $S = 0$, which results in an non-magnetic ground state. An energy gap $\Delta = J_1$ separates the ground state from the three excited triplet states with integer spin $S = 1$ and with $S_z = +1$, $S_z = 0$, and $S_z = -1$. The system remains non-magnetic down to zero temperature. Due to small interdimer interactions J_i $(i > 1)$, which couple the dimers in three dimensions, the excitations become mobile. The triplet state is then described by a band with the dispersion relation in first order approximation

$$E(\boldsymbol{k}) = J_1 - \frac{1}{2}\sum_i J_i \cos(\boldsymbol{k} \cdot \boldsymbol{d}_i) \text{ [107, 108].} \tag{71}$$

$\boldsymbol{d}_i$ is the vector connecting two interacting dimers. The band width is defined by the interdimer

interactions. For instance in the case of weakly coupled spin chains the band width is mainly given by the intrachain coupling J_2.
When applying a magnetic field H, Zeeman splitting occurs resulting in a lowering of the energy of the triplet $S_z = +1$ by $E_{\text{Zeeman}} = g\mu_B H S_z$, where g is the g-factor and μ_B the Bohr magneton. Fig. 4.1 reveals the consequences of the Zeeman splitting to the energy states: At a critical field H_{c1} the gap between triplet band and the ground state is closed. The triplets are regarded as hard core bosons and are called triplons, which start to condensate into the ground state at H_{c1}. A field induced phase transition into the (long-range ordered) BEC-phase occurs at H_{c1} even at zero temperature, which defines this point as a quantum critical point. Since triplons are formed at H_{c1}, the magnetization M_z in the field direction increases abruptly. The magnetic field acts like a chemical potential. It controls the density of triplons, which is a linear function of the magnetization [109]. For higher fields more and more triplons condense up to a second quantum critical point at H_{c2} at which all triplons are condensed. At this point, the magnetization M_z is saturated.

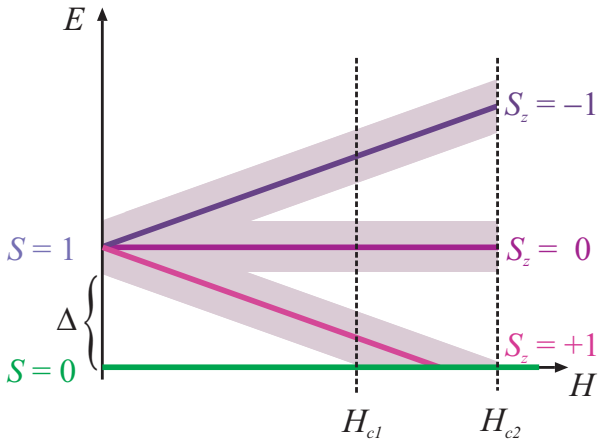

Fig. 4.1: Schematic figure of a BEC of triplons: at zero field the triplet states are separated from the singlet state by an energy gap Δ. Small interdimer interactions lead to triplet bands. Due to an applied magnetic field the gap is closed (Zeeman splitting) between the triplet state $S_z = +1$ and the ground state at a critical field H_{c1} defining the onset of the triplon condensation. At the second critical field H_{c2} all triplons are condensed.

In the BEC phase each individual state of a dimer can be described by a coherent superposition of a triplet $S_z = +1$ and a singlet component resulting in a staggered magnetization perpendicular to the applied magnetic field, which spontaneously breaks the rotational symmetry [109,110]. The transverse magnetic order between the two critical fields can be directly measured for instance via neutron diffraction. The magnetic order corresponds to the wave function in the primary BEC theory of a Bose gas [110].
Close to the critical field H_{c1} the evolution of the critical temperature is predicted to be described by the following power law

$$T_c \sim (H - H_{c1})^{\phi}, \tag{72}$$

with the universal exponent $\phi = \frac{2}{d}$ [110], while d represents the dimension.

The concept of BEC was first applied to the 3D interacting dimer system $TlCuCl_3$, as a cusp in the magnetic susceptibility was interpreted as a feature of the BEC [36]. Later, other materials like the quasi two dimensional system $BaCuSi_2O_6$ [39] or the systems $Ba_3Cr_2O_8$ [111] and $Sr_3Cr_2O_8$ [112], in which the dimers are forming double stacked triangular lattices, were investigated and discussed in terms of BEC. Structural simpler dimer systems, which are exhibiting BEC as well, are the quasi one-dimensional ladder system $(C_5H_{12}N)_2CuBr_4$ (abbreviated $(Hpip)_2CuBr_4$) at very low temperatures [42] and the chain system $Pb_3V_2O_9$ [28]. Furthermore, BEC was not only observed for spin $S = \frac{1}{2}$ systems but also for the spin $S = 1$ chain $NiCl_2$-$4SC(NH_2)_2$ [41].

Another promising candidate for undergoing a BEC is the dimerized spin $S = \frac{1}{2}$ chain system copper nitrate ($Cu(NO_3)_2{\cdot}2.5H_2O$), which first was extensively studied in the 1970s. In this period a field induced long-range ordered phase was observed, which was interpreted at that time as a canted antiferromagnetic phase [113, 114]. Only recently has this phase been discussed in the context of BEC [115].

For this kind of quasi one dimensional spin $S = \frac{1}{2}$ system another fascinating phase can occur: the Tomonaga-Luttinger liquid regime (LL). This regime can appear for temperatures $Tk_B > J_{\text{interchain}}$, where the dimers are coupled only within the chain. In this case no long-range order can develop due to the 1D character of the magnetic coupling as stated by Mermin and Wagner in 1966 [116]. The Luttinger liquid develops when the gap between singlet ground state and the triplet band closes at a critical field similar to the BEC phase. In contrast to the BEC the excitations are not bosonic triplons but spinons, which behave as spinless fermions. The LL regime was for example intensively studied for the uniform spin chain compound $KCuF_3$ [19] and the spin 2-leg ladder system $(Hpip)_2CuBr_4$ [34]. $(Hpip)_2CuBr_4$ shows a Luttinger liquid phase for temperatures $J_{\text{interchain}} < Tk_B < J_{\text{intrachain}}$ as well as a long-range ordered phase (LRO) at temperatures $Tk_B < J_{\text{interchain}}$, with the latter discussed in terms of BEC. The phase diagram of $(Hpip)_2CuBr_4$ is depicted in Fig. 4.2. The LRO phase forms a small asymmetric dome in the magnetic phase diagram, which extends up to $\sim 100\,\text{mK}$ while the LL regime encloses the LRO phase also forming a dome. The LL extends up to 1.5 K. As H_{c1} and H_{c2} are quantum critical points, regions like a quantum disordered regime, where quantum fluctuations are dominant, as well as a quantum critical regime exist in the phase diagram [106]. The phase diagram at the left hand side of Fig. 4.2 is able to distinguish between the quantum disordered (QD) region (spin liquid), which is characterized by a gapped excitation spectrum and a singlet ground state, and the quantum critical (QC) region.

Indications of phase boundaries of the LL and BEC regimes are manifold. Transitions into a LRO phase are observable directly with neutron diffraction when magnetic Bragg peaks are appearing, or with NMR when a line splitting occurs. To decide if the LRO phase is a BEC phase is much more difficult. As the Bose-condensate corresponds to magnetic order which is formed by the transverse spin components, a requirement for BEC is an antiferromagnetic spin alignment perpendicular to the applied magnetic field, which can also be detected with neutron diffraction. Furthermore, the phase boundary of the BEC phase in the magnetic phase

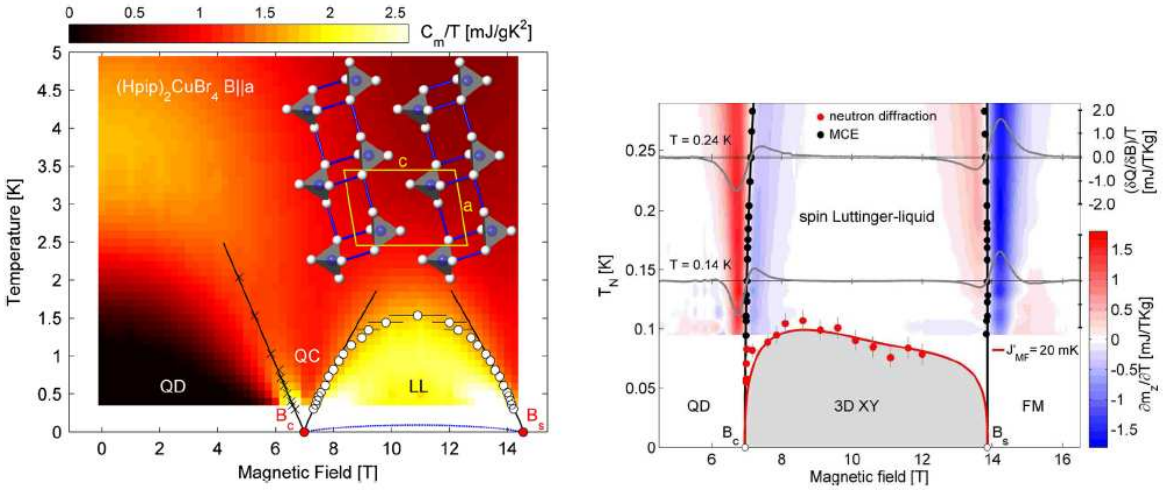

Fig. 4.2: Phase diagram of the ladder system $(Hpip)_2CuBr_4$ showing both long-range order and a Luttinger liquid. The LL was determined by magnetocaloric effect measurements as well as heat capacity measurements, while the long-range ordered phase was determined by neutron diffraction. The figures are taken from Refs. [35] and [42].

diagram is expected to follow the universality described by Eq. (72). A Luttinger liquid can be detected using inelastic neutron scattering measurements, which reveal a spinon continuum in this regime [19]. Furthermore, the behavior of the NMR relaxation rate T_1 can indicate the presence of a LL regime [117, 118].

Thermodynamic measurements also show features which can be attributed to phase transitions into LL and BEC phases. For $TlCuCl_3$ a cusp like minimum in the temperature dependent longitudinal magnetization $M(T)$ was interpreted as a transition into a BEC phase [36] for applied fields larger than H_{c1} but smaller than the field corresponding to the top of the BEC-dome. For larger fields a cusp-like maximum is expected, which could not be observed experimentally up to date since for most materials showing a BEC very high magnetic fields (more than 40 T) are required. For the crossover into the LL regime round minima and maxima are expected in the $M(T)$ evolution based on theoretical considerations [119–121] and were in fact observed for $(Hpip)_2CuCl_4$ experimentally [33]. When crossing the LL regime and finally entering the BEC phase, an extremum in $M(T)$ is expected for the crossover into the LL regime, followed by a kink for the transition into the LRO state [121]. Both features could not be observed experimentally for the same magnetization scan so far, as all compounds which show a LL reveal the transition into the LRO state at too low temperatures. Also the evolution of the field dependent magnetization $M(H)$ shows transitions at the phase boundaries. In the derivative $\mathrm{d}M/\mathrm{d}(\mu_0 H)$ two maxima indicate the transition into the LL regime, which was predicted by theory and observed experimentally [33, 120]. In the magnetic heat capacity C_m the crossover into the LL is characterized by a broad peak for applied magnetic fields close to the center of the gapless LL regime [120,122]. The prediction of this feature was recently confirmed experimentally [35]. A sharp peak indicates the transition into the LRO state.

In this context, the quasi one-dimensional compound copper nitrate is the most promising can-

didate for studying a BEC phase as well as a LL regime in detail. In contrast to other systems, the relatively low critical field H_{c2} and the experimentally accessible transition temperature into the LRO phase allow an extensive study of the different features predicted for the transitions into the BEC phase and LL regime, and this way enabling to establish the complete magnetic phase diagram.

4.2 Physical Properties of Copper Nitrate

4.2.1 Crystal Structure

Copper nitrate is described by the chemical formula $Cu(NO_3)_2{\cdot}2.5H_2O$, in which "$2.5H_2O$" denotes the crystal water. Copper nitrate crystallizes in the monoclinic structure $I2/c$ with the lattice parameters $a = 16.4539\,\text{Å}$, $b = 4.9384\,\text{Å}$, $c = 15.6921\,\text{Å}$, and $\beta = 93.765°$ at room-temperature [123, 124]. The crystal structure is shown in Fig. 4.3 in a projection onto the ac

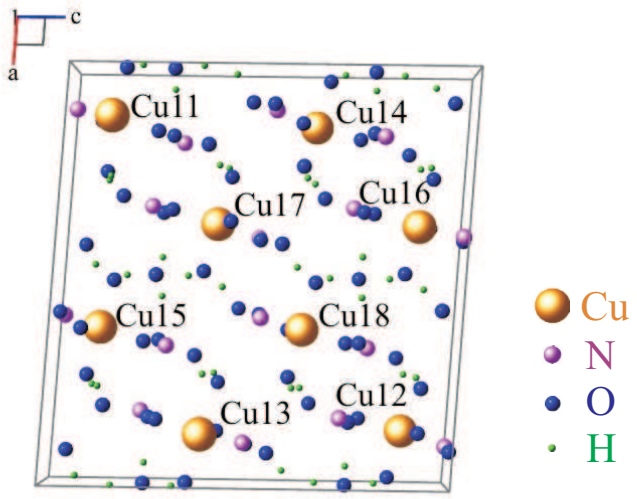

Fig. 4.3: Crystal structure of copper nitrate based on the atomic coordinates from Morosin *et al.* [124]. It is shown the projection onto the ac plane. For the numbering of the copper atoms see Tab. 2

plane. The Cu-atoms are placed at the Wyckoff position $8f$ with x =0.12613(2)a, y =0.01352(6)b, z =0.11376(2)c [124]. The Cu-atom positions are summarized in Tab. 2 and were labeled as in Ref. [125].

Cu11	x	y	z
Cu12	$-x$	$-y$	$-z$
Cu13	$-x$	y	$1/2-z$
Cu14	x	$-y$	$1/2+z$
Cu15	$1/2+x$	$1/2-y$	z
Cu16	$1/2-x$	$1/2+y$	$-z$
Cu17	$1/2-x$	$1/2-y$	$1/2-z$
Cu18	$1/2+x$	$1/2+y$	$1/2+z$

Tab. 2: Copper positions in copper nitrate. The copper atoms are at Wyckoff position $8f$ of the structure $I2/c$ with x =0.12613(2)a, y =0.01352(6)b, z =0.11376(2)c [124].

4.2.2 Magnetic Properties

The magnetic properties of copper nitrate were investigated for the first time in the 1960s. In 1963 Berger *et al.* suggested on the basis of magnetic susceptibility measurements that the magnetic copper ions Cu^{2+} are coupled antiferromagnetically and form either independent spin pairs (dimers) or linear one-dimensional chains [126]. The independent dimer model accounted slightly better for the data. These two proposed models were fit in 1968 to heat capacity data measured by Friedberg *et al.* [127]. In agreement with the susceptibility results the independent dimer model fit best. In the same year Wittekoek *et al.* published proton magnetic resonance spectra, which confirmed the dimer model [128]. Furthermore, measurements of the magnetization performed by Myers *et al.* in 1969 gave evidence of a weak antiferromagnetic interaction between the dimers [129].

After the crystal structure of copper nitrate was determined by Garaj *et al.* and Morosin *et al.* [123, 124], Bonner *et al.* suggested two possible interdimer coupling models by considering possible superexchange paths [130]. Both models had a one-dimensional character.

The first one is the so called "ladder model". Here, the dimers are related to the rungs of a ladder and are coupled along the b direction by weak interdimer interactions forming the long sides (legs) of the ladder. In the second model, the dimers, coupled by the exchange interaction J_1, are arranged in zig-zag alternating chains of the form -Cu-J_1-Cu-J_2-Cu-J_1-Cu- in the ac plane, where J_2 is the interdimer exchange interaction (see figure 4.4). Later the "ladder model" was ruled out by Diederix *et al.* and Eckert *et al.* by means of proton resonance measurements and neutron measurements, respectively [113, 114]. For the alternating chain the exchange paths would include two oxygen atoms so that couplings as Cu-O-O-Cu-O-O-Cu-.. are realized. The chains are oriented alternately along the [1,1,1] and the [1,-1,1] direction in such a way that the copper atoms Cu11, Cu17, Cu18 and Cu12 form chains along [1,1,1] and the others chains along [1,-1,1].

The Hamiltonian of the alternating antiferromagnetic Heisenberg chain can be written as

$$\hat{H} = -J_1 \sum_i \left(\boldsymbol{S}_{2i-1} \cdot \boldsymbol{S}_{2i} + \alpha \boldsymbol{S}_{2i} \cdot \boldsymbol{S}_{2i+1} \right), \tag{73}$$

where $\alpha = J_2/J_1$ is the alternation parameter. In the limiting case $\alpha = 0$ the ions are arranged in noninteracting pairs (dimers), while in the case $\alpha = 1$ the ions form an antiferromagnetic linear Heisenberg chain. On the basis of NMR and heat capacity data Diederix *et al.* calculated in 1978 the intradimer J_1 and intrachain J_2 interactions [125]. They found $J_1 = -5.2\,\mathrm{K}$ and $J_2 = -1.4\,\mathrm{K}$ leading to $\alpha = 0.27$. Both couplings are small due to the magnetic exchange involving two oxygen atoms and are antiferromagnetic due to the Goodenough-Kanamori-Anderson rule for exchange angles significantly larger than 90°. In 1983 Bonner *et al.* analyzed the old experimental data from Berger *et al.* [126], Friedberg *et al.* [127], and Myers *et al.* [129] for a second time and showed that the alternating chain model fits to these data much better than the isolated pair model

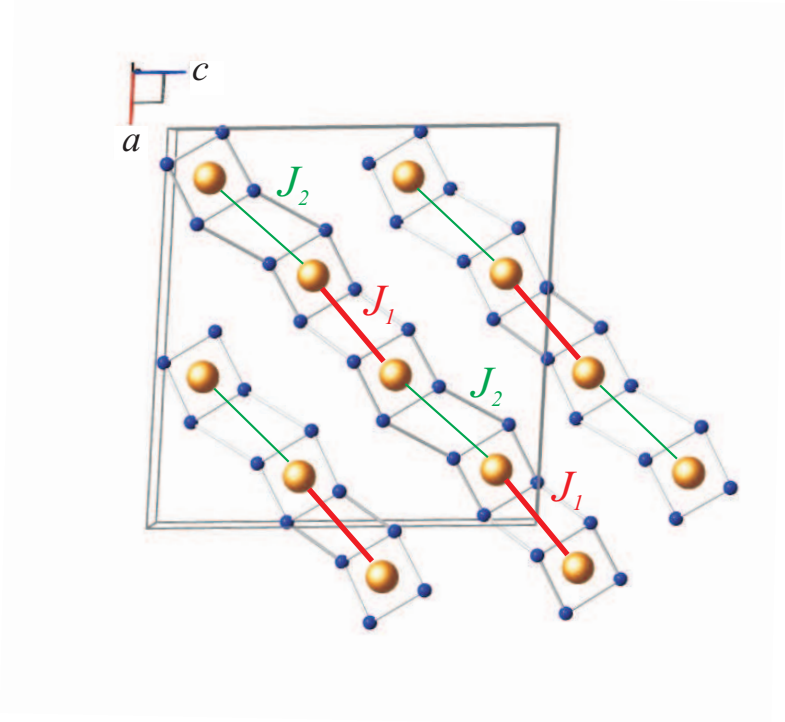

Fig. 4.4: Alternating chain model in copper nitrate. Only the copper and oxygen atoms contributing to the superexchange interaction within the chains are shown. J_1 describes the intradimer exchange interaction (red) and J_2 the interdimer exchange interaction (green).

[29]. From these revised fits an intradimer coupling $J_1 = -5.16\,\mathrm{K}$ and an intrachain coupling $J_2 = -1.39\,\mathrm{K}$ was obtained, which is in agreement with the exchange constants published by Diederix *et al.* [125].

About 20 years later in 2000 Xu *et al.* performed inelastic neutron scattering measurements in zero field down to temperatures of 0.3 K [108]. The dispersion relation of an excited triplet band, as it is expected for dimerized spin systems, was obtained. Using Eq. (71) the interdimer coupling was determined as $J_1 = -5.13\,\mathrm{K}$, while the intrachain interaction $J_2 = -1.23\,\mathrm{K}$ was found, leading to an α value of 0.24, which is slightly smaller than the previously determined value. Apart from the intrachain couplings, weak interchain couplings were found. Eckert *et al.* and Diederix *et al.* found a ferromagnetic coupling along the b axis as well as an antiferromagnetic coupling in the ac plane [113, 114]. The absolute values of both coupling constants were found in the range of 0.06 K in the study of Diederix *et al.*, while Xu *et al.* obtained larger coupling constants which are in the range of 0.1 to 0.2 K [108, 113]. These different interchain interactions could be the reason for the discrepancy of the α values.

Further, the interchain interaction can lead to long-range order, which was first observed by means of proton magnetic-resonance experiments in 1971 [131]. For zero magnetic field no long-range order is possible due to the energy gap between the singlet ground state and the excited triplet band. In a magnetic field however, Zeeman-splitting of the triplet band occurs leading to a closing of the gap as it is described in section 4.1. The Zeeman-splitting of the triplet band

was investigated in 2007 by means of inelastic neutron scattering. The closing of the energy gap is shown in Fig. 4.5 [132].

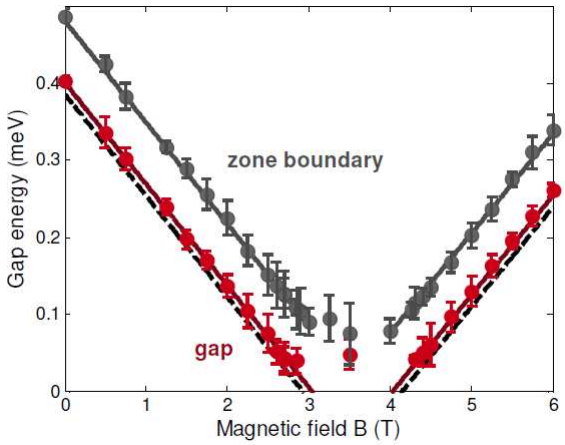

Fig. 4.5: By applying a magnetic field Zeeman-splitting of the triplet state occurs leading to a closing of the gap. The data were obtained by inelastic neutron scattering experiments on copper nitrate at 120 mK. The magnetic field was applied along the b axis. The figure is taken from Ref. [132].

From the splitting of proton-resonance lines in NMR experiments the magnetic phase diagram was previously defined. Two phase diagrams have been published for applied magnetic fields along the b direction, which were both obtained by NMR technique. They are summarized in Fig. 4.6. The phase diagrams show a field induced LRO phase, which differs particularly in temperature. While the dome of one data set extends up to temperatures of about 160 mK at ∼3.6 T, the other extends up to about 175 mK [113, 131]. The critical fields were found to be $H_{c1} = 2.8\,\mathrm{T}$ and $H_{c2} = 4.3\,\mathrm{T}$ by means of adiabatic susceptibility measurements and were added to the phase diagram [133]. For magnetic fields applied parallel to the ac plane the critical fields shift to higher values due to the anisotropy in the g-factor: $g_{\|b} = 2.33(2)$ and $g_{\perp b} = 2.09(2)$ [125]. Furthermore, the dome of the phase diagram extends up to ∼222 mK at 4.1 T for fields parallel to the ac plane [113]. These different maximum temperatures for the two different orientations were attributed to the anisotropy of the interchain coupling.
Moreover, in the NMR spectra two sublattice magnetizations were observed indicating antiferromagnetic order. The spectra were further interpreted in terms of canted magnetic moments [113]. The magnetic moment component parallel to the applied magnetic field and the component perpendicular to the field behave differently. While the parallel component saturates for fields larger than H_{c2}, the other component lying in the ac plane increases at H_{c1} and falls back to zero at H_{c2}. The result is an effective spin canting in the field range between the two critical fields. At the second critical field all spins finally point along the field direction (see Fig. 4.7). Similar conclusions were drawn by means of elastic neutron diffraction studies performed by Eckert *et al.* [114], which are described in the following in more detail.
For the experiment Eckert *et al.* [114] used a deuterated copper nitrate single crystals with the D:H ratio of about 90:10 and the dimensions $4.5\times5\times3\,\mathrm{mm}^3$. A magnetic field was applied along

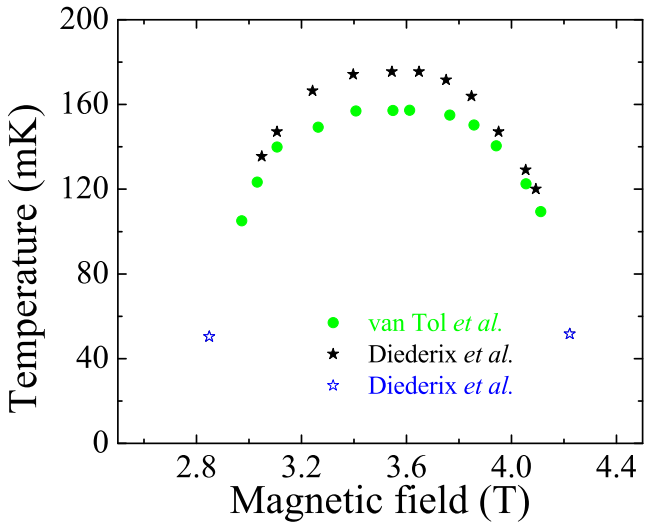

Fig. 4.6: Phase diagrams determined by van Tol *et al.* and Diederix *et al.* for applied magnetic fields along the b axis. Both used the splitting of the proton-resonance lines in NMR experiments to define the phase boundaries [113, 131]. The phase boundary at 50 mK (blue stars) was also determined by Diederix *et al.* by means of adiabatic susceptibility measurements [133].

the crystallographic b axis. The data were obtained by $\theta - 2\theta$-scans at 125 mK and at neutron wavelengths of 2.46 Å, 1.23 Å, and 0.82 Å. Two types of magnetic Bragg peaks were observed: the peaks hkl, which fulfill the equation $h + l = 4n \pm 2$ and h, l both even, were accounted for by an antiferromagnetic alignment of magnetic moments in the ac plane with the sequence $+--++--+$. This sequence means that the spins of the copper atoms with number 1,4,5, and 8 all point in one direction in the ac plane while the spins of the atoms 2,3,6, and 7 point in the opposite direction. Here, the same numbering was used as in Tab. 2 and Fig. 4.3. These aforementioned peaks show an increase in the intensity starting between 2.9 T and 3.1 T, which corresponds to the transition into the long-range ordered state H_{t1}. At a field of 4.2 T the intensity decreases defining the upper boundary of the long-range ordered phase at the transition field H_{t2} (Fig. 4.8(a)). At zero temperature the transition fields are expected to coincide with the critical fields H_{c1} and H_{c2}. Bragg peaks obeying $h + l = 4n$ and h, l even are supposed to stem from a ferromagnetic spin component along the b direction. These peaks show an increase of the intensity at about 3 T and a saturation at about 4.2–4.6 T (Fig. 4.8(b)).

From the analysis of their data Eckert *et al.* concluded that the antiferromagnetic axis is lying 45° ±10° off the a axis [114]. The behavior of the two types of magnetic Bragg peaks has thus been accounted for by a canted antiferromagnetic structure of classical spins as proposed by Diederix *et al.*, with one type of Bragg peak showing ferromagnetic spin alignment, where the spins point along the field direction and saturate at H_{c2}, and the other type denoting antiferromagnetic alignment in the ac plane developing at H_{c1} and vanishing at H_{c2}. It remains unclear why the intensity evolution for the antiferromagnetic component is asymmetric as it is shown in 4.8 (a).

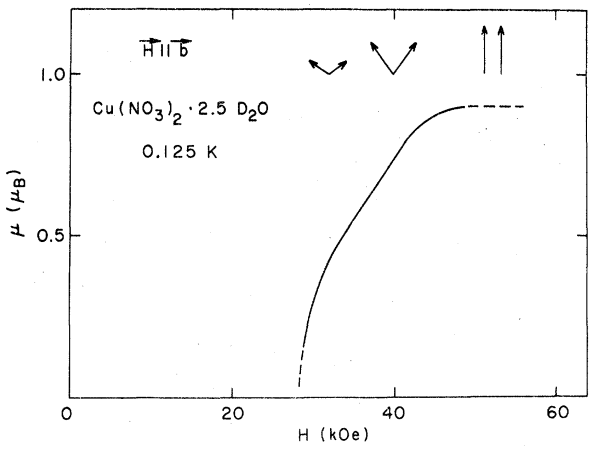

Fig. 4.7: Interpretation of the behavior of the two types of magnetic Bragg peaks: Canting of the moments from Ref. [114]; for details see text.

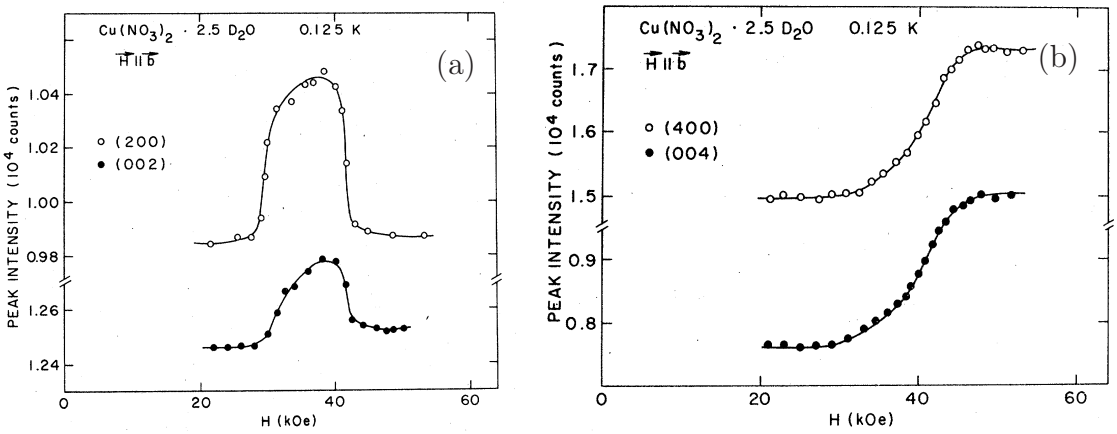

Fig. 4.8: Results from Eckert *et al.*: Variation of peak intensities as a function of magnetic field [114]; for details see text.

Furthermore, the long-range ordered phase was investigated with bulk techniques like heat capacity measurements [134]. Relaxation measurements were performed using a 2 g single crystal and heat pulses of 50 s. The heat capacity data show a transition into the long-range ordered state as well as a broad peak between 200 mK and 300 mK at 3.57 T (Fig. 4.9).
More recently, the spin excitation spectrum of copper nitrate was the focus of detailed investigations. By means of inelastic neutron scattering experiments a two-magnon continuum was observed as well as evidence of a two-magnon bound states was found [135]. Furthermore, at higher temperatures intraband scattering within the one-magnon band was observed [136, 137].

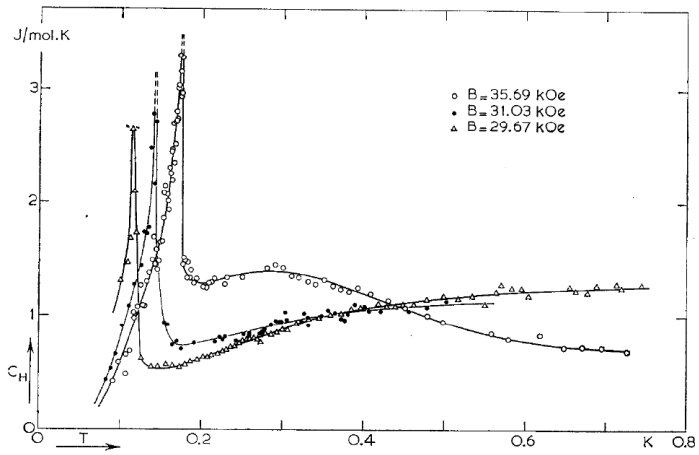

Fig. 4.9: Heat capacity data crossing the phase boundary into the long-range ordered phase from Ref. [134]. The magnetic field was applied along the crystallographic b axis.

4.3 Crystal Growth and Characterization

4.3.1 Crystal Growth and Handling

For comprehensive measurements of the magnetic properties of copper nitrate a uniaxial magnetic field must be applied, which requires high quality single crystals. These can be grown out of a saturated solution and must fulfill the size and quality requirements for elastic neutron scattering experiments. Therefore, the single crystals preferably should have a mass of about 0.5–1 g. Furthermore, the hydrogen should be replaced by deuterium since hydrogen is a strong incoherent scatterer for neutrons and would produce a large background signal in the neutron scattering spectra. In contrast, deuterium, with an incoherent scattering cross section almost two orders of magnitude smaller [81], rarely scatters neutrons incoherently and produces no background.

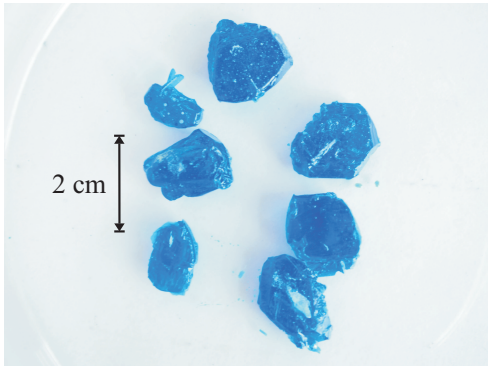

Fig. 4.10: Copper nitrate single crystals were grown from a saturated solution. The biggest crystal has a mass of about 4 g, while the smallest has a mass of ∼0.8 g.

The crystal growth of deuterated copper nitrate was performed in three steps according to Notbohm and Xu [132, 138]. The first step is the distillation process. The aim of this step is to replace the crystal water H_2O by heavy water D_2O. Therefore, copper nitrate powder was dissolved in D_2O. By distillation and afterwards adding D_2O to the solution, the crystal water was successively replaced by heavy water during 18 distillation processes. For more details of the distillation process see Ref. [139]. During this process the solution temperature was kept at 65 °C by means of an oil bath. In the second step small needle shaped seed crystals, with the long axis the crystallographic b axis, were produced by fast cooling of the saturated solution. In the last step the single crystals were grown out of a saturated solution on the seed crystals by cooling the solution slowly with a cooling rate of 4.2 mK/min from 85°C to 40°C. The maximum temperature of the solution should be lower than 90°C throughout the growth process since copper nitrate is only stable up to 90°C (see next chapter). As well, crossing the lower borderline temperature of 26°C needs to be avoided since at temperatures below 25°C a second phase $Cu(NO_3)_2{\cdot}6D_2O$ would be stabilized during the growth process [140]. Finally, by cutting the crystals, nice shiny faces could be obtained, which correspond to the $(10\bar{1})$ plane.

Since copper nitrate is highly hygroscopic, the crystal growth has to take place under argon atmosphere. Afterwards the crystals must be protected from air contact, otherwise the moisture in the air would destroy the crystals. Therefore, the crystals were stored and prepared in a glove box under nitrogen atmosphere. For the neutron and bulk experiments the crystals had only very short contact with air (max. 3 min.). For sample orientation on the x-ray Laue instrument it was possible to wrap the crystals in thin paraffin wax foil to keep them dry. Further, for the experiments the crystals cannot be glued to the particular instrument platform using a glue

containing solvents. Therefore, the good thermally conductive Apiezon N grease or Stycast, which is a water free epoxy glue, were used for attaching the samples in the experiments.

4.3.2 Powder X-Ray Diffraction

Deuterated single crystals with at least 98.6 % D_2O were crushed and measured in a Bruker D8 advanced x-ray diffraction instrument under N_2-gas flow at room-temperature. Furthermore, a furnace, which achieved temperatures up to 300 °C, was available. The observed and fitted spectra at room-temperature are shown in Fig. 4.11. Due to texture effects in this powder the fitting of the intensities is not very good, resulting in an crystallographic R_F factor from the refinement of only 36, but a good agreement between calculated and observed peak positions was achieved. Here, the R_F factor, which measures the agreement between the model and the data, is defined as $R_F = 100\frac{|\sum_h F_{obs,h} - F_{calc,h}|}{\sum_h |F_{obs,h}|}$, where F_{obs} and F_{calc} denote the oberved and calculated structure factors, respectively. From the refinement, the following lattice parameters were obtained: a =16.45003 Å, b =4.93644 Å, c =15.96076 Å, and β =93.7606°, which agree very well with the parameters for non-deuterated copper nitrate published by Morosin [124].

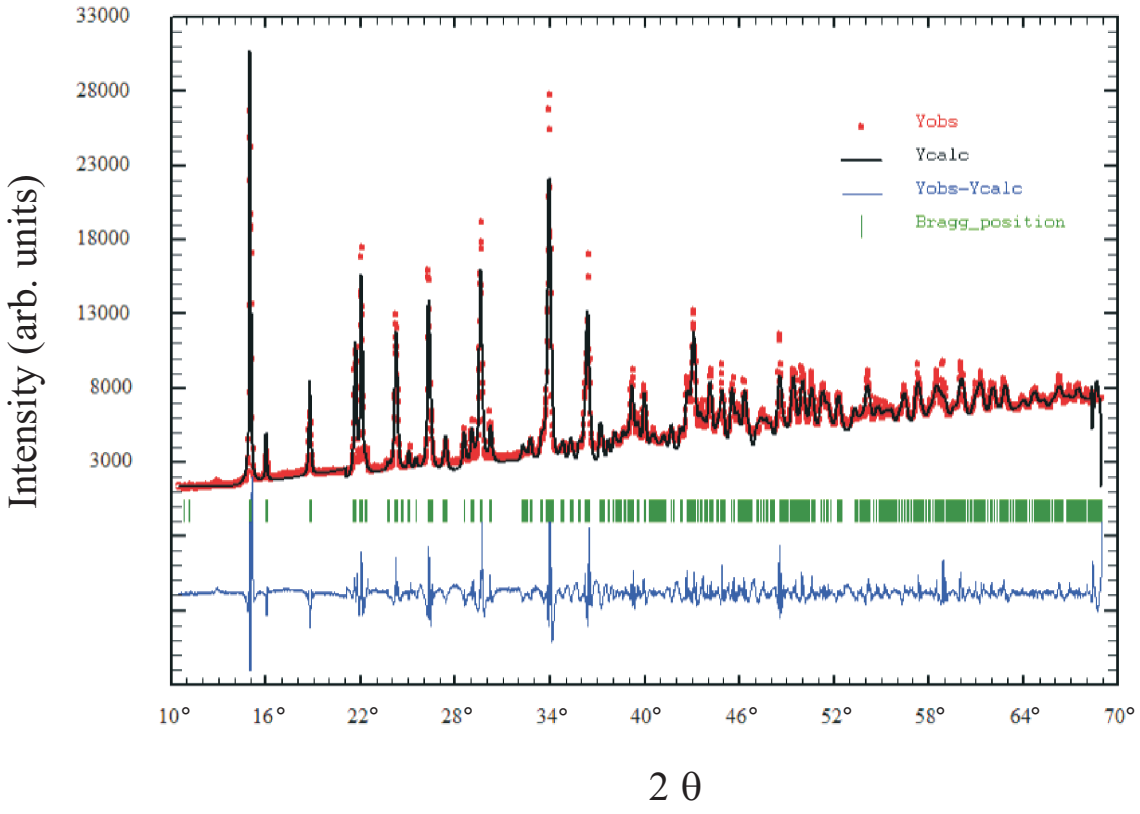

Fig. 4.11: Powder x-ray diffraction on deuterated copper nitrate; red dots: observed data points, black line: Rietveld-fit, blue line: difference between observed and fitted data, green vertical lines: expected peaks for the given structure model from Morosin [124].

The behavior of deuterated and undeuterated copper nitrate at higher temperatures was inves-

tigated using the furnace. The material is stable up to 90 °C (Fig. 4.12). For higher temperatures it looses crystal water and transforms into a second phase which can be identified as $Cu(NO_3)_2{\cdot}1H_2O$ [141]. For even higher temperatures the material undergoes several decomposition processes before it decomposes at 230 °C into CuO (a detailed analysis of the decomposition processes was performed for example by Morozov *et al.* [141]). The behavior of deuterated copper nitrate is very similar to undeuterated copper nitrate. Only the transition temperatures changed slightly. Basically, the transition temperatures for deuterated copper nitrate are about 10 °C higher than the transition temperatures for undeuterated copper nitrate.

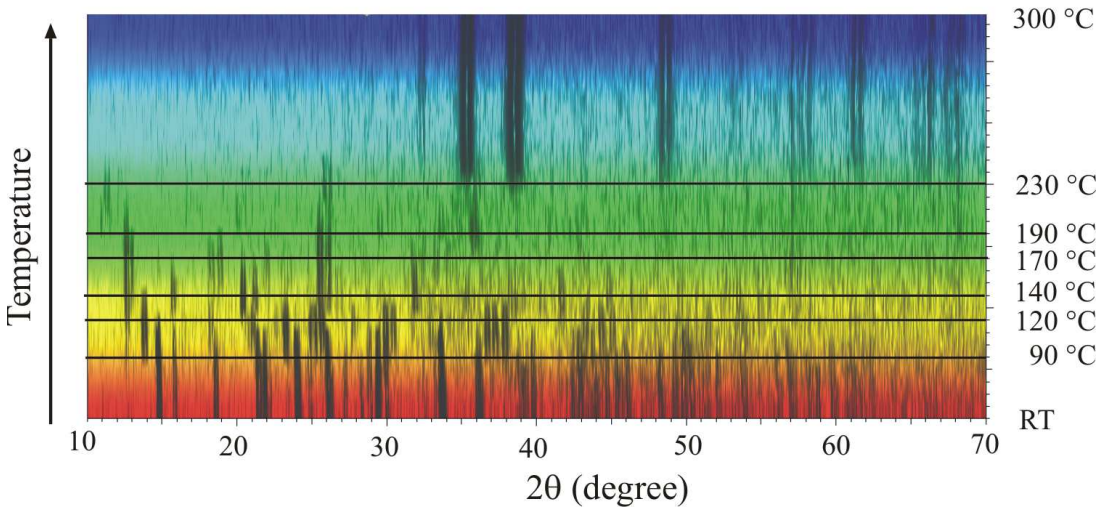

Fig. 4.12: Powder x-ray diffraction patterns for temperatures up to 300 °C showing several decomposition processes of deuterated copper nitrate, which start at 90 °C.

4.3.3 Magnetization Measurements Using the PPMS VSM

The magnetic properties of deuterated copper nitrate for temperatures down to 1.8 K were investigated with a PPMS VSM. In this temperature range neither a long-range ordered phase nor Luttinger-liquid behavior is expected to occur due to the weak interdimer exchange interaction in this system. For the measurements two deuterated copper nitrate single crystals with at least 98.6 % D_2O and a mass of 5.675 mg and 11.251 mg were aligned using an x-ray Laue instrument. The samples were glued to the sample stick with Stycast (epoxy) in such a way that the applied magnetic field was parallel to the crystallographic b axis for the smaller sample and parallel to the [101] direction for the bigger one. The field dependent magnetization was measured for temperatures down to 1.8 K and in fields between 0 T and 14 T (Fig. 4.13, left panel). The magnetization increases with increasing magnetic field and saturates at M_{sat} =1.15(1) μ_{B} /Cu for an applied magnetic field parallel to the b axis and M_{sat} =1.054(10) μ_{B} /Cu for a magnetic field parallel to the [101] direction. The difference in the saturation moments is due to the anisotropy of the g-factor. Using the relation $M_{\mathrm{sat}} = \frac{1}{2} g \mu_{\mathrm{B}}$ the saturation values correspond to $g_{\|b}$ =2.30(1) and $g_{\|[101]}$ =2.11(1), which is in agreement with the values for non-deuterated copper nitrate

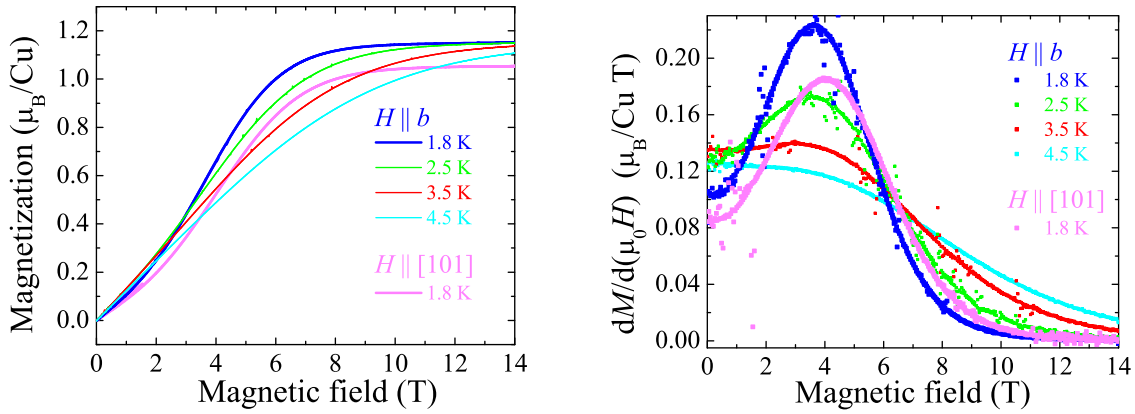

Fig. 4.13: Magnetization curves of copper nitrate (left) and the field derivative (right) for applied magnetic fields along the crystallographic b axis and along the [101]-direction.

published by Diederix *et al.* ($g_{\parallel b}$ =2.33(2) and $g_{\perp b}$ =2.09(2) [125]). As it is expected for a g-value anisotropy the saturation field is smaller for an applied magnetic field parallel to the b axis. For 1.8 K the magnetization curve also shows an inflection point which is more pronounced in the field derivative $\mathrm{d}M/\mu_0\mathrm{d}H$ (shown in the right panel of Fig. 4.13). The presence of these types of inflection point in the magnetization curves is typical for a one-dimensional dimerized spin system at temperatures larger than the crossover temperature into the Luttinger liquid regime [120]. For the two different orientations the maximum in the derivative is shifted due to the difference in the g-values. For an increase of the temperature the maximum becomes smaller until for 4.5 K the maximum is at zero field, which indicates the crossover into the classical regime [120].

The temperature dependent magnetization measured at 1 T (smaller than H_{c1}) increases with temperature decreasing from 300 K to ∼3 K, while it starts to decrease exponentially for lower temperatures indicating the existence of a gap between the ground state and the first excited state (Fig. 4.14 (top)). This behavior of the magnetization is typical for low dimensional spin gap systems and was found for example for the systems $TlCuCl_3$ and $(Hpip)_2CuBr_4$ [31,142]. For applied magnetic fields larger than H_{c2} the magnetization increases continuously upon lowering temperature and levels off exponentially at the saturation magnetization M_{sat} as it is predicted for these one-dimensional spin gap systems [120]. This behavior is shown in Fig. 4.14 (lower panels) for an applied magnetic field of 14 T. For applied magnetic fields between the two critical fields H_{c1} and H_{c2} different features are expected. To study these features, temperatures which are about one magnitude smaller are necessary. These measurements were performed using other instruments and are discussed in chapter 4.4.3.

The magnetization was also calculated using the exact diagonalization method in order to compare the experimental data quantitatively with the theoretical model. For this purpose the open-source software ALPS (Algorithms and Libraries for Physics Simulations) release 2.0 was used [143, 144]. As a model a one-dimensional isotropic Heisenberg Hamiltonian with external

field and alternating exchange constants was used. The magnetization was calculated for a ring of 14 spins using the exchange constants published by Bonner *et al.* [29]. By taking into account the g value for an applied magnetic field along the b axis, the calculated data were adjusted to the experimental data for this sample orientation. The results are depicted in the right panels of Fig. 4.14, where a good agreement is found between the experimental and theoretical curves.

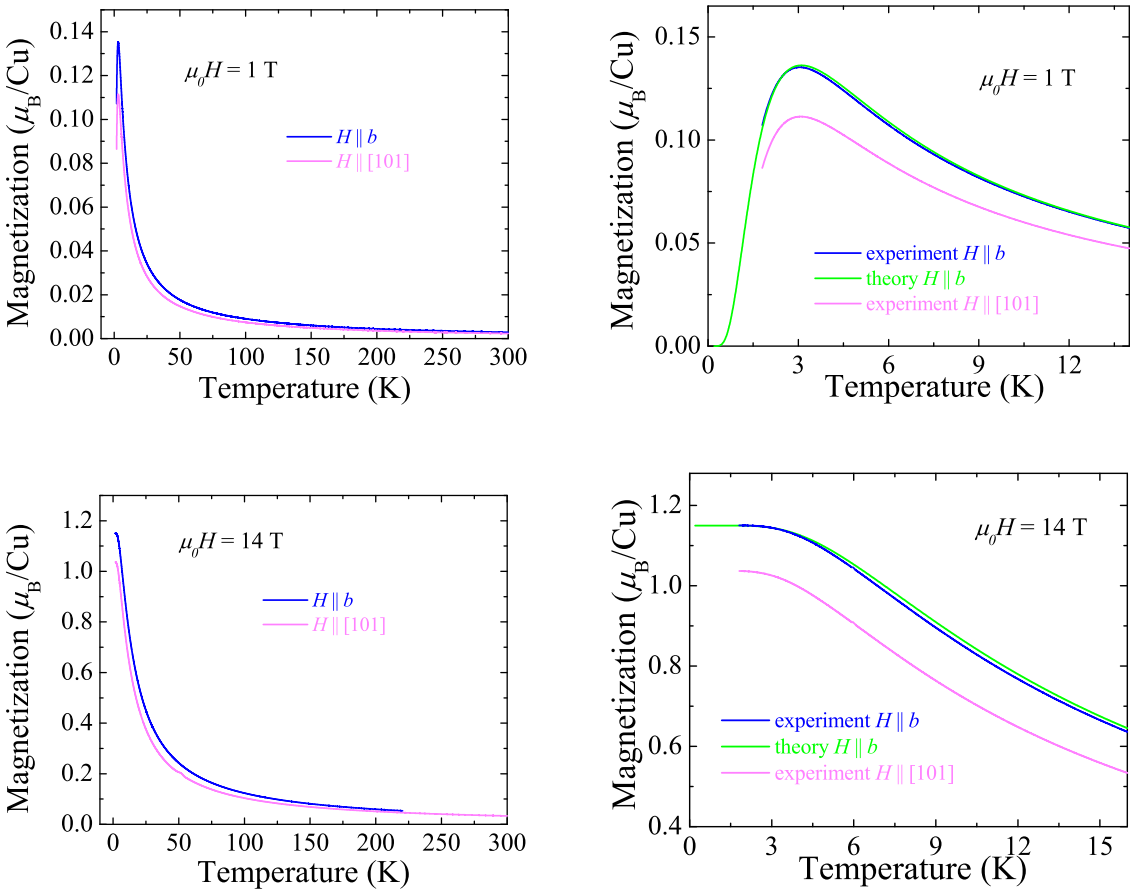

Fig. 4.14: Temperature dependent magnetization of copper nitrate for magnetic fields of 1 T (upper panels) and 14 T (lower panels) applied in two different directions. A similar behavior was found for both orientations. The graphs on the right hand side show a close-up of the magnetization of the low temperature region. The green curves represent the calculated magnetization for $J_1 = -5.16$ K and $J_2 = -1.38$ K. For details see text.

To summarize, all features expected for this quasi one-dimensional dimerized spin system were found in the "high temperature" region down to 1.8 K, which would be far above the transition into a Luttinger liquid regime. Furthermore, a quantitative agreement with the theoretical curves using the model and exchange constants published by Bonner *et al.* was obtained, which indicates that the deuteration of the crystals does not change the magnetic properties.

4.4 Determination of the Magnetic Phase Diagram

Since two rather inaccurate phase diagrams were published which additionally disagree with each other, one aim of this study was the determination of a detailed phase diagram, with a special focus on the shape of the dome describing the phase boundary of the long-range ordered state. This phase diagram could be the basis for calculations to determine the strength of the interchain couplings which are known only imprecisely. Neutron diffraction, magnetization, and magnetocaloric effect measurements were performed to define the phase boundaries as well as relaxation pulses, which show a change of the heat capacity at the phase boundary. All measurements were performed for applied magnetic fields along the crystallographic b axis. Only in this orientation the axial symmetry can be broken, which is required for a BEC-phase.

4.4.1 Neutron Diffraction Study

With field dependent neutron diffraction measurements the evolution of the antiferromagnetically coupled moments lying in the plane perpendicular to the applied magnetic field can be measured. Therefore, a direct observation of the phase boundary into the long-range ordered phase is possible.

Neutron diffraction data were obtained from measurements on WISH at ISIS as well as on E2 at HZB. For the experiments a 782 mg single crystal with dimensions of $5\times9\times13.5$ mm^3 and a deuteration ratio of 99.9 % was used. The sample was glued with Apiezon N grease on an Al-sample holder and was fixed with additional Al-wires in such a way that the crystallographic b-axis was parallel to the vertical magnetic field (Fig. 4.15). The crystal was preliminary oriented with a x-ray-Laue instrument. At ISIS the orientation was checked again with the neutron-alignment instrument ALF. The crystal was aligned within 0.5° of the b axis. In this configuration only Bragg peaks in the ac plane, which means $h0l$-peaks, could be investigated. For the experiment at WISH a cryomagnet with a maximum magnetic field of 13.5 T and a

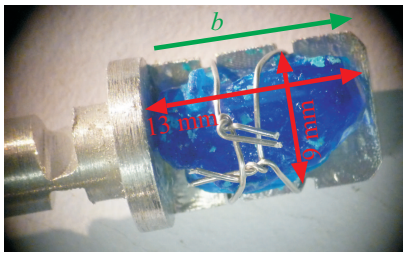

Fig. 4.15: Copper nitrate crystal which was used for the neutron diffraction experiments at WISH and at E2.

dilution insert with a base temperature of 40 mK were used. The magnet had a 340° in-plane opening and -5°/+10° out-of-plane opening. For the experiment at E2 the vertical magnet VM2 with a maximum field of 6.5 T and an in-plane opening of ±5° and a dilution insert with a base temperature of 40 mK were used. The sample could be rotated with the rotation angle ω in the ac plane.

Magnetic Bragg peaks could be observed on top of the nuclear peaks 004, 002, 200, 400, and $40\bar{2}$ as it was reported by Eckert *et al.* [114]. Intensity versus d-spacing plots of the 004 and the $40\bar{2}$ Bragg peak obtained at the instrument WISH for different applied fields are shown in Fig. 4.16.

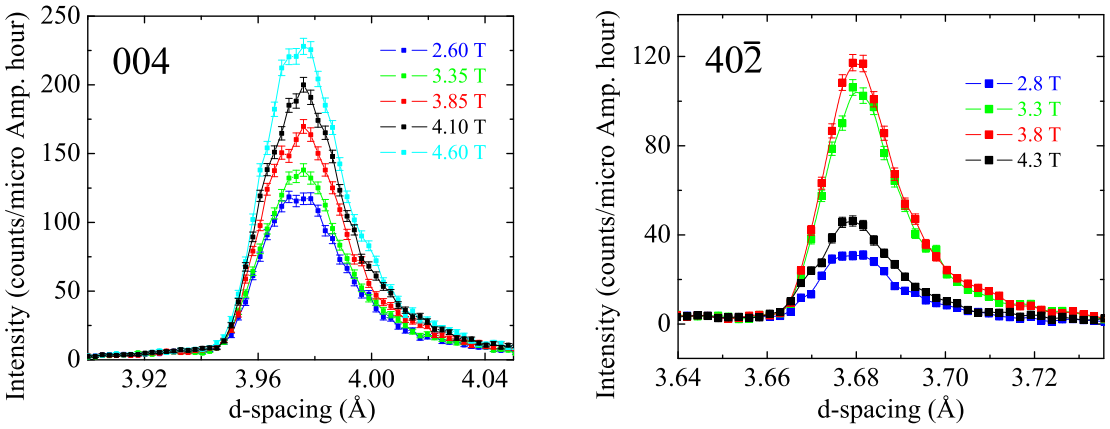

Fig. 4.16: Intensity versus d-spacing of the Bragg peaks 004 at 60 mK (left) and $40\bar{2}$ at 40 mK (right) of copper nitrate in different magnetic fields show the magnetic contribution on top of the nuclear peaks.

As it is already indicated in Fig. 4.16, there are two different kinds of magnetic Bragg peaks. The integrated intensities of the peaks hkl with $h+l = 4n$ such as 004 and 400 increase starting at about 2.85 T and saturate at about 4.35 T (see Fig. 4.17, left). The intensities of the peaks hkl with $h+l = 4n\pm2$ such as 200, 002, and $40\bar{2}$ increase at the transition into the long-range ordered phase H_{t1}, reach a maximum at higher fields and then decrease, which defines the transition field H_{t2} (Fig. 4.17, right). Note, that only at zero temperature the transition fields $H_{t1,2}$ are equal to the critical fields $H_{c1,2}$.

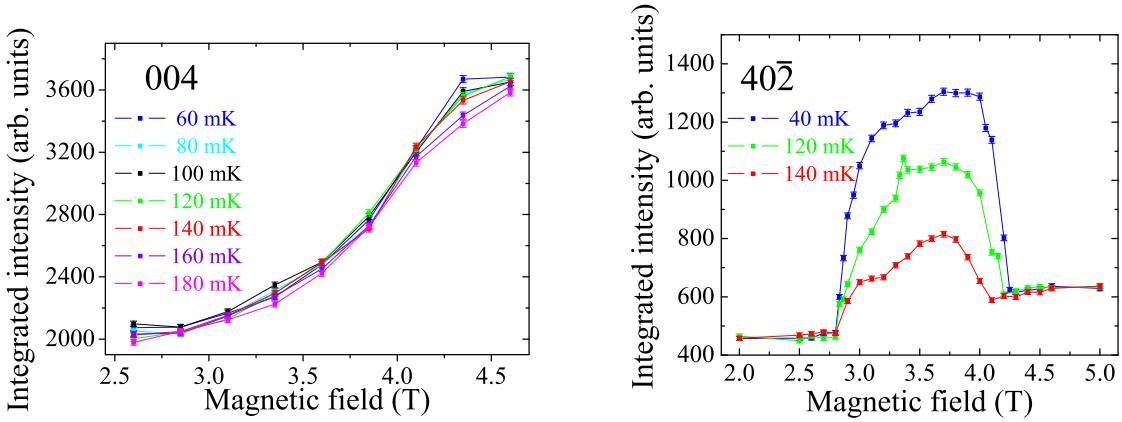

Fig. 4.17: Integrated intensity versus magnetic field of the 004 peak (left) and the $40\bar{2}$ peak (right) of copper nitrate.

Due to the crystal symmetry only four different spin sequences are expected. They are summarized in Tab. 3. The intensity evolution of the Bragg peaks 400 and 004 suggests that these peaks represent mostly the ferromagnetic moment along the field direction (b axis). These peaks follow the spin sequence of Γ_1 with only a component along y. Simulations using FullProf [145] showed that the peaks 400 and 004 give high intensities for this spin alignment, while for 200, 002, and $40\bar{2}$ only very small intensities were found. The evolution of the magnetic Bragg peaks 200, 002, and $40\bar{2}$ indicate that these peaks show an antiferromagnetic spin alignment. Simulations show that only Γ_2 gives a large contribution to these peaks indicating that the antiferromagnetic alignment has the sequence $+--++--+$ as it was found out by Eckert *et al.* [114]. This antiferromagnetic alignment does not have a strong effect on the intensity of the Bragg peaks 400 and 004. All in all, there are two spin structures in copper nitrate, which agree with the picture of the BEC. At H_{c1} long-range antiferromagnetic order is developing which follows the sequence of Γ_2. According to Eckert *et al.* the spins lie roughly in the ac plane and $45°\pm10°$ off the a axis [114]. Moreover, the condensation of the triplons starts as well, which means that the spins are aligned parallel to the applied magnetic field resulting in a ferromagnetic component along the b axis. In summary, there are two spin configurations for fields larger than H_{c1}: The antiferromagnetic one with spins in the ac plane, which vanishes at H_{c2}, and the ferromagnetic one with spins along the b direction, which saturates at H_{c2}.

	Cu11, Cu18			Cu12, Cu17			Cu13, Cu16			Cu14, Cu15		
	x	y	z	x	y	z	x	y	z	x	y	z
Γ_1	+	+	+	−	+	−	+	+	+	−	+	−
Γ_2	+	+	+	−	+	−	−	−	−	+	−	+
Γ_3	+	+	+	+	−	+	+	+	+	+	−	+
Γ_4	+	+	+	+	−	+	−	−	−	−	+	−

Tab. 3: Possible spin sequences for copper nitrate obtained from a symmetry analysis performed with BasIReps (FullProf suite) [145]. The plus and minus signs indicate the magnetic moment directions for each copper atom. The atoms are numbered as in Tab. 2. The sequence of Γ_1 represents the ferromagnetic spin alignment along the b direction (blue cells). The antiferromagnetic spin alignment in the ac plane is represented by Γ_2 (magenta cells).

The field dependence of the **004 Bragg peak** representing the ferromagnetic component and therefore the longitudinal magnetization of the sample is shown in Fig. 4.17 (left panel). The saturation field shifts with increasing temperature to higher fields as it is expected, while the increase of the intensity at about 3 T seems to be temperature independent. The reason could be that due to the magnetocaloric effect the sample temperature differs from the set temperature in this field range.

In principle the critical fields could be obtained by extrapolating the magnetization data to zero temperature where the critical fields are defined by a sudden increase of the magnetization at H_{c1} and a sudden saturation at H_{c2}. Unfortunately, the magnetization curves are not detailed enough for such an analysis.

From the field dependence of the **40$\bar{2}$ Bragg peak**, which is shown in Fig. 4.17 (right panel), the critical fields $\mu_0 H_{c1}$ and $\mu_0 H_{c2}$ can be determined as 2.81(5) T and 4.22(5) T, respectively. The critical fields are determined directly by the jump of the intensity and the drop at 40 mK as the antiferromagnetic component perpendicular to the field direction strongly affects the intensity of this peak. Furthermore, it was assumed that the phase transitions at 40 mK are nearly the same as at zero temperature so that $H_{t1,2}(40\,\mathrm{mK}) \approx H_{c1,2}$. The 40$\bar{2}$ Bragg peak also contains a small contribution from the ferromagnetic structure. Therefore, for fields higher than H_{c2} the intensity does not drop to its initial value but stays constant at a slightly higher level. A distinct decrease of the overall intensity between the two critical fields with increasing temperature is observed, indicating that the magnetic moment component perpendicular to the field direction is decreasing for temperatures close to the phase transition of the long-range ordered phase as expected. Furthermore, a similar temperature behavior is observed for the 40$\bar{2}$ Bragg peak as it is for the 004 Bragg peak. The transition field H_{t1} does not change much with temperature while the second transition field does. Again, this behavior might arise from an incorrect temperature due to the magnetocaloric effect and an insufficient thermalization of the sample. A further consequence of the magnetocaloric effect could be the very asymmetric evolution of the integrated intensity with field, which could be described as a double-peak-like structure between the two critical fields. For example, a heating of the sample due to the magnetocaloric effect in the field range between $H_{t,1}$ and the midpoint field of the long-range ordered phase and a cooling in the field range after the midpoint would result in such a double-peak-like structure.

Temperature dependent measurements were performed on the 40$\bar{2}$ Bragg peak at the instrument E2. A temperature scan at 3.8 T is shown in Fig. 4.18. At each point the intensity was counted for one hour. In spite of this long exposure time, large hysteresis effects were observed when cooling down and heating up, indicating a bad thermalization of the sample. The plot also shows that the transition temperature at a field of 3.8 T, according to these data, is between 140 mK and 190 mK, which is in the range of previous reports on the phase diagram.

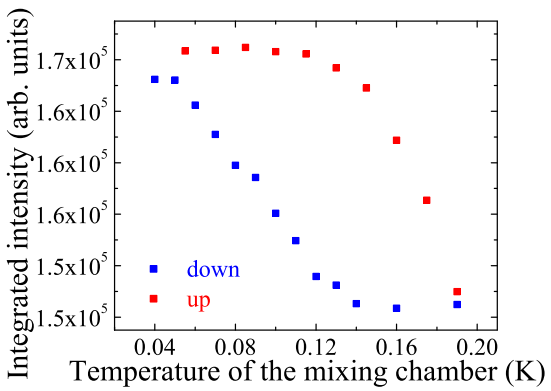

Fig. 4.18: Temperature scan of the magnetic 40$\bar{2}$ peak at 3.8 T for decreasing (down) and increasing (up) temperature. The large hysteresis indicates insufficient thermalization of the sample.

It seems that the slow thermalization of the sample in combination with the magnetocaloric effect strongly affects the neutron diffraction data. Therefore, it appears that accurate data to construct a detailed phase diagram are unaccessible by means of neutron scattering. It would be too time-consuming to map out the phase diagram with the neutron diffraction technique in detail since each point of a field scan at a certain temperature requires about 10 min

time at the instrument WISH and about 1 hour at the instrument E2. For these reasons, bulk techniques were further used to map out the phase diagram since access to such instruments is possible over a longer period. Furthermore, smaller samples were used where a better thermal contact is expected. Magnetization measurements were performed in order to attribute features in the magnetization $M(T)$ such as kinks and extrema or maxima in the derivative $\mathrm{d}M/\mathrm{d}H$ to the phase boundaries.

4.4.2 Magnetization Measurements Using the Cantilever Magnetometer

The direct way to obtain the magnetization of a sample is by using a magnetometer. In order to achieve very low temperatures the cantilever magnetometer described in section 3.4.2 was used. A deuterated copper nitrate single crystal sample was prepared with sand paper in such a way that a flat face perpendicular to the crystallographic b axis was obtained. The sample was from the same batch as the samples measured with the PPMS VSM (98 % D_2O) and had a mass of 0.491(20) mg. It was attached with the flat face on the cantilever using Apiezon N grease. In this configuration, the magnetic field was applied along the b axis with a maximal missalignment of 10° (Fig. 4.19). In order to improve the thermal contact and to avoid contact with the moisture of the air during the installation of the cantilever-option in the dilution fridge, the whole crystal was covered with grease.

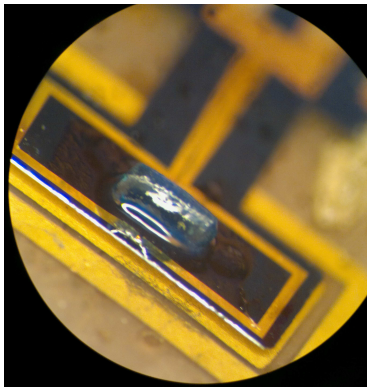

Fig. 4.19: Copper nitrate single crystal attached to the cantilever of the magnetometer.

The magnetization was measured for different temperatures in fields between 2 T and 5 T. The magnetization curves show an increase of the magnetization at about $\mu_0 H_i = 2.55\,\mathrm{T}$ and a saturation at about $\mu_0 H_{\mathrm{sat}} = 4.65\,\mathrm{T}$ for the lowest temperatures, while in between these fields an inflection point at half of the magnetization $M_{\mathrm{sat}}/2$ is present (Fig. 4.20). The saturation moment of $M_{\mathrm{sat}} = 1.18(6)\,\mu_{\mathrm{B}}/\mathrm{Cu}$ is in good agreement with the value of $1.15(1)\,\mu_{\mathrm{B}}/\mathrm{Cu}$ obtained by the PPMS VSM measurements (section 4.3.3), which verifies that the orientation of the crystal was correct. The magnetization curves also show that the saturation field H_{sat} is increasing for increasing temperatures, while the field H_i is decreasing, meaning that the curves are smearing out with temperature, due to the thermally activated triplets. Unfortunately, even at the lowest temperature the curve is too smooth to determine the critical fields with very high accuracy.

In order to compare the ferromagnetic moment evolution obtained in the neutron diffraction study with these magnetization data, the data points attributed to the ferromagnetic scattering contribution were added to the magnetization diagram. For this purpose the square root of the neutron intensity $\sqrt{I - I_0}$ of the 004 peak was extracted, which is proportional to the magnetization M. The data were then normalized to the saturation moment obtained by the cantilever magnetometer. This way, good agreement between the two sets of data was found

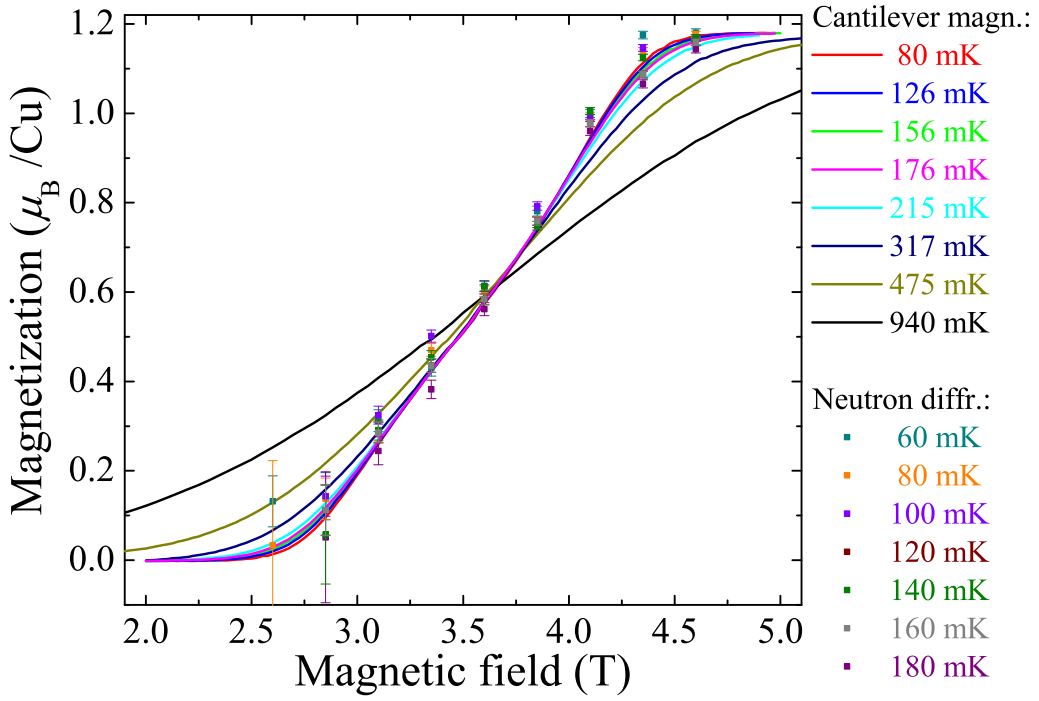

Fig. 4.20: Magnetization data of copper nitrate using the cantilever magnetometer. The temperatures stated in the figures indicate the temperature of the mixing chamber. For comparison the ferromagnetic magnetization shown by the Bragg 004 peak was added to the plot.

down to ∼150 mK, indicating that the interpretation of the 400 and 004 neutron peaks is correct. Further, it is the second proof that the orientation of the sample used for the magnetization measurements was correct. Otherwise, the magnetization curves would be shifted in field according to the different g-factor. However, different saturation fields H_{sat} were observed at temperatures below 150 mK when comparing the neutron data and the cantilever magnetometer data. This difference may be attributed to a temperature of the sample on the cantilever being higher than the mixing chamber temperature.

Since the field derivative of the magnetization defines the boundaries into a Luttinger liquid regime and at lower temperatures into the long-range ordered phase, the magnetization curves were correspondingly treated (Fig. 4.21). The derivative of the magnetization has a double peak structure for temperatures up to 215 mK. For the lowest temperature the first maximum is observed at 3.05 T and the second at 4.02 T. These fields do not fully agree with the critical fields obtained from the antiferromagnetic contribution of the neutron diffraction study indicating again that the temperature of the mixing chamber is lower than the temperature of the sample. The two maxima shift towards each other with increasing temperature until for 317 mK only one peak is remaining, which shows a maximum at 3.6 T. The position of the maximum is in

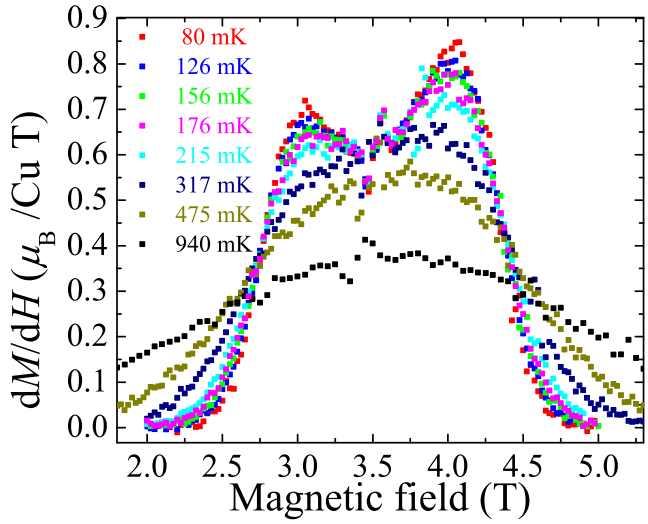

Fig. 4.21: Derivatives of the magnetization data shown in Fig. 4.20. The temperatures stated in the figures indicate the temperature of the mixing chamber. Anomalies in the derivative at 3.5 T are artefacts stemming from the instrument.

agreement with the PPMS VSM data at 1.8 K, indicating that the single maximum does not shift further between 317 mK and 1.8 K.

As stated above, the sample temperature was most likely only correct down to ∼150 mK, which made it impossible to observe the expected minima/maxima and kinks for the crossover into the LL and the transition into the LRO phase, respectively, in temperature dependent magnetization scans. For this reason magnetocaloric effect measurements were performed, as the magnetocaloric effect measures also the magnetization or – more precisely – the derivative of the magnetization $\mathrm{d}M/\mathrm{d}T$. As for this technique the temperature of the sample is measured directly, it is expected that the experimental temperatures are correct. Further, the naturally flat faces perpendicular to the $[10\bar{1}]$ direction of copper nitrate, which arises by simply cutting the crystal, make it possible to use very flat samples with very shiny flat faces. With these shiny faces a better thermalization is expected.

4.4.3 Magnetocaloric Effect Measurements

The magnetocaloric effect was measured using the calorimeter described in chapter 3.2.3. A flat 1.879 mg sample of copper nitrate with a deuteration level of at least 98.6 % D_2O was mounted with Apiezon N grease with the flat face on the calorimeter chip. To improve the thermal contact and to avoid contact with moisture the whole crystal was covered with the grease in a nitrogen filled glovebox. In order to investigate the long-range ordered phase, temperatures below 160 mK and fields up to 5 T are needed, which were obtained using the dilution refrigerator and cryomagnet described in [33]. For all measurements the sample was oriented in such a way

that the applied magnetic field was parallel to the crystallographic b direction with a maximum misalignment of $\sim 5°$. Field sweeps at a constant bath temperature were performed without using the heater on the calorimeter chip in order to avoid heating of the chip caused by noise of the heater power supply and the cables. Hysteresis effects were observed, which could originate from the slow internal relaxation rates of the sample. Microcracks within the sample for instance may lead to these slow relaxation rates. Further, the thermal resistance of the sample surface could have an influence. Therefore, a very small sweep rate of 6 mT/min was chosen leading to a measurement time of about 24 hours for each field scan.

Different kinds of information can be obtained from the magnetocaloric effect. First, the data show features such as jumps and zero crossings of the temperature difference between sample and bath, which define the magnetic phase diagram. Furthermore, the data can be analyzed quantitatively: From the temperature difference between sample and bath as well as from the sweeping rate $\mu_0 \partial H/\partial t$ and the thermal conductivity k the quantity $-\frac{1}{T}\frac{\mathrm{d}Q_{\mathrm{magcal}}(H)}{\mathrm{d}(\mu_0 H)}$ is obtained. It equals the derivative of the magnetization $\mathrm{d}M/\mathrm{d}T$ as well as the derivative of the entropy $\mathrm{d}S/\mathrm{d}(\mu_0 H)$ due to Maxwell's relations (compare Eq. (65)). Therefore, the entropy $S(H)$ as well as the magnetization $M(T)$ can be calculated from the magnetocaloric effect data.

The magnetocaloric effect was measured at different temperatures. In the left hand side panels of Fig. 4.22, 4.24, 4.25, and 4.26, the temperature evolution of the sample while sweeping the magnetic field (raw data) is shown for a bath temperature between 116 mK and 290 mK, while the panels on the right hand side show the quantity $-\frac{1}{T}\frac{\mathrm{d}Q_{\mathrm{magcal}}(H)}{\mathrm{d}(\mu_0 H)}$ as well as the entropy. Note that sometimes spikes in the sample temperature may appear below 2.5 T. Those are due to spikes of the bath temperature during the field sweeps and can therefore be neglected. For the further analysis the spikes are in some degree retractable since only the temperature difference between bath and sample is regarded. (The spikes appear in both sample and bath temperature at the same field.) The raw data at all temperatures show for the up sweeps at fields of 2.73 T and 4.28 T a pronounced maximum and minimum, respectively, while for the down sweeps the curves are inverted. These extrema are typical for magnetocaloric effect data of dimerized spin systems and do not indicate phase transitions. In between these extrema additional features are observed such as jumps, zero crossings of $-\frac{1}{T}\frac{\mathrm{d}Q_{\mathrm{magcal}}(H)}{\mathrm{d}(\mu_0 H)}$ or both. A **jump** can be identified as the transition into the long-range ordered (LRO) phase since it indicates a kink in the entropy, which is a signature of a second order phase transition. Due to Maxwell's relations the jump also indicate a kink in the evolution of the magnetization $M(T)$. The jump is more pronounced when leaving the LRO phase, which is due to the curvature of the phase boundary (Fig. 4.6): For entering the LRO phase e.g. from low fields, the sample temperature is increasing close to the phase transition due to the magnetocaloric effect, so that the transition field is moving to higher fields following the curvature of the phase boundary. Upon leaving the LRO phase the temperature of the sample also increases at the transition, but the curvature of the phase boundary is reversed. Thus, the temperature increase moves the sample further away from the phase boundary in the temperature versus field diagram and a sharp transition is observed. For

that reason the evolution of the up and down sweeps are not exactly identical and an averaging of up and down sweep data is not possible. Further, only the sharp transitions are used to define the transition fields H_{c1} and H_{c2} of the phase diagram, and for calculating $-\frac{1}{T}\frac{\mathrm{d}Q_{\mathrm{magcal}}(H)}{\mathrm{d}(\mu_0 H)}$ only the regions showing the sharp transitions are used. Since these regions do not exactly match each other in the medium field range, small regions were omitted. The graphs of $-\frac{1}{T}\frac{\mathrm{d}Q_{\mathrm{magcal}}(H)}{\mathrm{d}(\mu_0 H)} = \mathrm{d}M/\mathrm{d}T = \mathrm{d}S/\mathrm{d}H$ show also **zero crossings**. These are points where $\mathrm{d}M/\mathrm{d}T = \mathrm{d}S/\mathrm{d}H = 0$ and therefore the magnetization and entropy show extrema.

For low temperatures (116 mK see Fig. 4.22) the temperature jumps extend up very close to the value of the following temperature maximum/minimum. Here, the jump crosses the zero level, which implies that an extremum of the magnetization curve $M(T)$ coincide with a kink. The result is a cusp like extremum in the $M(T)$-evolution, which will be shown later. This feature is analogous to the minimum observed at the transition into the BEC-phase for $TlCuCl_3$ at low fields [146]. For fields closer to H_{c2} a maximum is expected [121].

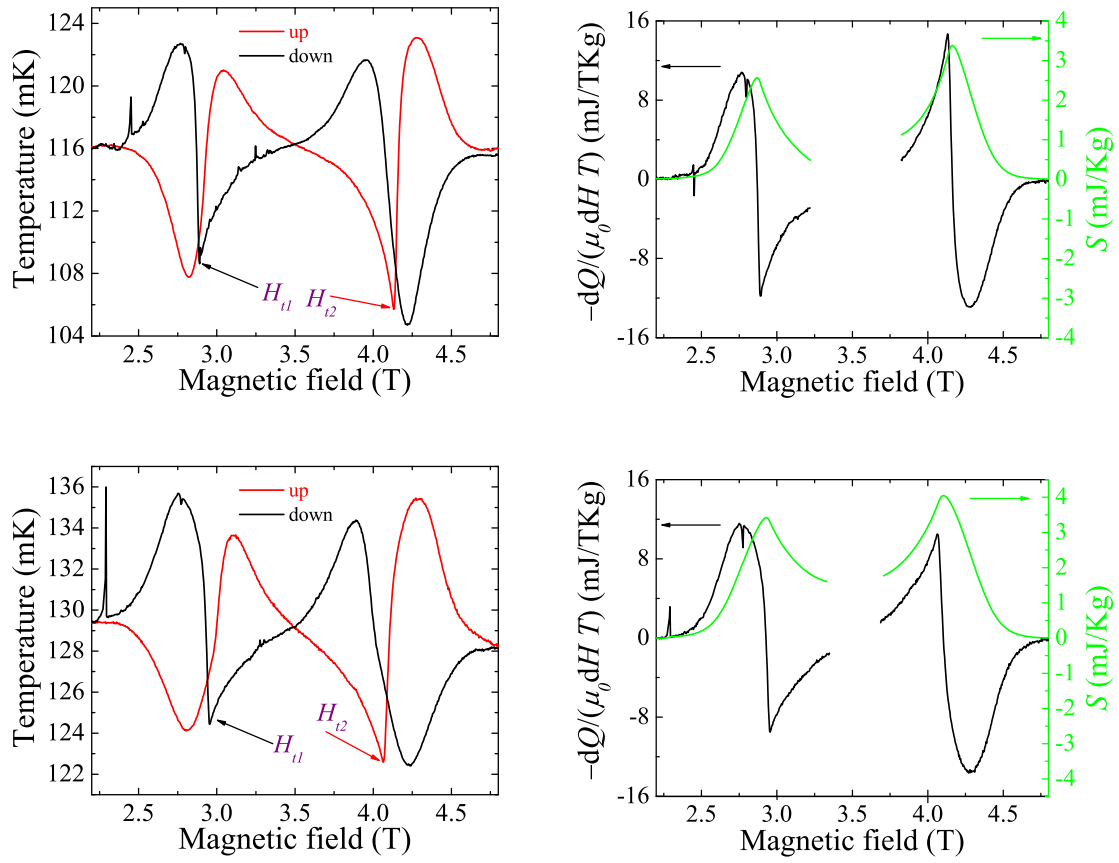

Fig. 4.22: Magnetocaloric effect of copper nitrate in the low temperature regime at 116 mK (upper panels) and at 129 mK (lower panels). Spikes are caused by spikes on the bath temperature. Left: sample temperature evolution while sweeping the magnetic field. Right: $-\frac{1}{T}\frac{\mathrm{d}Q_{\mathrm{magcal}}(H)}{\mathrm{d}(\mu_0 H)}$ and entropy S for sweeps across the borderline of the BEC-phase.

By an integration of the $-\frac{1}{T}\frac{\mathrm{d}Q_{\mathrm{magcal}}(H)}{\mathrm{d}(\mu_0 H)}$ data the entropy is obtained, which is included in Fig. 4.22. As the sample reaches saturation, the integration constant is known ($S(H > H_{\mathrm{sat}}) = 0$) so that the entropy can be shown in quantitative values. The entropy is maximized near the transition fields as it is predicted for quantum phase transitions [147]. Furthermore, the maxima in the entropy coincide with kinks of the entropy (see also Fig. 4.23 for a zoom-in of the entropy evolution), which indicate the second order phase transitions. For higher temperatures at about 129 mK the jumps end before reaching the maximum/minimum value but they still cross the zero value, which would lead to cusp like extrema as well. The entropy evolution at 129 mK is similar to the entropy at 116 mK, but the entropy between the transitions increases for an increasing temperature. In summary, for this temperature regime a direct transition into the long-range ordered phase is observed.

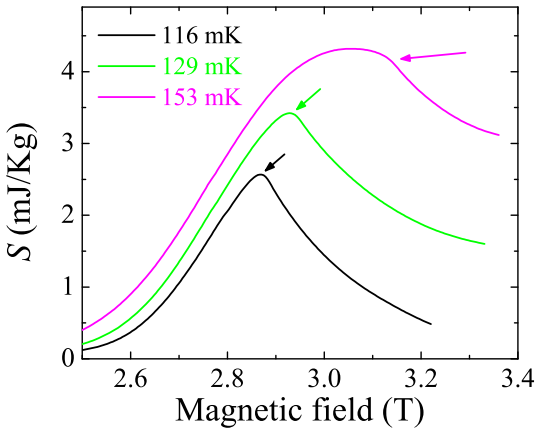

Fig. 4.23: Temperature evolution of the entropy of copper nitrate, where the arrows point at the kinks (transitions into the LRO phase). At 116 mK and 129 mK the maximum of the entropy coincide with a kink, while at 153 mK it does not, indicating that the crossover into the LL regime and the phase transition into the LRO phase occur at different magnetic fields.

At temperatures near the upper phase boundary of the LRO phase, e.g. at a temperature of 153 mK (Fig. 4.24), the jumps end before the zero level is reached. Therefore, the jump (transition into the LRO phase) and the zero crossing (extrema in the magnetization) do not coincide. The entropy $S(H)$ shows consequently two round maxima at the fields H'_{t1} and H'_{t2} as well as two kinks indicating the phase transitions at H_{t1} and H_{t2}. The entropy evolution is depicted in Fig. 4.23 in more detail, where it is compared to the entropy at lower temperatures (116 mK and 129 mK) in order to highlight the difference between these two temperature regions. In the magnetization $M(T)$ a round extrema is expected as well as a kink for lower temperatures, which is shown later. The points of zero-crossing can be identified as crossover fields H'_{t1} and H'_{t2}. These are not transitions into a long-range ordered phase, but they indicate a crossover into a Luttinger-liquid regime, which develops due to the 1D character of the spin chain. The Luttinger-liquid regime also shows extrema in the magnetization with respect to temperature, but these are round [119–121]. Similar zero crossings were identified as transitions into a Luttinger-liquid

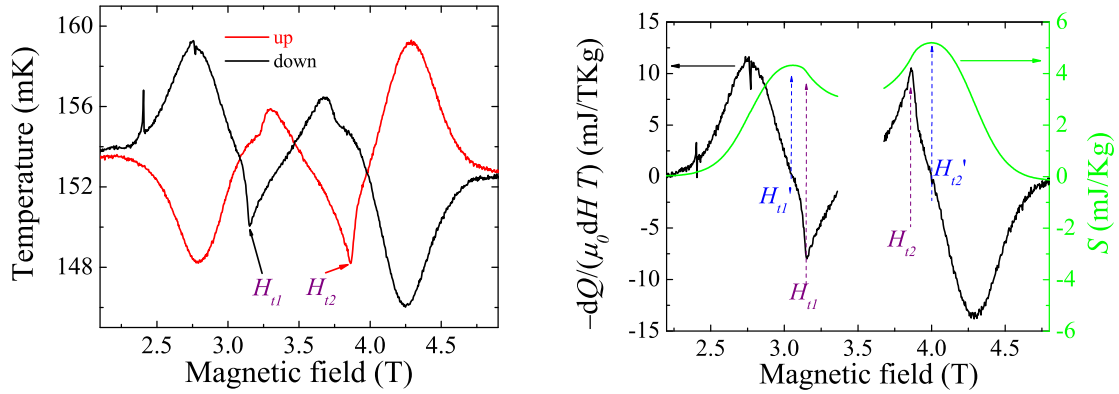

Fig. 4.24: Magnetocaloric effect of copper nitrate at 153 mK (intermediate temperature regime). Spikes in the sample temperature are due to spikes on the bath temperature. Left: sample temperature evolution while sweeping the magnetic field. Right: $-\frac{1}{T}\frac{\mathrm{d}Q_{\mathrm{magcal}}(H)}{\mathrm{d}(\mu_0 H)}$ and entropy when leaving the BEC-phase. Here, both features are observed, a jump as well as a smooth zero crossing.

regime for $(\mathrm{Hpip})_2\mathrm{CuBr}_4$ and $(\mathrm{Hpip})_2\mathrm{CuCl}_4$ [33,35,42], but in these materials only the transition into the Luttinger liquid regime was measured by magnetocaloric effect measurements. Copper nitrate is the first material where both transitions, the transition into the LL regime and into the LRO phase, is observed in the same magnetocaloric data set.

For higher temperatures, e.g. 173 mK (Fig. 4.25), the jumps vanish, but the zero crossings are still present. The entropy and the magnetization do not show kinks any more but only smooth extrema. That indicates that for these temperatures no transition into the LRO phase is present, but a crossover into the LL regime. The LL regime extends to higher temperatures than the LRO phase as expected since the LRO develops for temperatures $Tk_B < J_{\mathrm{interchain}}$, while a LL is present for $J_{\mathrm{interchain}} < Tk_B < J_{\mathrm{intrachain}}$. The raw data of the up and down sweeps are nearly identical apart from the sign, so that an averaging between up and down sweeps is possible to reduce systematic errors. The zero crossings lead to two maxima in the entropy, which move closer together as the temperature increases. The two zero crossings were observed for temperatures up to 205 mK.

At even higher temperatures, e.g. 290 mK, the two zero crossings vanish indicating that the LL regime is no longer present. This is shown in Fig. 4.26. The entropy shows only a single maximum, which becomes more and more symmetric as the temperature is increased.

All in all, for copper nitrate four different temperature regimes were found: at low temperatures up to 145 mK direct transitions into the LRO are observed. In the intermediate temperature regime, which extends up to 163 mK, a crossover into the LL regime as well as a transition into the LRO regime is observed for different magnetic fields. For temperatures up to 205 mK only indications of a crossover into the LL regime are present, while for even higher temperatures the material is paramagnetic.

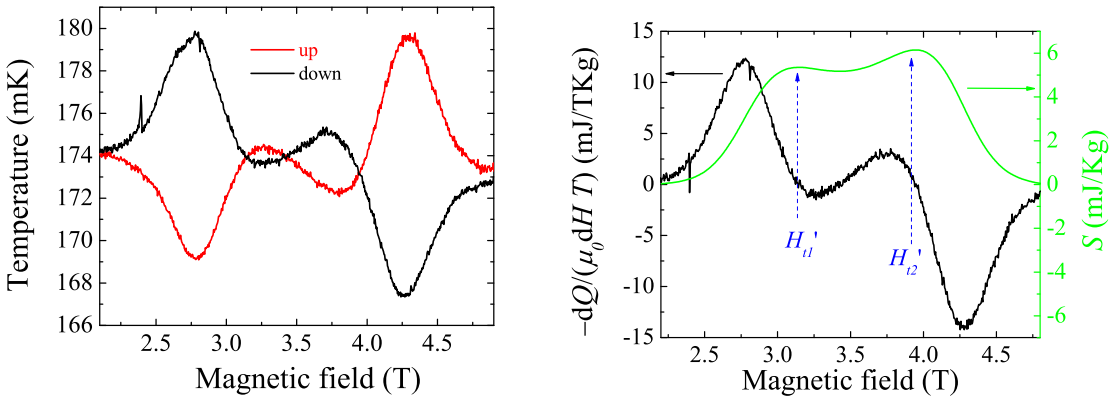

Fig. 4.25: Magnetocaloric effect of copper nitrate at 173 mK. Spikes in the temperature are due to spikes on the bath temperature. Left: sample temperature evolution while sweeping the magnetic field. Right: $-\frac{1}{T}\frac{\mathrm{d}Q_{\mathrm{magcal}}(H)}{\mathrm{d}(\mu_0 H)}$ and entropy. Zero crossings are observed showing that for this temperature only a crossover into the LL regime is present.

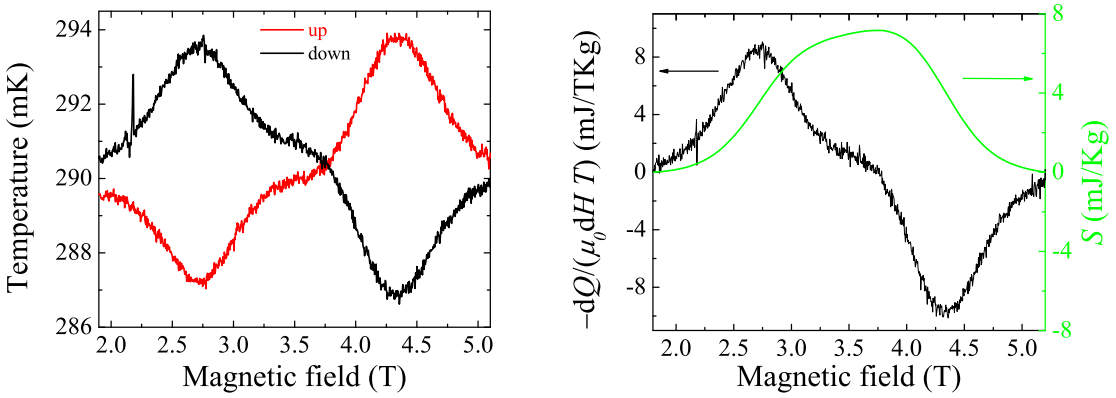

Fig. 4.26: Magnetocaloric effect of copper nitrate at 290 mK. Spikes in the temperature are due to spikes on the bath temperature. Left: sample temperature evolution while sweeping the magnetic field. Right: $-\frac{1}{T}\frac{\mathrm{d}Q_{\mathrm{magcal}}(H)}{\mathrm{d}(\mu_0 H)}$ and entropy. In this temperature regime no feature of a transition/crossover was observed, which indicates that for this temperature the material is paramagnetic.

Evolution of the Magnetization $M(T)$

In the previous discussion the phase boundaries and crossovers were obtained through a qualitative interpretation of the data, but the magnetocaloric effect data provides even more information. In this section, a quantitative analysis of the magnetization follows. As it is stated above and also in section 3.3, the derivative of the magnetization $\mathrm{d}M/\mathrm{d}T$ can be calculated out of the magnetocaloric effect data. The values of the derivative were gathered for all scans at four different magnetic fields (2.95 T, 3.10 T, 3.92 T, and 4.10 T). Integration of the data with respect to the temperature, leads to the magnetization $M(T)$. In order to obtain the correct integration constant, the magnetization data were compared with the data obtained by the cantilever magnetometer at temperatures above 150 mK. In this way, the magnetization can be presented in absolute values (Fig. 4.27).
For an applied magnetic field of 2.95 T a clear minimum defines the phase transition into the long-range ordered phase, while at 4.10 T a maximum indicates the transition. Since in the derivative the minimum/maximum is observed as a zero transition, which is accompanied by a clear jump, the extrema can be characterized as a cusp like extrema. This is similar to the cusp like minimum found for BEC materials such as $TlCuCl_3$, which was interpreted as the boundary for BEC of triplons [36, 146].
For applied fields closer to the top of the phase diagram's dome, two features can be observed. At 3.10 T a round minimum indicates the transition into the LL phase, while a kink defines the transition into the long-range ordered phase. The kink has not a very clear signature in the magnetization data due to the limited number of magnetocaloric effect scans, but the transition is very pronounced in the derivative, where a peak defines the transition. Further, the minimum is indicated by a zero crossing of the derivative. For 3.92 T the situation is similar, but the minimum is replaced by a maximum. This magnetization evolution with a minimum/maximum for a crossover into a LL regime and a kink for a transition into a 3D ordered phase is exactly what Wessel *et al.* predicted for a spin ladder [121]. Therefore, the interpretation of the features (jumps and zero crossings) in the magnetocaloric effect raw data as phase transitions and crossovers is fully consistent with the expectation of the features of the magnetization curve $M(T)$. That justifies the use of the features observed in the MEC data to define the phase diagram.

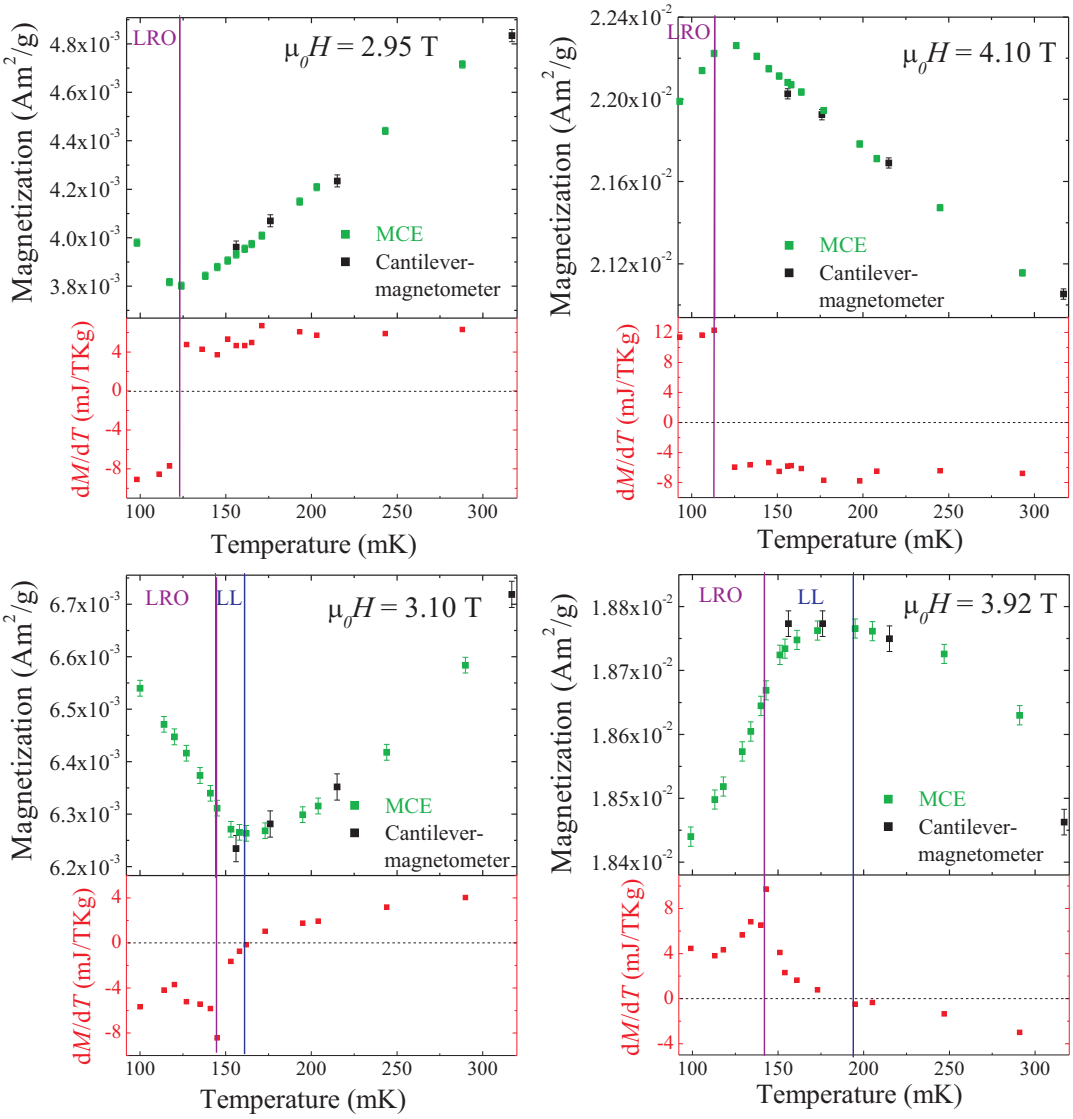

Fig. 4.27: Magnetization $M(T)$ at 2.95 T, 4.10 T, 3.10 T, and 3.92 T obtained from MCE data. The magenta lines indicate the transition into the long-range ordered phase (LRO), while the blue lines mark the transition into the Luttinger liquid regime (LL).

4.4.4 Relaxation Pulses

Magnetocaloric effect measurements are optimal for determining vertical phase boundaries of a $T_c(\mu_0 H_t)$-phase diagram, but horizontal phase boundaries are hard to define. A technique, which sweeps the temperature, is more efficient for this purpose. This is the domain of heat capacity measurements. Therefore, a relaxation method was used for the determination of the upper phase boundary of copper nitrate. First, heat pulses were performed at 3 T covering a temperature range between 100 mK and 300 mK (Fig. 4.28). After each pulse a waiting time of 60 minutes was implemented until the sample was in thermal equilibrium. For a second order phase transition a jump in the heat capacity is expected and therefore a change of the time constant of the relaxation process. Already in the raw data the abrupt decrease of the time constant for temperatures above the transition temperature is clearly visible.
Further, two relaxation processes are present (inset of Fig. 4.28): one with a very short relaxation time and the other with a long time. The small relaxation time is due to the thermal conductivity between chip and bath, while the large one is due to the thermal conductivity between the sample and the chip. This is surprising since the sample was very flat and had a shiny face, which had contact with the calorimeter chip. Probably, the bad thermal contact, which was also observed during the neutron scattering measurements, is an issue of the material itself.
For obtaining the heat capacity out of this data the method for two-τ-relaxation processes proposed by Shepherd was used [99]. The two-τ-behavior leads to a relatively large error for the heat capacity, but nevertheless the transition into the long-range ordered state at T_c is observed as it was by van Tol *et al.* [134] (compare Fig. 4.28 to Fig. 4.9).
Since the phase boundary of the BEC phase is clearly seen from the decrease of the relaxation time when leaving the BEC phase, it is sufficient to apply heat pulses which pass the boundary to determine the upper phase boundary. An example of such a heat pulse is shown in Fig. 4.29. The transition points were added to the phase diagram.

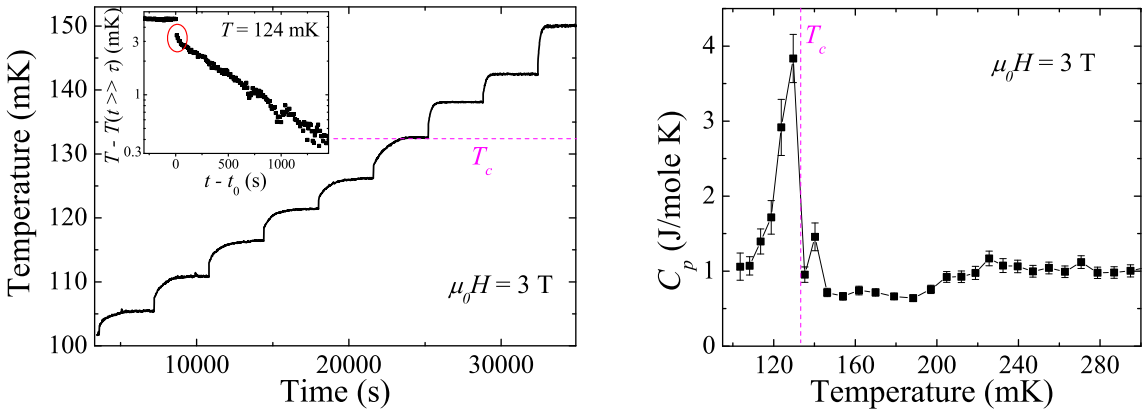

Fig. 4.28: Left: relaxation pulses for copper nitrate at 3 T. The magnetic phase transition is observed at about 132 mK. The inset shows a logarithmic plot of the sample temperature minus the equilibrium temperature at the end of the pulse versus the time for $T = 124$ mK. The relaxation pulse was performed within the LRO phase and therefore does not show a phase transition. Marked is the beginning of the pulse where a significant change of the slope indicates the two-τ-behavior. Right: heat capacity of copper nitrate calculated via the method proposed by Shepherd [99].

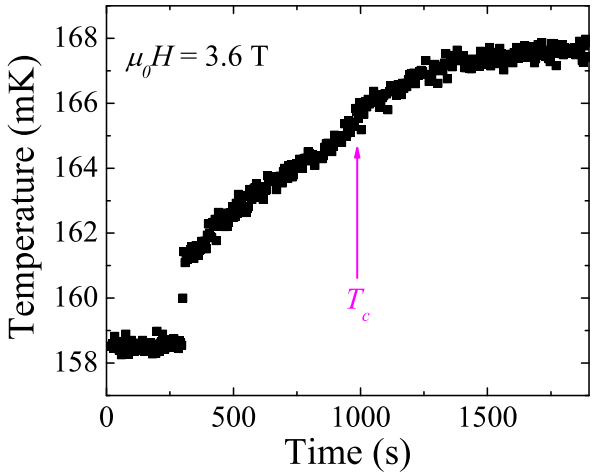

Fig. 4.29: Heat pulse at 3.6 T: the time constant is changing abruptly when crossing the phase boundary at T_c, resulting in a kink.

4.4.5 The Phase Diagram of Copper Nitrate

The features observed in the magnetocaloric effect as well as in the heat pulse method were used to define the phase diagram of copper nitrate, which is presented in Fig. 4.30. The transition fields for 40 mK obtained by the neutron diffraction study were also added to the phase diagram. Since during these measurements problems with the sample temperature were noticed, the error bars were chosen to be ± 10 mK. Furthermore, the two maxima of the derivative $\mathrm{d}M/\mathrm{d}H$ obtained from the cantilever magnetometer measurements were added as they indicate phase transitions into the LL phase. These two maxima develop since in the LL the magnetization follows a square root function near the critical fields [118]. Down to 150 mK the data fit perfectly with the magnetocaloric effect data, but for lower temperatures they disagree. This can result either from an incorrect sample temperature, from non-square root evolution of the magnetization near H_c, or both. As already stated in section 4.4.2 problems with the temperature of the cantilever magnetometer sample were noticed for temperatures below 150 mK, which would be the most obvious explanation for the discrepancy between the data points obtained by the cantilever magnetometer and the magnetocaloric effect measurements in the phase diagram. Another reason for this discrepancy could be the weak 3D interactions, which cannot be ignored in this temperature region where long-range order is found. The 3D coupling would lead to a linear increase of the magnetization very close to the critical field [109], which was already found for $(\mathrm{Hpip})_2\mathrm{CuBr}_4$ [148]. A mixing of linear and square root behavior could possibly lead to a double peak structure in the derivative, where the maxima do not coincide with the transition fields. The maxima in the derivative of the magnetization are therefore only good indicators for the crossover into the LL. Thus, it is reasonable to neglect the transitions points for temperatures below 150 mK stemming from the cantilever magnetization.

The phase boundary of the long-range ordered (LRO) phase is described by a very symmetric dome, which extends up to 166 mK at about 3.52 T. At higher temperatures indications of a Luttinger liquid were observed. The LL forms also a dome, which is located on top of the dome of the LRO phase. In contrast to the LRO-phase, the LL dome is more asymmetric in shape. The LL extends up to temperatures between 215 mK and 244 mK. Interestingly, copper nitrate seems to show a region where a direct transition into the LRO phase without crossing the LL regime is possible by simply decreasing the temperature.

Since for a BEC-phase a critical behavior with the universal critical exponent $\phi = 2/d$ is expected, the phase boundary was fitted according to Eq. (72). Unfortunately the evolution of the phase boundary is very steep and the uncertainty in the measurements is not small enough to obtain accurate values for ϕ. Fits with ϕ between 0.40 and 0.78 are possible within the error bars. A fit with $\phi = 2/3$, which would be the exponent for a BEC phase in 3D, is added exemplarily to the phase diagram. With this fit a critical field of $H_{c1} = 2.73$ T is obtained. Although this model fits to the data, a BEC behavior cannot be clearly confirmed by this fit due to the large error bars.

In order to distinguish between the gapped quantum disordered (QD), the quantum critical (QC), and the fully polarized regime, the position of local maxima in the heat capacity were added. These were obtained from simulations, which are described in the next section. A contour plot was added to the phase diagram as well, which represents the quantity $-\frac{1}{T}\frac{\mathrm{d}Q_{\mathrm{magcal}}(H)}{\mathrm{d}(\mu_0 H)}$. The maximum and minimum values are close to the crossovers between the different regimes.

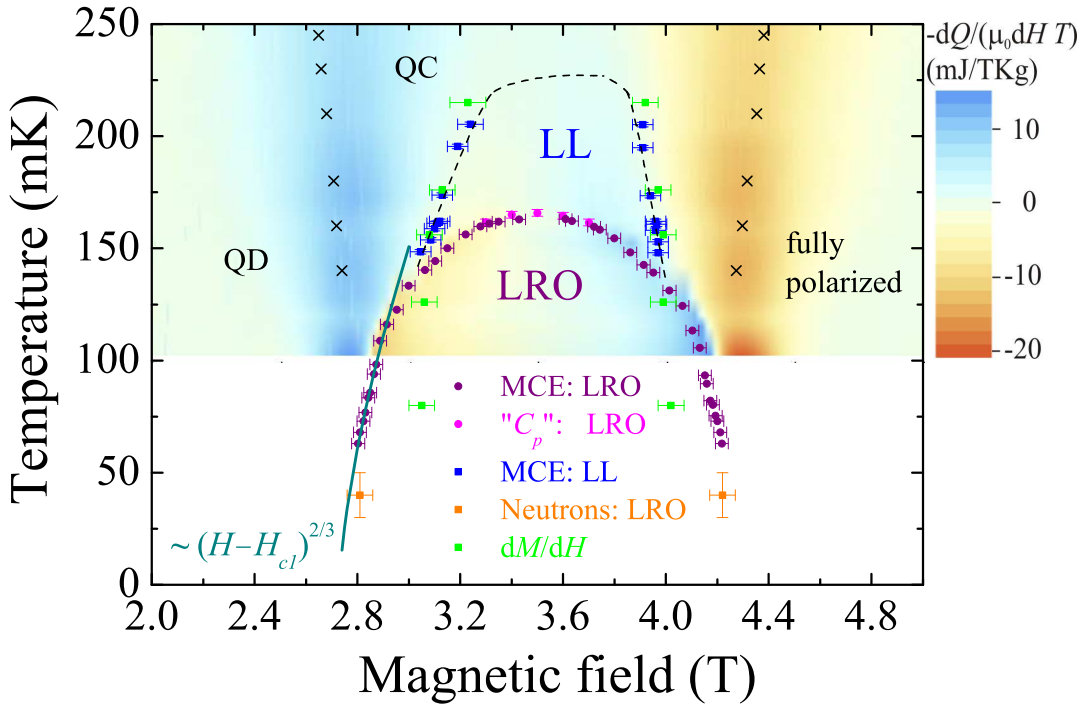

Fig. 4.30: Phase diagram of copper nitrate for applied magnetic fields along the b direction. The dashed line is a guide to the eye. The contour plot represents the data $-\frac{1}{T}\frac{\mathrm{d}Q_{\mathrm{magcal}}(H)}{\mathrm{d}(\mu_0 H)}$. The crosses indicate the local maxima in the heat capacity and can be considered as crossovers between the quantum disordered (QD), the quantum critical (QC), and the fully polarized regime. For details see text.

4.5 Discussion

In the previous sections various measurements of the thermodynamics of copper nitrate were presented. In order to compare the experimental data with the model of an alternating antiferromagnetic chain, simulations using the exact diagonalization method were performed. For this purpose the software ALPS was used, which was introduced in section 4.3.3. Like the previous simulations, a one-dimensional isotropic Heisenberg Hamiltonian with external field and alternating exchange constants was used. The magnetization and the magnetocaloric effect were calculated for a ring of 14 spins. The best agreement between experimental data and theory was obtained for the exchange constants $J_1 = -5.10(2)\,\mathrm{K}$ and $J_2 = -1.20(2)\,\mathrm{K}$ (Fig. 4.31) resulting in a ratio α =0.24. These values agree very well with the exchange couplings found by Xu *et al.* ($J_1 = -5.13\,\mathrm{K}$, $J_2 = -1.23\,\mathrm{K}$ [108]) although the interchain couplings were neglected in the current model. This simple model is only applicable for temperatures above the transition into the LRO phase. Good agreement between calculation and experiment was found for temperatures down to 195 mK. For lower temperatures the interchain couplings need to be regarded as well. Furthermore, for temperatures lower than 200 mK the effects of the finite number of spins become gradually noticeable.

With the exchange constants $J_1 = -5.10\,\mathrm{K}$ and $J_2 = -1.20\,\mathrm{K}$ the upper boundary of the Luttinger liquid dome was found at $T_{c,\mathrm{max,\,LL}} = 220(5)\,\mathrm{mK}$ by taking the zero crossings of the calculated magnetocaloric effect as crossover fields. This value of the upper boundary is in agreement with the experimental data, where the transition was determined to occur at temperatures between 215 mK and 244 mK. The asymmetry in the evolution of the entropy as well as the asymmetry of the derivative $\mathrm{d}M/\mathrm{d}B$ found in the experimental data is also observed in the calculations using the 1D model and is therefore a characteristic treat of this spin system. Furthermore, the asymmetry of the LL dome can be understood in the context of the 1D model. Since the curvatures in the medium field regime of the magnetocaloric effect data are not symmetric with respect to the zero level (red dashed line in Fig. 4.31) and seem to be shifted to higher values, the low field boundary of the LL is less steep than the high field boundary.

The data presented in this thesis give clear evidence of a Luttinger liquid regime as all features, which are expected for the evolution of the magnetization and entropy, were really observed in the experimental data. A proof of a LL, however, is still missing. Inelastic neutron scattering could definitively decide if this region is a LL regime as the characteristic two spinon continuum can be observed. Unfortunately, all inelastic neutron scattering studies published so far were not performed in this field and temperature range. Notbohm performed inelastic neutron scattering experiments at 3 T and 120 mK, which is relatively close to the edge of the LL [132]. In this study features were interpreted as indications of a LL, but a clear evidence of the two spinon continuum was not produced.

Another proof of the existence of a LL could be provided by the behavior of the magnetic heat capacity C_{mag}, where $C_{\mathrm{mag}} \sim T$ is expected [120,122]. Since this property could not be measured

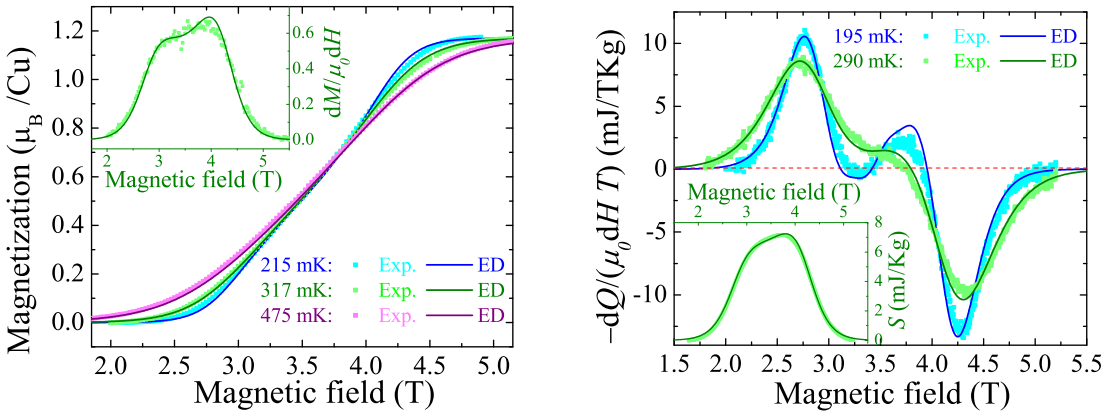

Fig. 4.31: Simulation of the magnetization (left diagram), magnetocaloric effect (right diagram), and entropy (inset of the right panel) compared to the experimental data using the exact diagonalization (ED) method of a 1D model. The inset in the left panel shows the derivative of the magnetization at 317 mK. For details see text.

here with high accuracy, simulations were performed using the same method and exchange constants as for the simulations of the magnetization and magnetocaloric effect introduced above. Since the evolution of $\mathrm{d}S/\mathrm{d}H$ (magnetocaloric effect) could be successfully calculated using the same model, the evolution of the calculated heat capacity $C = T\partial \mathrm{S}/\partial T$ should equally match experimental data. Therefore, C_{mag} was calculated for the three different field regimes: the gapped spin liquid region $H < H_{c1}$, the gapless region $H_{c1} < H < H_{c2}$, and the fully polarized region $H_{c2} < H$ (Fig. 4.32). In all regions a very broad maximum was obtained between 1.7 K and 2.7 K, which was interpreted for the ladder model as the contribution of the gapped triplet states [122]. Only in the region $H_{c1} < H < H_{c2}$ an additional peak at lower temperatures can be observed with a linear temperature dependence for temperatures below the maximum. The beginning of the linear temperature dependence is shown in the plot of C_{mag}/T, where the evolution of C_{mag}/T becomes constant at low temperatures (Fig. 4.32, right). This linear behavior of the heat capacity indicates the presence of gapless spinon excitations [35, 122]. The low temperature maximum of C_{mag} for fields close to the center of the LL at $H_m = (H_{c1} + H_{c2})/2$ can therefore be interpreted as the crossover into the LL. The maximum of the LL was determined with this method to $T_{c,\mathrm{max,\ LL}} = 220(3)$ mK in agreement with the crossover temperature stated above. For fields $H < H_{c1}$ and $H > H_{c2}$, but close to the critical fields, shoulders develop in the heat capacity at low temperatures (upper and middle left panel of Fig. 4.32). These were observed in a theoretical study of the ladder model by Wang *et al.* as well and do not indicated any crossover [120]. Evidence of the agreement between simulated and experimental data is given by the results of van Tol *et al.* [134]. Their data are shown in Fig. 4.9 (section 4.2.2). A weak maximum of the heat capacity for an applied magnetic field of 3.57 T is observed between 200 mK and 300 mK, which confirms the presence of a low temperature maximum of the heat capacity in this field range.

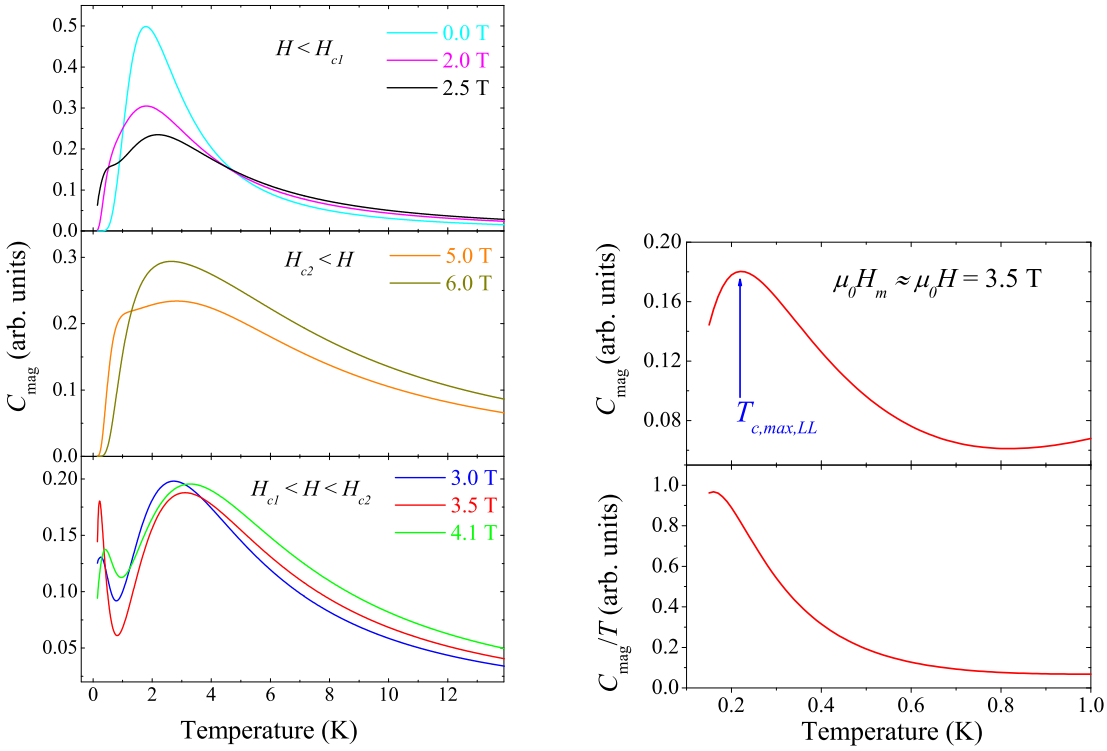

Fig. 4.32: Simulation of the magnetic heat capacity C_{mag} using exact diagonalization with the parameters $J_1 = -5.10\,\mathrm{K}$ and $J_2 = -1.20\,\mathrm{K}$. Three different field regimes are depicted: $H < H_{c1}$ (upper left panel), $H_{c2} < H$ (middel left panel), and $H_{c1} < H < H_{c2}$ (lower left panel). The upper right panel shows a zoom-in of the curve at 3.5 T, which is close to the center of the LL, while the lower right panel shows the heat capacity divided by the temperature at 3.5 T.

In order to define the crossovers from the quantum critical (QC) regime to the quantum disordered (QD) and fully polarized regime, the magnetic heat capacity was simulated at constant temperatures using the same parameters as before (Fig. 4.33). The shape of the curves is very similar to the curves of the ladder compound $(\mathrm{Hpip})_2\mathrm{CuCl}_4$ [33]. A broad maximum is observed at H_m, while local maxima are found next to this maximum. These local maxima can be attributed to the crossovers from the QC regime to the QD and fully polarized regime [35]. They occur due to thermally activated excitations and shift with temperature, indicating the closing of the spin gap and the reopening for fields larger than H_{c2}. The local maxima from these calculations were used to define the crossovers between the quantum disordered, the quantum critical, and the fully polarized regime in the phase diagram shown in Fig. 4.30.

Altogether, the magnetic phase diagram of copper nitrate seems to be very similar to the phase diagram of the ladder compound $(\mathrm{Hpip})_2\mathrm{CuBr}_4$, which was studied in much detail recently. The magnetic phase diagram of this system was shown already in the introduction (chapter 4.1, Fig. 4.2). Using the magnetocaloric effect and heat capacity measurements the crossover into the LL regime was determined for the compound $(\mathrm{Hpip})_2\mathrm{CuBr}_4$. The same features of the magnetocaloric effect data were used as for copper nitrate to define the boundaries, namely the zero

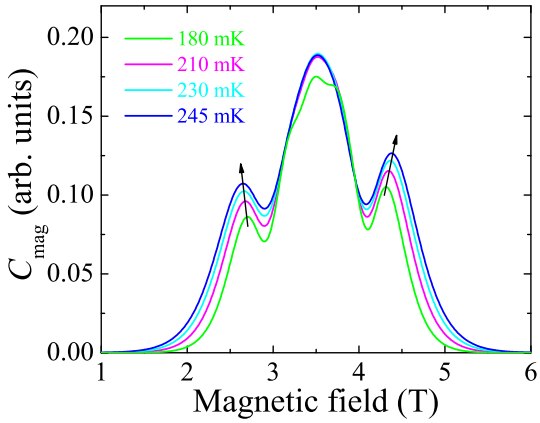

Fig. 4.33: Simulation of the magnetic heat capacity $C_{\mathrm{mag}}(\mu_0 H)$ at constant temperatures using the exact diagonalization method. The funny shape of the maximum at 180 mK could be due to the finite number of spins used for this simulation.

crossings indicating the extrema in the magnetization [35]. Inelastic neutron scattering experiments on $(\mathrm{Hpip})_2\mathrm{CuBr}_4$ confirmed the assumption of a Luttinger liquid, as a broad continuum of spinon excitations was found in this region [34]. Furthermore, the behavior of the NMR relaxation rate T_1 was found to follow the expectations of a Luttinger liquid [148]. Neutron diffraction and the splitting of NMR lines were used to define the phase boundary of the long-range ordered state [42, 148]. As well the shape of the phase boundary of the long-range ordered state was found to be very asymmetric with respect to $H_m = (H_{c1} + H_{c2})/2$. This asymmetry in $(\mathrm{Hpip})_2\mathrm{CuBr}_4$ was accounted for by the influence of the upper two triplet bands. The shape was described by weakly coupled ladders using only one interladder coupling constant [148]. The phase boundary of copper nitrate on the other hand is symmetric as it was found for the 3D system $\mathrm{BaCuSi_2O_6}$ [39]. It seems that one reason for the discrepancy in the shape of the LRO dome between $(\mathrm{Hpip})_2\mathrm{CuBr}_4$ and copper nitrate could be the different 3D couplings with respect to the 1D coupling and not only the upper triplet states. For $(\mathrm{Hpip})_2\mathrm{CuBr}_4$ a clear separation between the energy regimes is possible as $J_{\mathrm{intradimer}} >> J_{\mathrm{intraladder,1D}} >> J_{\mathrm{interladder,3D}}$ is fulfilled. In this case the intraladder (1D) coupling is two magnitudes larger than the 3D coupling. For copper nitrate however, this separation is not so clear. Here, the intrachain coupling is only about one magnitude larger than the interchain coupling. Therefore, the 1D character is more pronounced in $(\mathrm{Hpip})_2\mathrm{CuBr}_4$. The different coupling ratios also explain that the LL regime extends over a much larger temperature regime for the compound $(\mathrm{Hpip})_2\mathrm{CuBr}_4$, while for copper nitrate the LL is observable only for temperatures just above the LRO state. Interestingly, the phase diagram of copper nitrate suggests that the LL regime sits on top of the LRO in such a way that a direct transition into the LRO state without crossing the LL regime seems possible by just lowering the temperature at a constant magnetic field. That is in contrast to $(\mathrm{Hpip})_2\mathrm{CuBr}_4$, where the transition fields for the LL regime coincide with the critical fields (at zero temperature) for a

large temperature regime.
Summing up, there exist two model systems, copper nitrate and $(Hpip)_2CuBr_4$, which provide different possibilities to cross the different regimes at experimentally accessible fields and temperatures. These could help to understand the dimensional crossover between the 1D LL with fermionic excitations and the 3D phase with bosonic behavior, which is an area of great interest, since all real components do order at sufficient low temperatures due to weak 3D couplings [2,149].

4.6 Summary

Deuterated single crystals of copper nitrate were grown and characterized extensively for temperatures down to 1.8 K. The deuteration neither shows an effect on the lattice parameters nor on the magnetization curves. A small effect was observed only for the decomposition of the compound for temperatures above ∼80°C.

Using these crystals, the magnetic phase diagram was determined in detail using several experimental techniques. Throughout the use of all techniques problems with the thermalization of the sample were observed hinting at an intrinsic issue connected to the sample. With magnetocaloric effect measurements the problem could be handled most easily since for these measurements a small and flat sample with a shiny face, which served as a contact plane, could be used. Furthermore, this technique allows an almost direct measurement of the sample temperature so that errors due to incorrect sample temperatures can be avoided. Moreover, very small sweep rates of the magnetic field are possible since the magnetocaloric effect option was built for this purpose and could be used at HZB for several weeks.

A LRO phase and strong indications for a LL regime were observed within the detailed magnetocaloric effect study, which was used to define the magnetic phase diagram. Copper nitrate is established as a quasi 1D system where both Luttinger liquid and a long-range order were observed. The long-range ordered phase shows a very symmetric dome extending up to 166 mK, while the boundary of LL regime forms an asymmetric dome extending up to ∼220 mK. Due to the larger transition temperature into the LRO state compared with other quasi one-dimensional systems, the crossover between the 1D LL with fermionic behavior and the 3D LRO state with bosonic behavior can be studied more easily on copper nitrate. Surprisingly, the LL dome does not seem to enclose the dome of the LRO phase in the way it does for the ladder compound $(Hpip)_2CuBr_4$. Moreover, the asymmetry of the phase boundary of the LRO state found in $(Hpip)_2CuBr_4$, was not observed for copper nitrate, which could be due to a difference of the microscopic coupling scheme, viz. the interchain/ladder couplings in these systems.

The continuous measurement of the magnetocaloric effect determines the phase transitions into the LRO state with an accuracy of ±25 mT. This comparatively large error is also due to the problems encountered in the thermalization of the sample and prohibits a determination of the critical exponent ϕ accurately. ϕ was found to be in the range of 0.40 and 0.78, which is in the range of the expected value of $\frac{2}{3}$ for a BEC phase, but due to the large inaccuracy it cannot be definitely confirmed that the LRO phase is a BEC phase.

Furthermore, from the magnetocaloric effect data the magnetization $M(T)$ could be obtained, which shows for the first time all the features which are expected for transitions into a BEC and LL regime such as kinks and extrema.

Neutron diffraction measurements confirmed the observations of Eckert *et al.* [114]. Two different types of magnetic Bragg peaks were found indicating the ferromagnetic spin alignment along the field direction (b axis) and the antiferromagnetic alignment within the ac plane. The ferro-

magnetic component behaves like the longitudinal magnetization measured with the cantilever magnetometer. The magnetization is increasing at the first critical field and saturates at the second critical field. Contrary to this, the Bragg peaks corresponding to the antiferromagnetic component only exist between the two critical fields and show a very asymmetric intensity evolution. The origin of this asymmetry remains unclear. To decide if the asymmetry stems from the temperature change caused by the magnetocaloric effect or not, further measurements are necessary.

5 Frustrated Chain: Linarite

In the previous chapter a relatively simple quasi 1D system was studied, which could be described by only nearest neighbor interactions. Systems, where next nearest neighbor interactions become important, show a more complex behavior since these interactions can compete with the nearest neighbor interactions leading to frustration in these systems. An example of such a frustrated system is linarite. An extensive study of this compound is presented in this chapter demonstrating the exotic properties of this frustrated compound in magnetic fields. Beginning with a short introduction of the underlying physical model in the following section, section 5.2 gives an overview of the properties of linarite which were already known from the literature. Revised atomic positions are added to this section. In section 5.3 a description and characterization of the investigated samples is presented. Section 5.4 focuses on measurements at zero magnetic field, which allow to determine the spin structure in the ground state as well as the order of the phase transition into the ground state. In section 5.5 the magnetic phase diagram of linarite is presented. It was determined using microscopic as well as bulk thermodynamic techniques, which are presented in detail. In section 5.6 the results are discussed in the context of observations for related compounds. Section 5.7 summarizes the results of this chapter.

5.1 *nn fm-nnn afm* Spin Chains

Frustrated low dimensional quantum spin systems are investigated due to their rich and varied magnetic properties. Different types of frustrated systems can be realized depending on the dimensionality and geometry. A simple model is the one dimensional spin $S = \frac{1}{2}$ chain with competing interactions. The model can be called *nn fm-nnn afm* spin chain since it is characterized as follows: The ***n***earest ***n***eighbor interaction $J_1 > 0$ couples the spins $\mathbf{S}_l$ and $\mathbf{S}_{l+1}$ ***f***erro***m***agnetically (*nn fm*), while the coupling $J_2 < 0$ between the ***n***ext ***n***earest ***n***eighbor spins $\mathbf{S}_l$ and $\mathbf{S}_{l+2}$ is ***a***nti***f***erro***m***agnetic (*nnn afm*) resulting in a frustrated topology (Fig. 5.1).

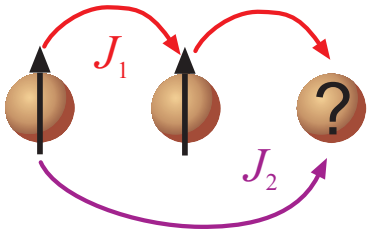

Fig. 5.1: Schematic drawing of the frustrated *nn fm-nnn afm* spin chain. The nearest neighbor interaction is ferromagnetic ($J_1 > 0$), while the next nearest nearest neighbor interaction is antiferromagnetic ($J_2 < 0$).

This type of system can be described by the Hamiltonian

$$\hat{H} = -J_1 \sum_l (\boldsymbol{S}_l \cdot \boldsymbol{S}_{l+1}) - J_2 \sum_l (\boldsymbol{S}_l \cdot \boldsymbol{S}_{l+2}) - h \sum_l S_l^z, \tag{74}$$

where h is an external field. For the model (74) various ground states are predicted depending on the ratio $\alpha = J_2/J_1$. In the limit of a classical isotropic model, the ground state is ferromagnetic for a ratio $\alpha > -1/4$. For $\alpha = -1/4$ it becomes degenerate with a singlet state, while for $\alpha < -1/4$ the ground state is predicted to be incommensurate depending on the periodicity vector $q = \arccos(J_1/4J_2)$ [150–152]. Taking into account quantum fluctuations for spins $S = \frac{1}{2}$, the ground state is expected to show vector chiral order, which is the equivalent of the classical helical spin order [50, 51]. In applied magnetic fields a variety of multipolar phases are predicted depending on the α-ratio. Depending on the dominant correlation, the phases can be characterized either as being a spin-density-wave phase (SDW_p) for dominant spin-density wave correlation, or nematic ($p = 2$), triatic ($p = 3$) or quartic phase ($p = 4$) for dominant multipolar correlations, which can be described as Luttinger liquids of p-magnon bound states [51, 52, 153, 154]. The situation in strictly one dimension was investigated in much detail leading for example to the magnetic phase diagram shown in Fig. 5.2. According to this study, for low fields a vector chiral phase is expected, while for higher fields multipolar phases are predicted. The dotted lines indicate the crossover between the spin-density wave regime at lower fields and the nematic, triatic, and quartic regime for fields close to the saturation [51]. For detailed descriptions of the different phases, I refer to the publication of Hikihara *et al.* [52] and Sudan *et al.* [51].

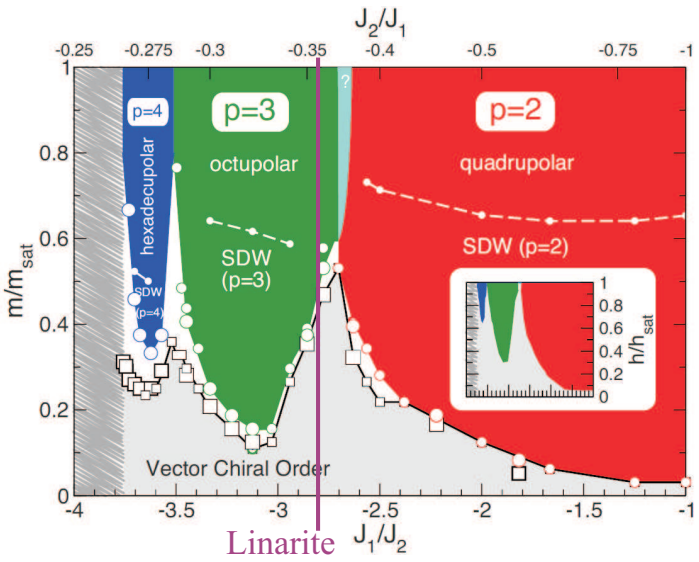

Fig. 5.2: Phase diagram derived for the model Eq. (74). Different types of multipolar phases are predicted to exist, depending on the α-ratio and strength of the magnetic field. The figure was taken from Ref. [51]; for details see text.

For weak interchain couplings, which are always present in real materials, only a few studies exist up to now. It was reported that they can destabilize the multimagnon bound states, while exchange anisotropy can lead to a stabilization [155, 156]. Furthermore, the 3D coupling is supposed to induce true long-range order, so that for example spin-nematic and incommensurate longitudinal spin-density-wave long-range ordered states are possible [157]. A 3D nematic phase

was for example predicted for real materials for magnetic fields very close to the saturation [158]. Experimental realizations of the Hamiltonian (74) in the range of $\alpha < -1/4$, for which the variety of different exotic phases were predicted, include the copper oxide systems $LiCuVO_4$, $Rb_2Cu_2Mo_3O_{12}$, $LiCu_2O_2$, $NaCu_2O_2$, Li_2ZrCuO_4, $LiCuSbO_4$, and $PbCuSO_4(OH)_2$ (linarite) [53–55, 57, 159–167]. Magnetism in these copper oxide materials arises from the spin $S = \frac{1}{2}$ moments carried by the Cu^{2+} ions. The strength of the magnetic couplings vary strongly in magnitude and sign, depending on the actual geometry and environment of the copper oxide bonds involved according to the mechanism of superexchange. The ratios J_2/J_1 of the aforementioned copper oxide systems are summarized in Fig. 5.3. Weak interchain couplings in these materials lead to phase transitions into magnetically long range ordered states at temperatures between 2 K and 20 K [54, 164–166, 168] (except for $Rb_2Cu_2Mo_3O_{12}$ and $LiCuSbO_4$ for which no long-range order has been reported down to 2 K and 100 mK, respectively). For the magnetically ordered systems the spin structure of the ground state was found to be an incommensurate helix [54, 164, 169, 170].

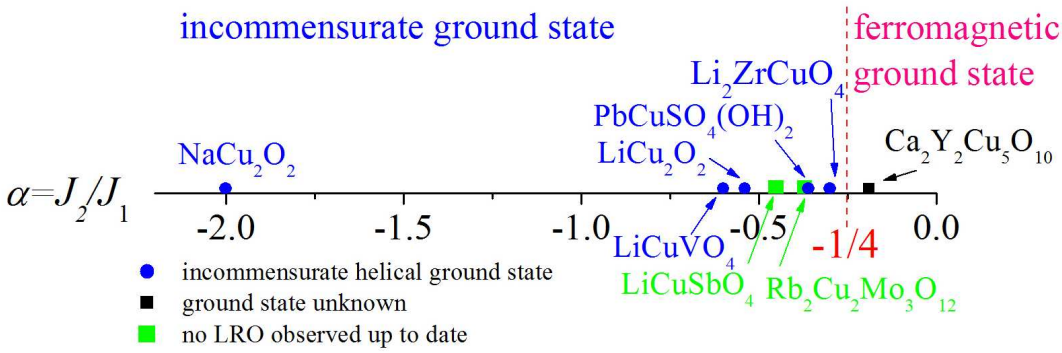

Fig. 5.3: Realizations of frustrated spin $S = \frac{1}{2}$ chains with different ratios of ferromagnetic nearest neighbor interactions J_1 and antiferromagnetic next nearest neighbor interactions J_2. Exchange constants and spin structure of the ground state were taken from Refs. [54–57, 163–167, 169–172].

Theoretical studies show that a helical spin structure can induce ferroelectric behavior [173, 174], which subsequently was found for $LiCu_2O_2$, $LiCuVO_4$, and $PbCuSO_4(OH)_2$ [175–177]. In the spin spiral phase not only is the time-reversal symmetry broken, as it is for magnetic ordered phases, but also the inversion symmetry, which allows ferroelectricity. The breaking of inversion symmetry is a direct consequence of the spin spiral since "a change of the sign of all coordinates inverts the direction of the rotation of the spins in the spiral" [178]. Due to this direct coupling of magnetic order and ferroelectricity these frustrated systems belong to a special class of multiferroics.

Unfortunately, most of the above introduced materials have quite high saturation fields like $LiCuVO_4$ with a saturation field of 44–52 T or $LiCu_2O_2$ with an estimated saturation field of 110 T [162, 179]. Other materials are not available as single crystals like Li_2ZrCuO_4. Therefore, many experimental tests of theoretical modelings of Eq. (74) are still lacking. Especially studies

of high field phases are rare. Only the natural mineral linarite, $PbCuSO_4(OH)_2$, is a *nn fm-nn afm*-material which combines an accessible saturation magnetization field of $\sim$10 T with the availability of single crystals, making it an ideal testing ground for studies of this elemental model.

5.2 Physical Properties of Linarite

5.2.1 Crystal Structure

The natural mineral linarite, $PbCuSO_4(OH)_2$, crystallizes in the monoclinic space group $P2_1/m$ [180–183]. The lattice parameters at room temperature are $a = 9.682$ Å, $b = 5.646$ Å, $c = 4.683$ Å, and $\beta = 102.66°$ [182,183]. Two different sets of atomic positions were published so far. They are summarized in Tab.4. The older set was published by Effenberger in 1987 [182]. It was obtained from x-ray diffraction studies and therefore did not contain the atomic positions of the hydrogen atoms. In 2009 Schofield *et al.* published a set of atomic positions on the basis of single crystal neutron diffraction studies [183]. This set additionally contains the hydrogen positions, but the z-positions of the atoms do not correspond to the positions found by Effenberger. No comment was made as to why there was a discrepancy. Therefore, neutron diffraction measurements were performed using the four-circle diffractometer D10 at the Institute Laue-Langevin within the study of the magnetic structure in zero field (chapter 5.4.1) in order to determine an accurate set of positional parameters for each atomic position.

	Effenberger			Schofield *et al.*		
atom	x/a	y/b	z/c	x/a	y/b	z/c
Pb	0.3420	0.25	0.3284	0.3420	0.25	0.0123
Cu	0	0	0	0	0	0
S	0.6681	0.25	0.1155	0.6687	0.25	0.5560
O1	0.5246	0.25	0.9344	0.5254	0.25	0.5900
O2	0.6653	0.25	0.4307	0.6624	0.25	0.2340
O3	0.2531	0.5355	0.9426	0.2527	0.5372	0.3107
O4	0.9658	0.25	0.7136	0.9662	0.25	0.2526
O5	0.0952	0.25	0.2667	0.0959	0.25	0.8265
H4				0.8682	0.25	0.256
H5				0.0555	0.25	0.605

Tab. 4: Atomic positions of the atoms in $PbCuSO_4(OH)_2$ at room temperature published by Effenberger and Schofield *et al.* [182, 183].

786 inequivalent Bragg peaks were measured at room temperature using a neutron wavelength of 1.26 Å. The nuclear refinement using the program XTAL (R_F-factor: $R_F = 100 \sum_n [|F_{obs,n} - \sqrt{\sum_k F^2_{calc,k}}|] / \sum_n F_{obs,n}$ =6.7, where F represents the structure factor) confirmed the z-positions reported by Effenberger [182] and additionally the hydrogen positions were obtained, which are summarized in Tab. 5.

The revised crystal structure of linarite is shown in Fig. 5.4. The magnetic Cu^{2+} ions are sitting on the atomic coordinates 0,0,0 and 0,$\frac{1}{2}$,0 (Wyckoff position 2a) forming spin $S = \frac{1}{2}$ chains along the b direction. The oxygen atoms labeled with O4 and O5 are arranged in tetragons, which surround the copper ions in such a way that the CuO_4-units form buckled edge-sharing chains along the b direction. The normals of the CuO_4-units are not orientated along a crystallographic

atom	x/a	y/b	z/c	U_{11}	U_{22}	U_{33}	U_{12}	U_{13}	U_{23}
Pb	0.3416(2)	0.25	0.3292(2)	0.65(5)	1.05(8)	1.29(5)	0	-0.08(3)	0
Cu	0	0	0	0.71(3)	0.71	0.71	0	0	0
S	0.6692(4)	0.25	0.1159(6)	0.47(6)	0.47	0.47	0	0	0
O1	0.5256(2)	0.25	0.9331(4)	0.44(9)	0.89(13)	1.64(7)	0	-0.01(5)	0
O2	0.6635(2)	0.25	0.4279(4)	1.93(10)	2.38(17)	0.77(6)	0	0.58(6)	0
O3	0.2535(1)	0.5364(4)	0.9420(3)	0.91(6)	0.54(9)	2.12(5)	-0.26(7)	0.29(3)	0.21(7)
O4	0.9666(2)	0.25	0.7130(4)	1.00(11)	0.30(11)	0.74(7)	0	0.08(6)	0
O5	0.0953(2)	0.25	0.2698(3)	0.51(9)	0.24(11)	0.90(7)	0	0.01(6)	0
H4	0.8667(4)	0.25	0.6166(8)	1.48(19)	1.84(25)	2.50(15)	0	0.11(12)	0
H5	0.0586(4)	0.25	0.4537(7)	2.63(18)	1.76(24)	1.50(13)	0	0.52(11)	0

Tab. 5: Atomic positions of $PbCuSO_4(OH)_2$ at room temperature obtained using neutrons with a wavelength of 1.26 Å. The thermal parameters U_{ij} (given in 100 Å^2) are in the form $\exp[-2\pi^2(U_{11}h^2a^{*2} + \ldots + 2U_{13}hla^*c^*)]$. The thermal displacement of sulfur was treated as isotropic since sulfur is a weak scatterer, which is acceptable since sulfur is not a light atom.

axis, but roughly along the $[10\bar{1}]$ direction. SO_4 tetrahedras and Pb atoms separate the chains from each other in the a direction.

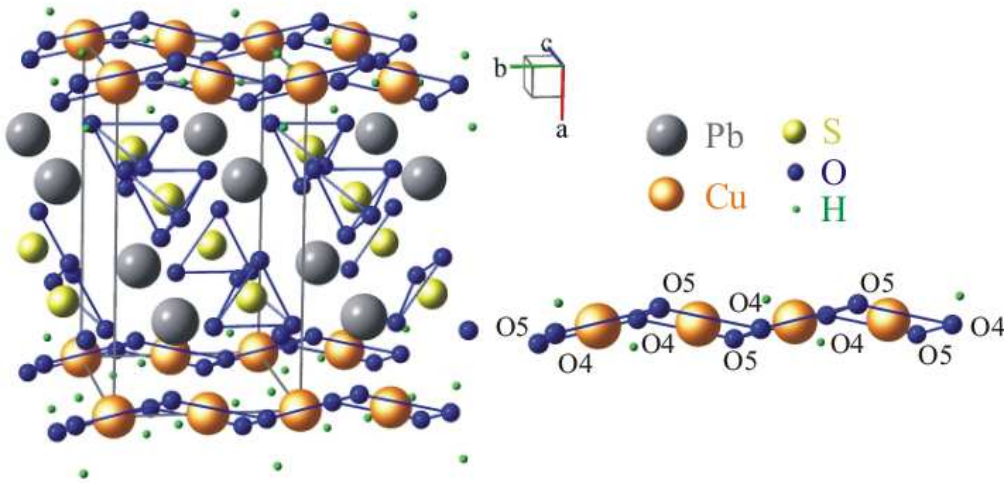

Fig. 5.4: Crystal structure of linarite based on the atomic coordinates from Tab. 5. The left hand figure shows the unit cell of linarite, while on the right hand side a zoom-in shows the spin $S = \frac{1}{2}$ chain.

5.2.2 Magnetic Properties

The interactions between copper atoms in edge-sharing copper oxide chains obey the Goodenough-Kanamori-Anderson rules of superexchange [60, 61, 184, 185]. These rules indicate that the coupling to the nearest neighbor depends on the Cu−O−Cu bond angles. For an angle of 90° the spins will couple ferromagnetically, but for an increasing angle the coupling will change to antiferromagnetic. In the case of linarite the exchange can be realized with an exchange path Cu−O4−Cu or Cu−O5−Cu, which results in angles of 94.2° and 90.8°, respectivily (for numbering of the oxygen atoms see Fig. 5.4 or Tab. 5). According to Goodenough-Kanamori-Anderson

rules, this would lead to ferromagnetic nearest neighbor exchange. The next nearest neighbor exchange path would be along Cu−O4/O5−O5/O4−Cu with an angle much greater than 90° leading to an antiferromagnetic coupling. This conclusion was confirmed with susceptibility and magnetization measurements indicating that linarite belongs to the *nn fm-nnn afm* chain systems described before [57, 168].

For linarite three different pairs of exchange constants have been published [57, 168, 177]. Two research groups concluded that the copper atoms in linarite have dominant nearest neighbor FM interactions $J_1 > 0$ and a weaker next nearest neighbor AFM coupling $J_2 < 0$. Baran *et al.* reported values of $J_1 = 30\,\mathrm{K}$ and $J_2 = -15\,\mathrm{K}$ leading to a ratio $\alpha = -0.5$ [168], while Wolter *et al.* found exchange constants of $J_1 = 100\,\mathrm{K}$ and $J_2 = -36\,\mathrm{K}$ leading to $\alpha = -0.36$, which implies that α lies very close to the critical value of -0.25 [57]. Completely different exchange constants were published by Yasui *et al.* who reported for J_1 a smaller value than for J_2 ($J_1 = 13\,\mathrm{K}$ and $J_2 = -21\,\mathrm{K}$), which results in $\alpha = -1.62$ [177].

Linarite shows a phase transition into a long-range ordered state at $T_N = 2.8\,\mathrm{K}$ [57, 168]. The observation of this state implies the presence of residual interchain couplings, which are one order of magnitude smaller than the intrachain coupling [57]. From susceptibility data a positive Curie-Weiss temperature θ_{CW} of 27(2) K was obtained indicating the predominance of a ferromagnetic coupling [57]. Further, the transition and Curie-Weiss temperature lead to a ratio θ_{CW}/T_N of about 10. This ratio represents an empirical measure of frustration [186] since frustration depresses long range order. The value of 10 found for linarite shows that frustration plays an important role in this material.

Tentatively, the ordered phase has been discussed in terms of a possible helical ground state with an acute pitch angle due to the α value being smaller than -0.25 [168]. Moreover, a recent study of this material claiming multiferroicity has also been interpreted in terms of a helical magnetic ground state [177]. Based on preliminary neutron diffraction measurements a propagation vector (0, 0.189, 1/2) was derived [187]. Since only magnetic Bragg peaks which lie in the *bc* plane could be collected in that study, a full determination of the magnetic structure was impossible. Nevertheless, by combining the neutron diffraction with the magnetization measurements it was concluded that the spins are rotating within the CuO_2 planes.

Significant anisotropy was found in the saturation values of the magnetization M_{sat} and the saturation fields H_{sat}. By applying a magnetic field perpendicular to the *bc* plane $M_{\mathrm{sat},\perp bc} = 1.16\,\mu_{\mathrm{B}}/\mathrm{Cu}$ and $\mu_0 H_{\mathrm{sat},\perp bc} = 7.6\,\mathrm{T}$ was found, while for fields parallel to the *b* and *c* axis values of $M_{\mathrm{sat},||b} = 1.05\ \mu_{\mathrm{B}}/\mathrm{Cu}$ and $\mu_0 H_{\mathrm{sat},||b} = 10.5\,\mathrm{T}$ and $M_{\mathrm{sat},||c} = 1.15\ \mu_{\mathrm{B}}/\mathrm{Cu}$ and $\mu_0 H_{\mathrm{sat},||c} = 8.5\,\mathrm{T}$, respectively, were determined [57].

Anisotropy was observed as well in the magnetization curves in the long-range ordered ground state at 1.8 K. While for applied magnetic fields along the *c* axis and perpendicular to the *bc* plane only one anomaly was detected in $\mathrm{d}M/\mathrm{d}H$ indicating a phase transition, for an applied magnetic field along the crystallographic *b* axis (which is equal to the chain direction) three transitions were observed [57].

From ESR measurements the g-factors along the crystallographic axis were obtained: $g_a = 2.34$, $g_b = 2.10$, and $g_c = 2.28$. These values explain the anisotropy for temperatures above T_N, but do not explain the anisotropy for temperatures below T_N [57].
The study of Wolter *et al.* [57], which shows the special behavior of linarite when applying a magnetic field along the b axis, was the starting point of this thesis, in which the magnetic phase diagram for fields along the b axis is investigated. Further, the spin structure in the ground state is determined as well as in applied magnetic fields along the b axis. Parallel to the measurements presented in this thesis Markus Schäpers perfomed NMR measurements and further bulk measurements on linarite [188]. The phase boundaries obtained from these measurements were also added to the magnetic phase diagrams shown in Fig. 5.16 and 5.17.

5.2.3 Ferroelectric Properties

Yasui *et al.* studied the ferroelectric behavior at zero field for three different orientations of the electric field (Fig. 5.5): along the chain direction (b direction), perpendicular to the CuO_4-squares, so that the electric field was approximately oriented along the $[10\bar{1}]$ direction (it was called c'), and perpendicular to c' and b, which was called a' [177]. Only for an electric field along a' a broad anomaly was found at about T_N. Thus, both the ferroelectric and the magnetic long-range order transition could coincide, which would imply that the ferroelectricity and long-range magnetic order are coupled. Linarite could therefore belong to the special class of multiferroic materials in which ferroelectricity is induced by a spiral spin structure. No measurements in a magnetic field were performed, which would allow to check whether the phase transition of the ferroelectric phase follows the phase boundary of the spiral spin state in magnetic fields.
Therefore, further measurements of the dielectric constant are needed to identify the transition temperature into the ferroelectric state more precisely and to investigate the phase boundary in magnetic fields. This was the motivation of the measurements for the ferroelectric phase transitions presented in section 5.5.5.

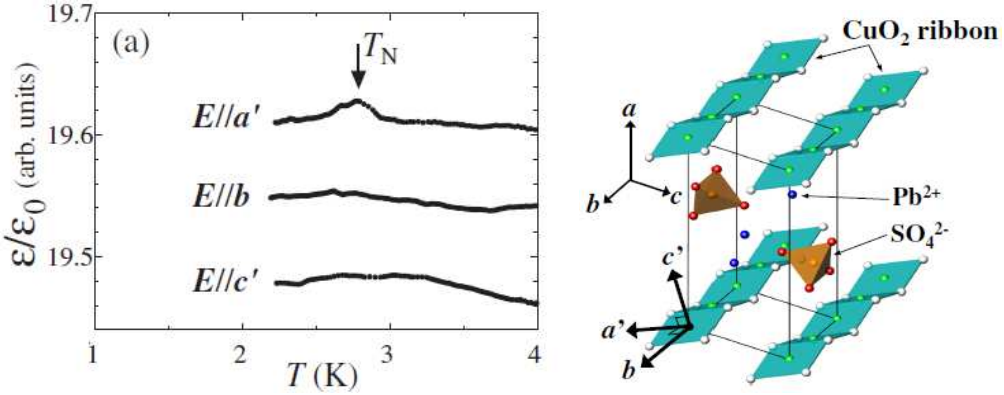

Fig. 5.5: Measurements of the dielectric constant in zero field show a broad anomaly at a temperature of about T_N. Figures are taken from Ref. [177].

5.3 Samples and Sample Characterization

All crystals studied for this thesis are naturally grown single crystals. Linarite grows in form of needle shaped crystals whose long axis corresponds to the crystallographic b axis. Crystals from two different origins (see Tab. 6) have been investigated in neutron scattering experiments and thermodynamic measurements. The smallest and the biggest sample are shown in Fig. 5.6.

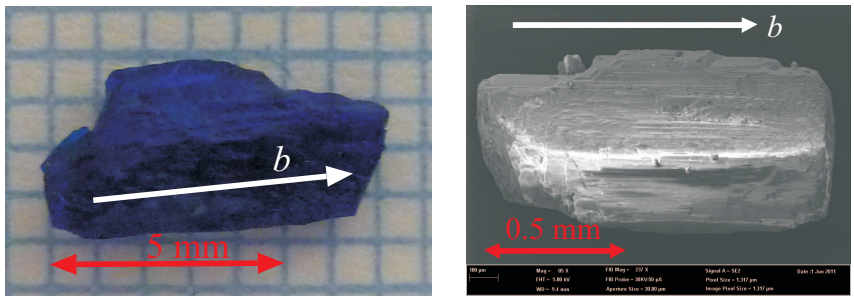

Fig. 5.6: Linarite single crystals: the photograph on the left hand side shows sample IIa, which was used for the neutron diffraction measurement on the instrument E4. On the right hand side an electron microscope image of sample Ib is shown (SEM-image). This sample was used for the magnetization and magnetocaloric effect measurements.

Amongst others a PPMS VSM was used for characterizing the samples. The following characterization results will be collated into a phase diagram, which will be discussed in detail in section 5.5.

The magnetization at 1.8 K for applied magnetic fields along the b direction shows three transitions defined by peaks in the first derivative $\mathrm{d}M/\mathrm{d}(\mu_0 H)$ (Fig. 5.7). The peaks are more pronounced in the sample Ib. Especially, the curves of the second transitions at about 3.1 T are different. For the sample IIa from Grand Reef Mine the transition is indicated only by a weak broad peak in the derivative, while for the sample Ib from the Blue Bell Mine it is a pronounced and narrow peak. Even three different samples from Grand Reef Mine do not fully behave in the same way (not shown), which is an indication of a varying degree of purity in these naturally grown samples. The clearest features at the transitions were found in the sample IIa with a mass of 105 mg, which was used for the neutron experiment at the instrument E4 (see section 5.4.2). For this experiment the phase transition into the long range ordered ground state at zero field was investigated. Therefore, the susceptibility for sample IIa and Ib at small fields were compared (Fig. 5.8). The plot shows that both crystals from different origins show the same behavior in the susceptibility entering the long range ordered ground state at small fields. Thus, the sample with the greatest mass could be used for the neutron scattering experiment. For the neutron diffraction study at D10, in which the high field phases were investigated, the crystal Ia was used since for this experiment the transitions into the different phases need to be well-defined. Magnetocaloric effect measurements were performed on crystals from both origins (section 5.5.3). The tendencies about the quality of the crystals described above are in agreement with the magnetocaloric effect data, where the sample with higher purity show sharper

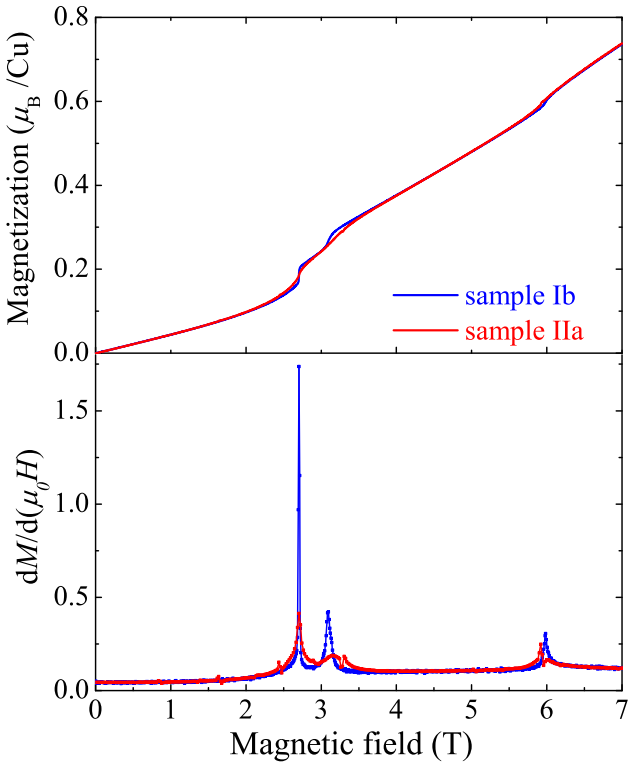

Fig. 5.7: Magnetization data for crystals with different origins at 1.8 K and its field derivative. Sample Ib is from Blue Bell Mine, while sample IIa is from Grand Reef Mine. The data from sample IIa were normalized to the data from sample Ib since the PPMS VSM is not able to determine the absolute values of the magnetic moment for large samples properly.

transitions.

Multiple crystal patterns were observed in linarite using the neutron Laue instrument CYCLOPS at the Institute Laue-Langevin in Grenoble (Fig. 5.9). The patterns show only slight offsets in reciprocal space indicating that the sample consists of a number of grains. Therefore, during the neutron measurements at D10 (investigation of the spin structures in the ground state and in the high field phases) it was focused on the biggest grain.

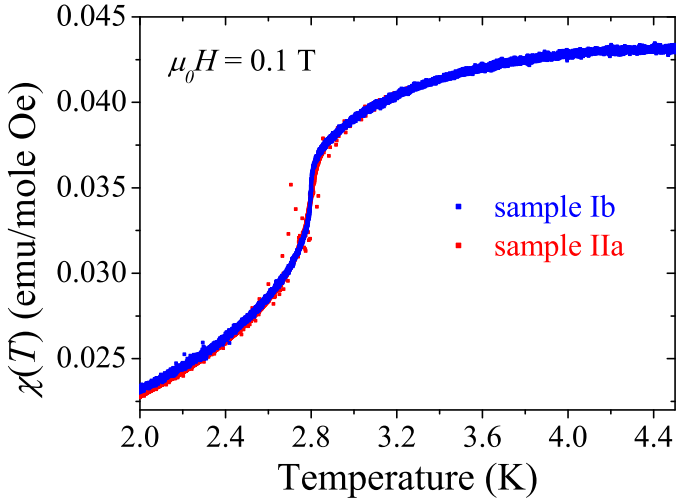

Fig. 5.8: Sample characterization using the PPMS VSM: Susceptibility measurements at 0.1 T. The data were normalized to each other at 4 K.

sample	origin	mass (mg)	technique
Ia	Blue Bell Mine, California	26.5	neutron diffraction on D10
Ib	Blue Bell Mine, California	0.98	$M(H)$ ($H \parallel b$), $\chi(T)$, C_p, MCE
IIa	Grand Reef Mine, Arizona	105.6	neutron diffraction on E4
IIb	Grand Reef Mine, Arizona	1.43	MCE
IIc	Grand Reef Mine, Arizona	31.6	dielectric constant, $M(H)$ ($H \perp b$)
IId	Grand Reef Mine, Arizona	2.0	$M(H)$ (angular dependent)

Tab. 6: Linarite samples studied for this thesis and their different origins. Ia and Ib as well as IIa, IIb, IIc, and IId are brother crystals from the same batch. Sample Ia was used for recent NMR measurements [57].

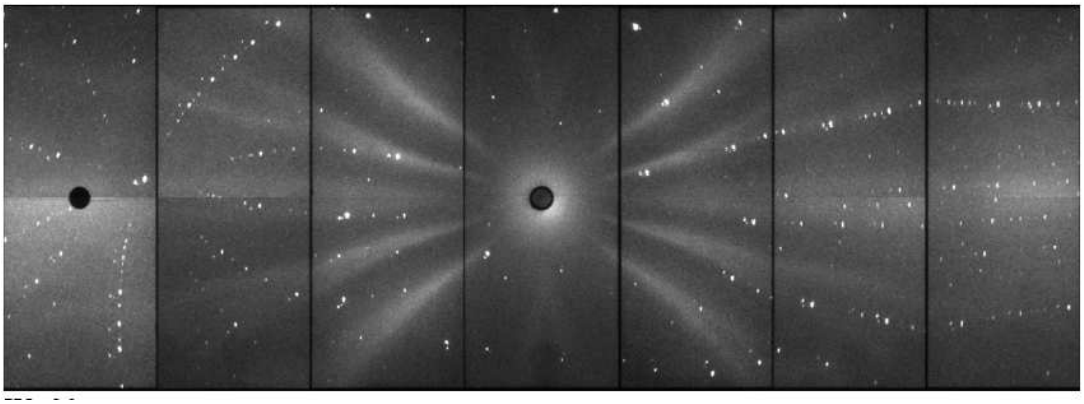

Fig. 5.9: Neutron Laue image of the linarite crystal Ia to test crystallinity.

5.4 Zero Field Measurements

Neutron diffraction experiments at zero field were performed in order to determine the spin structure in the magnetically long-range ordered ground state and the hydrogen positions at room temperature. Additionally, the transition into the ground state was investigated via neutron diffraction and heat capacity measurements.

5.4.1 Spin Structure of the Ground State

Neutron diffraction data were collected using the four circle diffractometer D10 at the Institute Laue-Langevin (section 3.1.6) with a neutron beam of the wavelength 2.36 Å and a helium-flow cryostat in order to reach temperatures well below the ordering temperature of 2.80 K. For the measurements sample Ib was used. The sample with the dimensions $5\times2\times1\,\mathrm{mm}^3$ has a mass of 26.5 mg. The rod shaped sample was mounted on an Al-pin and loaded into the rotating He-flow cryostat in such a way that the b-axis was in the nominal vertical position. In this orientation neutron absorption by the crystal was kept to a minimum. As shown in chapter 5.3 the linarite crystal contains several grains. For defining the orientation of the crystal with respect to the axis of the instrument (defining the UB-matrix) only the biggest crystal grain was used.
Nuclear as well as magnetic Bragg peaks were measured at a temperature of 1.8 K. The intensities of the peaks were measured with the position sensitive detector and were subsequently integrated using the program RACER [189].
In order to find an accurate propagation vector, mesh-scans through the reciprocal space were performed. These are scans performed systematically with fixed h and l while varying k. For each scan the h value was changed and afterwards the same set of scans with a different l value was performed. With this method a full region in steps of 0.1 in reciprocal space was mapped out. At the (hkl)-position (0 0.186 0.5) a peak was observed, where no nuclear peak would be expected. This peak vanished for temperatures above the ordering temperature indicating that this peak is a magnetic reflection (Fig. 5.10).

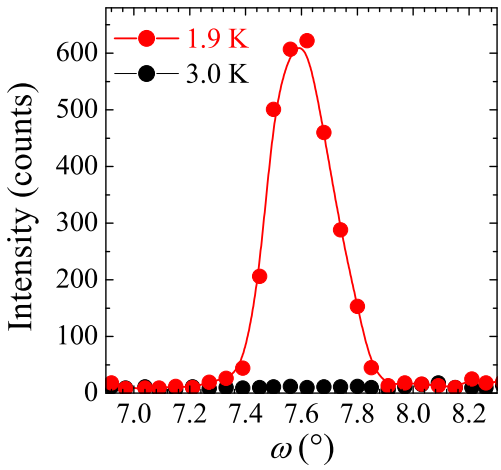

Fig. 5.10: Rocking-scan of the magnetic Bragg peak (0, 0.186, $\frac{1}{2}$) below and above the transition temperature. Lines are guides to the eyes.

By observing a large intensity in the peaks (1, 0.186, 0.5)$_M$ and (1, 0.186, -0.5)$_M$ the propagation vector $\boldsymbol{K}$ = (0, 0.186, 0.5) was deduced in agreement with the work of Yasui *et al.* [187]. The propagation vector is the basis for further analysis. According to the propagation vector the spins are ordered ferromagnetically along the a axis and antiferromagnetically along the c axis.

The spin structure along the b axis is incommensurate.
By using the equation $(hkl)_M = (hkl)_N \pm \boldsymbol{K}$ a set of satellites was generated where magnetic Bragg peaks were expected. The magnetic intensities were only found for the satellites which were generated from the nuclear reflections $(hkl)_N$ with $k = 2n$. This clearly shows that the magnetic moments of the two copper atoms Cu11 and Cu12 (in the Wyckoff position $2a$ of $P2_1/m$) in (0,0,0) and (0,0.5,0) are coupled parallel. But due to the incommensurate vector component $k_y = 0.186$ along the b axis the phase factor between the two Cu-atoms is $\phi = 1/2k_y = 0.093$ (in fractions of 2π), which is equivalent to a pitch angle of 33.5°. Thus, the model of the pitch angle $\theta = \arccos(-J_1/4J_2) = 46°$ for classical spins does not predict the correct value, which is most likely due to quantum fluctuations in linarite. Similar observations were made for $LiCuVO_4$ [53].
A full set of nuclear as well as magnetic Bragg peaks were collected. The nuclear structure was refined in order to obtain an accurate scale factor for the magnetic refinement using the program FullProf [145]. The refinement of the crystal structure is in accord with the refinement presented in chapter 5.2.1.
For the refinement of the magnetic structure a total of 76 observable reflections (25 unique) was used as well as 26 positions at which no peak could be observed owing to the rule $k = 2n$.

In general, periodically arranged magnetic moments in a crystal can be described with a Fourier series (see Eq. (32)):

$$\boldsymbol{\mu}_{n,j} = \sum_{\boldsymbol{K}} \boldsymbol{S}_{\boldsymbol{K}j} \exp\left(-i\boldsymbol{K} \cdot \boldsymbol{R}_n\right). \tag{75}$$

j indicates the magnetic atom at the lattice point $\boldsymbol{R}_n$ and $\boldsymbol{K}$ is the propagation vector. Note that the propagation vector is of the form $\boldsymbol{K} = k_1\boldsymbol{b}_1 + k_2\boldsymbol{b}_2 + k_3\boldsymbol{b}_3$ where $\boldsymbol{b}_i$ are the primitive vectors of the reciprocal space, but the vector $\boldsymbol{R}_n$ is a linear combination of the primitive vectors of the direct lattice $r_1\boldsymbol{a}_1 + r_2\boldsymbol{a}_2 + r_3\boldsymbol{a}_3$. Thus, the scalar product is $\boldsymbol{R}_n \cdot \boldsymbol{K} = 2\pi(r_1k_1 + r_2k_2 + r_3k_3)$. Therefore, Eq. (75) can be defined as follows:

$$\boldsymbol{\mu}_{n,j} = \sum_{\boldsymbol{K}} \boldsymbol{S}_{\boldsymbol{K}j} \exp\left(-2\pi i\boldsymbol{K'} \cdot \boldsymbol{R'}_n\right), \tag{76}$$

with $\boldsymbol{K'} = (k_1, k_2, k_3)$ and $\boldsymbol{R'} = (r_1, r_2, r_3)$. For a system like linarite with only a single pair of propagation vectors $\boldsymbol{K}$ and $-\boldsymbol{K}$ this equation simplifies to

$$\boldsymbol{\mu}_{n,j} = \boldsymbol{S}_{\boldsymbol{K}j} \exp\left(-2\pi i\boldsymbol{K'} \cdot \boldsymbol{R'}_n\right) + \boldsymbol{S}^*_{\vec{K}j} \exp\left(2\pi i\boldsymbol{K'} \cdot \boldsymbol{R'}_n\right), \tag{77}$$

where * means its complex conjugated.
The Fourier coefficients $\boldsymbol{S}_{\boldsymbol{K}j}$ are of the form

$$\boldsymbol{S}_{\boldsymbol{K}j} = 1/2(\boldsymbol{R} + i\boldsymbol{I}) \exp(-2\pi i\phi). \tag{78}$$

Constraints for the vectors $\boldsymbol{R}$ and $\boldsymbol{I}$ are obtained from the symmetry analysis. Equations (77)

#	structure type	representation	atom	$\vec{R}$	$\vec{I}$	further constraints	R_F
1	sine wave	Γ_1	Cu11 Cu12	(R_x,R_y,R_z) ($-R_x$,R_y,$-R_z$)	(0,0,0) (0,0,0)		17.7
2	sine wave	Γ_2	Cu11 Cu12	(R_x,R_y,R_z) (R_x,$-R_y$,R_z)	(0,0,0) (0,0,0)		32.4
3	sine wave	$\Gamma_1 \oplus \Gamma_2$	Cu11 Cu12	(R_x,R_y,R_z) (R_x,R_y,R_z)	(0,0,0) (0,0,0)		14.0
4	helical (circular)	$\Gamma_1 \oplus \Gamma_2$	Cu11 Cu12	(R_x,0,R_z) (R_x,0,R_z)	(0,I_y,0) (0,I_y,0)	$\lvert\boldsymbol{R}\rvert = \lvert\boldsymbol{I}\rvert$ $\lvert\boldsymbol{R}\rvert = \lvert\boldsymbol{I}\rvert$	9.7
5	helical (elliptical)	$\Gamma_1 \oplus \Gamma_2$	Cu11 Cu12	(R_x,0,R_z) (R_x,0,R_z)	(0,I_y,0) (0,I_y,0)	$\lvert\boldsymbol{R}\rvert \neq \lvert\boldsymbol{I}\rvert$ $\lvert\boldsymbol{R}\rvert \neq \lvert\boldsymbol{I}\rvert$	7.0

Tab. 7: Possible spin configurations for linarite. $\boldsymbol{R}$ and $\boldsymbol{I}$ were refined with FullProf resulting in the stated R_F values ($R_F = 100 \sum_n [|F_{obs,n} - \sqrt{\sum_k F^2_{calc,k}}|] / \sum_n F_{obs,n}$).

and (78) lead to the following expression, which describes the magnetic moment vectors for all copper atoms in the linarite crystal:

$$\boldsymbol{\mu}_{n,j} = \boldsymbol{R} \cos\left(2\pi(\boldsymbol{K'} \cdot \boldsymbol{R'}_n + \phi)\right) + \boldsymbol{I} \sin\left(2\pi(\boldsymbol{K'} \cdot \boldsymbol{R'}_n + \phi)\right). \tag{79}$$

Eq. (79) can be used to describe the whole magnetic structure of linarite.

From the symmetry analysis using the program BasIReps (available in the FullProf suite) two one-dimensional irreducible representations Γ_1 and Γ_2 were obtained. The Fourier coefficients of Γ_1 for the site $2a$ are $S_{k11} = (u, v, w)$ for the atom Cu11 and $S_{k12} = (-u, v, -w)$ for the atom Cu12 and for Γ_2 the coefficients are $S_{k11} = (u, v, w)$ and $S_{k12} = (u, -v, w)$, respectively. Due to the symmetry only five spin configurations are possible, which are summarized in Tab. 7. First, there is the possibility of a sine wave modulated structure. The most obvious configurations for a sine wave modulated structure are configurations 1 and 2. For these configurations the Fourier coefficients of both of the irreducible representations Γ_1 and Γ_2 are used separately. The refinements led to residual R_F factors (defined as $R_F = 100 \sum_n [|F_{obs,n} - \sqrt{\sum_k F^2_{calc,k}}|] / \sum_n F_{obs,n}$, where F represents the structure factor) larger than 17. A better R_F value of 14.0 could be obtained, when the magnetic structure is described by a reducible representation $\Gamma = \Gamma_1 \oplus \Gamma_2$ (configuration 3 in Tab. 7). By taking into account that the spins have to be aligned collinear with the *ac* plane, a decoupling of the moment components along the *b* axis from those in the *ac* plane is expected. The Fourier coefficients of Γ_1 along the *b* axis are $S_{k11} = (0, v, 0)$ and $S_{k12} = (0, v, 0)$. The coefficients of Γ_2 in the monoclinic *ac* plane are $S_{k11} = (u, 0, w)$ and $S_{k12} = (u, 0, w)$. To obtain a more reliable R_F value, a helical spin configuration involving either a circular or elliptical envelope was considered (configurations 4 and 5 in Tab. 7). The helical structure with an elliptical envelope gives the best fit to our data resulting in a R_F value of 7.0. The refined component of the moment $\mu_y = 0.833(10)\ \mu_B$ along the *b* axis is slightly larger

than the component $\mu_{xz} = 0.638(15)\,\mu_B$ in the ac plane. The turning angle between neighboring Cu-atoms ($y = 1/2$) along the b direction is $\phi = 33.5°$ as it was discussed before. The spinning plane of the moments is perpendicular to the monoclinic ac plane and is $-27(2)°$ off the a axis. Therefore, the spinning plane is almost parallel to $[10\bar{1}]$. Furthermore, the spinning plane is roughly perpendicular to the buckled $Cu(OH)_4$-chains in such a way that the spin components in the ac plane are always perpendicular to the O4-O5-squares. The magnetic structure of $PbCu(SO_4)(OH)_2$ is shown in Fig. 5.11. Eq. (80) gives the magnetic moment for the copper atom j at the lattice point $\boldsymbol{R'}_n$, where $\boldsymbol{u}_{xz}$ is the unit vector which is $-27°$ off the a axis, $\boldsymbol{v}_y$ is the unit vector along the b axis, $\mu_{xz} = 0.638\,\mu_B$ and $\mu_y = 0.833\,\mu_B$:

$$\boldsymbol{\mu}_n = \mu_{xz} \cos\left(2\pi(\boldsymbol{K'} \cdot \boldsymbol{R'}_n)\right) \boldsymbol{u}_{xz} + \mu_y \sin\left(2\pi(\boldsymbol{K'} \cdot \boldsymbol{R'}_n)\right) \boldsymbol{v}_y. \tag{80}$$

Here, $\boldsymbol{K'}$ is the propagation vector as defined above. This detailed analysis yields a spin structure which disagrees with the preliminary structure proposed by Yasui *et al.* [187].

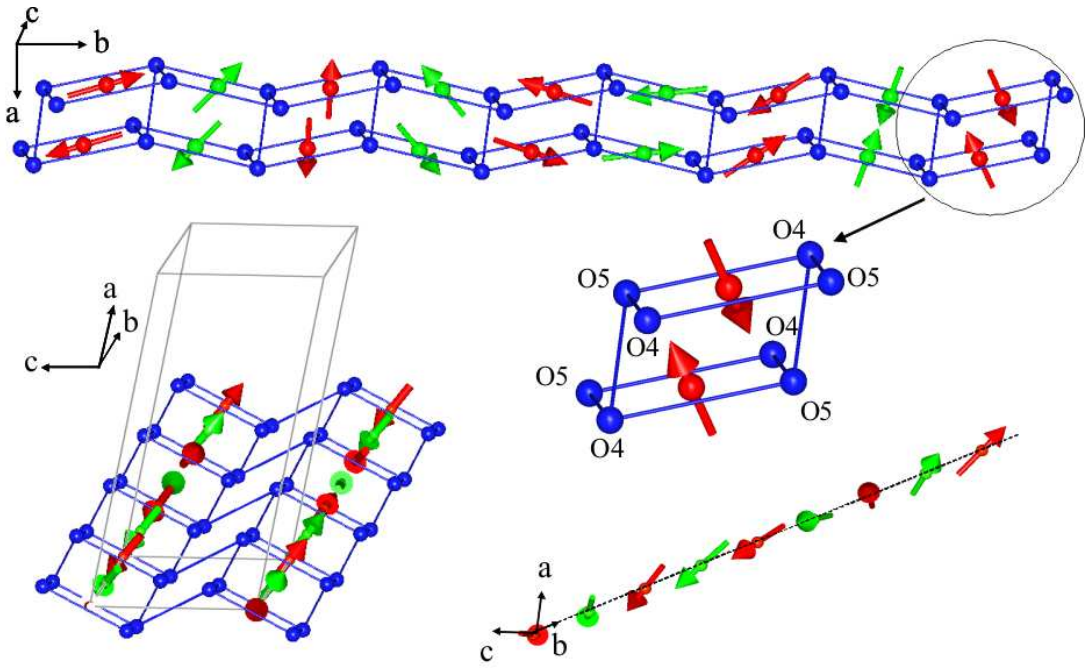

Fig. 5.11: Magnetic structure of linarite, which is the structure of the configuration labeled with #5 in Tab. 7. Only the magnetic Cu^{2+} ions with the spin and the oxygen atoms O4 and O5 are shown. The two different spin-colors represent the two copper sites. Both Cu atoms are part of the same helix leading to an angle between neighboring spins of 33.5°. The helical spin arrangement occurs along the buckled $Cu(OH)_4$-units, where the two components are along [010] and almost parallel to $[10\bar{1}]$.

Since the helical structure of linarite consists of a combination of two irreducible representations, it includes special characteristics of the phase transition into the long range ordered ground state. It is discussed in the following section.

5.4.2 Phase Transition into the Long-Range Ordered Ground State at Zero Field

By changing the temperature or other thermodynamic parameters of a system, it can be driven into other phases. The phase transition includes a sudden break in the symmetry of the system, where an order parameter η represents the symmetry. η is nonzero for temperatures below the transition point and zero for temperatures above the transition. In case of a ferromagnet or an antiferromagnet the transition point is the Curie-point or Néel-point, while the order parameter is the magnetization or staggered magnetization, respectively.

In general, there are two types of phase transitions: first order transitions or continuous phase transitions (also called second order transitions). At first order phase transitions the first derivative of one or more thermodynamic potentials shows a discontinuity. In contrast, at continuous phase transitions the first derivative remains continuous [190, 191]. This kind of transition is characterized by a divergence or discontinuous change of higher order derivatives such as heat capacity or susceptibility at the transition point (critical point). It was found that for continuous phase transition critical exponents λ can be defined close to the critical points as [190]:

$$\lim_{x\to 0+} \frac{\ln(f(x))}{\ln(x)} = \lambda. \tag{81}$$

In case of magnetism the function $f(x)$ can be the isothermal susceptibility $\chi_T = \lim_{H\to 0} \left(\frac{\partial M}{\partial H}\right)_T$, the spontaneous magnetization M or the heat capacity at zero field $C_{H=0}$. The critical exponents are then defined as follows, where t is the reduced temperature $(T - T_c)/T_c$:

$$\chi_T \sim t^{-\gamma} \ ; \ T > T_c, H = 0, \tag{82}$$

$$\chi_T \sim t^{-\gamma'} \ ; \ T < T_c, H = 0, \tag{83}$$

$$M \sim (-t)^{\beta} \ ; \ T < T_c, H = 0, \tag{84}$$

$$C_{H=0} \sim t^{-\alpha} \ ; \ T > T_c, H = 0, \tag{85}$$

$$C_{H=0} \sim (-t)^{-\alpha'} \ ; \ T < T_c, H = 0. \tag{86}$$

The critical exponents are related to each other via the Rushbrooke inequality [192]:

$$\alpha' + 2\beta + \gamma' \geq 2, \tag{87}$$

where in most cases the inequality becomes an equality [191]. For an antiferromagnet the magnetization and the susceptibility need to be replaced by the sublattice magnetization and the sublattice susceptibility, respectively. These parameters can obviously not be measured via bulk measurements, but with techniques like neutron scattering.

Typical values of the critical exponents found in experiments are $0.2 \leq \beta \leq 0.4$ and $-0.3 \leq \alpha, \alpha' \leq 0.3$ [191]. For the Heisenberg model in 3 dimensions (d = 3, D = 3) exponents of $\beta =$

0.367 and $\alpha = -0.121$ were calculated [191].

A theoretical approach for analyzing phase transitions involves the Landau theory. It uses a Taylor series expansion of the Landau free energy F as a function of the order parameter about the transition point. In this context, the free energy is a thermodynamic potential, which allows to determine the equilibrium state of the system by minimizing the free energy for given external conditions. The Landau theory of phase transitions connects the symmetry characteristics with the physical properties of the transition [193]. Group theoretical aspects were used for structural phase transitions, which are also applicable to magnetic structures by regarding the time-reversal. A simple conclusion is that at second order transitions only one irreducible representation will become critical [85].

In monoclinic systems like linarite the irreducible representations are only one-dimensional, which was the reason why for the helical structure the reducible representation $\Gamma_1 \oplus \Gamma_2$ was used to construct the helix. In this configuration two order parameters are present corresponding to the two irreducible representations. One irreducible representation alone would lead to a sine wave modulation of the spins. Often the energies of both helical and sine wave modulation are similar. Therefore, the phase transition can consist either of two successive first or second order transitions or if the energies are equal, the phase transition appears to be first order [85]. Materials which show two transitions are for example $TbMnO_3$, $LiCu_2O_2$, and $Ni_3V_2O_8$, where for a decrease of the temperature a transition into a sine wave modulated structure was found. Measurements at lower temperatures also revealed a transition into a helical spin arrangement [194–196]. In contrast, a direct transition from the paramagnetic regime into a helical spin structure was found for instance for $LiCuVO_4$ and α-$CaCr_2O_4$ [54, 197].

Phase Transition Investigated by means of Neutron Scattering Experiments

In order to investigate the phase transition from the paramagnetic into the long-range magnetically ordered ground state of linarite, the evolution of the intensity of the magnetic Bragg peak with temperature was measured. For an antiferromagnet the intensity of the magnetic Bragg peak is proportional to the square of the sublattice magnetization $M'(T)$:

$$I(T) \sim M'(T)^2 \sim (T_\mathrm{N} - T)^{2\beta}, \tag{88}$$

where β is the critical exponent introduced in Eq. (84).

A preliminary experiment was performed at D10 at the ILL within the measurements for determining the spin structure in the ground state (sample Ia: 26 mg crystal from the Blue Bell mine). For these measurements an analyzer in combination with a point detector was used, which reduces the background in comparison with using the two-dimensional position sensitive detector. Especially for looking at the temperature dependence of the weak magnetic peaks, the analyzer option gives a clearer signal for focusing on one grain more efficiently. The integration for this type of detector was performed with the program COLL5. The integrated intensity of

the strongest magnetic Bragg peak (0, 0.186, 0.5) was measured at temperatures between 1.9 K and 4.0 K. The magnetic Bragg peak intensity shows a rapid decrease for temperatures approximating the Néel temperature. The peak gains about half of the intensity within 50 mK cooling down from T_N. Due to considerable fluctuations of the sample temperature it was not possible to obtain very precisely the characteristics of the phase transition from these data alone. Therefore, a new sample stick with a temperature stability of ±0.5 mK was designed and the experiment was repeated on the instrument E4 at the Helmholtz-Zentrum Berlin (see section 3.1.6).
A 105 mg sample (sample IIa from Grand Reef mine) was mounted with GE-varnish to ensure good thermal contact (isolating vacuum) on an Al-pin sample holder in such a way that the *bc* plane was roughly the scattering plane. In this configuration the magnetic Bragg peak (0, 0.186, 0.5) could easily be achieved. The sample contains three bigger grains, which are split for the (0, 0.186, 0.5) peak by 3° or 4° from each other, so that it was possible to investigate only the magnetic Bragg peak (0, 0.186, 0.5) of the biggest grain. The intensity of the Bragg peak of that grain had about 1/3 of the overall intensity so that a mass of about 35 mg was investigated in the experiment. After a rough scan in 50 mK steps in the temperature range near T_N, the slits of the incoming beam and of the detector were adjusted to minimize the background. Therefore, the intensities needed to be normalized to the data of the new configuration. The intensity of the three data sets (one set from D10, two from E4) were normalized to each other at 2 K (Fig. 5.12). Good agreement was found with the data of the experiment at D10 at the ILL using another crystal from another origin. Some of the data were taken for an increasing temperature and some for an decreasing temperature. No hysteresis was found within the error bars.
T_N was found to be 2.802(2) K, which is in fine agreement with bulk measurements. It should be emphasized that only one transition was found. The data were fit using the critical behavior for second order phase transitions

$$I(T) = A \cdot ((T_N - T)/T_N)^{2\beta}. \tag{89}$$

A fit for temperatures from 2.8 K down to about 2.4 K results in a β-value of 0.13(1), which is much smaller than the values found for other materials. To achieve reasonable values for β the data must be fitted in the very small temperature regime from 2.76 K to 2.802 K. The fit leads to a critical exponent of β =0.27(3), but the prefactor was found to be A = 1479(440), which is a very large value for this variable. In addition, the fit shows already large discrepancies to the data points at temperatures below 2.76 K (Fig. 5.12). In summary, it appears to not be possible to use Eq. (89) to obtain a reasonable fit to the data, which strongly indicates that the transition is not of second order but rather of first order.

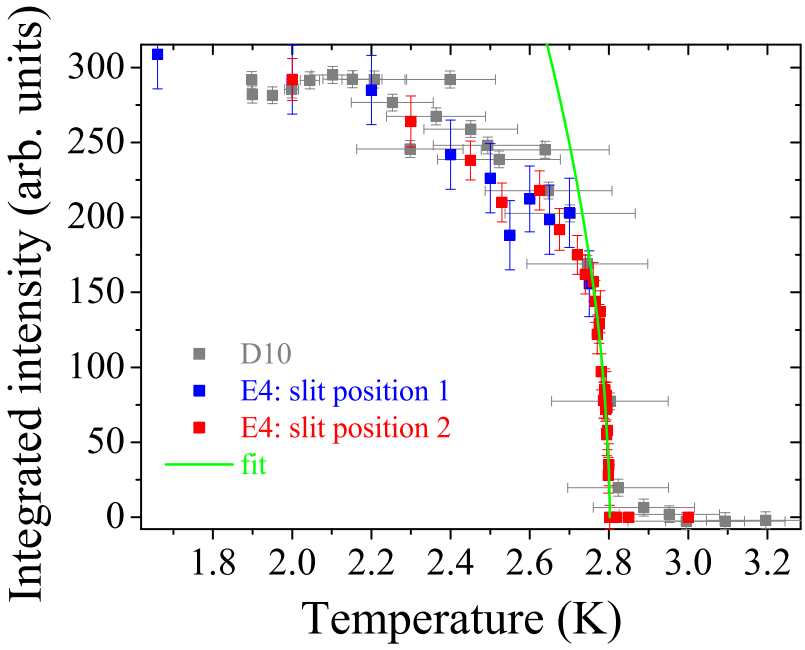

Fig. 5.12: Temperature dependence of the magnetic Bragg peak (0, 0.186, 0.5) of linarite. The fit $I(T) = A \cdot ((T_N - T)/T_N)^{2\beta}$ in the very small temperature regime led to the values $\beta = 0.27(3)$, $A = 1479(440)$, and $T_N = 2.802(2)$ K indicating that the transition is of first order.

Phase Transition Investigated by means of Heat Capacity Measurements

Another way to characterize the phase transition is the measurement of the heat capacity as it is the second derivative of a thermodynamic potential. For this purpose the dual-slope technique is most applicable since this technique measures the heat capacity at a specific temperature, which allows a determination of the heat capacity at temperatures very close to the transition temperature (see chapter 3.2.2). For these measurements sample Ib was used in the calorimeter described in chapter 3.2. First, the sample temperature versus time was investigated for a steady increase and decrease of the heating power. The data show an anomaly in the first derivative, which coincides with the point of the phase transition. For up and down sweeps of the heating power hysteresis was found depending on the sweep rate. To more closely characterize the hysteresis in the limit of slow sweep rates, the hysteresis was measured using different sweep rates (Fig. 5.13 left hand side). For slow sweep rates the width of the hysteresis levels out at about 1–2 mK, which indicates as well that the phase transition is of first order.

Due to the hysteresis the raw data of the dual-slope method need to be shifted in temperature in such a way that the heat capacity of the dual-slope and relaxation method are in full agreement (Fig. 5.13 right hand side).

Only one transition from the paramagnetic state into the long-range ordered helical state was found in agreement with the neutron diffraction study. Therefore, it is a direct transition into the helical state, which is described by a mixing of two irreducible representations. This is in

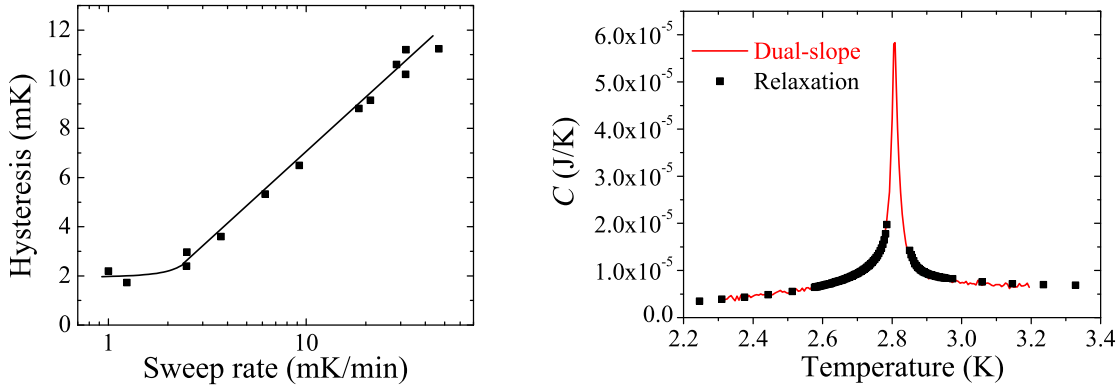

Fig. 5.13: Left: Hysteresis of linarite for different sweep rates of the heating power. The line is a guide to the eye. Right: Correction of the dual-slope data: the raw data were shifted in temperature to correct for the hysteresis effect so that they agree with the relaxation method data (shown is the heat capacity of both the sample and the chip). Only the relaxation data, in which the heat pulse does not cross the phase transition, are plotted.

contrast to materials such as $TbMnO_3$ [194], in which first a transition into a sine wave modulated structure was observed and described by only one irreducible representation, before a transition into the helical spin structure occurs at lower temperatures.

For a closer investigation of the phase transition of linarite, first, the heat capacity of the calorimeter chip needs to be subtracted to obtain the heat capacity of only the sample. This is determined from a measurement of the empty chip. Afterwards the magnetic contribution of the heat capacity needs to be extracted.

In general, the measured heat capacity is a summation of the lattice, magnetic, and electric contribution:

$$C = C_{\text{lattice}} + C_{\text{mag}} + C_{\text{el}}. \tag{90}$$

For the isolating material linarite C_{el} can be ignored. In order to obtain only the magnetic contribution, the lattice contribution, which was determined in Ref. [198], was subtracted.

From C_{mag} the entropy can be calculated by dividing C_{mag} by the temperature and integrating these data according to Eq. (46). In case of a first order phase transition of special interest is the area around T_{N}, which is shown in Fig. 5.14. Here, a step-like feature is observed at T_{N}, which again indicates a first order character of the transition.

The case of a direct transition into a state involving the mixing of two irreducible representations to describe a helical spin structure was studied by Chapon *et al.* and was applied to α-$CaCr_2O_4$ [197]. In their case, Landau theory was used in which the canonical free energy F was described using two order parameters η_1 and η_2 due to the two irreducible representations. The triggering mechanism discussed by Holakovsky [199] was used leading to [197]:

$$F = F_0 + \frac{1}{2}\alpha_1\eta_1^2 + \frac{1}{4}\beta_1\eta_1^4 + \frac{1}{6}\gamma_1\eta_1^6, \tag{91}$$

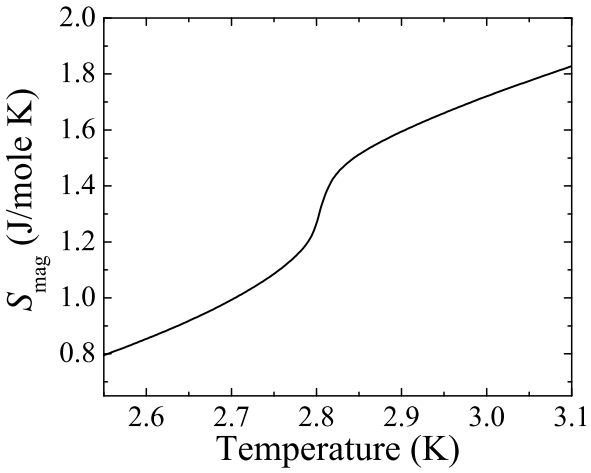

Fig. 5.14: Magnetic contribution to the entropy determined from the heat capacity data using Eq. (46). The integration constant was obtained by normalizing the entropy to the values in [198] at 3 K. A step-like feature was observed at the critical temperature indicating that the transition is of first order.

with $\alpha_1 = \alpha(T - T_\mathrm{N})$, $\alpha > 0$, $\beta_1 < 0$, and $\gamma_1 > 0$. In this case the triggering parameter η_2 effects all thermodynamic variables using Eq. (91) by only multiplicative or additive constants [197]. Further, the heat capacity below T_N was calculated as

$$C_p = -T\frac{\partial^2 F(T)}{\partial T^2} = C_p^0(T) + \frac{\alpha^2 T}{(\beta_1^2 - 4\alpha\gamma_1(T - T_\mathrm{N}))^{0.5-\delta}} \tag{92}$$

with $0 < \delta < 0.25$ [197]. The model of Eq. (92) was fitted to the heat capacity data leading to the values $\alpha = 0.70$, $\beta_1 = -0.04$, $\gamma_1 = 0.28$, $\delta = 0$, and $T_\mathrm{N} = 2.803\,\mathrm{K}$ (Fig. 5.15). The prediction about $\Delta T = \frac{\beta_1^2}{4\alpha\gamma_1}$ leads to a hysteresis of 2 mK, which agrees with the experimentally observed value. Thus, the phase transition at zero field into the long-range ordered ground state can be described by the model of Ref. [197], which contains a mixing of two modes corresponding to two different irreducible representations.

In summary, only one transition temperature was observed in zero field, which is a direct transition into the helical ground state indicating that the sine wave modulated structure and the helical structure have equal energies. The transition was found to be of first order as it is expected for a direct transition into a helical ground state in monoclinic systems. These findings fully confirm the helical spin arrangement resulting from the neutron diffraction refinement.

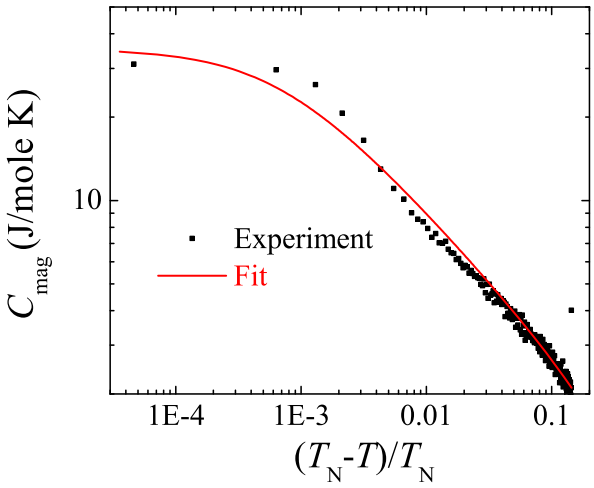

Fig. 5.15: Magnetic contribution to the heat capacity of linarite. The fit was obtained using the model described by Eq. (92). For details see text.

5.5 Field Induced Phases

5.5.1 Phase diagram

When applying a magnetic field along the b axis five different phases/regions were observed. To map out the whole phase diagram (magnetic field versus temperature) data from different bulk property measurement techniques were combined. These include magnetization, heat capacity, magnetocaloric effect, thermal expansion, as well as magnetostriction measurements. The various features from these measurements were then used to define the phase boundaries as seen in Fig. 5.16. Further, Markus Schäpers used NMR to determine the phase boundaries of phase V in the field range of 3–6 T [188]. The boundaries of the multiferroic phases were determined by a peak in the dielectric constant and were added to the phase diagram as well.

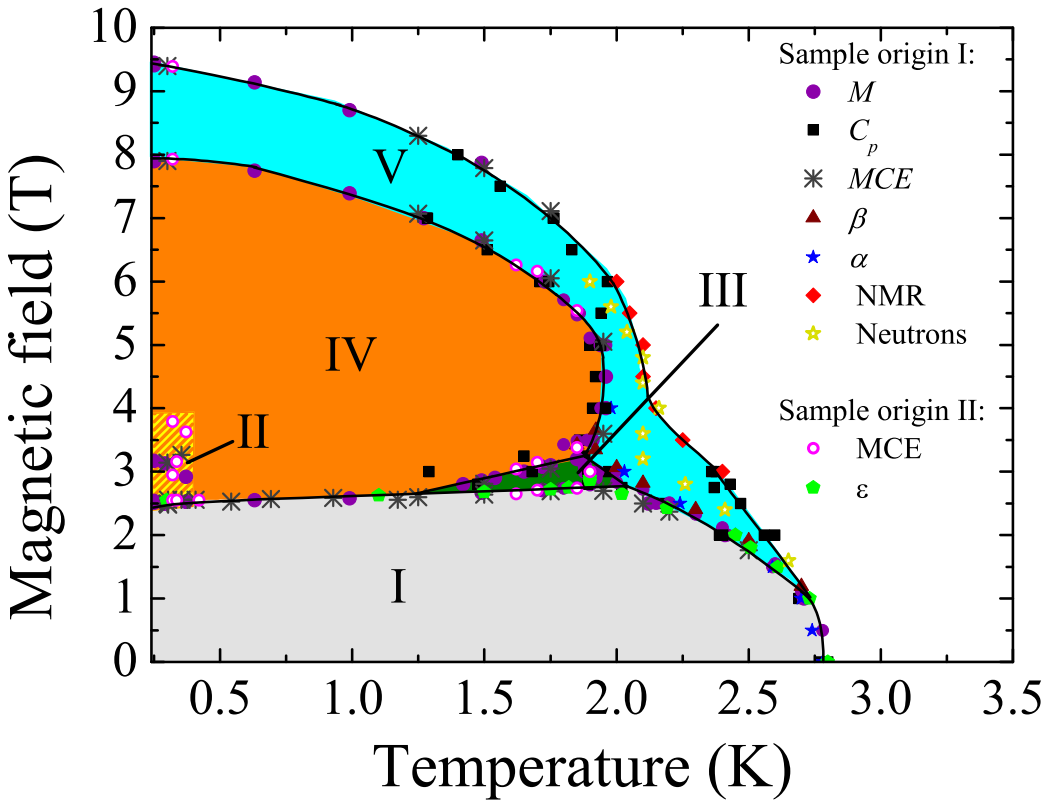

Fig. 5.16: Magnetic phase diagram of linarite for an applied magnetic field parallel to the b axis determined for samples of two different origins. Origin I is the Blue Bell Mine including sample Ia and Ib, while origin II is the Grand Reef Mine including samples IIa-IIc. Measurements of the magnetization M, heat capacity C_p, magnetocaloric effect MCE, thermal expansion α, and magnetostriction β define the phase boundaries. Further, NMR measurements were used to determine the phase boundaries of phase V. Points labeled with "neutrons" indicate the fields and temperatures at which q-scans were performed within the neutron diffraction study presented in chapter 5.5.4. Measurements of the dielectric constant ϵ define the multiferroic phases. The lines are guides to the eye.

Phase I is the helical ground state discussed in the previous section, which extends up to 2.8 K and 2.6 T. Region II was found for temperatures up to ∼0.4 K and magnetic fields between 2.5 T and 4.0 T (sections 5.5.2 and 5.5.3). It shows hysteretic behavior: the transition into region II was observed only for an increasing field, while for a decreasing field there appears to be a direct transition from phase IV into phase I. Further, the transition into region II is strongly sample dependent. Region III is wedge-shaped and is enclosed by phase I, IV, and V. It exists for temperatures between 1.25 K and 2 K and applied magnetic fields between 2.8 T and 3.2 T. Phase IV was found in a wide temperature and field regime. It extends up to 1.95 K and ∼8 T. Phase V for higher magnetic fields and temperatures shows only very weak features in the thermodynamic measurements (sections 5.5.2 and 5.5.3). The phase boundary of phase V for applied magnetic fields between 3 T and 6 T was determined within the NMR study. Since the signal was very weak, with this technique a characteristic spectrum could not be obtained in the whole field and temperature region of phase V. Therefore, the temperature at which the paramagnetic signal vanishes was defined as the phase boundary. Neutron diffraction measurements show very weak magnetic Bragg peaks indicating that phase V is long-range ordered on the experimental scale of neutron scattering (see chapter 5.5.4).

The cantilever magnetization and the magnetocaloric effect measurements are shown in the following two sections. The thermal expansion, magnetostriction, and heat capacity data we used for determining the phase boundaries of the different phases will be presented by Markus Schäpers in his thesis [188]. Section 5.5.4 contains a neutron diffraction study for phases III, IV, and V. Section 5.5.5 presents measurements of the dielectric constant in order to investigate the multiferroic phases.

When applying a magnetic field perpendicular to the b axis, it was supposed on the basis of magnetization data $M(H)$ down to 1.8 K and heat capacity data $C(T)$ down to 0.3 K that only one phase is present [198]. As is shown in Ref. [198], phase I extends up to ∼7 T. Furthermore, it was demonstrated that the phase diagram is very similar when applying the magnetic field along the c axis and along a^* (a^* is the direction perpendicular to the bc plane). Measurements with applied magnetic fields along the b axis seemed to be more interesting since for this field direction different phase transitions could be observed very easily. Therefore, this thesis is focused mainly on measurements with applied magnetic fields along the b direction. Only recently, additional magnetization measurements down to 100 mK show evidence of multiple phases just below the saturation field for magnetic fields perpendicular to the b axis. The provisionally extended phase diagram is shown in Fig. 5.17. By means of angular dependent magnetization measurements down to 1.8 K the different phases observed for fields perpendicular to the b axis were put into relation to the phases for fields parallel to b, although it should be noted that this classification is only preliminary. To decide how the spins are arranged in these phases, further investigations are needed.

The magnetization data for fields perpendicular to the b axis as well as the angular dependent

data are shown in section 5.5.6.

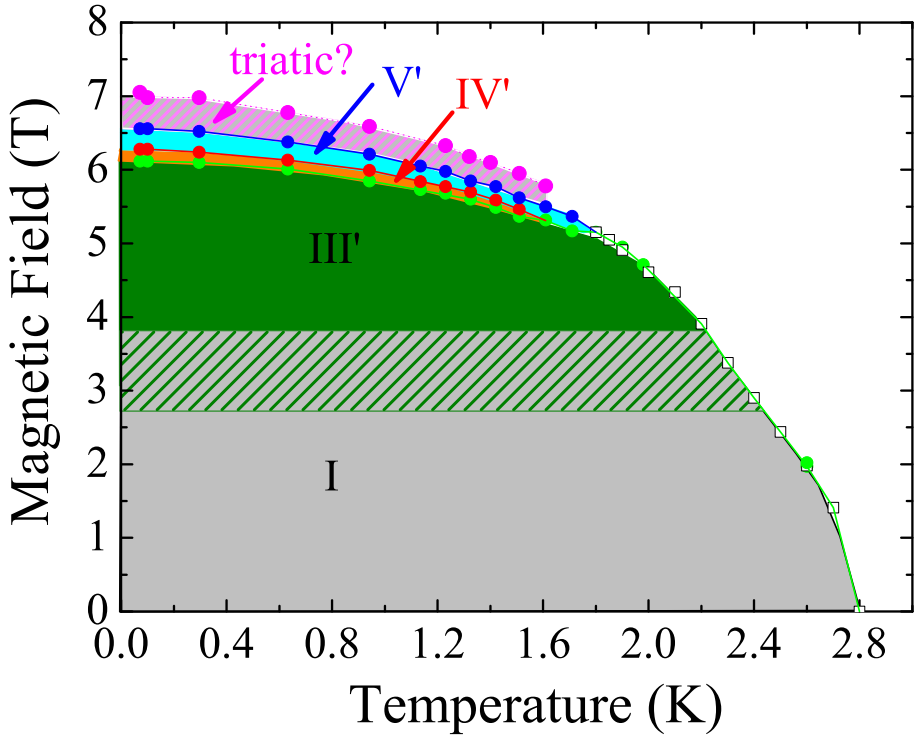

Fig. 5.17: Provisional magnetic phase diagram of linarite for an applied magnetic field perpendicular to the crystallographic b axis (almost perpendicular to the $(\bar{1}01)$ plane). Closed cycles denote the low temperature magnetization data obtained from the cantilever magnetometer, while the open squares are the results from Ref. [198]. The labels III', IV', and V' indicate that these phases could have similarities to the phases observed for fields parallel to the b direction, but they are most probably not identical.

5.5.2 Magnetization Measurements ($H \parallel b$)

The magnetization and susceptibility measurements were performed down to temperatures of 0.24 K using the cantilever magnetometer at the Helmholtz-Zentrum Berlin (see section 3.4.2). For the magnetization measurements the single crystal Ib was used. The crystal had a mass of 0.98 mg and was aligned in such a way that the applied magnetic field was along the crystallographic b axis (Fig. 5.6).
Magnetization measurements were performed at temperatures between 0.24 K and 1.72 K and fields up to 12 T. The applied magnetic field was swept at rates between 3 mT/min and 6 mT/min. The DC-susceptibility $\chi = M/(\mu_0 H)$ was measured for fields between 1 T and 7 T and temperatures between 0.9 K and 2.9 K.

$\chi(T)$-Measurements

Susceptibility measurements are horizontal scans through the magnetic phase diagram shown in Fig. 5.16. The data for all magnetic fields are summarized in Fig. 5.18. In the scans up to

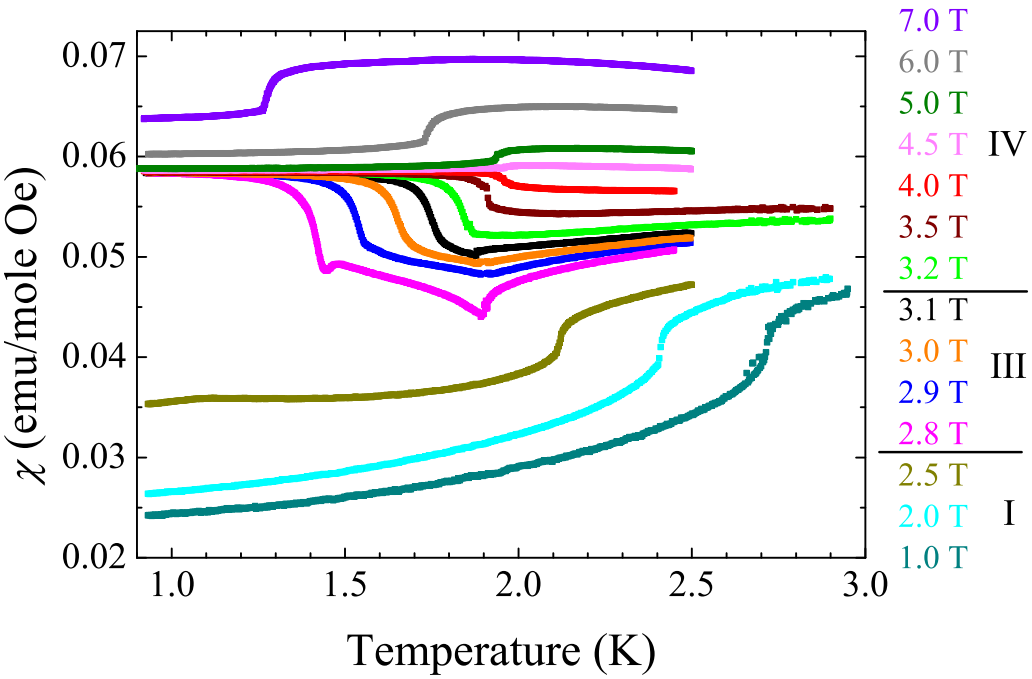

Fig. 5.18: DC-Susceptibility data of linarite determine the vertical phase boundaries of the magnetic phase diagram.

2.5 T a step like increase was observed at the transition from the long-range ordered ground state (phase I) into phase V. The temperature of the phase transition was defined as the temperature at which the derivative shows a maximum. A very rapid decrease of susceptibility was observed for decreasing the temperature. For example at a field of 2 T the loss of susceptibility in the

temperature region between 2.42 K and 2.40 K is ∼10 % of the overall loss between 0.9 K and 2.9 K. That corresponds to a loss of magnetic moment of 0.012 μ_B per Cu in 20 mK.

For fields between 2.8 T and 3.1 T two transitions were found. A sharp drop defines the phase transition from phase IV into phase III, while a kink determines the boundary from phase III into phase V. The phase boundaries were again determined by taking the extrema of the derivative.

For higher fields up to 7 T only one transition was observed again, which defines the phase boundary of phase IV to phase V. At a magnetic field of 4.5 T the slope of the susceptibility data changed from negative to positive. In the magnetocaloric effect measurements no evidence for a transition was found at 4.5 T indicating that this is not a phase boundary but rather a change of the characteristics of phase IV.

No indication of the phase boundary from phase V into the paramagnetic regime was found in the susceptibility data.

$M(B)$-Measurements

The magnetization measurements represent vertical scans through the phase diagram so that horizontal phase boundaries can be nicely investigated.

In Fig. 5.19 the characteristics defining region II are shown. Indications of the existence of region II were found in the magnetization data only at temperatures below 0.63 K. For an increasing field two steps are observed in the magnetization curves at $H_{c1,II}$ and $H_{c2,II}$ determining the boundaries of this region, while for a decreasing field only one step was found at $H_{c1,II}$. Thus, a direct transition from phase IV into the ground state occurs for a decreasing field indicating that region II may not be a distinct thermodynamic phase.

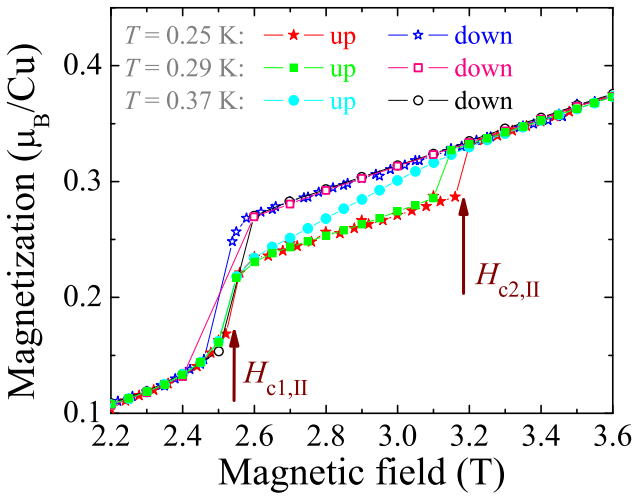

Fig. 5.19: Magnetization measurements defining the boundaries of region II in linarite. Region II shows a hysteretic behavior: for an increasing field (up) two transition fields $H_{c1,II}$ and $H_{c2,II}$ are observed, while for decreasing fields (down) only one transition field at $H_{c1,II}$ was found.

For higher temperatures a direct transition from phase I into phase IV is present, which is indicated by a step in the magnetization. These transitions are shown for temperatures of 0.63 K and 0.99 K as examples in Fig. 5.20.

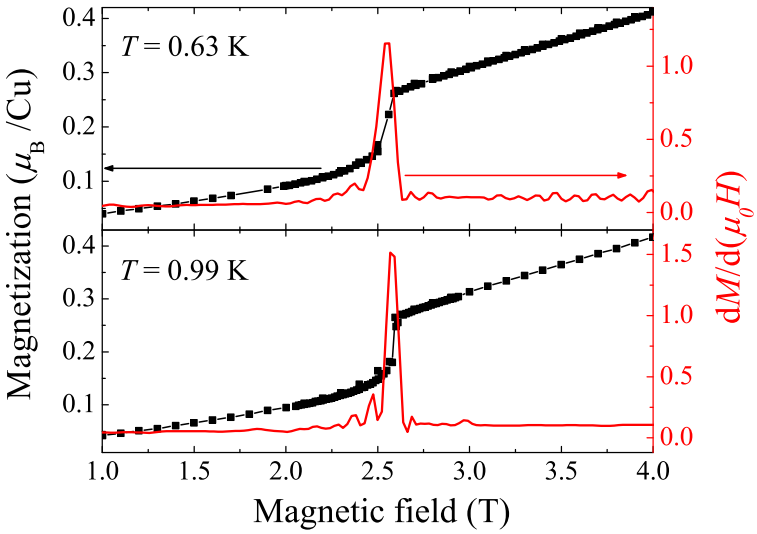

Fig. 5.20: Direct phase transition from phase I into phase IV, as seen in the low temperature magnetization measurements on linarite.

For temperatures of 1.49 K and 1.72 K two transitions were found defining phase III. The boundaries of phase III were observed as small steps in the magnetization, which cause pronounced peaks in the first derivative (Fig. 5.21). From these peaks in the derivative the transition fields were obtained to define the boundaries of phase III. For lower temperatures the two transition fields move closer together resulting in the wedge-shape of phase III.

The phase transition from phase IV into region V and from region V into the paramagnetic regime is shown in Fig. 5.22. The boundary between phase IV and phase V is clearly seen in the first derivative. The transition from phase V into the paramagnetic regime is defined by the weak feature in the derivative, which increases for lower temperatures. The signature of the transition into phase V might be influenced by thermal fluctuations, which decrease for lower temperatures so that the feature becomes more pronounced. From the magnetization data alone phase V would not be expected to be a long-range ordered phase since the boundary is only defined by this very weak feature in the first derivative. The neutron diffraction study however (described in section 5.5.4) shows that phase V is long-ranged ordered.

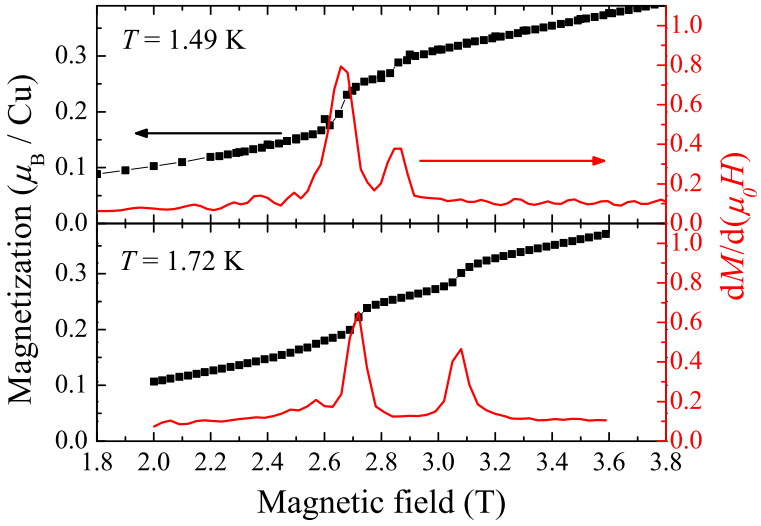

Fig. 5.21: Magnetization data showing the phase boundaries of phase III of linarite.

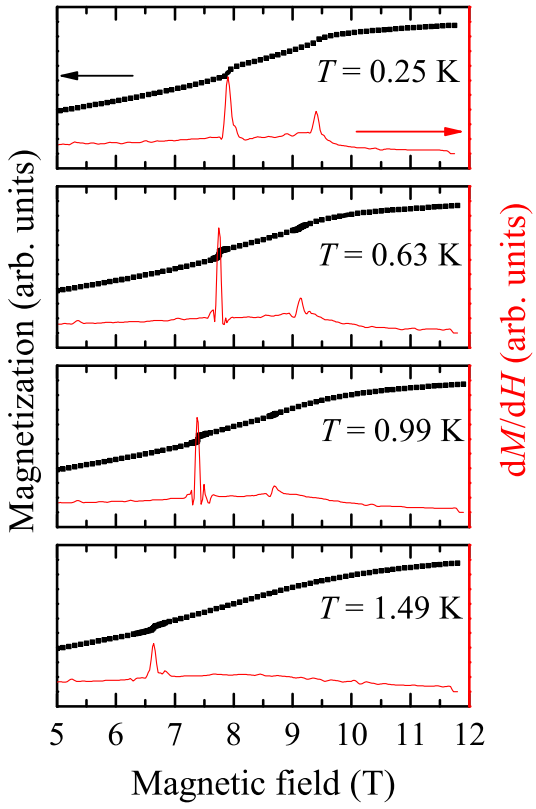

Fig. 5.22: Magnetization data on linarite, where peaks in the derivative define the phase boundaries of phase V. Since the absolute values are only correct up to 7 T the magnetization is plotted in arbitrary units.

Magnetization Component Perpendicular to the Applied Field

As anisotropy of a system can lead to a magnetization component perpendicular to the applied field, it is worthwhile to take a look at this component. Together with the magnetization in field direction, the cantilever magnetometer always also measures the magnetization component perpendicular to the applied field due to the torque contribution of the static field (see chapter 3.4.2). By separating the magnetization component perpendicular to the static field from the data the evolution of the magnetization in Fig. 5.23 is obtained. In contrast to the step of the magnetic moment component along the static field, the phase transition from phase I into phase III causes a minimum in the magnetization component perpendicular to the static field. At the transition from phase III into phase IV a step of the magnetization is obtained similar to the parallel component. These data clearly show that anisotropy has great importance for this material.

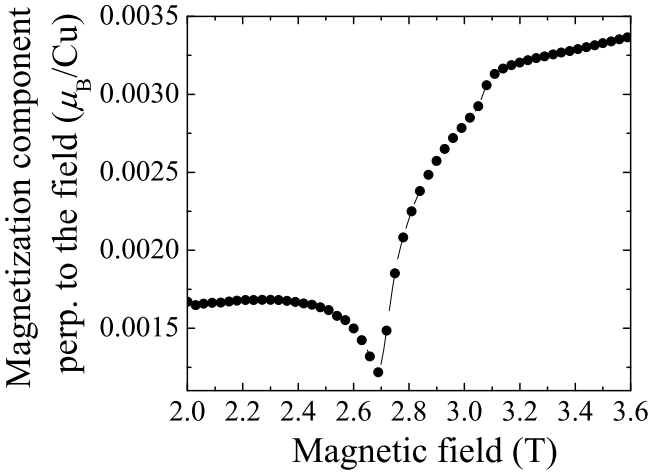

Fig. 5.23: Magnetization component perpendicular to the applied magnetic field at 1.72 K crossing phase III. A minimum indicates the phase transition from the ground state into phase III.

5.5.3 Magnetocaloric Effect Measurements ($H \parallel b$)

The aim of the magnetocaloric effect measurements presented here was primarily to define the phase boundaries in the phase diagram in order to combine these data with the data from other techniques. For that reason a field sweeping rate of 75 mT/min was sufficient to measure the magnetocaloric effect. This fast sweeping rate leads to an error in the absolute values for $\mathrm{d}Q/(\mu_0 \mathrm{d}H\ T)$ of about $4 \cdot 10^{-4}$ J/TKg and a maximum difference in the transition field for up and down sweeps of 0.2 T.

For the magnetocaloric effect measurements two samples from the different origins were used. Sample Ib is the same sample as the one used for the magnetization measurements (origin: Blue Bell Mine, California). Sample IIb is from Grand Reef Mine, Arizona.

Representative plots for the different phases/region are shown in Fig. 5.24, 5.26, and 5.27. In Fig. 5.24 the low temperature region II is shown for both samples. For an increasing magnetic field two transitions at ∼2.5 T and 3.1 T were observed for sample Ib, while for a decreasing field only one was found at 2.5 T. This agrees well with magnetization measurements (Fig. 5.19), which were performed on the same sample. Different features were observed in sample IIb. For an increasing field even three transitions were observed at ∼2.5 T, 3.0 T, and 3.5 T, while for a decreasing field the same transition was observed as for sample Ib. This shows that region II is sensitive to the sample quality.

The magnetocaloric effect data also showed that the second transition for the up sweep is not fully reproducible. The second transition observed for sample Ib varied for example in a range of about 150 mT. Furthermore, a hysteresis between the data of the up and down sweep could be observed at the first transition at 2.5 T, where the peak for the down sweep is broader than for the up sweep.

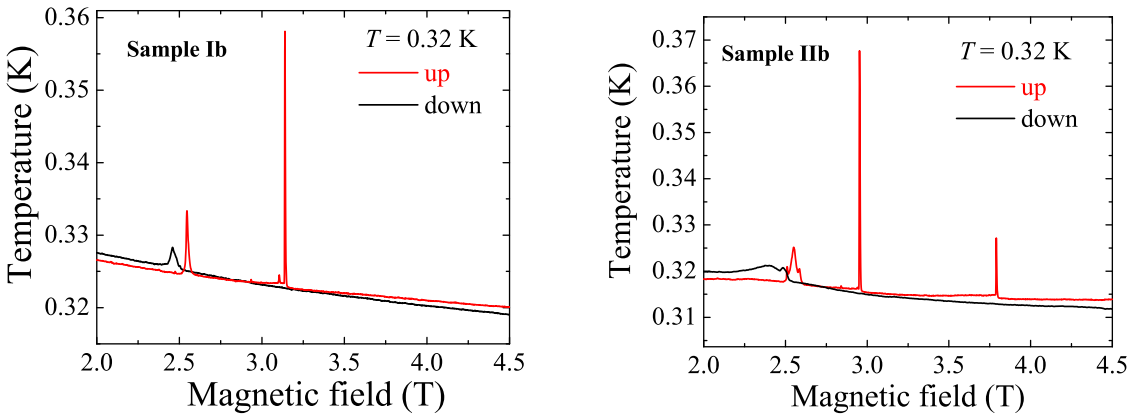

Fig. 5.24: Sample temperature of linarite at a bath temperature $T = 0.32$ K while sweeping the magnetic field showing region II (left: sample Ib; right: sample IIb).

It should be emphasized that in the temperatures region at about 300 mK for both increasing and decreasing field the sample temperature increases, which can only be the result of disequilibrium effects. This dissipative contribution was further investigated using sample Ib and a sweeping rate of 25 mT/min. For several temperatures between 304 mK and 1167 mK field scans were performed for increasing as well as for decreasing fields (see Fig. 5.25). At 1167 mK the data of the up and down sweep are similar but the temperature change has an opposite sign. This is what would be expected for equilibrium processes. For lower temperatures, however, the temperature difference $T_{\mathrm{bath}} - T_{\mathrm{sample}}$ of the down sweeps decreases until for about 407 mK the dissipative contribution equals the equilibrium contribution. At this temperature almost no feature is observable for the down sweep. For even lower temperatures the dissipative contribution is larger than the equilibrium one so that the temperature of the sample increases also for the down sweep. Moreover, an increase of the hysteresis between up and down sweep is observed.

All these observed features lead to the conclusion that pinning effects might be dominant in this regime. Since sample IIb, which was characterized as a sample with lower crystal quality compared to sample Ib, shows more peaks in the sample temperature for an increase of the magnetic field, it suggests that pinning on defects might occur.

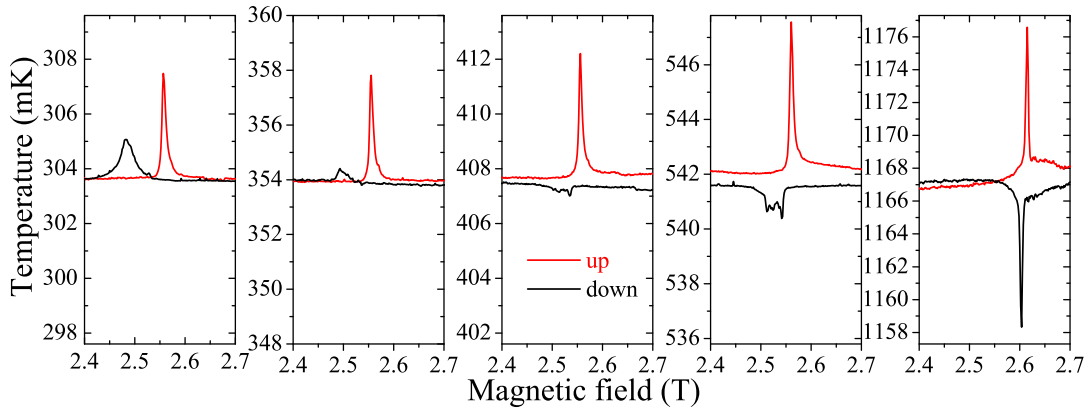

Fig. 5.25: Temperature dependent measurements of the magnetocaloric effect at fields between 2.4 T and 2.7 T and at bath temperatures of 304 mK, 354 mK, 407 mK, 542 mK, and 1167 mK.

Fig. 5.26 shows phase III, which is enclosed by phase I and phase IV, for sample Ib and IIb at 1.75 K and 1.70 K, respectively. In this temperature regime, for an increasing magnetic field the temperature change has the opposite sign than for an decreasing field so that no disequilibrium effects are present and the quantity $\mathrm{d}Q_{\mathrm{magcal}}/(\mu_0 \mathrm{d}H\ T)$ is the same for up and down sweep. The transition from phase I into phase III is defined by a sharp peak at 2.7 T in the data,

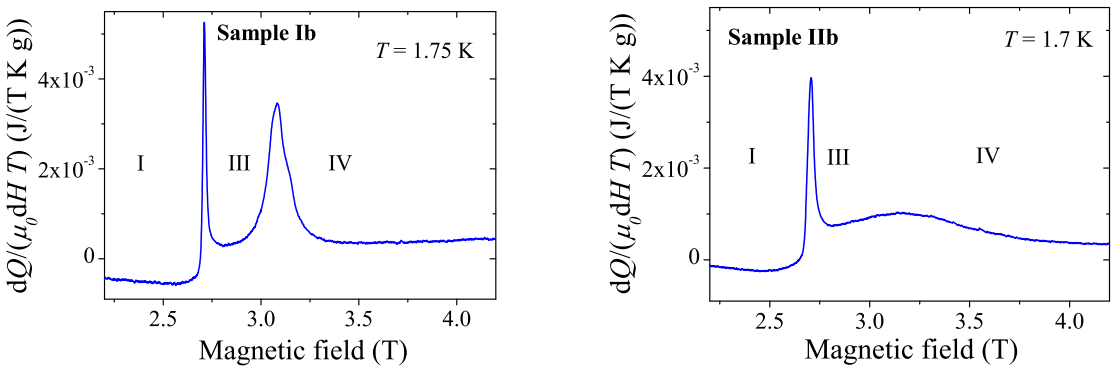

Fig. 5.26: Magnetocaloric effect measurements of linarite upon crossing phase III (left: sample Ib at 1.75 K; right: sample IIb at 1.70 K).

while the peak for the transition into phase IV at 3.1 T is broader. This broader peak could indicate that the spin structure transforms over a larger field region, which is consistent with

the neutron diffraction study described in section 5.5.4. Especially for sample IIb the transition into phase IV is indicated by a very broad feature. It seems that again sample impurities have a remarkable effect on this transition. In contrast to the sample dependent broadness of this peak, the transition fields for both samples agree very well with each other and also with the magnetization measurements (Fig. 5.21). Regarding the relationship between $\mathrm{d}Q_{\mathrm{magcal}}/(\mu_0 \mathrm{d}H\ T)$ and the change in entropy: $-\mathrm{d}S/(\mu_0 \mathrm{d}H) = \mathrm{d}Q_{\mathrm{magcal}}/(\mu_0 \mathrm{d}H\ T)$ (Eq. (65)), the peaks to positive values of $Q_{\mathrm{magcal}}/(\mu_0 \mathrm{d}H\ T)$ show that for an increase in magnetic field the entropy decreases at the transition from phase I into III and from phase III into IV.
The magnetocaloric effect measurements for phase V are shown in Fig. 5.27. The transition from phase IV into region V is defined by a pronounced peak in the magnetocaloric effect data, indicating that this transition involves a large change of entropy. The transition into the paramagnetic regime is indicated only by a very weak feature, which is getting stronger with decreasing temperature, similar to the feature in the first derivative of the magnetization data (Fig. 5.28). For an increasing field the entropy increases at both transitions.

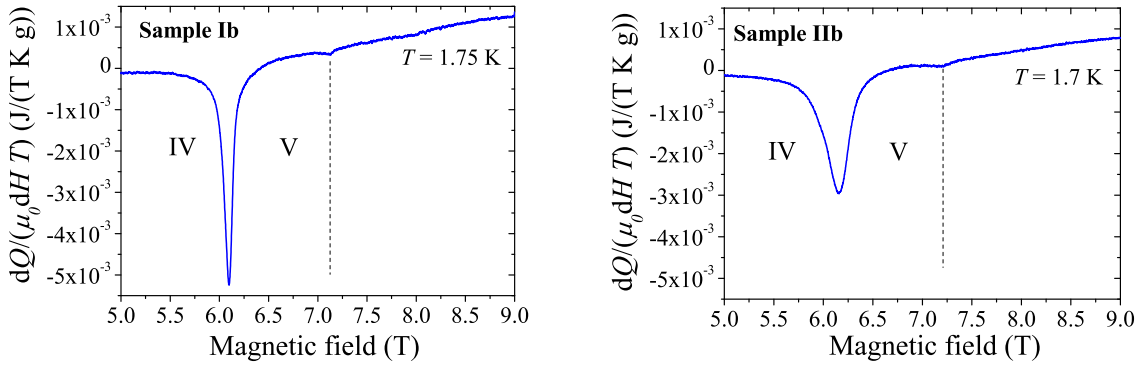

Fig. 5.27: Magnetocaloric effect measurements of linarite upon crossing phase V (left: sample Ib; right: sample IIb). The dashed line indicates the transition field from phase V into the paramagnetic regime.

Further, Fig. 5.29 displays the transition from the ground state into phase V for sample Ib. At the transition point the system gains entropy. The transition from phase V into the paramagnetic regime is observed at 2.5 T.

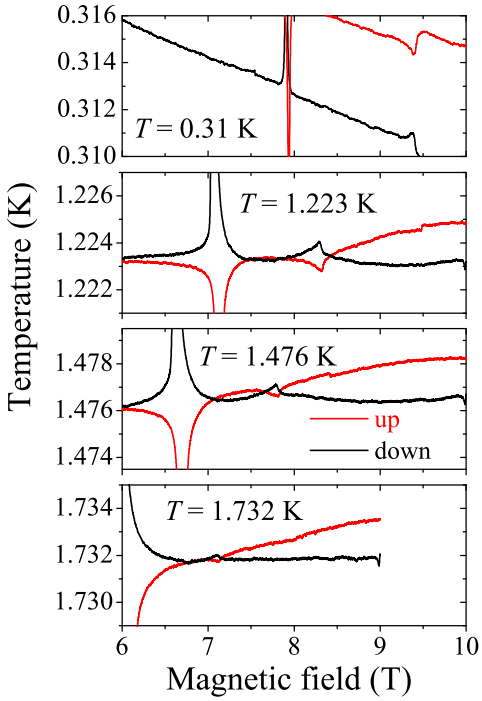

Fig. 5.28: Magnetocaloric effect measurements of linarite (sample Ib). The transition from phase V into the paramagnetic regime is temperature dependent. The curves at $T = 0.31\,\mathrm{K}$ for up and down sweeps do not lie on top of each other between the transitions due to a drift in the bath temperature.

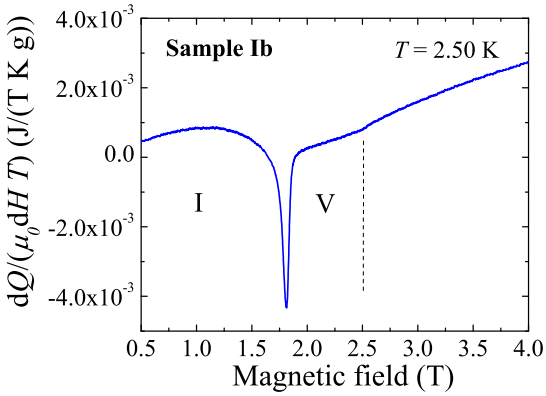

Fig. 5.29: Magnetocaloric effect data at 2.5 K showing the transition of sample Ib from phase I into phase V. The dashed line indicates the transition field from phase V into the paramagnetic regime.

5.5.4 In-Field Neutron Diffraction Measurements (H || b)

In order to investigate the spin structure of phase III, phase IV, and phase V neutron diffraction measurements on D10 were performed in magnetic fields up to 6 T. The same sample was used as for the determination of the spin structure at zero field. The flat face, which was the bc plane of the crystal, was glued on an Al-plate in such a way that the crystallographic b axis was along the applied magnetic field (misalignment 1°–2°). The magnet had an opening of ±8°, which restricted the access of the Bragg peaks hkl in the b direction to $-0.25 < k < 0.25$. The data were obtained at temperatures between 1.7 K and 2.65 K.

Field Scans through Phases I, III, and IV

First, q-scans were performed while varying the applied magnetic field at 1.7 K (Fig. 5.30). These scans show that the incommensurate propagation vector (0, 0.186, 0.5) remains constant throughout phase I, while near the phase boundary to phase III an additional propagation vector (0, 0, 0.5) was found. It demonstrates that phase III is a coexisting phase which consists of two spin structures at the same time. At 3 T the incommensurate propagation vector vanishes and only the commensurate propagation vector was found.

Altogether, below a magnetic field of 2.6 T only phase I could be observed, which has a helical spin arrangement with the incommensurate propagation vector (0, 0.186, 0.5) as it was described in section 5.4.1. At 2.6 T the second spin structure occurs with a commensurate propagation vector (0, 0, 0.5) (shown in Fig. 5.31). Thus, the commensurate structure was found in fields where thermodynamic measurements suggest that the spin structure is still the structure of phase I.

At 2.7 T the integrated intensity of the magnetic peak (0, -0.186, 0.5) shows a sharp step to lower intensities, which coincides with the phase transition into phase III observed by thermodynamic measurements. The intensity of the magnetic Bragg peak (0, 0, 0.5) increases with field, while the peak (0, 0.186, 0.5) continues decreasing from 2.85 T. At

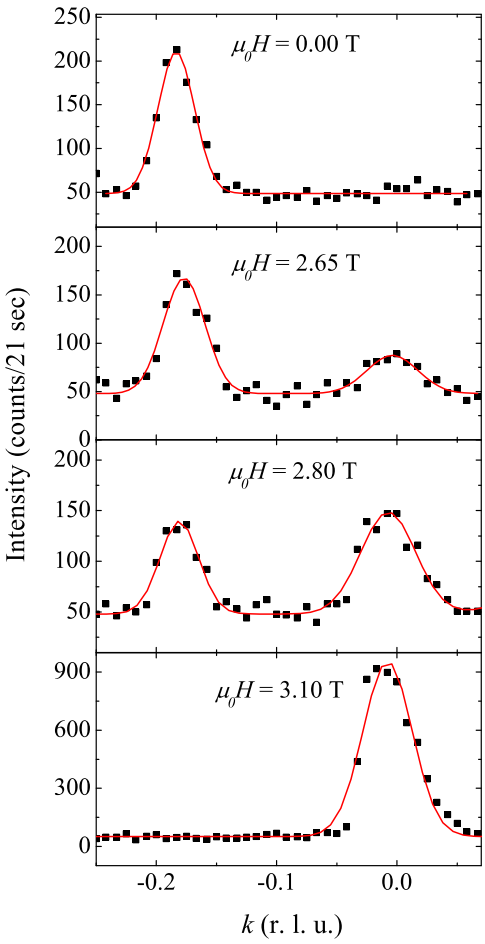

Fig. 5.30: q-scans along k at 1.7 K for linarite: field dependence of the (0, -0.186, 0.5) and the (0, 0, 0.5) Bragg peak from phase I to phase IV crossing phase III. The red curves are Gaussians, which were fitted to the data in order to determine the accurate peak positions.

fields above 2.9 T only the commensurate phase is observable. The peak intensity shows a severe increase, which could define the transition into phase IV. In phase IV the intensity of the magnetic Bragg peak (0, 0, 0.5) gradually decreases with field. Within the error bars the full width

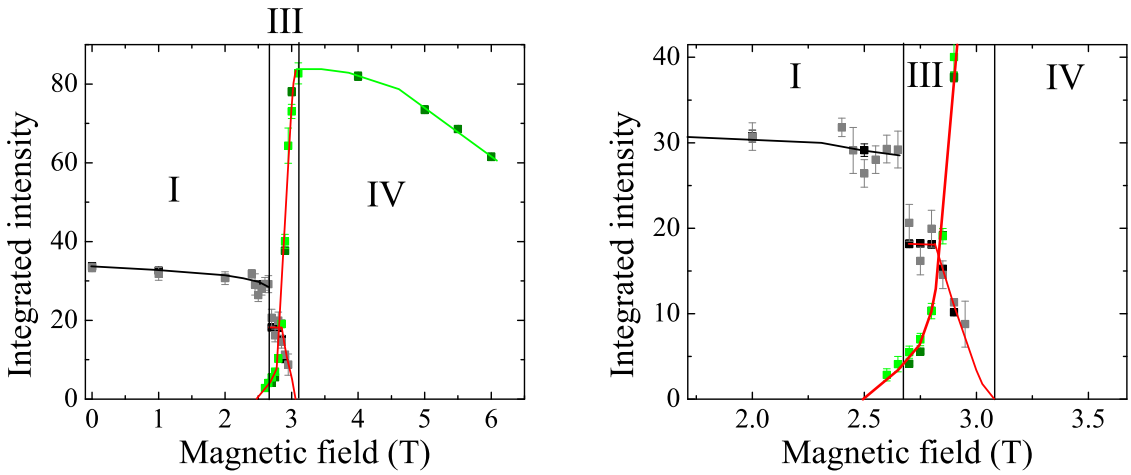

Fig. 5.31: Integrated intensities of the incommensurate Bragg peak (0, -0.186, 0.5) (gray and black squares) and the commensurate peak (0, 0, 0.5) (green squares) at 1.7 K for different magnetic fields crossing phase III of linarite. Lines are guides to the eyes. The plot of the right hand side is a zoom-in. Since for some of the measurements smaller slits were used, the integrated intensities were normalized to each other.

half maxima of the observed magnetic Bragg peaks in phase I, III, and IV equal the full width half maxima of the nuclear Bragg peaks.

Refinement of the Data Sets in Phase IV

Two complete data sets with magnetic Bragg peaks $(h,0,l)_M = (h,0,l)_N \pm (0,\ 0,\ 0.5)$ were collected in phase IV at 4 T and 5.5 T at a temperature of 1.7 K. The two fields were chosen in order to compare the region in which the susceptibility shows a negative slope with the region where a positive slope was observed. 33 peaks (20 were inequivalent) were measured at 4 T, while 20 inequivalent peaks were measured at 5.5 T. The refinements at both fields show that in phase IV the spins flop into the *ac* plane where the spins have the same angle ($-27(1)^\circ$) to the *a* axis as the rotating plane of the helix has in the ground state (Fig. 5.32). No change in the spin arrangement was observed within the error bars for 4 T and 5.5 T. A magnetic moment of $0.79(1)\,\mu_B$ was found per Cu atom at 4 T, while at 5.5 T a slightly smaller moment of $0.73(2)\,\mu_B$ was obtained (see peak intensity of the (0, 0, 0.5) Bragg peak in Fig. 5.31). Note that the refined moment is just the component of the total moment lying in the *ac* plane (perpendicular to the applied magnetic field). The crystallographic R_F-factor was 9.5 % for the refinement at 4 T, while for 5.5 T it was 12.5 %. The slightly larger value for the data set at 5.5 T is due to the fact that the steps and the ranges of the ω-scans at different 2θ values were not entirely optimized to the resolution curve of the instrument for the measurements at 5.5 T.

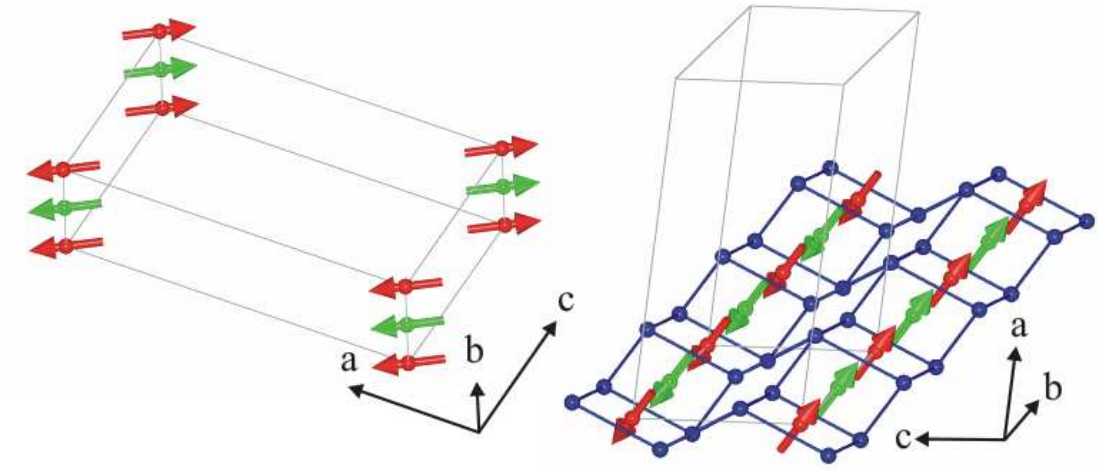

Fig. 5.32: Commensurate spin structure of linarite in phase IV. The spins are aligned ferromagnetically along the a and b direction, while they are aligned antiferromagnetically along the c direction.

Refinement of the Data Sets in Phase III

The spin structure in phase III was investigated at 2.8 T (1.7 K) since at this field the commensurate Bragg peak (0, 0, 0.5) and the incommensurate peak (0, -0.186, 0.5) have nearly the same intensity (Fig. 5.31). In this case Bragg peaks of both incommensurate and commensurate structure can be observed for the same field. Additionally, at 2.7 T a data set of the incommensurate structure was measured.

On the basis of 15 Bragg peaks (14 inequivalent peaks) the same spin structure was found for the commensurate phase as it was found in phase IV. The scale factor was refined in order to obtain the percentage of the commensurate structure. With the scale factor of the commensurate phase the overall scale factor was divided into two parts (incommensurate and commensurate phase). At 2.8 T a percentage of 17 % of phase III shows the commensurate spin structure found also in phase IV.

For the refinement the symmetry analysis performed in section 5.4.1 was used to find the correct spin structure. For the incommensurate phase in phase III at 2.8 T a *circular* helix was found based on a dataset of 18 inequivalent peaks (R_F =14.5 %). A magnetic moment of $\mu_z = \mu_y$ =0.64(2) μ_B is rotating in the bc plane (Fig. 5.33):

$$\boldsymbol{\mu}_n = \mu_z \cos\left(2\pi(\boldsymbol{K'} \cdot \boldsymbol{R'}_n)\right) \boldsymbol{u}_z + \mu_y \sin\left(2\pi(\boldsymbol{K'} \cdot \boldsymbol{R'}_n)\right) \boldsymbol{v}_y, \tag{93}$$

where the unit vector $\boldsymbol{u}_z$ is parallel to the c axis and $\boldsymbol{v}_y$ parallel to the b axis. $\boldsymbol{R'}_n$ is a lattice point and $\boldsymbol{K'}$ the propagation vector (0, 0.186, 0.5).

The refinement at 2.7 T (11 inequivalent Bragg peaks) yields the same structure as obtained at 2.8 T within the error bars.

All in all, the commensurate spin structure in phase III is the same as it was found in phase IV. The spins in the incommensurate structure of phase III forming a helix with the same pitch

angle as in phase I, but it was found that the helix is circular and that the spins rotate in a different plane (*bc* plane).

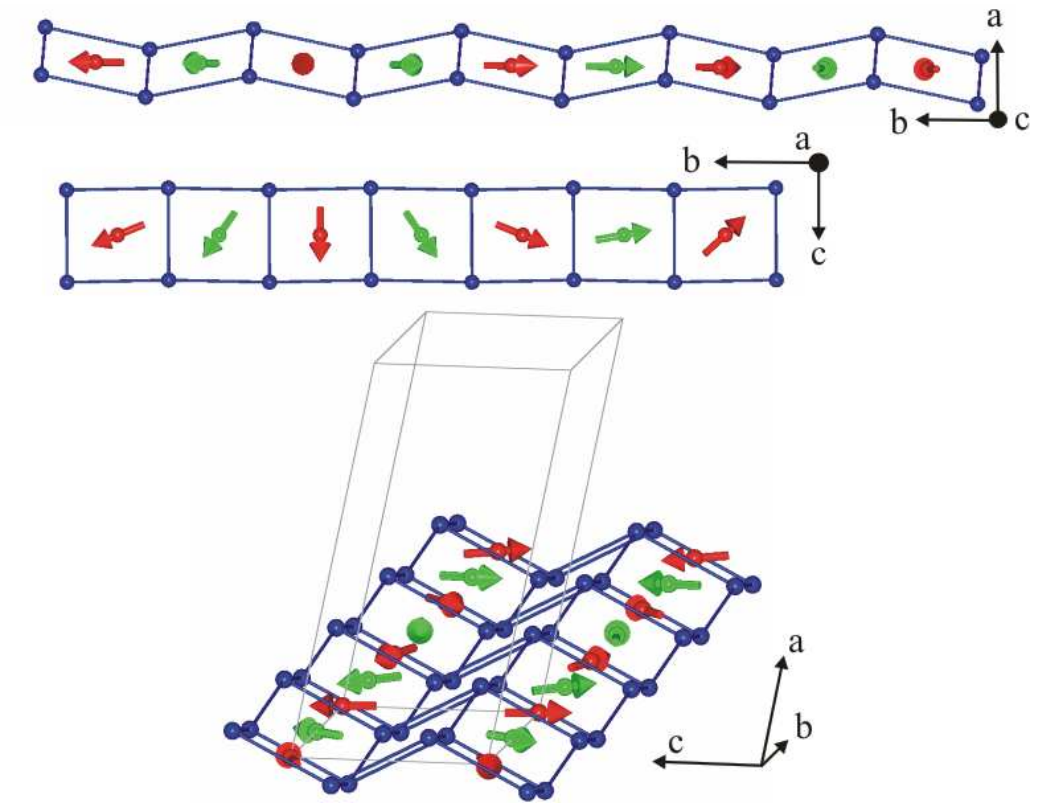

Fig. 5.33: Incommensurate spin structure in phase III of linarite. The upper figure is a projection onto the *ab* plane, while the figure in the middle is a projection onto the *bc* plane. The lower figure shows the spin structure from a perspective near the *b* direction.

Field Scans through Phase V

In phase V between 1.6 T and the maximum field of 6 T weak magnetic Bragg peaks were found. They had integrated intensities which were more than four times smaller than the magnetic peak (0, 0.186, 0.5) measured at 0 T. *q*-scans along *k* show that the k_y-component of the propagation vector is shifting with field (Fig. 5.34).

Starting with a k_y-component of 0.164 at 1.6 T the k_y-value is decreasing with field down to 0.060 at 6 T (Fig. 5.35 left hand side). It seems that the propagation vector stays constant for fields from 5.2 T to higher fields. ω-scans for (0, k_y, 0.5), (0, $-k_y$, 0.5), and (1, k_y, 0.5) were performed in each field to ensure that all observed Bragg peaks at all fields are Bragg peaks belonging to the same crystal domain.

The Bragg peak intensities in phase V change with applied magnetic field as well. The intensity evolution of the Bragg peak (0, $-k_y$, 0.5) is shown in Fig. 5.35, right hand side. The intensity increases from 1.6 T up to 2.4 T. For higher magnetic fields the intensity decreases to the minimum value at ∼4.0 T then increases again for higher fields. This minimum was also observed in ω-scans of the Bragg peaks (0, k_y, 0.5) and (1, k_y, 0.5).

The peaks were measured at different temperatures due to the temperature dependent phase boundaries. To choose the temperature for each scan, a temperature close to the border line to phases I, III, and IV, but alleged in phase V, was set. The scattered neutrons were counted for a (0, k_y, 0.5) position, where a Bragg peak was expected. When no intensity was found, the temperature was slightly increased until the Bragg peak could be observed. The resulting temperatures were added to the phase diagram (Fig. 5.16). For some measurements the chosen temperature can be closer to the temperature of the phase transition. Therefore, the integrated peak intensities can be slightly smaller for measurements near the phase boundary due to the power law decrease of phase transitions, but it cannot explain the intensity evolution shown in Fig. 5.35. However, the intensity evolution of the Bragg peak agrees roughly with the intensity evolution of the small feature obtained by heat capacity measurements at the transition from the paramagnetic regime into phase V.

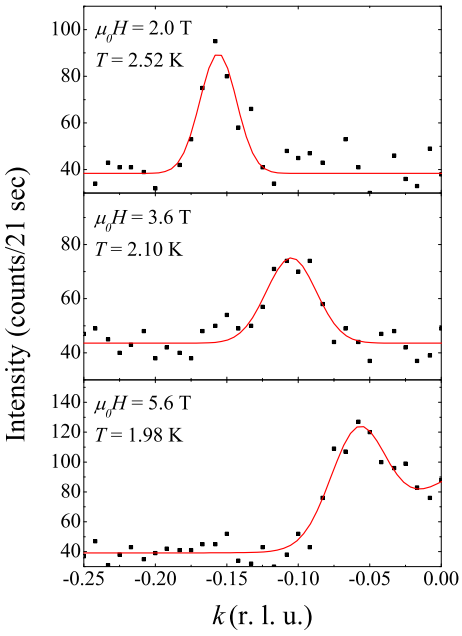

Fig. 5.34: q-scans along k in phase V of linarite: shift of the (0, $-k_y$, 0.5) Bragg peak with the applied magnetic field. The peaks were fitted with a Gaussian (red line). The increase of intensity at 5.6 T for $k \geq 0$ is due to the symmetry equivalent Bragg peak (0, $+k_y$, 0.5). The fit for the peak at this field was obtained by using two Gaussians.

No line broadening was observed for the most intense magnetic Bragg peak (0, k_y, 0.5) during the field scans. The peak widths obtained by ω-scans are the same as for the nuclear peaks.

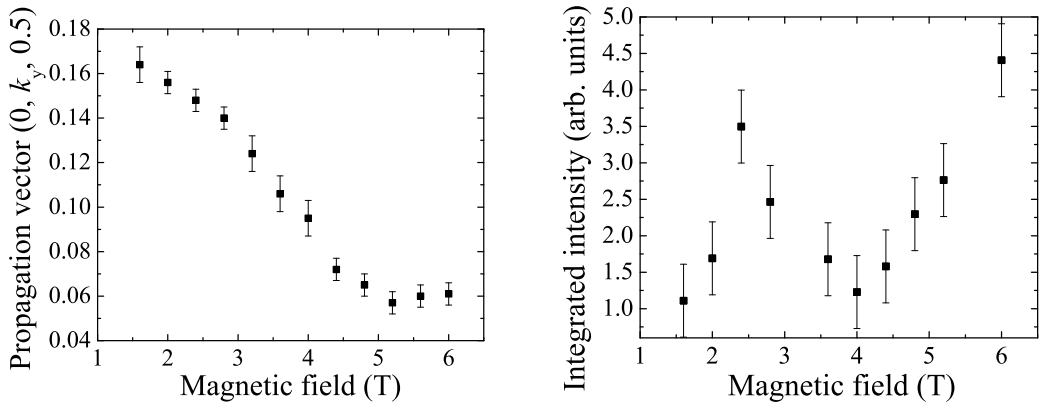

Fig. 5.35: left: Shift of the propagation vector with applied magnetic field (stars in the phase diagram, Fig. 5.16, indicate the temperatures and fields at which the data were obtained); right: Intensity evolution of the Bragg peak (0 $-k_y$ 0.5) in phase V obtained from q-scans along k.

Refinement of the Data Set in Phase V

In order to observe as many different Bragg peaks as possible the data set for phase V was collected at a magnetic field of 6 T (at 1.9 K). In this field the Bragg peaks were most intense (Fig. 5.35). Nevertheless, the intensities were very small so that in phase V only 8 Bragg peaks (inequivalent) could be observed. The refinement of the Bragg peaks ($R_F = 7\,\%$) indicates a sine wave modulated structure, which has only a b component with a maximum value of only $\mu_y = 0.44(1)\,\mu_\mathrm{B}$ (Fig. 5.36):

$$\boldsymbol{\mu}_n = \mu_y \sin\left(2\pi(\boldsymbol{K'} \cdot \boldsymbol{R'}_n)\right) \boldsymbol{v}_y, \tag{94}$$

with $\boldsymbol{v}_y$ being the unit vector along the b direction. For a magnetic field of 6 T the propagation vector $\boldsymbol{K'}$ is (0, 0.06, 0.5).

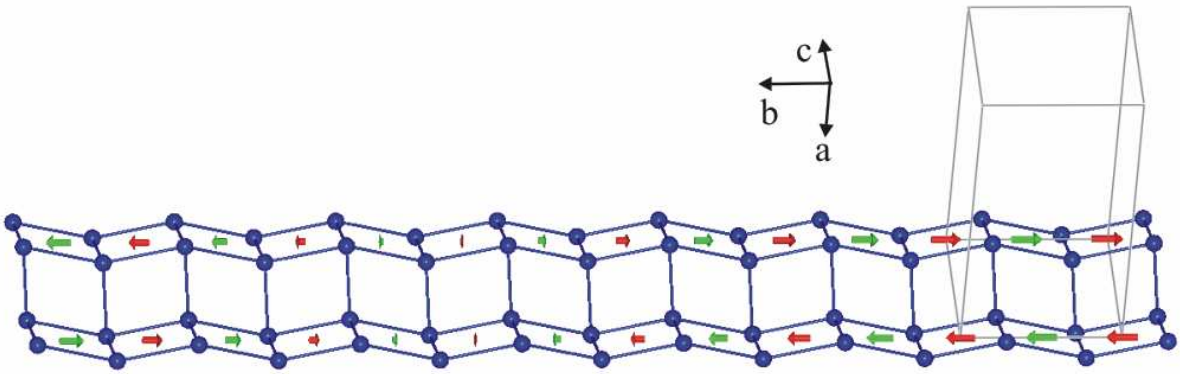

Fig. 5.36: Sine wave modulated spin structure in phase V at 6 T.

Field Dependence of the Nuclear Peak 200

The weak nuclear peak 200 was chosen to investigate any ferromagnetic spin alignment in the sample with field as well. Any change in the intensity would be more detectable on a weak peak than on stronger peaks.

An increase of the intensity of the peak with field was observed for field scans through phases I, III, and IV and for field scans through phase V (Fig. 5.37). For the scan crossing phase III the phase transitions of phase III can be guessed at. Using the relation $I \sim M^2$ the integrated intensities on top of the nuclear peaks were compared with the magnetization obtained in the PPMS VSM at 1.8 K and 2.1 K. Within the error bars the magnetic signal on top of the nuclear peaks corresponds to the bulk magnetization in field direction.

To take account for the ferromagnetic spin alignment, in all phases a ferromagnetic component of the magnetic moment along the b direction needs to be added to the spin structures according to the magnetization curve. The total moment of the spins in phase IV can be calculated by using the b component from the magnetization measurements and the component in the ac plane from the neutron diffraction data. The total moment at 4 T is $0.88\,\mu_\mathrm{B}$ while at 5.5 T it is $0.91\,\mu_\mathrm{B}$. Thus, for an increasing field the total moment increases as it is expected.

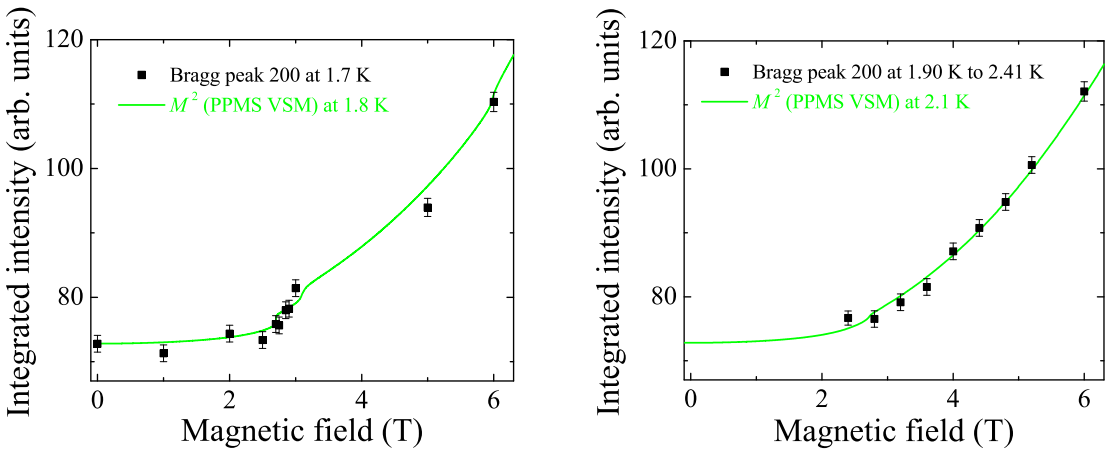

Fig. 5.37: Comparison between the Bragg peak intensity of the nuclear peak 200 and the magnetization measured with the PPMS VSM. The magnetization data were squared and normalized to the Bragg peak intensities. On the left hand side a magnetic field scan through phases I, III, and IV was performed, while on the right hand side the field scan through phase V is shown.

5.5.5 Dielectric Properties ($H \parallel b$)

Several materials with competing exchange interactions like $LiCu_2O_2$, $LiCuVO_4$, $TbMnO_3$, and $Ni_3V_2O_8$ show a noncollinear incommensurate spin structure at low temperatures [54, 164, 194, 200]. When the noncollinear spin ordering sets in, a uniform electrical polarization is induced, which breaks the spatial inversion symmetry [176, 201–203]. The simultaneous onset of ferroelectric order and the magnetic transition characterized these materials as a special kind of multiferroic material.

The uncommon correlation between the spin structure and the polarization has been investigated theoretically by Mostovoy and Katsura *et al.* [173, 174]. A relation between the polarization $\boldsymbol{P}$ and two spins $\boldsymbol{S}_i$ and $\boldsymbol{S}_{i+1}$ was derived:

$$\boldsymbol{P} \sim \boldsymbol{e}_{i,i+1} \times (\boldsymbol{S}_i \times \boldsymbol{S}_{i+1}) , \tag{95}$$

where $\boldsymbol{e}_{i,i+1}$ is the unit vector connecting the magnetic moments. The relation can be explained with the *inverse* Dzyaloshinskii-Moriya effect [178]: The anisotropic Dzyaloshinskii-Moriya effect is a correction of the superexchange mechanism to the Hamiltonian, which arises due to the spin-orbit interaction [204]. The correction term is given by the arrangement of the spins $\boldsymbol{S}_i$:

$$\boldsymbol{D}_{i,i+1} \cdot (\boldsymbol{S}_i \times \boldsymbol{S}_{i+1}) . \tag{96}$$

$\boldsymbol{D}_{i,i+1}$ is the Dzyaloshinskii vector, which is a function of the shift $\boldsymbol{x}$ of the ligands (here: oxygen) from the line $\boldsymbol{r}_{i,i+1}$ connecting the two magnetic ions (here: copper):

$$\boldsymbol{D}_{i,i+1} \sim \boldsymbol{x} \times \boldsymbol{r}_{i,i+1} . \tag{97}$$

From Eq. (97) it is clear that the energy of the Dzyaloshinskii-Moriya interaction increases for increasing displacements of the ligands $\boldsymbol{x}$.

Since for helical spin structures $\boldsymbol{S}_i \times \boldsymbol{S}_{i+1}$ has always the same sign, the Dzyaloshinskii-Moriya effect pushes the negatively charged oxygen ions O^{2-} in one direction which is perpendicular to the chain containing the positive charged copper ions Cu^{2+}. Therefore, ferroelectricity is induced. The mechanism can also be described by means of spin currents resulting in the same relation for the polarization (Eq. (95)) [173].

For the ground state of linarite, in which the spins are rotating roughly in a plane containing the b axis and the $[10\bar{1}]$ direction, a polarization in the $[10\bar{1}]$ direction is expected from Eq. (95). Therefore, to measure the dielectric constant, the electric field from an AC-capacity bridge should be applied approximately along the $[10\bar{1}]$ direction. Due to the sample geometry it was only possible to apply the electric field $\sim 35°$ off the $[10\bar{1}]$ direction. For the measurements a frequency of 1 kHz and a voltage of 15 V was used. Only the capacitance of the plate capacitor with the sample in between the plates was measured, which reflects the behavior of the dielectric constant when changing the temperature or the magnetic field. Peaks in the capacitance are expected to coincide with the phase transitions since the dielectric constant diverges at the onset of ferroelectricity [104].

In the above described geometry nice sharp peaks were observed at the transition temperature T_N at zero field (Fig. 5.38), which is in contrast to the very broad features observed in the measurements performed by Yasui *et al.* [177]. They found a broad anomaly at about T_N only for an applied electric field perpendicular to the b direction and parallel to the CuO_4 squares (chapter 5.2.3). For an electric field approximately along the $[10\bar{1}]$ direction they found no anomaly. One can speculate if the actual geometry is the optimal one to observe the ferroelectric phase transition, which would be in contrast to the prediction of Eq. (95), or if a wrong orientation of the crystal in the experiment of Yasui *et al.* [177] is the reason for their poor results.

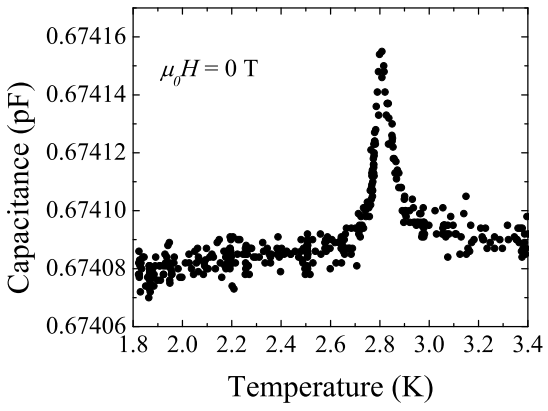

Fig. 5.38: Ferroelectric transition of linarite at zero field.

For an applied magnetic field along the crystallographic b direction the phase boundaries of phase I could be observed as a peak in the capacitance signal using field as well as temperature scans (Fig. 5.39). In the field scan at 1.82 K, which crosses also phase III, only the transition into phase I could be observed. From Eq. (95) at the transition into phase III ferroelectricity is expected due to the helical spin structure. But since in phase III the helix is rotating in the bc plane, the chosen geometry may not well suited to observe a ferroelectric transition. Only the component of the polarization pointing along the direction of the electric field can be detected, which means that the expected signal would be weak. The signal from the transition into phase I might be too strong to observe the weak signal from phase III in the field scans. Therefore, additional temperature scans were performed to check whether the phase boundary from the sine wave modulated phase V (without ferroelectricity) into phase III is visible. At 2.85 T and 2.90 T weak peaks could be observed indicating the helical spin structure in phase III (Fig. 5.40, left hand side). As it was expected no ferroelectric signal was observed at the transitions into the collinear phases IV and V.

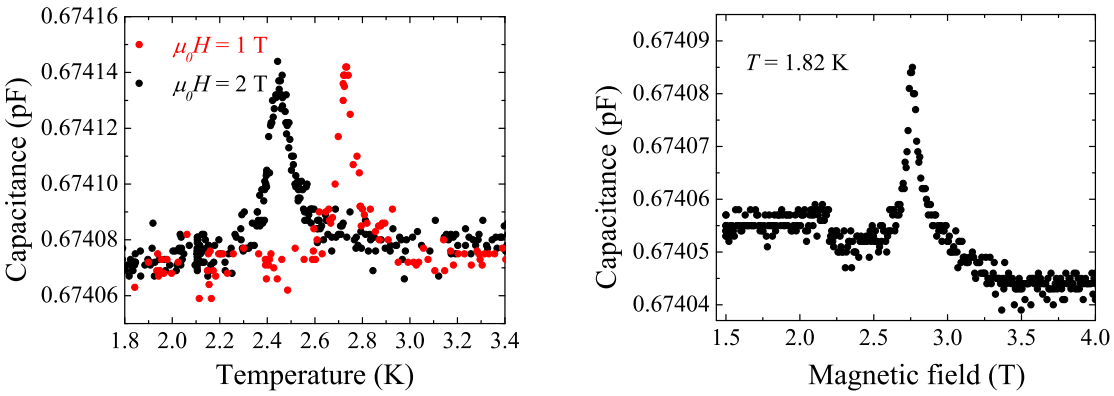

Fig. 5.39: Representative plots of the phase boundaries into the ferroelectric phase of linarite, which agree with the boundaries of phase I. Left: temperature scans at 1 T and 2 T; Right: field scans at 1.82 K. The scan at 1.82 K crosses phase III, but only the transition into phase I is visible.

Field sweeps were performed at 300 mK for increasing as well as for decreasing fields (Fig. 5.40, right hand side). For an increasing field a sharp but weak peak at 2.58 T was observed indicating the transition into region II. No further transitions were found within the resolution which could be allocated to a transition into phase IV. Therefore, the spin structure of phase I has definitively changed substantially at the transition into region II. About a possible second transition for an increasing magnetic field no definite conclusion can be drawn. As the observed peaks at 2.5 T are already very small, another transition might not be observable within the resolution. It should be emphasized that the dielectric properties were only measured with an electric field applied along a certain direction. Thus, there are two possibilities. At the transition at 2.5 T a change of the rotating plane of the helix can occur similar as it was found for phase III or the spin structure could change into a collinear structure.

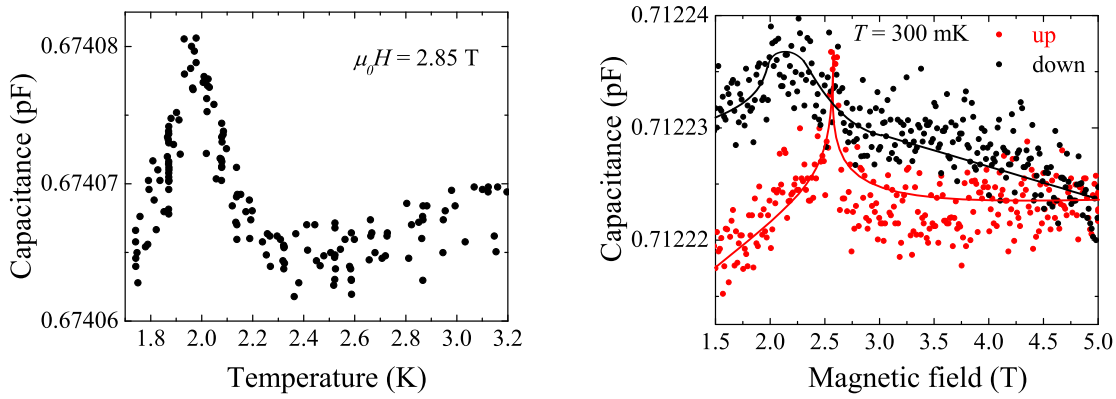

Fig. 5.40: Left: Temperature scan at 2.85 T, which shows a peak at 1.95 K indicating the phase boundary between phase III and phase V; right: Field scans for an increasing and decreasing field at 300 mK. For an increasing field a clear transition indicates the transition from phase I into region II, while for a decreasing field a weak broad feature was observed. Lines are guides to the eye.

For a decreasing field only a very weak and broad anomaly was found at about 2.2 T, which could correspond to the transition into phase I again. This broader peak for the down sweep agrees with the broader peak found in the down sweep of the magnetocaloric effect measurements. Furthermore, a hysteresis between up and down sweep is present as it was observed in the magnetocaloric effect data.

Interestingly, the sharp peak for an increase of the field could not be observed in the temperature range between 1.2 K and 0.47 K. Probably the peak is smaller than the resolution of the instrument since in the magnetization data a clear step was observed for 0.63 K and 0.99 K.

All in all, these data cannot completely confirm the model of Eq. (95), since due to the sample geometry an electric field could only be applied 35° off the direction, where the largest effect is expected. Nevertheless, the measurements in an applied magnetic field showed, that the ferroelectric transitions coincide perfectly with the phase boundaries of the helical phases. That confirms that the helical spin arrangement is closely connected to the ferroelectricity.

5.5.6 Magnetization Measurements ($H \perp b$)

In order to obtain magnetization data for applied magnetic fields perpendicular to the b axis at temperatures down to 100 mK, a similar set-up was used as described in section 3.4.2. Here, the small silicon cantilever could not be used as the sample causes such a strong torque to the cantilever that the cantilever touches the lower plate at fields of about 4 T due to the anisotropy of the sample. Therefore, a more stable copper cantilever was used in combination with a bigger sample (sample IIc). The field was applied roughly perpendicular to the $(\bar{1}01)$ plane.

The magnetization shows three clear kinks, which are more pronounced in the derivative (Fig. 5.41). The three features are also prominent in the torque signal without gradient field (not shown) indicating that these features are not artifacts. It seems also that they cannot be inter-

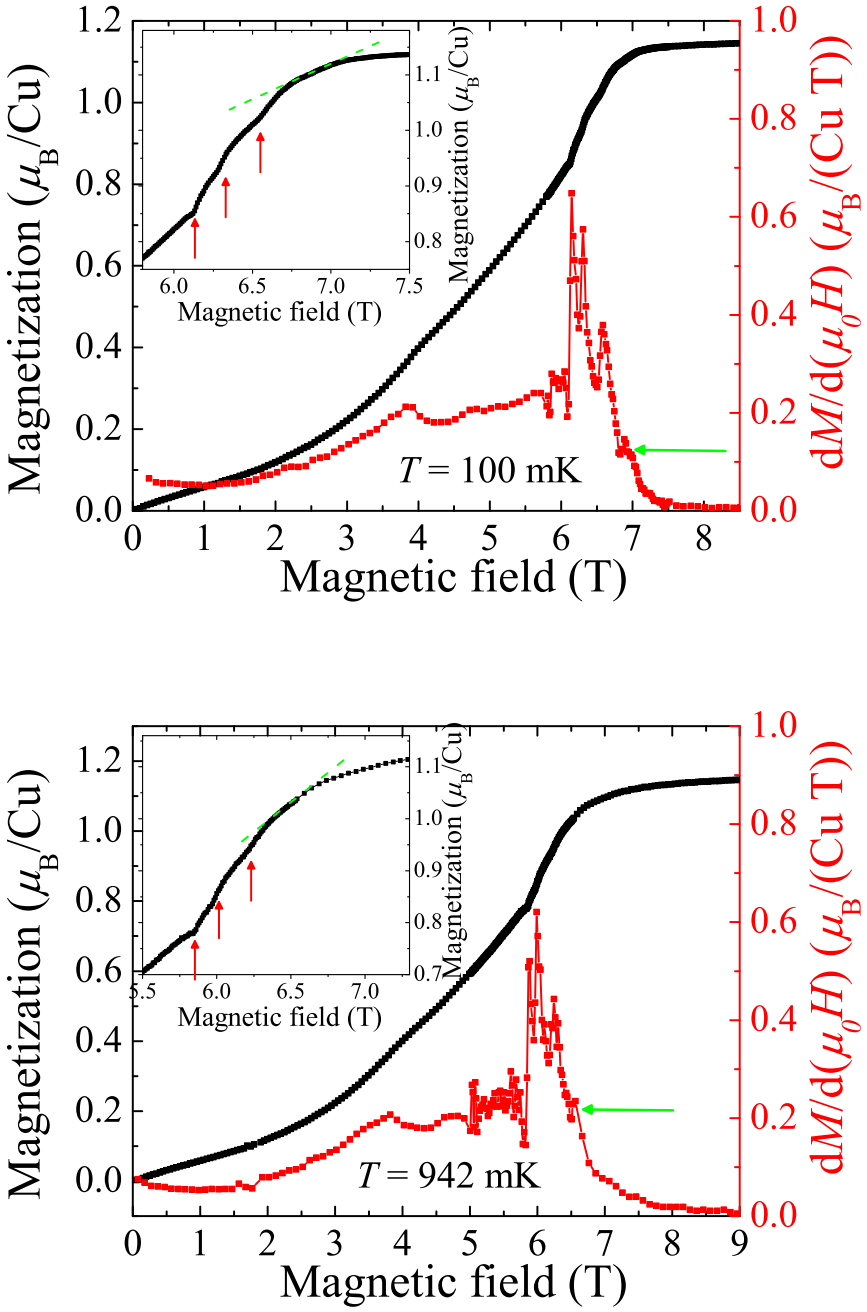

Fig. 5.41: Magnetization data of linarite for applied magnetic fields perpendicular to the b axis at 100 mK (upper panel) and 942 mK (lower panel) and its field derivative. The inset shows a zoom-in of the magnetization curve just below the saturation. Red arrows mark the transition fields, while the green arrow shows a region, in which the magnetization rises at a nearly constant rate before the saturation is reached. The magnetization curves are normalized to the saturation value determined in Ref. [198].

preted as one feature of three grains with different orientations as the temperature evolution of the amplitude of the peaks in the derivative are different (compare the upper and lower panel in Fig. 5.41). At low temperatures, e.g. at 100 mK, the first peak of the derivative is the largest.

At higher temperatures the first peak decreases, while the second peak increases. At 942 mK the second peak is larger than the first one. Furthermore, the first and the third peak are separated from each other by a too large field difference to explain the occurrence of the third peak with a large mosaicity of the crystal.
Close to the saturation a region was observed, in which the slope of the magnetization is nearly constant (green dashed line and green arrow in Fig. 5.41), before at the saturation field the magnetization shows a small kink.
All these features are more pronounced at low temperature. Especially the small kink just below the saturation is only seen for temperatures up to 1.6 K. With higher temperature the curves become rounder, which is shown in Fig. 5.42 (left panel). Interestingly, the torque signal (measurement without gradient field) looks similar to the data obtained for an applied magnetic field along the b direction (see Fig. 5.23). At about 3 T a round minimum is observed below the transition temperature, while for a magnetic field parallel to the b axis a sharp minimum indicates the phase transition into phase III with a reorientated helix. This similarity suggests that also for an applied field perpendicular to the b axis a reorientation occurs. In contrast to the field direction $H||b$, this could be a continuous process and not a spin-flop. The curves of the torque signal above the transition temperature do not show such a minimum, which is in agreement with this interpretation.

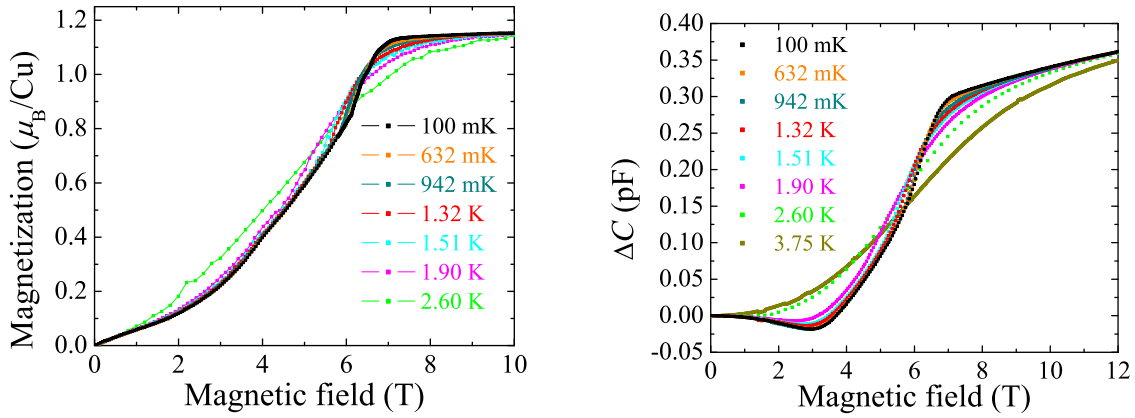

Fig. 5.42: Magnetization curves at different temperatures (left) and torque signal at different temperatures (right) for linarite. The magnetization curves are normalized to the saturation value determined in Ref. [198]. A round minimum of the torque signal is present for temperatures below the transition temperature.

Angular Dependence

In order to compare the phase diagrams for different sample orientations, the angular dependent magnetization was measured using the PPMS VSM at a temperature of 1.8 K. For these measurements sample IId was rotated in the a^*b plane (a^* denotes the direction, which is perpendicular to the bc plane). Fig. 5.43 (left panel) shows the derivative of the magnetization. For fields parallel to the b axis three transitions can be observed as expected. These are transitions from phase I into phase III, from phase III into phase IV, and from phase IV into phase V. (The transition into the paramagnetic regime is not observable at this temperature.) For a tilt of 16° a remarkable shift of the second transition to higher fields as well as a shift of the third transition to lower fields is observed. For larger tilts these trends are followed until at 29° the third transition is no longer visible. The shift of the second transition, however, is observable up to 90°. Therefore, phase III increases at the cost of phase IV with increasing angle. In contrast, the first transition is shifting only very slightly and vanishes at tilts larger than 36°. The three transition fields were plotted versus the tilting angle in Fig. 5.43 (right panel). Only the solid black lines are results from the magnetization curves, all other lines are suggestions. These could explain the low temperature magnetization data. Thus, the feature at about 3 T observed in the torque signal could be a continuous reorientation of the helix as mentioned above. The first phase transition in the low temperature magnetization data ($H \perp b$) could be a transition into a collinear phase similar to phase IV. The second transition would correspond to the transition into the sine wave modulated phase V. The region between phase V and the saturation will be discussed in the following chapter. The interpretation of the different features in the magnetization data are preliminary. For a final interpretation e.g. neutron diffraction measurements would be helpful.

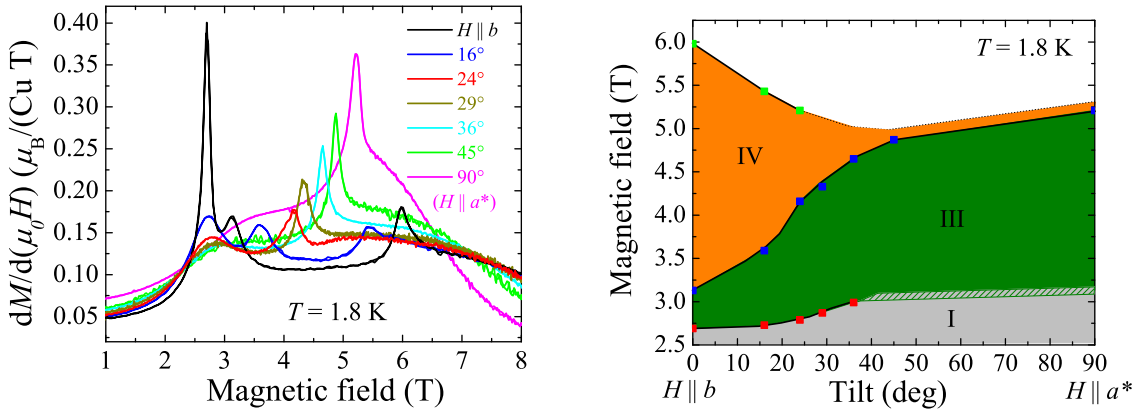

Fig. 5.43: Angular dependence of the derivative of the magnetization of linarite measured at a temperature of 1.8 K (left) and the shift of the transition fields (right).

5.6 Discussion

The spin structure of the ground state of linarite was determined as incommensurate and helical, as it was found for all other known materials belonging to the *nn fm-nnn afm* systems with a coupling ratio $\alpha < -1/4$. The behavior of these other systems in an applied magnetic field was investigated in more detail only for the compounds $LiCuVO_4$ and $LiCu_2O_2$. These systems show several similarities with linarite but also differences. To compare the properties of linarite with other *nn fm-nnn afm* systems the magnetic phase diagrams of the two aforementioned compounds are briefly sketched in the following.

$LiCuVO_4$ can be described as a spin chain with competing nearest and next nearest neighbor interactions. The exchange constants were discussed controversially in the past. While Enderle *et al.* proposed the next nearest neighbor interactions to be stronger than the nearest neighbor interactions [53], Sirker *et al.* and Drechsler *et al.* found out that the nearest neighbor interaction is stronger, leading to an α ratio of 0.5–0.75 [171, 205]. For temperatures of 2.1 K the system shows a transition into a long-range ordered state, where the spins rotate in the *ab* plane [54]. When applying a magnetic field along the *a* or *b* direction a spin-flop transition was observed at about 2.5 T by means of NMR measurements [160]. The spins still are forming a helix in the spin-flop phase, but the rotating plane was then found to be perpendicular to the applied magnetic field (see Fig. 5.44). For fields of about 7 T another phase transition was found for all field directions. This phase was discussed in terms of a sine wave modulated structure with spins all pointing along the field direction [161].

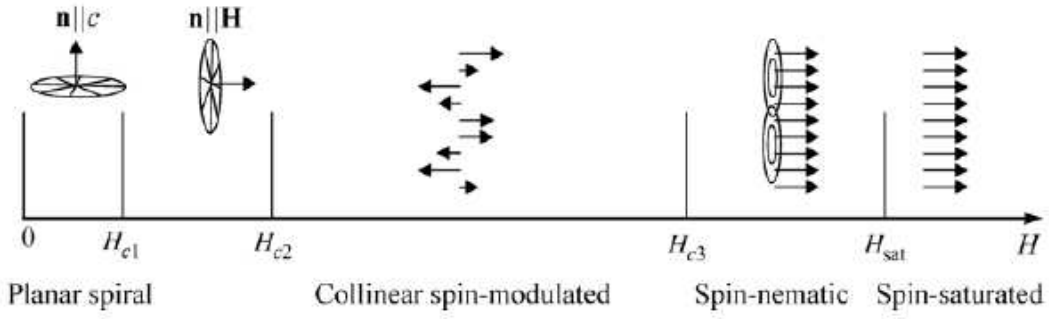

Fig. 5.44: Schematic phase diagram of $LiCuVO_4$ as published by Svistov *et al.* [162]. The transition at $\mu_0 H_{c1} = 2.5\,\mathrm{T}$ was observed only for fields along the *a* and *b* direction. The transitions $\mu_0 H_{c2} \approx 7\,\mathrm{T}$ and $\mu_0 H_{c3} \approx 47\,\mathrm{T}$ were found for all field directions.

For fields close to the saturation a change in the slope of the magnetization curve was observed, which was attributed to a transition into a spin nematic phase [162]. The corresponding magnetization data are depicted in Fig. 5.45. Between the field labeled by H_{c3} and the saturation field H_{sat} the region was characterized as a nematic phase. The magnetization shows a small kink at the saturation field, while in the derivative a small step-like feature is observed. The interpretation was based on predictions about a spin nematic phase in this material made by Zhitomirsky *et al.* [158]. Only recently, a neutron scattering study showed features of a bound

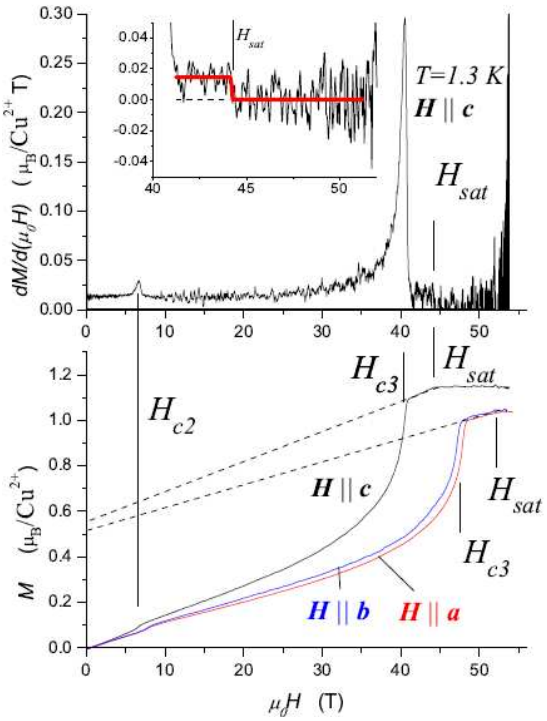

Fig. 5.45: Magnetization curves of $LiCuVO_4$ as published by Svistov *et al.* [162].

quadrupolar phase in the field regime between ∼8 T and 14.5 T [206]. Within this study a shift of the incommensurate propagation vector stemming from a spin structure with spins pointing along the applied magnetic field was found. The shift could be described according to the relation

$$k_{IC} = \left(1 - \frac{M(H)}{M_{\text{sat}}}\right)\frac{\pi}{p}, \tag{98}$$

where $M(H)$ is the magnetization curve, M_{sat} the saturation magnetization, and $p = 2$. This behavior was predicted for the wave-vector of the longitudinal spin-correlations in 1D multipolar phases [52]. In these phases two types of correlations are important: the incommensurate longitudinal spin correlation and the multipolar correlation like nematic, triatic, or quartic correlation. Depending which correlation dominates, the phase is either a spin density wave phase or a nematic (triatic, quartic) phase, which can be characterized as condensation of bound p-magnons. For weak interchain couplings these phases can order three-dimensional [157]. In this case the wave vector of the SDW ordered phase is expected to follow the same behavior as described by Eq. (98) with a modulation along the field direction [51, 157].

The shift in propagation vector found for $LiCuVO_4$ was interpreted therefore as a proof of the presence of quadrupolar correlations. Furthermore, a broadening of the magnetic Bragg peaks was found at the transition field into this phase, which was taken as a proof that the order parameter is not dipolar. It was argued that the phase transition into this phase, which was observed in heat capacity data as a sharp peak, does not stem from a dipolar order parameter, but that the phase transition is driven by quadrupolar correlations.

The system $LiCu_2O_2$ can be described by a chain with an α ratio of $\sim$0.54 [55, 56]. In zero field the compound shows two phase transitions. For temperatures between T_{c1} =24.5 K and T_{c2} =22.8 K the spin structure was found to be sine wave modulated [195], while for temperatures $T < T_{c2}$ a helical arrangement was found. The rotating plane of the spins in the ground state was discussed controversially. While Masuda *et al.* first found the rotating plane of the helix to be in the *ab* plane [164], Seki *et al.* suggested the *bc* plane to be the rotating plane [175]. Later, Kobayashi *et al.* found the rotating plane to be parallel to the *c* axis and parallel to a vector in the *ab* plane which is 45° off the *b* axis [195]. Furthermore, the spin-helix was found to be elliptical with a larger component along the *c* axis. For applied magnetic fields along the *b* axis a sample dependent phase transition was found [179] (Fig. 5.46, left panel). It was argued that this could be a spin-flop transition similar to that found for $LiCuVO_4$, where the rotation plane of the helical spin-arrangement is supposed to flop into the plane perpendicular to the field direction [162, 179]. For higher fields along the *c* direction a second transition was found, which was discussed in terms of a sine wave modulated spin structure [179] (Fig. 5.46, right panel).

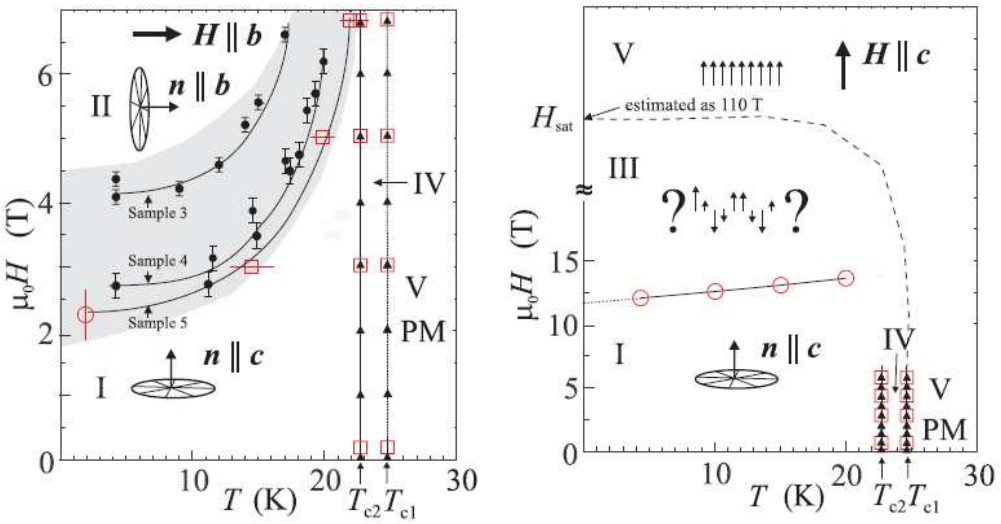

Fig. 5.46: Phase diagrams of $LiCu_2O_2$ for applied magnetic fields along the *b* direction (left) and along the *c* direction (right). Figures are taken from Ref. [179].

In both materials a spin-flop transition was observed at which the rotating plane of the spin-helix flopped to the plane perpendicular to the field direction. In linarite for applied fields along the *b* direction, however, such a spin-flop into the *ac* is not possible according to group theoretical aspects due to the monoclinic crystal symmetry. As mentioned in section 5.4.1 from the symmetry analysis two one-dimensional irreducible representations Γ_1 and Γ_2 were obtained. The Fourier coefficients of Γ_1 for the site 2a are $S_{k11} = (u, v, w)$ for the atom Cu11 and $S_{k12} = (-u, v, -w)$ for the atom Cu12; for Γ_2 the coefficients are $S_{k11} = (u, v, w)$ and $S_{k12} = (u, -v, w)$, respectively. Thus one finds a collinear antiferro- or ferromagnetic ordering within the monoclinic *ac* plane. A helical magnetic structure can only be described by a reducible representation $\Gamma = \Gamma_1 \oplus \Gamma_2$,

where the Fourier coefficients of Γ_1 are $S_{k11} = (0, v, 0)$ and $S_{k12} = (0, v, 0)$ (along the monoclinic b axis) and the coefficients of Γ_2 are $S_{k11} = (u, 0, w)$ and $S_{k12} = (u, 0, w)$ (in the monoclinic ac plane). In this case, one component of the helix is in the monoclinic ac plane and the other is parallel to b. For this reason the spins can only arrange in a *collinear* spin structure in the ac plane. Nevertheless, linarite shows a kind of spin-flop. It is realized in a two-step process for temperatures down to 1.4 K: in phase III the spins start to flop into the ac plane forming a collinear spin arrangement, while a helical spin structure is retained forming a coexisting phase. It seems however that it is energetically more favored to change the helix into a circular helix with the spinning plane in the bc plane rather to maintain the elliptical helix with the large moment along the field direction. For large enough fields all spins are flopped into the ac plane forming the collinear phase IV. In the context of a spin-flop transition, the magnetization data can be understood as well. It was shown in section 5.5.2 that the longitudinal magnetization component shows a step at the transition at 2.5 T, while the transverse component exhibits a dip. A similar behavior is expected for a two-sublattice collinear antiferromagnet with an external applied magnetic field, which is applied slightly off the easy-axis [207]. In the case of linarite, it is most likely that the magnetic field was not applied exactly along the easy-axis (b axis), but was off by $\sim \pm 5°$, which could lead to such a dip in the transverse magnetization component as it was observed.

The spin-flop process was also investigated by NMR measurements performed by Markus Schäpers (Fig. 5.47). In phase I a spectrum with eight lines was obtained (two of them are hidden by other more pronounced peaks) indicating a complex spin structure. Furthermore, Markus Schäpers found in the field range of phase IV a simpler spectrum with only four lines, which could be the spectrum of a collinear spin structure. In phase III two spectra were found: one spectrum shows the characteristic lines of the spectrum found in phase IV. The other is complex as the spectrum found in phase I, but differs from that. This is in agreement with the modified helix and the collinear spin structure of phase IV, which was found by neutron diffraction in phase III. Furthermore, for an increasing magnetic field, the volume of the spectrum with four lines (commensurate) increased while the other decreased, which seems to be similar to the behavior found by neutron diffraction [188].

Surprisingly, no multicritical point was observed in the phase diagram as it would be expected for an ordinary spin-flop process in an antiferromagnet [208]. The coexisting phase III is not entirely enclosed by the phase boundaries of the pure phases I and IV. Instead, it seems that it has a true boundary to phase V. One explanation of the absence of a multicritical point could be the presence of the sine wave modulated phase V. The ground state phase as well as the spin-flop phases does not border on the paramagnetic regime as it is usually assumed for a simple spin-flop transition, which is described for example in Ref. [208], but it borders on phase V. Apparently the situation is more complex due to phase V. Furthermore, phase III is not a coexistence of phase I and phase IV but a coexistence of a phase, which is just similar to phase I, and phase IV. Probably, phase III should be characterized by a distinct helical structure rather than by a

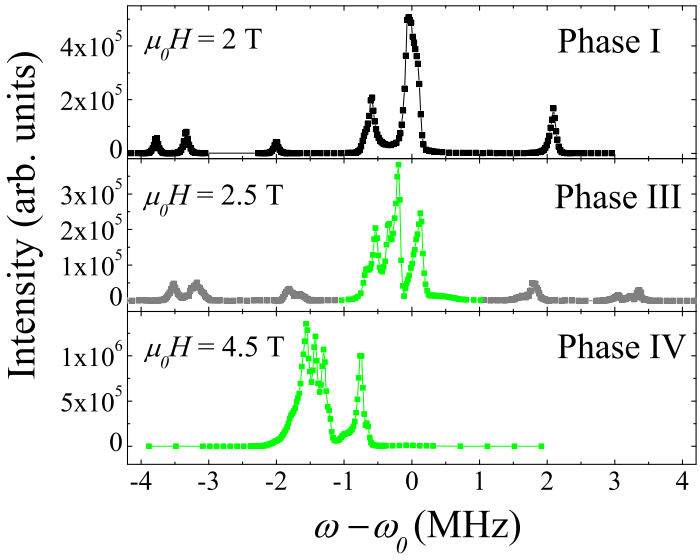

Fig. 5.47: ^{1}H-NMR spectra of linarite from Markus Schäpers [188]. In phase I eight lines are present, where two of them are hidden by other stronger lines. In phase III 12 lines are observable in the spectrum. Four of them (green) show the same characteristics as the four lines found in phase IV. The other eight lines (gray) remind of the lines observed in phase I.

coexistence.

For temperatures below 1.4 K the spin-flop occurs directly, so that no intermediate phase develops. At the phase boundary from phase I into phase IV at temperatures below ∼1 K a region was found, in which disequilibrium effects are dominant. At temperatures below ∼0.4 K additional features could be observed for an increasing magnetic field in the magnetization as well as in the magnetocaloric effect data, which defined region II. Magnetocaloric effect measurements lead to the conclusion that pinning on defects might be the reason for the disequilibrium effects. Due to the additional step present in the magnetization data at 250 mK at the boundary of region II, it seems that the magnetic structure is pinned in this region in such a way, that parts of the crystal change the spin structure at 2.5 T into the collinear structure of phase IV, while other parts still show the spin structure of phase I. Unclear are the details of the pinning process. In principle, the spin structure can be pinned by magnetic impurities. In this case, however, a Curie-tail would be expected in the susceptibility data, which was not observed. Another possibility could be a coincidence of the magnetic phase transition with a structural deformation, which can be pinned on nonmagnetic impurities. Further investigations are needed to test whether such a structural deformation takes place in linarite.

Let us now focus on phase V. Linarite shows at zero field a direct transition into the long-range ordered phase with a helical spin arrangement similar to $LiCuVO_4$, but in contrast to $LiCu_2O_2$. $LiCu_2O_2$ shows two successive phase transitions: one transition into a phase with sine wave modulated structure and for lower temperatures a transition into a helical phase. For linarite,

the phase transition at zero field into the long-range ordered ground state was found to be of first order due to the two irreducible representations needed for describing the helix. That suggests that the helical and sine wave modulated structure have the same energy at zero field [85]. For an applied magnetic field however, the sine wave modulated structure is energetically favored in the higher temperature region so that a sine wave modulated structure is developing, which is reminiscent of the case of $LiCu_2O_2$. This sine wave modulated structure, which was labeled with phase V, hardly shows any features in the thermodynamic properties. It seems that phase V is not an ordinary spin-wave-modulated long range ordered phase. Furthermore, while the features indicating phase V become more pronounced for low temperatures, in the field region of about 4 T in the high temperature region no signatures of a phase transition into phase V were found in the thermodynamic data. Only neutron diffraction and the NMR technique show evidence of phase V in this field regime.

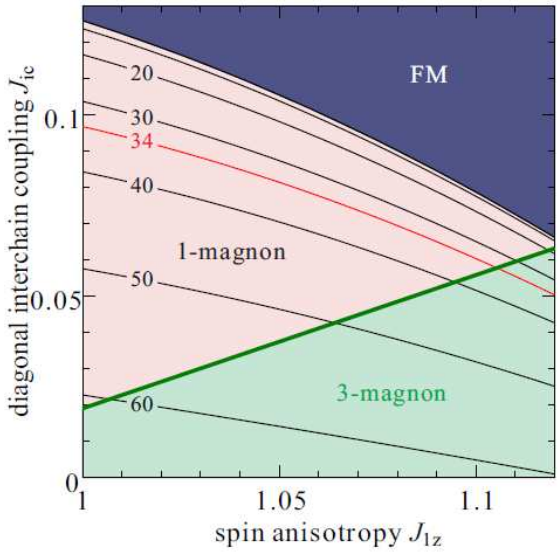

Fig. 5.48: Phase diagram regarding interchain couplings J^{IC} and a uniaxial exchange anisotropy for different α ratios (black lines). The α ratio for linarite is depicted as a red line. For a large anisotropy linarite falls in the range of a 3-magnon bound states. The figure is taken from Ref. [198].

The sine wave modulated structure found in linarite shows a shift of the propagation vector with the magnetic field, similar to $LiCuVO_4$ in the fields above ∼7 T, which was interpreted as a result of quadrupolar correlations. In contrast to $LiCuVO_4$, linarite is predicted to show an octupolar phase, which can be characterized as a condensation of three-magnon bound states, due to the larger α-ratio (see Fig. 5.2). This prediction is only valid for real 1D-systems. For materials with weak interchain interactions these multipolar phases can be destroyed. Easy axis exchange anisotropy however can stabilize these phases dramatically [156]. It was found that linarite exhibits a 10 % easy-axis anisotropy along the b axis, which could lead to a 3-magnon bound (octupolar) phase as it is shown in Fig. 5.48 [198]. If phase V of linarite is dominated by density waves of bound 3-magnons, the shift of the propagation vector measured by neutron

diffraction would follow Eq. (98) with $p = 3$. To test whether this relation describes the data, the magnetization curves measured at 2.1 K were used and k_{IC} was calculated for $p = 2$,3, and 4 (see Fig. 5.49). Since the magnetization curve for 2.1 K shows a phase transition into phase I below 2.8 T, for fields below 2.8 T the magnetization was gathered from the temperature dependent magnetization curves shown in section 5.5.2. Up to 2.8 T the curve for an octupolar phase perfectly describes the shift of the propagation vector. For higher fields, however, they disagree, while for 6 T it seems that they approach each other again. Alike for $LiCuVO_4$, multipolar correlations can explain the shift in the low field regime [206]. In contrast to $LiCuVO_4$, however, no line broadening was found in the neutron diffraction study. The magnetic Bragg peaks in phase V show the same width as the nuclear peaks. However, due to the mosaic spread in the crystal, the peaks are broader than the instrumental resolution and lead to a minimum magnetic correlation length in phase V of only $100 - 200$ Å. Therefore, it could be possible that the correlation length is reduced in phase V compared to the other long-range ordered phases, but it could not be proven. If the correlation length would be indeed only $100 - 200$ Å, the small magnetic moment of $0.44\,\mu_B$ found in phase V could be due to fluctuations. That could be also the reason for the very weak feature at the phase transition observed in the bulk techniques.

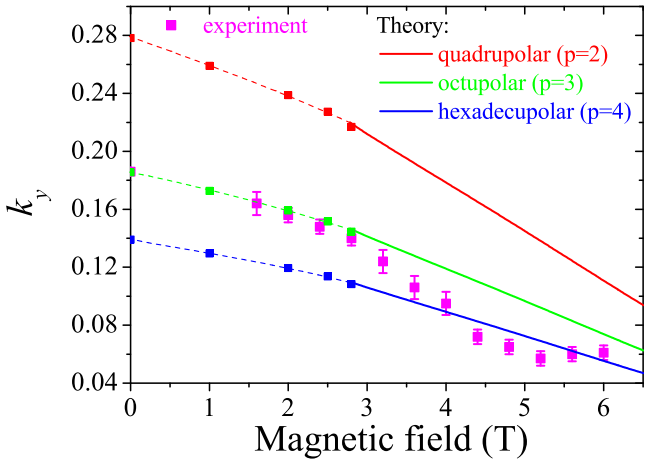

Fig. 5.49: Shift of the propagation vector of linarite compared to the theoretical model for quadrupolar, octupolar and hexadecupolar phases. Theory lines include the magnetization curve at 2.1 K as well as magnetization points obtained from temperature dependent magnetization scans. The propagation vector is given in reciprocal lattice units. For details see text.

A recent theoretical study of Sato *et al.* showed that a long range spin-nematic phase (SN) is accompanied by a 3D spin-density wave phase (SDW) with a shift of the propagation vector according to Eq. (98). In this case, the SDW phase is dominant at low fields extending up to relatively high temperatures, while the SN phase is dominant at high fields close to the saturation at very low temperatures [157]. From this point of view phase V could be a SDW caused by the formation of 3-magnon bound states. Unclear is whether a triatic phase is also present in phase V. One can speculate that such a triatic phase could cause the very small features in the

heat capacity, when it coexists with the SDW phase. That would, however, disagree with the prediction that these nematic or triatic phases can be stabilized only close to the saturation. Unclear is if the presence of strong anisotropy, as in case of linarite, can change the situation, so that a triatic phase can be stabilized even in lower fields. Furthermore, the less pronounced features found in the field region of 4 T remain mysterious. It seems that some kind of fluctuations destroy or suppress the long range order in this regime. Here, further investigations are required. A more promising region to find a triatic phase would be the region close to the saturation for applied magnetic fields perpendicular to the b axis. In this region the magnetization was found to be similar to the data of $LiCuVO_4$ (Fig. 5.45), where a small step in the derivative of the saturation was interpreted as transition of a nematic phase. The reason that such a behavior was not found for applied magnetic fields parallel to the b axis, could be due the fact that the saturation is too close to phase V. An additional small kink would not observable in this case. To test the interpretation of a triatic phase for fields perpendicular to the b axis, a neutron diffraction and NMR study would be necessary.

5.7 Summary

The frustrated spin-chain compound linarite shows several different long-range ordered phases, which were investigated extensively during this study. Linarite undergoes a first order phase transition into a long range ordered ground state at 2.8 K in zero field, which was studied by means of neutron diffraction as well as heat capacity measurements. Thermodynamic measurements such as magnetization and magnetocaloric effect measurements indicated a very rich phase diagram for an applied magnetic field along the crystallographic b axis including four different phases and one hysteretic crossover region.

Neutron diffraction studies showed the variety of the different spin structures present in this material for fields along the b direction. The spin structure in the ground state was found to form an elliptical helix with a magnetic moment of $0.833\,\mu_B$ along the b axis and a moment of $0.638\,\mu_B$ in the ac plane. The rotating plane is parallel to the b axis and $-27°$ off the a axis, which means that it is almost parallel to $[10\bar{1}]$. The first order phase transition into this phase is due to the monoclinic symmetry of linarite and suggests that a sine wave modulated structure has the same energy as the helical spin structure.

For higher magnetic fields a spin-flop transition occurs, resulting in an antiferromagnetic collinear spin arrangement, where the spins have an angle of $-27°$ from the a axis and a magnetic moment of $0.79\,\mu_B$ at 4 T. For temperatures between ∼1.4 K and 1.9 K the spin-flop is realized in a two step process. At 2.5 T the spin helix changes to a circular helix with a magnetic moment of $0.64\,\mu_B$, where the spins rotate roughly in the bc plane. In the same field regime the collinear spin structure develops, so that two spin structures coexist. For higher fields the helix vanishes and only the collinear spin structure remains. Ferroelectric phase transitions were found at the phase boundaries to the ground state phases and the coexisting phase, where a helical spin arrangement was observed, while no transition was found for the collinear ordered phase at higher magnetic fields. That is in agreement with the concept of inverse Dzyaloshinskii-Moriya effect and confirms the spin structures found by neutron diffraction. For temperatures below ∼0.6 K a hysteretic region was found in the magnetization data. For increasing magnetic fields two steps in the magnetization curve were present, while for a decreasing magnetic field only one step could be observed. Similar observations were made by magnetocaloric effect measurements. As this region shows a strong sample dependency, it was interpreted as a region, where pinning effects on defects are essential.

Surrounding the aforementioned phases another phase was found. This one shows an extraordinary behavior. In thermodynamic measurements only weak features could be observed at the phase boundary to the paramagnetic regime. With neutron diffraction small magnetic Bragg peaks were found, indicating a sine wave modulated spin structure with spins parallel to the field direction and a maximal magnetic moment of $0.44\,\mu_B$ at 6 T. Apparently in a magnetic field the sine wave modulated structure is energetically more favorably than the helical structure. When changing the magnetic field, a shift in the propagation vector could be observed, which could

indicate density waves of bound 3-magnons. It remains unclear whether in this material a triatic phase could be also present, which is usually expected very close to the saturation. Since the role of anisotropy is not understood in detail, it gives rise for speculations. It is for example possible that due to the strong anisotropy a triatic phase extends down to lower fields. On the basis of low temperature magnetization data, it was also speculated that such a triatic phase is present very close to the saturation for external applied magnetic fields perpendicular to the b axis.

6 Conclusions

In this thesis the three quasi one-dimensional copper oxide systems azurite, copper nitrate, and linarite have been studied by means of neutron scattering as well as thermodynamic methods.
The diamond chain compound azurite has been taken as an example to explain how the character of the involved orbitals in the magnetic superexchange can influence the magnetic properties. By means of neutron diffraction with polarized neutrons it became apparent that the $d_{x^2-y^2}$ orbitals of the copper atoms participate in the magnetic exchange. For a magnetic field of 9 T applied along the a axis, an induced moment of $0.39\,\mu_B$ was found on the monomer sites, while only $0.07\,\mu_B$ was found for the dimer sites in agreement with a recent NMR study. Furthermore, indications of a small magnetic moment sitting on one of the oxygen atoms was found.
The aim of the investigations of the alternating chain compound copper nitrate was to establish a detailed magnetic phase diagram for applied magnetic fields along the crystallographic b axis. Using neutron diffraction a field induced long-range ordered state was observed, where antiferromagnetically aligned spins lie in the plane perpendicular to the applied magnetic field. Furthermore, a gradual increase of a ferromagnetic alignment of the spins parallel to the field direction was found, which agrees with the concept of Bose-Einstein condensation of triplons. Due to problems with the thermalization of the sample and the lack of beam-time a detailed phase diagram could not be obtained with this technique. Magnetization measurement using a cantilever magnetometer were performed, but alike the neutron diffraction measurements problems with the thermalization were present. This problem could be handled with magnetocaloric effect measurements. For this purpose a new measurement option has been built during this thesis, which allowed magnetocaloric effect measurements at temperatures down to ∼100 mK. The magnetic phase diagram could be mapped out in great detail using this technique. It shows a phase boundary, which has the shape of a symmetric dome, of a field induced long-range ordered state for temperatures below 166 mK and fields between 2.8 T and 4.3 T. Furthermore, features in the magnetocaloric effect data at temperatures up to 220 mK were discussed in terms of a crossover into a Luttinger liquid regime for the first time. By means of simulations using the method of exact diagonalization the experimental data in the temperature regime above the long-range ordered phase could be understood and complemented using a one-dimensional model containing only two exchange constants. During this thesis it turned out, that copper nitrate could be used as a model material to study the dimensional crossover between one-dimensional and three-dimensional behavior. Since the final proof of the Luttinger liquid is still missing, future studies including inelastic neutron scattering experiments in this field and temperature regime would be worthwhile. Moreover, further information about the weak interchain couplings could be obtained by calculations, which include these interactions and use the detailed experimental phase diagram as a comparison.

The frustrated compound linarite was studied due to the prediction of exotic field induced phases. At zero field a first order phase transition into a long-range ordered state was observed at 2.8 K. In order to investigate the characteristics of this phase transition, the heat capacity had to be measured with very high accuracy, which was only possible with the new measurement option mentioned above. As a complementary method the magnetic ordering transition was investigated with neutron diffraction, where a very good temperature stability was required. For this purpose, a new sample stick has been built for a standard Orange Cryostat, which has a stability of ±0.5 mK. Thermodynamic measurements have been used to map out the phase diagram for applied magnetic fields along the chain direction. The determination of the phase diagram was carried out within a collaboration, where this thesis concentrated on the magnetization and magnetocaloric effect measurements in the more demanding temperature region below 1.8 K. Four different magnetic phases have been detected. By means of neutron diffraction the spin structures in these phases have been determined. In the ground state (phase I) the spins form an elliptical helix, where one component is parallel to the b axis and the other approximately parallel to the $[10\bar{1}]$ direction. Ferroelectric transitions were found, which coincide with the magnetic phase boundary of phase I, pointing out that this helical phase is a multiferroic phase. A complex spin-flop process was observed for applied magnetic fields larger than 2.5 T and temperatures above 1.4 K, which is realized in two steps. At the first step the spin-helix changed to a circular helix with the rotation plane being the bc plane. At the same field a collinear spin arrangement with spins lying in the ac plane develops. At the second step the helical spin arrangement vanishes and only the collinear spin structure remains. At temperatures below 1.4 K the spin-flop was realized in only one step. Below 0.6 K a hysteretic region (region II) at about 2.5 T was observed, which was attributed to pinning effects. Moreover, in the high temperature region an extraordinary sine wave modulated spin structure has been detected (phase V). In this phase the wave vector is shifting with the magnetic field. This phase was interpreted in terms of a spin density wave phase, which can be described with density waves of bound three-magnons. Linarite would be the first material, which shows such a phase. Magnetization measurements with an applied magnetic field perpendicular to the chain direction revealed a small kink close to the saturation, which could probably be a sign of a triatic phase. Summarizing, although linarite can be described by a relatively simple model with basically two exchange constants, it shows several different phenomena such as multiferroicity, a complex spin-flop transition, pinning effects, and probably density waves of 3-magnon bound states, which are all experimentally accessible in contrast to other frustrated spin chains such as $LiCuVO_4$ and $LiCu_2O_2$. Some of these properties are definitely worthwhile to investigate further. In region II the pinning process can be studied with neutron diffraction measurements, which can give evidence whether phase I survives in some domains of the sample for fields larger than the transition at ∼2.5 T. Furthermore, a detailed investigation of the nuclear structure could show if a structural deformation accompanies the magnetic transition in order to decide whether the nuclear structure is what pins on defects. Phase V also leaves room for further investigations as it is still unclear if besides the spin density

phase also a 3D-ordered triatic phase is present. Possibly a triatic phase is only observable for applied magnetic fields perpendicular to the b axis. Furthermore, a weakening of the magnetic Bragg peaks in phase V in the range of 4 T was observed, which is not understood up to now.

A Appendix: Heat Capacity and Magnetocaloric Effect Measurement Option

The heat capacity option for temperatures down to 300 mK was constructed during this thesis, and which was can also used for magnetocaloric effect measurements down to 74 mK. The option was designed after Klaus Kiefer's device for temperatures down to 300 mK [98].
The calorimeter, which is described in section 3.2.3 in more detail, consists of a copper frame (bath) which is in good thermal contact with the ^{3}He-pot of a ^{3}He-Stick, or for lower temperatures with the mixing chamber of a dilution refrigerator. The resistivity of the bath-temperature sensor located on the frame is measured by a LakeShore resistance bridge LS370. In the frame a sapphire chip containing a heater, a sample temperature sensor, and the sample is installed, hanging on nylon cords. Since a fast reading of the resistance of the sample sensor is necessary for several methods of measuring the heat capacity, the resistance of the sensor is determined by a Wheatstone bridge and a Lock-In Amplifier described in the following section. Section A.2 depicts the bias power provided to the heater along with the production of small heat pulses. Further, the temperature sensors used for the experiment are characterized in section A.3.

A.1 Measurement of the Sample Temperature

For measuring the resistivity of the sample temperature sensor R_m a Wheatstone bridge and a potential divider is used. The schematic circuit diagram used for the measurement of the sensor resistivity is shown in A.1. The resistances used in these measurements are listed in Tab. 8.
The voltage U_d between the points A and B of the Wheatstone bridge is measured by a Lock-In Amplifier SR380 (Stanford Research), which has a maximum and reasonable minimum excitation voltage of 5 V and 0.1 V, respectively. The voltage U_d is given by the relation

$$U_d = U_{ws}\left(\frac{R_d + R_{dl}}{R_1 + R_d + R_{dl}} - \frac{R_m + R_{ml}}{R_2 + R_m + R_{ml}}\right). \tag{99}$$

R_m is the resistance of the sample sensor, R_d is an adjustable resistance (Burster decade 1423 with a maximum resistance of 111,111 Ω) and R_{ml} and R_{dl} are the resistances of the wires connecting the sensor and the decade, respectively. U_{ws} is the voltage connected at the Wheatstone bridge, which is dependent on the resistances $R_{t,1}$ and $R_{t,2}$ of the potential divider. The resistances R_1 and R_2, which complete the Wheatstone bridge, are chosen to be equal.
The Wheatstone bridge is in balance for $R_d + R_{dl} = R_m + R_{ml}$. Then the voltage U_d is zero. By knowing R_d, R_{dl}, and R_{ml} the resistivity of the sample sensor can be determined very precisely in this case. Therefore, the resistance R_d is chosen in such a way that U_{ab} is nearly zero. If U_d is not exactly zero, R_m can be calculated using Eq. (99). Since the resistances of the wires to the temperature sensor (in the cryostat) are temperature dependent, it is not sufficient to simply fix R_{ml}. The temperature effect can be reduced to a minimum by leading the wires connecting the decade into the cryostat as well so that R_{dl} and R_{ml} behave in the same way. In this case

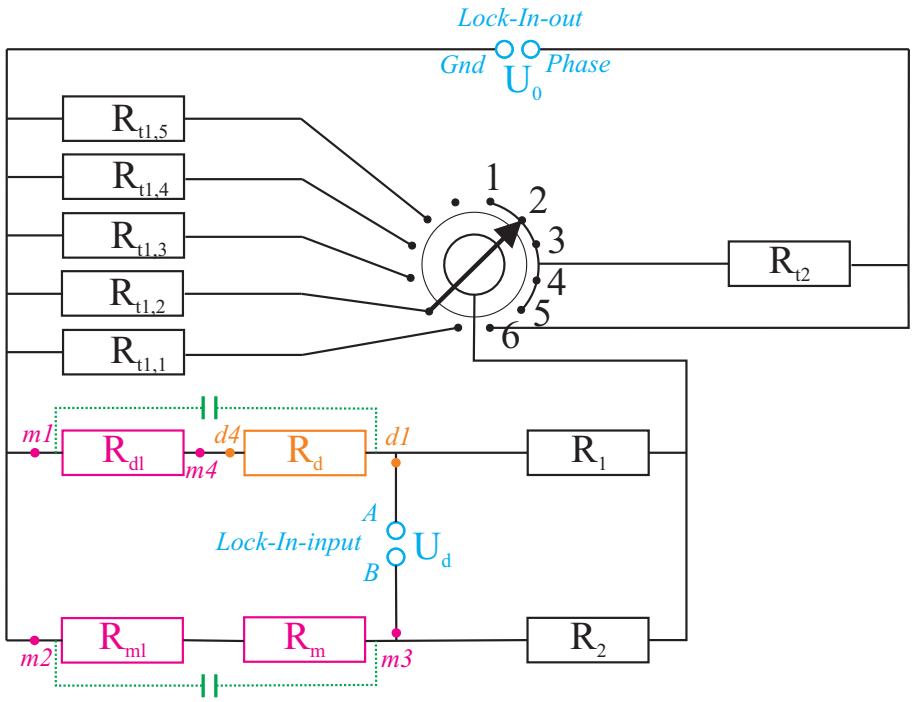

Fig. A.1: Schematic circuit diagram of the resistivity measurement of the sample sensor. The connections $d1$ and $d2$ are used for the decade, while $m2$ and $m3$ are connected to the sample temperature sensor. Wires are connected to $m1$ and $m4$ to obtain the resistivity R_{dl}, which has the same temperature dependent resistivity as the wires connecting the sample sensor R_{ml}. The capacitances added in green reflect the capacitances of the cables and the decade (see section A.1.1).

both legs of the Wheatstone bridge are affected similarly, so that the temperature effect can be neglected.

By changing the resistance R_{t1} the magnitude of the voltage connected at the Wheatstone bridge U_{ws}, and therefore the voltage connected to the temperature sensor, can be adjusted to the resistance of the sensor in a special temperature regime. For the sensor, which was used in this experiment, an excitation voltage of 2 mV was applied at about 2 K and 0.4 mV at about 300 mK. With these excitations the noise is reduced to a minimum and a sensor heating is avoided.

Since the sensor has a resistance of about 350 Ω at 2 K and about 2000 Ω at 300 mK, the optimal resistance is $R_{t1,4}$= 5000 Ω for the "high" temperature regime and $R_{t1,2}$= 500 Ω or $R_{t1,3}$= 1000 Ω for the low temperature regime.

A.1.1 Characterization of the Resistivity Measurement

For testing the accuracy of the resistivity measurement with the Wheatstone Bridge a second decade was used to simulate the temperature sensor. Measurements were taken when the bridge was in balance for different resistances of the sensor decade using an excitation frequency of the Lock-In amplifier of 1836 Hz. Further, the accuracy was tested using Eq. (99) for resistances of the bridge decade, which are up to 50 % larger or smaller than the resistivity of the sensor decade. The relative error $(R_{\text{sensor-decade}} - R_{\text{calc}})/R_{\text{sensor-decade}}$ for the resistance $R_{t1,3}$ up to 10 kΩ

	R (Ω)
$R_{t1,1}$	10.003
$R_{t1,2}$	500.015
$R_{t1,3}$	1,000.00
$R_{t1,4}$	4,999.79
$R_{t1,5}$	9,999.58
$R_{t1,6}$	∞
R_{t2}	20,000.36
R_1	99,919
R_2	99,958

Tab. 8: Burster resistances used for the temperature measurement of the CM8T instrument at HZB.

is shown in Fig. A.2. When the bridge is in balance, the relative error is 0.1–0.2 ‰. For other resistances $R_{t1,i}$ similar errors were found in this resistance range (not shown). Going to higher resistances of the decades the error became more than ten times larger (Fig. A.3, left hand side). It was found that when the bridge should be in balance the error is not the smallest as it is expected and as it was found in the range up to 10 kΩ. The reason is that for higher resistances the capacity of the decades and cables must be taken into account, which are different for the two legs of the bridge. The capacitances of the cables and the decades were measured using a capacity bridge. A capacitance in the range of 150 pF was found for both components with a frequency of 1836 Hz. The capacitance differs for the two legs of the bridge by 37 pF. Adding a capacitor parallel to the resistance of the decades and cables to Eq. (99) the relative error is only 1 ‰ when the bridge is in balance (Fig. A.3, right hand side). Further, by regarding the different capacitances the relative error is the smallest, when the bridge is in the balance. In summary, the resistivity measurement produces an error of 0.1–0.2‰ for resistances up to 10 kΩ without regarding the capacitances of the cables and decades, while for higher resistances the capacitances need to be taken into account leading to an error of 1 ‰. Therefore, no correction is needed for temperatures down to 300 mK since the sample sensor has a resistance of only 2 kΩ for that temperature.

Furthermore, the frequency dependence of the resistance measurement was tested. The Wheatstone bridge was tested in the balance for different resistances by taking into account the capacitances or lack thereof (Fig. A.4). The simple picture of adding a capacitance parallel to the decade and temperature sensor do not describe the full frequency range, but nevertheless the errors when regarding the capacitances are much smaller. For resistances up to 1 kΩ there is no need to consider the capacitances, while for higher resistances the errors are reduced by taking into account the capacitances of the wires and the decades. By regarding the capacitances for a resistance of 100 kΩ the error for frequencies up to 2 kHz is only 1.6 ‰. For higher frequencies however the error is increasing rapidly. Therefore, an excitation frequency of 2 kHz should be the maximum for measuring large resistances.

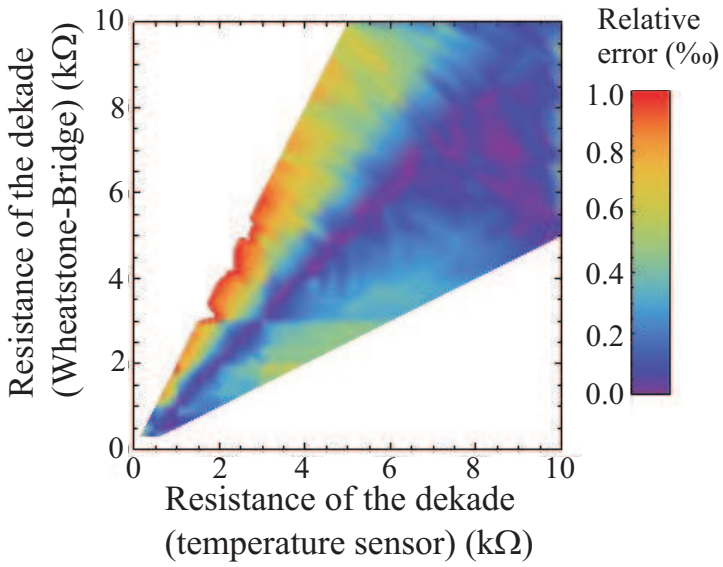

Fig. A.2: Testing the resistivity measurement of the Wheatstone Bridge for $R_{t1,3}$ and resistances up to 10 kΩ. The excitation frequency of the Lock-In Amplifier was 1836 Hz. The relative error, when the bridge is in balance, is 0.1–0.2‰.

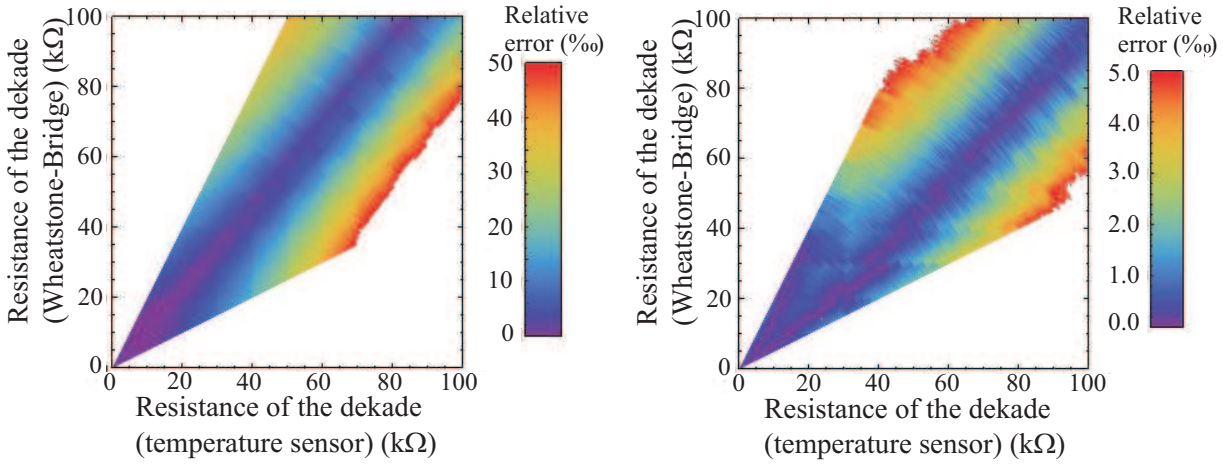

Fig. A.3: The left and right figure show the error of the resistivity measurement for $R_{t1,3}$ and 1836 Hz without and with taking the capacitances of the decade and cables into account, respectively.

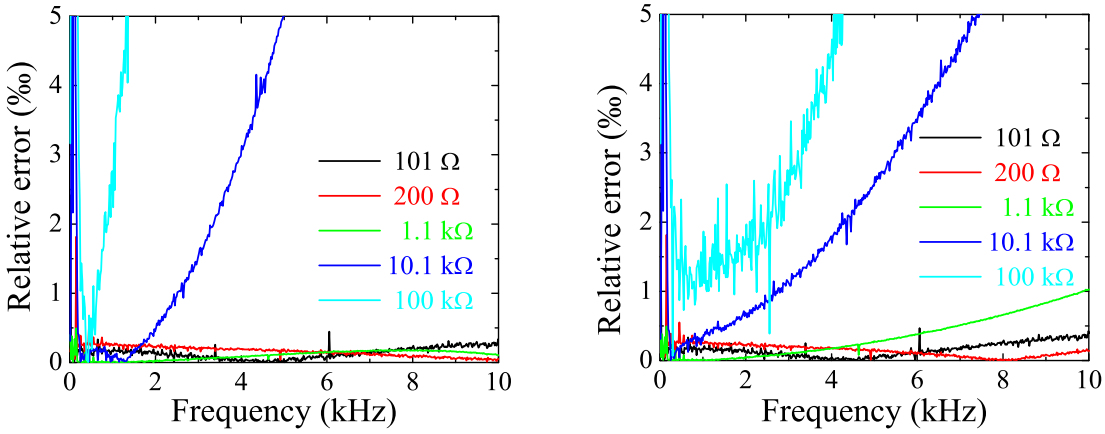

Fig. A.4: Frequency dependent tests of the resistance measurement. The left hand figure displays the experimental error without regarding the capacitances of the decades and cables, while in the figure on the right the capacitances are accounted for. The measurements depicted here were taken using the resistance $R_{t1,3}$. For other resistances the curves are similar.

A.2 Heat Input

For providing a bias power to the heater and creating an additional heat pulse the circuit diagram shown in Fig. A.5 is used. The resistances used are listed in Tab. 9.

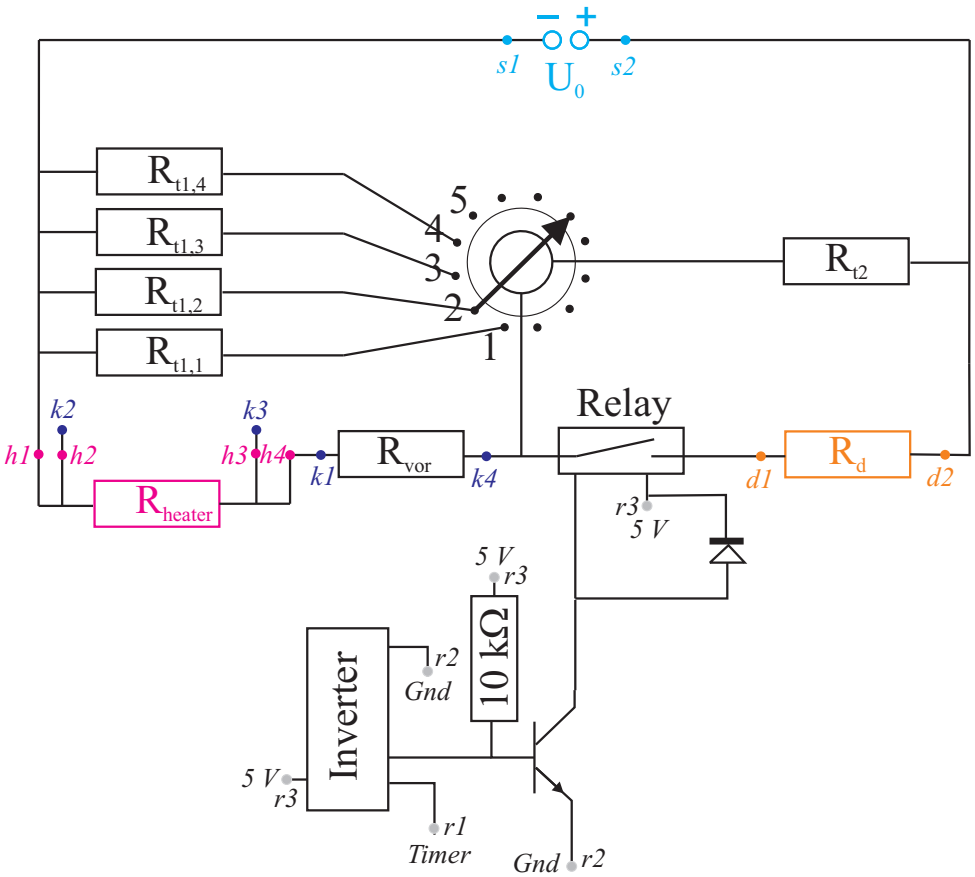

Fig. A.5: Schematic circuit diagram of the heater controller. The connection from the heater box to the heater is given by connections $h1$ to $h4$, while the decade is connected via $d1$ and $d2$. From the timer three connections are used: $r1$, which provides a pulse, $r2$ is ground and $r3$ remains constant at 5 V. One of the Keithleys measures the voltage over the heater R_{heater} ($k2$ and $k3$), while the other measures the voltage defining the current $I = U/R_{\text{vor}}$ ($k1$ and $k4$).

The heater power is provided by a Burster Digistant 4462 power supply with a maximum voltage of 15 V. By changing the resistance R_{t1} the range of the voltage connected to the heater can be adjusted. Further, by closing a relay the resistance R_d is added as a parallel resistance, which leads to an abrupt increase of the heating power. Since the increase of the temperature during the pulse needs to be adjusted, the resistance R_d is realized with a Burster decade 1422 with a maximum resistance of 11111.1 Ω. A timer (USB-CTR-15) provides a pulse in such a way that the voltage between $r1$ and $r2$ is ~ 0 V in the pulse and ~ 4 V before and after the pulse. Since the relay is closed when no voltage is connected, the signal needs to be reversed. This is realized with an inverter (Hex-inverter 74LS05N) and a simple amplifier circuit. An optical relay (AQY221R2S) is used, which closes within 90 µs and opens within 2 µs. During the tests it turned out that the current passing the relay should not be larger than ∼0.3 mA since otherwise

	R (Ω)
$R_{t1,1}$	5.051
$R_{t1,2}$	50.1195
$R_{t1,3}$	500.018
$R_{t1,4}$	4,999.69
$R_{t1,5}$	∞
R_{t2}	1,000.3
R_{vor}	49,974.4
R_2	99,958
R_{relay}	1.29

Tab. 9: Resistances used for the heater box for the CM8T instrument at HZB. Since the relay has a resistivity R_{relay} as well, it is taken into account by adding it to the resistivity of the decade ($R_d = R'_d + R_{\mathrm{relay}}$).

the relay changes its resistance significantly.

The heating power is measured by two Keithley 2000 multimeters (connection $k1$–$k4$). A heat pulse produced by the described heater box is shown in Fig. 3.9 in section 3.2.1.

A.3 Temperature Sensors

For measuring the bath temperature and the sample temperature Cernox^{TM} resistors CX-1010 from LakeShore are used which were fabricated in the same batch to ensure similar temperature and field behavior of the resistivity. Since these types of temperature sensors exhibit a significant field dependence at low temperatures, they were calibrated in several magnetic fields up to 8 T and temperatures down to 76 mK (Fig. A.6) in a dilution refrigerator. The calibration curves are very similar for both sensors. From these field scans fits at each temperature are obtained in order to determine the resistance for any field in the range between 0 T and 8 T at that specific temperature. Further, for all calibration temperatures the resistivity can be obtained so that a simple interpolation of the resistance versus temperature curve gives the temperature for a measured resistance. The calibration of the sample sensor at zero field is shown in Fig. A.7. To the calibration performed in the dilution refrigerator a calibration performed in the ^{3}He-Stick is added. Good agreement was found in the overlapping region. The dimensionless sensitivity $\frac{dR}{R}/\frac{dT}{T}$, which characterizes the sample sensor, is also depicted in the figure.

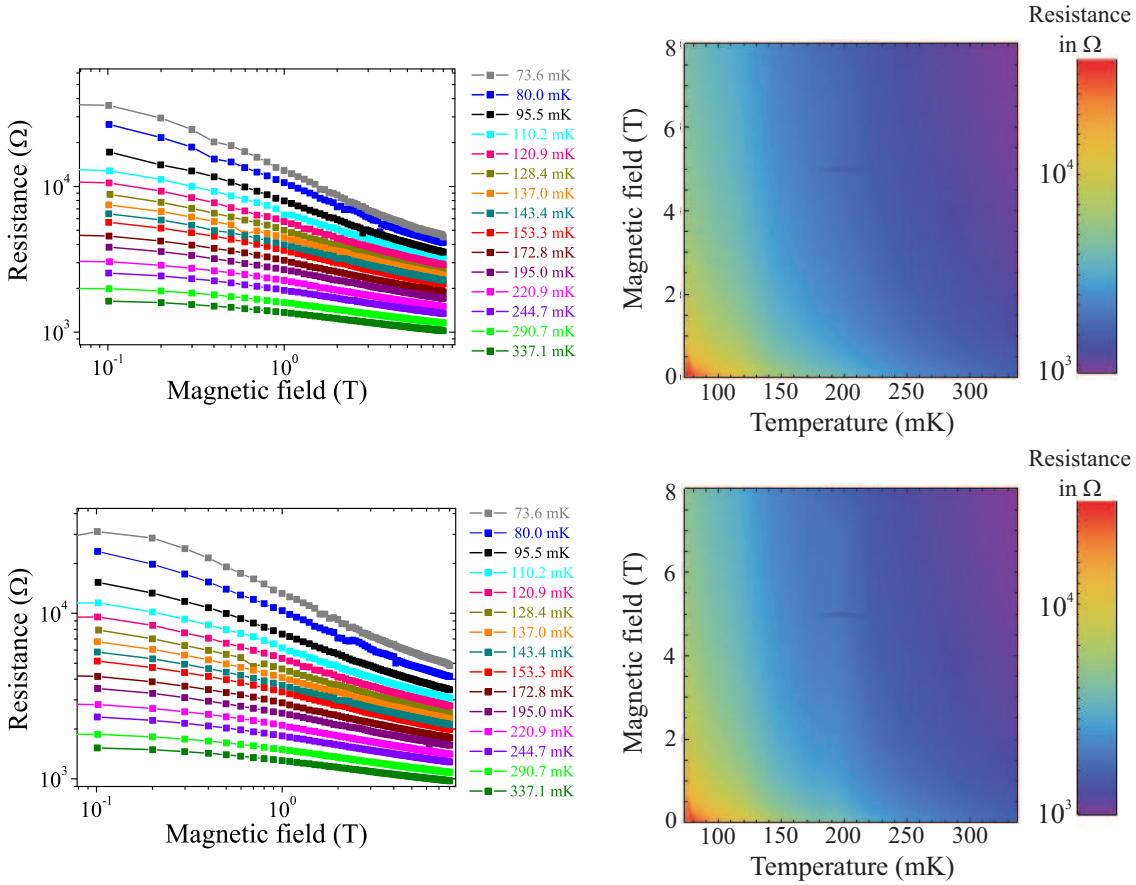

Fig. A.6: Resistances up to 337 mK of the sample sensor (upper figures) and the bath sensor (lower figures) in magnetic fields up to 8 T. Both sensors behave very similar in field and temperature.

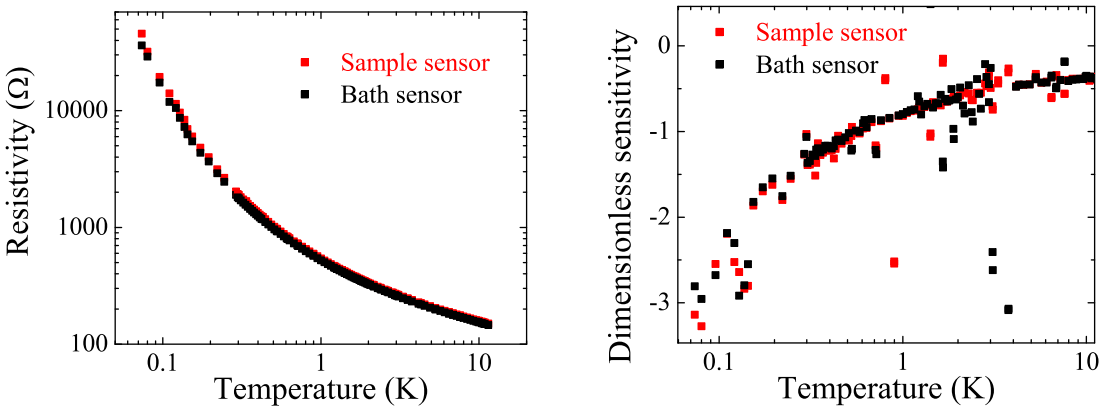

Fig. A.7: Temperature calibration of the sample and bath sensors at zero field (left), dimensionless sensitivity of the both sensors at zero field (right).

References

[1] U. Schollwöck, I. Richter, D. Farnell, and R. Bishop, *Quantum magnetism*, Springer, 2004.

[2] T. Giamarchi, *Quantum Physics in One Dimension*, Oxford University Press, 2004.

[3] H. Bethe, Zeitschrift für Physik **71**, 205 (1931).

[4] J. M. Luttinger, Journal of Mathematical Physics **4**, 1154 (1963).

[5] F. D. M. Haldane, J. Phys. C: Solid State Phys. **14**, 2585 (1981).

[6] F. D. M. Haldane, Phys. Rev. Lett. **47**, 1840 (1981).

[7] S. J. Tans, M. H. Devoret, H. Dai, A. Thess, R. E. Smalley, L. J. Geerligs, and C. Dekker, Nature **386**, 474 (1997).

[8] M. Bockrath, D. H. Cobden, J. Lu, A. G. Rinzler, R. E. Smalley, L. Balents, and P. L. McEuen, Nature **397**, 598 (1999).

[9] J. G. Bednorz and K. A. Müller, Z. Phys. B **64**, 189 (1986).

[10] P. W. Anderson, Science **235**, 1196 (1987).

[11] L. Balents, Nature **464**, 199 (2010).

[12] P. A. Lee, N. Nagaosa, and X.-G. Wen, Rev. Mod. Phys. **78**, 17 (2006).

[13] T.-H. Han, J. S. Helton, S. Chu, D. G. Nocera, J. A. Rodriguez-Rivera, C. Broholm, and Y. S. Lee, Nature **492**, 406 (2012).

[14] F. D. M. Haldane, Phys. Rev. Lett. **50**, 1153 (1983).

[15] F. Haldane, Physics Letters A **93**, 464 (1983).

[16] W. J. L. Buyers, R. M. Morra, R. L. Armstrong, M. J. Hogan, P. Gerlach, and K. Hirakawa, Phys. Rev. Lett. **56**, 371 (1986).

[17] R. M. Morra, W. J. L. Buyers, R. L. Armstrong, and K. Hirakawa, Phys. Rev. B **38**, 543 (1988).

[18] S. E. Nagler, D. A. Tennant, R. A. Cowley, T. G. Perring, and S. K. Satija, Phys. Rev. B **44**, 12361 (1991).

[19] B. Lake, D. A. Tennant, C. D. Frost, and S. E. Nagler, Nat. Mater. **4**, 329 (2005).

[20] T. Ami, M. K. Crawford, R. L. Harlow, Z. R. Wang, D. C. Johnston, Q. Huang, and R. W. Erwin, Phys. Rev. B **51**, 5994 (1995).

[21] N. Motoyama, H. Eisaki, and S. Uchida, Phys. Rev. Lett. **76**, 3212 (1996).

[22] O. Janson, W. Schnelle, M. Schmidt, Y. Prots, S.-L. Drechsler, S. K. Filatov, and H. Rosner, New J. Phys. **11**, 113034 (2009).

[23] R. Nath, D. Kasinathan, H. Rosner, M. Baenitz, and C. Geibel, Phys. Rev. B **77**, 134451 (2008).

[24] A. Belik, M. Azuma, and M. Takano, J. Solid State Chem. **177**, 883 (2004).

[25] M. D. Johannes, J. Richter, S.-L. Drechsler, and H. Rosner, Phys. Rev. B **74**, 174435 (2006).

[26] S. S. Salunke, M. A. H. Ahsan, R. Nath, A. V. Mahajan, and I. Dasgupta, Phys. Rev. B **76**, 085104 (2007).

[27] A. W. Garrett, S. E. Nagler, D. A. Tennant, B. C. Sales, and T. Barnes, Phys. Rev. Lett. **79**, 745 (1997).

[28] T. Waki, Y. Morimoto, C. Michioka, M. Kato, H. Kageyama, K. Yoshimura, S. Nakatsuji, O. Sakai, Y. Maeno, H. Mitamura, and T. Goto, J. Phys. Soc. Jpn. **73**, 3435 (2004).

[29] J. C. Bonner, S. A. Friedberg, H. Kobayashi, D. L. Meier, and H. W. J. Blöte, Phys. Rev. B **27**, 248 (1983).

[30] M. Hase, I. Terasaki, and K. Uchinokura, Phys. Rev. Lett. **70**, 3651 (1993).

[31] B. C. Watson, V. N. Kotov, M. W. Meisel, D. W. Hall, G. E. Granroth, W. T. Montfrooij, S. E. Nagler, D. A. Jensen, R. Backov, M. A. Petruska, G. E. Fanucci, and D. R. Talham, Phys. Rev. Lett. **86**, 5168 (2001).

[32] T. Tajiri, H. Deguchi, M. Mito, S. Takagi, H. Nojiri, T. Kawae, and K. Takeda, J. Magn. Magn. Mater. **272ï¿½276**, 1070 (2004).

[33] H. Ryll, *Magnetic and Caloric Properties of Ideal and Random Bond Quantum Spin Ladders in a Magnetic Field*, PhD thesis, TU Berlin, 2012.

[34] B. Thielemann, C. Rüegg, H. M. Rønnow, A. M. Läuchli, J.-S. Caux, B. Normand, D. Biner, K. W. Krämer, H.-U. Güdel, J. Stahn, K. Habicht, K. Kiefer, M. Boehm, D. F. McMorrow, and J. Mesot, Phys. Rev. Lett. **102**, 107204 (2009).

[35] C. Rüegg, K. Kiefer, B. Thielemann, D. F. McMorrow, V. Zapf, B. Normand, M. B. Zvonarev, P. Bouillot, C. Kollath, T. Giamarchi, S. Capponi, D. Poilblanc, D. Biner, and K. W. Krämer, Phys. Rev. Lett. **101**, 247202 (2008).

[36] T. Nikuni, M. Oshikawa, A. Oosawa, and H. Tanaka, Phys. Rev. Lett. **84**, 5868 (2000).

[37] M. Matsumoto, B. Normand, T. M. Rice, and M. Sigrist, Phys. Rev. Lett. **89**, 077203 (2002).

[38] C. Rüegg, N. Cavadini, A. Furrer, H.-U. Gï¿½del, K. Krï¿½mer, A. W. H. Mutka, K. Habicht, and P. Vorderwisch, Nature **423**, 62 (2003).

[39] M. Jaime, V. F. Correa, N. Harrison, C. D. Batista, N. Kawashima, Y. Kazuma, G. A. Jorge, R. Stern, I. Heinmaa, S. A. Zvyagin, Y. Sasago, and K. Uchinokura, Phys. Rev. Lett. **93**, 087203 (2004).

[40] S. E. Sebastian, N. Harrison, C. D. Batista, L. Balicas, M. Jaime, P. A. Sharma, N. Kawashima, and I. R. Fisher, Nature **441**, 617 (2006).

[41] V. S. Zapf, D. Zocco, B. R. Hansen, M. Jaime, N. Harrison, C. D. Batista, M. Kenzelmann, C. Niedermayer, A. Lacerda, and A. Paduan-Filho, Phys. Rev. Lett. **96**, 077204 (2006).

[42] B. Thielemann, C. Rüegg, K. Kiefer, H. M. Rønnow, B. Normand, P. Bouillot, C. Kollath, E. Orignac, R. Citro, T. Giamarchi, A. M. Läuchli, D. Biner, K. W. Krämer, F. Wolff-Fabris, V. S. Zapf, M. Jaime, J. Stahn, N. B. Christensen, B. Grenier, D. F. McMorrow, and J. Mesot, Phys. Rev. B **79**, 020408 (2009).

[43] K. Okamoto and K. Nomura, Phys. Lett. A **169**, 433 (1992).

[44] F. D. M. Haldane, Phys. Rev. B **25**, 4925 (1982).

[45] M. Hagiwara, Y. Narumi, K. Kindo, N. Maeshima, K. Okunishi, T. Sakai, and M. Takahashi, Physica B **294-295**, 83 (2001).

[46] N. Maeshima, M. Hagiwara, Y. Narumi, K. Kindo, T. C. Kobayashi, and K. Okunishi, J. Phys.: Condens. Matter **15**, 3607 (2003).

[47] H. Kikuchi, H. Nagasawa, Y. Ajiro, T. Asano, and T. Goto, Physica B **284-288**, 1631 (2000).

[48] K. Okunishi and T. Tonegawa, J. Phys. Soc. Jpn. **72**, 479 (2003).

[49] I. P. McCulloch, R. Kube, M. Kurz, A. Kleine, U. Schollwöck, and A. K. Kolezhuk, Phys. Rev. B **77**, 094404 (2008).

[50] S. Furukawa, M. Sato, and S. Onoda, Phys. Rev. Lett. **105**, 257205 (2010).

[51] J. Sudan, A. Lüscher, and A. M. Läuchli, Phys. Rev. B **80**, 140402 (2009).

[52] T. Hikihara, L. Kecke, T. Momoi, and A. Furusaki, Phys. Rev. B **78**, 144404 (2008).

[53] M. Enderle, C. Mukherjee, B. Fåk, R. K. Kremer, J.-M. Broto, H. Rosner, S.-L. Drechsler, J. Richter, J. Malek, A. Prokofiev, W. Assmus, S. Pujol, J.-L. Raggazzoni, H. Rakoto, M. Rheinstädter, and H. M. Rønnow, Europhys. Lett. **70**, 237 (2005).

[54] B. J. Gibson, R. K. Kremer, A. V. Prokofiev, W. Assmus, and G. J. McIntyre, Physica B **350**, E253 (2004).

[55] T. Masuda, A. Zheludev, B. Roessli, A. Bush, M. Markina, and A. Vasiliev, Phys. Rev. B **72**, 014405 (2005).

[56] V. V. Mazurenko, S. L. Skornyakov, A. V. Kozhevnikov, F. Mila, and V. I. Anisimov, Phys. Rev. B **75**, 224408 (2007).

[57] A. U. B. Wolter, F. Lipps, M. Schäpers, S.-L. Drechsler, S. Nishimoto, R. Vogel, V. Kataev, B. Büchner, H. Rosner, M. Schmitt, M. Uhlarz, Y. Skourski, J. Wosnitza, S. Süllow, and K. C. Rule, Phys. Rev. B **85**, 014407 (2012).

[58] H. Kikuchi, Y. Fujii, M. Chiba, S. Mitsudo, T. Idehara, T. Tonegawa, K. Okamoto, T. Sakai, T. Kuwai, and H. Ohta, Phys. Rev. Lett. **94**, 227201 (2005).

[59] J. Kanamori, J. Phys. Chem. Solids **10**, 87 (1958).

[60] J. B. Goodenough, Phys. Rev. **100**, 564 (1955).

[61] P. W. Anderson, *Magnetism I*, chapter 2: Exchange in Insulators: Superexchange, Direct Exchange, and Double Exchange, pages 25–83, Academic Press, New York and London, 1963.

[62] S. Blundell, *Magnetism in Condensed Matter*, Oxford, University Press, 2008.

[63] E. Koch, *Correlated Electrons: From Models to Materials*, chapter Exchange Mechanism, Forschungszentrum Jülich, 2012.

[64] H. A. Kramers, Physica **1**, 182 (1934).

[65] P. W. Anderson, Phys. Rev. **79**, 350 (1950).

[66] P. W. Anderson, Phys. Rev. **115**, 2 (1959).

[67] K. C. Rule, M. Reehuis, M. C. R. Gibson, B. Ouladdiaf, M. J. Gutmann, J.-U. Hoffmann, S. Gerischer, D. A. Tennant, S. Süllow, and M. Lang, Phys. Rev. B **83**, 104401 (2011).

[68] G. Gattow and J. Zemann, Acta Crystallographica **11**, 866 (1958).

[69] F. Zigan and H. D. Schuster, Zeitschrift für Kristallographie **135**, 416 (1972).

[70] E. L. Belokoneva, Y. K. Gubina, and J. B. Forsyth, Physics and Chemistry of Minerals **28**, 498 (2001).

[71] B. Gu and G. Su, Phys. Rev. Lett. **97**, 089701 (2006).

[72] K. C. Rule, A. U. B. Wolter, S. Süllow, D. A. Tennant, A. Brühl, S. Köhler, B. Wolf, M. Lang, and J. Schreuer, Phys. Rev. Lett. **100**, 117202 (2008).

[73] A. Filippetti and V. Fiorentini, Phys. Rev. Lett. **95**, 086405 (2005).

[74] H. Jeschke, I. Opahle, H. Kandpal, R. Valentí, H. Das, T. Saha-Dasgupta, O. Janson, H. Rosner, A. Brühl, B. Wolf, M. Lang, J. Richter, S. Hu, X. Wang, R. Peters, T. Pruschke, and A. Honecker, Phys. Rev. Lett. **106**, 217201 (2011).

[75] R. D. Spence and R. D. Ewing, Phys. Rev. **112**, 1544 (1958).

[76] H. Forstat, G. Taylor, and B. R. King, J. Chem. Phys. **31**, 929 (1959).

[77] M. C. R. Gibson, K. C. Rule, A. U. B. Wolter, J.-U. Hoffmann, O. Prokhnenko, D. A. Tennant, S. Gerischer, M. Kraken, F. J. Litterst, S. Süllow, J. Schreuer, H. Luetkens, A. Brühl, B. Wolf, and M. Lang, Phys. Rev. B **81**, 140406 (2010).

[78] F. Aimo, S. Krämer, M. Klanjšek, M. Horvatić, C. Berthier, and H. Kikuchi, Phys. Rev. Lett. **102**, 127205 (2009).

[79] J. Rodgrigues-Carvajal and C. Frontera, Collection SFN **7**, 41 (2007).

[80] G. L. Squires, *Introduction to the theory of thermal neutron scattering*, Dover Publications, Inc., 1996.

[81] V. F. Sears, Neutron news **3**, 26 (1992).

[82] P. Böni, A. Furrer, and J. Schefer, *Neutron scattering in novel materials*, chapter Principles of neutron scattering, World Scientific, 2000.

[83] S. W. Lovesey, *Nuclear scattering*, Oxford, Clarendon Press, 1987.

[84] D. L. Price and K. Sköld, *Methods of experimental physics, part A, Neutron Scattering*, volume 23, Academic Press, 1986.

[85] J. Rossat-Mignod, *Methods of experimental physics, part C, Neutron Scattering*, chapter 19: Magnetic structures, pages 69–154, Academic Press, 1987.

[86] W. H. Zachariasen, Acta Crystallographica **23**, 558 (1967).

[87] G. H. Stout and L. H. Jensen, *X-ray structure determination*, Wiley, 1989.

[88] G. H. W. Milburn, *X-Ray crystallography*, Butterworth & Co Ltd., 1973.

[89] C. C. Wilson, *Neutron Data Booklet*, chapter 2.3, Institut Laue-Langevin, OCP Science imprint, 2003.

[90] http://www.helmholtz-berlin.de/zentrum/grossgeraete/ber2/kernreaktor_de.html, (20.6.2012).

[91] http://www.ill.eu/reactor-environment-safety/high-flux-reactor/technical-characteristics/, (20.6.2012).

[92] http://www.ill.eu/instruments-support/instruments-groups/instruments/d3/characteristics/, (22.8.2013).

[93] http://www.ill.eu/instruments-support/instruments-groups/instruments/d10/, (19.01.2013).

[94] http://www.helmholtz-berlin.de/pubbin/igama_output?modus=einzel&sprache=en&gid=1698&typoid=39981, (26.2.2013).

[95] http://www.isis.stfc.ac.uk/about-isis/how-isis-works---in-depth4371.html, (20.6.2012).

[96] A. M. Tishin and Y. I. Spichkin, *The magnetocaloric effect and its applications*, Institute of Physics Publishing, 2003.

[97] R. Bachmann, J. F. J. DiSalvo, T. H. Geballe, R. L. Greene, R. E. Howard, C. N. King, H. C. Kirsch, K. N. Lee, R. E. Schwall, H.-U. Thomas, and R. B. Zubeck, Review of Scientific Instruments **43**, 205 (1972).

[98] K. Kiefer, *Kalorimetrische und magnetische Untersuchungen am Spin-Peierls-System $CuGeO_3$*, PhD thesis, Universität des Saarlandes, 2004.

[99] J. P. Shepherd, Review of Scientific Instruments **56**, 273 (1985).

[100] S. Riegel and G. Weber, Journal of Physics E: Scientific Instruments **19**, 790 (1986).

[101] F. Pobell, *Matter and Methods at Low Temperatures*, Springer, third edition, 2007.

[102] H. Ryll, *Aufbau und Vergleich verschiedener thermometrischer Messverfahren für den Temperaturbereich T = 0.005 -1.0 K in hohen Magnetfeldern bis 20 T*, Diploma thesis, TU Berlin, 2008.

[103] Quantum Design, *PPMS VSM Option User's Manual*, Rev. A-2, August 2004 .

[104] N. W. Ashcroft and N. D. Mermin, *Solid State Physics*, Brooks/Cole, Cengage Learning, 1976.

[105] E. A. Cornell and C. E. Wieman, Rev. Mod. Phys. **74**, 875 (2002).

[106] S. Sachdev, T. Senthil, and R. Shankar, Phys. Rev. B **50**, 258 (1994).

[107] T. Barnes, J. Riera, and D. A. Tennant, Phys. Rev. B **59**, 11384 (1999).

[108] G. Xu, C. Broholm, D. H. Reich, and M. A. Adams, Phys. Rev. Lett. **84**, 4465 (2000).

[109] T. M. Rice, Science **298**, 760 (2002).

[110] T. Giamarchi, C. Ruegg, and O. Tchernyshyov, Nature Physics **4**, 198 (2008).

[111] A. A. Aczel, Y. Kohama, M. Jaime, K. Ninios, H. B. Chan, L. Balicas, H. A. Dabkowska, and G. M. Luke, Phys. Rev. B **79**, 100409 (2009).

[112] A. A. Aczel, Y. Kohama, C. Marcenat, F. Weickert, M. Jaime, O. E. Ayala-Valenzuela, R. D. McDonald, S. D. Selesnic, H. A. Dabkowska, and G. M. Luke, Phys. Rev. Lett. **103**, 207203 (2009).

[113] K. M. Diederix, J. P. Groen, L. S. J. M. Henkens, T. O. Klaassen, and N. J. Poulis, Physica B+C **94**, 9 (1978).

[114] J. Eckert, D. E. Cox, G. Shirane, S. A. Friedberg, and H. Kobayashi, Phys. Rev. B **20**, 4596 (1979).

[115] B. Grenier, J.-P. Boucher, J.-Y. Henry, L.-P. Regnault, and T. Ziman, J. Magn. Magn. Mater. **310**, 1269 (2007).

[116] N. D. Mermin and H. Wagner, Phys. Rev. Lett. **17**, 1133 (1966).

[117] T. Giamarchi and A. M. Tsvelik, Phys. Rev. B **59**, 11398 (1999).

[118] R. Chitra and T. Giamarchi, Phys. Rev. B **55**, 5816 (1997).

[119] Y. Maeda, C. Hotta, and M. Oshikawa, Phys. Rev. Lett. **99**, 057205 (2007).

[120] X. Wang and L. Yu, Phys. Rev. Lett. **84**, 5399 (2000).

[121] S. Wessel, M. Olshanii, and S. Haas, Phys. Rev. Lett. **87**, 206407 (2001).

[122] P. Bouillot, C. Kollath, A. M. Läuchli, M. Zvonarev, B. Thielemann, C. Rüegg, E. Orignac, R. Citro, M. Klanjšek, C. Berthier, M. Horvatić, and T. Giamarchi, Phys. Rev. B **83**, 054407 (2011).

[123] J. Garaj, Acta Chem. Scand. **22**, 1710 (1968).

[124] B. Morosin, Acta Cryst. **B 26**, 1203 (1970).

[125] K. M. Diederix, J. P. Groen, L. S. J. M. Henkens, T. O. Klaassen, and N. J. Poulis, Physica B+C **93**, 99 (1978).

[126] L. Berger, S. A. Friedberg, and J. T. Schriempf, Phys. Rev. **132**, 1057 (1963).

[127] S. A. Friedberg and C. A. Raquet, J. Appl. Phys. **39**, 1132 (1968).

[128] S. Wittekoek and N. J. Poulis, J. Appl. Phys. **39**, 1017 (1968).

[129] B. E. Myers, L. Berger, and S. A. Friedberg, J. Appl. Phys. **40**, 1149 (1969).

[130] J. C. Bonner, S. A. Friedberg, H. Kobayashi, and B. E. Myers, *Proceedings of the Twelfth International Conference on Low Temperature Physics*, edited by E. Kanda (Keigaku, Tokyo 1971) , 691 (1971).

[131] M. W. van Tol, L. S. J. M. Henkens, and N. J. Poulis, Phys. Rev. Lett. **27**, 739 (1971).

[132] S. Notbohm, *Spin Dynamics of Quantum Spin-Ladders and Chains*, PhD thesis, University of St Andrews, 2007.

[133] K. Diederix, J. Groen, and N. Poulis, Physica B+C **86-88**, 1151 (1977).

[134] M. W. V. Tol, K. M. Diederix, and N. J. Poulis, Physica **64**, 363 (1973).

[135] D. A. Tennant, C. Broholm, D. H. Reich, S. E. Nagler, G. E. Granroth, T. Barnes, K. Damle, G. Xu, Y. Chen, and B. C. Sales, Phys. Rev. B **67**, 054414 (2003).

[136] S. Notbohm, D. Tennant, B. Lake, P. Canfield, J. Fielden, P. Kï¿½gerler, H.-J. Mikeska, C. Luckmann, and M. Telling, J. Magn. Magn. Mater. **310**, 1236 (2007).

[137] D. A. Tennant, B. Lake, A. J. A. James, F. H. L. Essler, S. Notbohm, H.-J. Mikeska, J. Fielden, P. Kögerler, P. C. Canfield, and M. T. F. Telling, Phys. Rev. B **85**, 014402 (2012).

[138] G. Xu, *Spin Correlations and Impurities in 1-D Gapped Spin Systems*, PhD thesis, Johns Hopkins University, Baltimore, 2001.

[139] F. Groitl, *High Resolution Spectroscopy with the Neutron Resonance Spin Echo Method*, PhD thesis, TU Berlin, 2012.

[140] F. A. H. Schreinemakers, G. Berkhoff, and K. Posthumus, Rec. Trav. Chim. **43**, 508 (1924).

[141] I. V. Morozov, K. O. Znamenkov, Y. M. Korenev, and O. A. Shlyakhtin, Thermochimica Acta **403**, 173 (2003).

[142] R. Dell'Amore, A. Schilling, and K. Krämer, Phys. Rev. B **78**, 224403 (2008).

[143] A. F. Albuquerque, F. Alet, P. Corboz, P. Dayal, A. Feiguin, S. Fuchs, L. Gamper, E. Gull, S. Gürtler, A. Honecker, R. Igarashi, M. Körner, A. Kozhevnikov, A. Läuchli, S. R. Manmana, M. Matsumoto, I. P. McCulloch, F. Michel, R. M. Noack, G. Pawlowski, L. Pollet, T. Pruschke, U. Schollwöck, S. Todo, S. Trebst, M. Troyer, P. Werner, and S. Wessel, J. Magn. Magn. Mater. **310**, 1187 (2007).

[144] B. Bauer, L. D. Carr, H. G. Evertz, A. Feiguin, J. Freire, S. Fuchs, L. Gamper, J. Gukelberger, E. Gull, S. Guertler, A. Hehn, R. Igarashi, S. V. Isakov, D. Koop, P. N. Ma, P. Mates, H. Matsuo, O. Parcollet, G. Pawlowski, J. D. Picon, L. Pollet, S. Santos, V. W. Scarola, U. Schollwöck, C. Silva, B. Surer, S. Todo, S. Trebst, M. Troyer, M. L. Wall, P. Werner, and S. Wessel, J. Stat. Mech. **P05001** (2011).

[145] J. Rodriguez-Carvajal, Physica B **192**, 55 (1993).

[146] A. Oosawa, M. Ishii, and H. Tanaka, J. Phys.: Condens. Matter **11**, 265 (1999).

[147] L. Zhu, M. Garst, A. Rosch, and Q. Si, Phys. Rev. Lett. **91**, 066404 (2003).

[148] M. Klanjšek, H. Mayaffre, C. Berthier, M. Horvatić, B. Chiari, O. Piovesana, P. Bouillot, C. Kollath, E. Orignac, R. Citro, and T. Giamarchi, Phys. Rev. Lett. **101**, 137207 (2008).

[149] E. Orignac, R. Citro, and T. Giamarchi, Phys. Rev. B **75**, 140403 (2007).

[150] T. Hamada, J. Kane, S. Nakagawa, and Y. Natsume, J. Phys. Soc. Jpn. **57**, 1891 (1988).

[151] T. Tonegawa and I. Harada, J. Phys. Soc. Jpn. **58**, 2902 (1989).

[152] A. V. Chubukov, J. Phys.: Condens. Matter **2**, 4455 (1990).

[153] F. Heidrich-Meisner, I. P. McCulloch, and A. K. Kolezhuk, Phys. Rev. B **80**, 144417 (2009).

[154] L. Kecke, T. Momoi, and A. Furusaki, Phys. Rev. B **76**, 060407 (2007).

[155] S. Nishimoto, S.-L. Drechsler, R. Kuzian, J. Richter, and J. van den Brink, arXiv:1005.5500v2 [cond-mat.str-el] (2010).

[156] S. Nishimoto, S.-L. Drechsler, R. Kuzian, J. Richter, and J. van den Brink, arXiv:1303.1933v1 [cond-mat.str-el] (2013).

[157] M. Sato, T. Hikihara, and T. Momoi, Phys. Rev. Lett. **110**, 077206 (2013).

[158] M. E. Zhitomirsky and H. Tsunetsugu, Europhys. Lett. **92**, 37001 (2010).

[159] M. G. Banks, F. Heidrich-Meisner, A. Honecker, H. Rakoto, J.-M. Broto, and R. K. Kremer, J. Phys.: Condens. Matter **19**, 145227 (2007).

[160] N. Büttgen, H.-A. Krug von Nidda, L. E. Svistov, L. A. Prozorova, A. Prokofiev, and W. Aßmus, Phys. Rev. B **76**, 014440 (2007).

[161] N. Büttgen, W. Kraetschmer, L. E. Svistov, L. A. Prozorova, and A. Prokofiev, Phys. Rev. B **81**, 052403 (2010).

[162] L. Svistov, T. Fujita, H. Yamaguchi, S. Kimura, K. Omura, A. Prokofiev, A. Smirnov, Z. Honda, and M. Hagiwara, JETP Letters **93**, 21 (2011).

[163] M. Hase, H. Kuroe, K. Ozawa, O. Suzuki, H. Kitazawa, G. Kido, and T. Sekine, Phys. Rev. B **70**, 104426 (2004).

[164] T. Masuda, A. Zheludev, A. Bush, M. Markina, and A. Vasiliev, Phys. Rev. Lett. **92**, 177201 (2004).

[165] S.-L. Drechsler, J. Richter, A. A. Gippius, A. Vasiliev, A. A. Bush, A. S. Moskvin, J. Málek, Y. Prots, W. Schnelle, and H. Rosner, Europhys. Lett. **73**, 83 (2006).

[166] S.-L. Drechsler, O. Volkova, A. N. Vasiliev, N. Tristan, J. Richter, M. Schmitt, H. Rosner, J. Málek, R. Klingeler, A. A. Zvyagin, and B. Büchner, Phys. Rev. Lett. **98**, 077202 (2007).

[167] S. E. Dutton, M. Kumar, M. Mourigal, Z. G. Soos, J.-J. Wen, C. L. Broholm, N. H. Andersen, Q. Huang, M. Zbiri, R. Toft-Petersen, and R. J. Cava, Phys. Rev. Lett. **108**, 187206 (2012).

[168] M. Baran, A. Jedrzejczak, H. Szymczak, V. Maltsev, G. Kamieniarz, G. Szukowski, C. Loison, A. Ormeci, S.-L. Drechsler, and H. Rosner, Phys. Status Solidi C **3**, 220 (2006).

[169] L. Capogna, M. Mayr, P. Horsch, M. Raichle, R. K. Kremer, M. Sofin, A. Maljuk, M. Jansen, and B. Keimer, Phys. Rev. B **71**, 140402 (2005).

[170] Y. Tarui, Y. Kobayashi, and M. Sato, J. Phys. Soc. Jpn. **77**, 043703 (2008).

[171] J. Sirker, Phys. Rev. B **81**, 014419 (2010).

[172] R. O. Kuzian, S. Nishimoto, S.-L. Drechsler, J. Málek, S. Johnston, J. van den Brink, M. Schmitt, H. Rosner, M. Matsuda, K. Oka, H. Yamaguchi, and T. Ito, Phys. Rev. Lett. **109**, 117207 (2012).

[173] H. Katsura, N. Nagaosa, and A. V. Balatsky, Phys. Rev. Lett. **95**, 057205 (2005).

[174] M. Mostovoy, Phys. Rev. Lett. **96**, 067601 (2006).

[175] S. Seki, Y. Yamasaki, M. Soda, M. Matsuura, K. Hirota, and Y. Tokura, Phys. Rev. Lett. **100**, 127201 (2008).

[176] Y. Naito, K. Sato, Y. Yasui, Y. Kobayashi, Y. Kobayashi, and M. Sato, J. Phys. Soc. Jpn. **76**, 023708 (2007).

[177] Y. Yasui, M. Sato, and I. Terasaki, J. Phys. Soc. Jpn. **80**, 033707 (2011).

[178] S.-W. Cheong and M. Mostovoy, Nat. Mater. **6**, 13 (2007).

[179] A. A. Bush, V. N. Glazkov, M. Hagiwara, T. Kashiwagi, S. Kimura, K. Omura, L. A. Prozorova, L. E. Svistov, A. M. Vasiliev, and A. Zheludev, Phys. Rev. B **85**, 054421 (2012).

[180] H. G. Bachmann and J. Zemann, Acta Crystallographica **14**, 747 (1961).

[181] T. Araki, Mineralogical Journal (Japan) **3**, 282 (1962).

[182] H. Effenberger, Mineralogy and Petrology **36**, 3 (1987).

[183] P. F. Schofield, C. C. Wilson, K. S. Knight, and C. A. Kirk, The Canadian Mineralogist **47**, 649 (2009).

[184] J. Kanamori, J. Phys. Chem. Solids **10**, 87 (1959).

[185] Y. Mizuno, T. Tohyama, S. Maekawa, T. Osafune, N. Motoyama, H. Eisaki, and S. Uchida, Phys. Rev. B **57**, 5326 (1998).

[186] A. P. Ramirez, Annual Review of Materials Science **24**, 453 (1994).

[187] Y. Yasui, Y. Yanagisawa, M. Sato, and I. Terasaki, J. Phys.: Conf. Ser. **320**, 012087 (2011).

[188] M. Schäpers, private communications.

[189] C. Wilkinson and H. W. Khamis, J. Appl. Cryst. **21**, 471 (1988).

[190] M. E. Fisher, Rep. Prog. Phys. **30**, 615 (1967).

[191] M. F. Collins, *Magnetic Critical Scattering*, Oxford University Press, 1989.

[192] G. S. Rushbrooke, J. Chem. Phys. **39**, 842 (1963).

[193] J.-C. Tolédano and P. Tolédano, *The Landau Theory of Phase Transitions*, World Scientific, 1987.

[194] M. Kenzelmann, A. B. Harris, S. Jonas, C. Broholm, J. Schefer, S. B. Kim, C. L. Zhang, S.-W. Cheong, O. P. Vajk, and J. W. Lynn, Phys. Rev. Lett. **95**, 087206 (2005).

[195] Y. Kobayashi, K. Sato, Y. Yasui, T. Moyoshi, M. Sato, and K. Kakurai, J. Phys. Soc. Jpn. **78**, 084721 (2009).

[196] M. Kenzelmann, A. B. Harris, A. Aharony, O. Entin-Wohlman, T. Yildirim, Q. Huang, S. Park, G. Lawes, C. Broholm, N. Rogado, R. J. Cava, K. H. Kim, G. Jorge, and A. P. Ramirez, Phys. Rev. B **74**, 014429 (2006).

[197] L. C. Chapon, P. Manuel, F. Damay, P. Toledano, V. Hardy, and C. Martin, Phys. Rev. B **83**, 024409 (2011).

[198] M. Schäpers, A. U. B. Wolter, S.-L. Drechsler, S. Nishimoto, M. Abdel-Hafiez, W. Schottenhamel, B. Büchner, J. Richter, B. Ouladdiaf, M. Uhlarz, R. Beyer, Y. Skourski, J. Wosnitza, K. Rule, H. Ryll, B. Klemke, K. Kiefer, M. Reehuis, B. Willenberg, and S. Süllow, arXiv:1305.6731 [cond-mat.str-el] (2013).

[199] J. Holakovsky, Phys. Status Solidi B **56**, 615 (1973).

[200] G. Lawes, M. Kenzelmann, N. Rogado, K. H. Kim, G. A. Jorge, R. J. Cava, A. Aharony, O. Entin-Wohlman, A. B. Harris, T. Yildirim, Q. Z. Huang, S. Park, C. Broholm, and A. P. Ramirez, Phys. Rev. Lett. **93**, 247201 (2004).

[201] S. Park, Y. J. Choi, C. L. Zhang, and S.-W. Cheong, Phys. Rev. Lett. **98**, 057601 (2007).

[202] T. Kimura, T. Goto, H. Shintani, K. Ishizaka, T. Arima, and Y. Tokura1, Nature **426**, 55 (2003).

[203] G. Lawes, A. B. Harris, T. Kimura, N. Rogado, R. J. Cava, A. Aharony, O. Entin-Wohlman, T. Yildirim, M. Kenzelmann, C. Broholm, and A. P. Ramirez, Phys. Rev. Lett. **95**, 087205 (2005).

[204] T. Moriya, Phys. Rev. **120**, 91 (1960).

[205] S.-L. Drechsler, S. Nishimoto, R. O. Kuzian, J. Málek, W. E. A. Lorenz, J. Richter, J. van den Brink, M. Schmitt, and H. Rosner, Phys. Rev. Lett. **106**, 219701 (2011).

[206] M. Mourigal, M. Enderle, B. Fåk, R. K. Kremer, J. M. Law, A. Schneidewind, A. Hiess, and A. Prokofiev, Phys. Rev. Lett. **109**, 027203 (2012).

[207] A. N. Bogdanov, A. V. Zhuravlev, and U. K. Rößler, Phys. Rev. B **75**, 094425 (2007).

[208] M. E. Fisher and D. R. Nelson, Phys. Rev. Lett. **32**, 1350 (1974).

List of Figures

Acknowledgements

I would like to say ***thank you*** to all people, who made this thesis possible due to their kind support.

First of all, I would like to express my gratitude to Prof. Dr. Stefan Süllow for giving me the opportunity to study the fascinating properties of all the wonderful blue crystals, for convincing me to go to Berlin, for the support, and for the supervision of this thesis.

As I stayed the three years of my PhD at the Helmholtz-Zentrum in Berlin, I really appreciate the local supervision of Dr. Kirrily Rule and Dr. Klaus Kiefer, who were like a "Doctor-Aunt" and "Doctor-Uncle". Especially, I would like to thank Kirrily for giving me a good start to our project and Klaus for giving me the opportunity to work in his lab. With sharing his expertise even challenging measurements were made possible.

I would also like to thank Prof. Dr. Michael Lang that he agreed to referee this thesis.

Special thanks go to Dr. Hanjo Ryll for the measurements using the cantilever-magnetometer and the dilution fridge, for sharing his expertise of magnetocaloric effect measurements and the knowledge of dimerized 1D-spin systems as well as for sharing the life beyond the lab.

I would like to thank Dr. Bastian Klemke, who introduced heat capacity and magnetocaloric effect measurements to me, as well as André Sokolowski and the other members of the sample environment group for their support in the lab.

Further, I would like to thank Dr. Manfred Reehuis for sharing his expertise in the determination of spin structures. He had always a couple of minutes (or even more) to answer questions as well as to check crystal orientations on his instrument E5.

I would also like to thank Dr. Felix Groitl and Dr. Katharina Rolfs for their effort in the crystal growth of large copper nitrate single crystals.

I must also not forget all the local contacts, who made the neutron scattering experiments possible and successful: Dr. Bachir Ouladdiaf, Dr. Laurent Chapon, Dr. Pascal Manuel, Dr. Dmitry Khalyavin, Dr. Slavormir Matas, and Dr. Illia Glavatskyi.

Thanks to Dr. Klaus Habicht, who gave me the opportunity to stay as a guest of his group at HZB and providing me a nice working environment.

Thanks to Markus Schäpers and Dr. Anja Wolter for the nice and fruitful collaboration on the linarite project. It was always fun to chat with Markus and discuss new data.

I would also like to thank Dr. Jennifer Schulz for the entertaining tea breaks as well as the sample environment group for the birthday-cake-gatherings, which both made the work even more enjoyable.

Thanks to the “Braunschweigers” Daniela Rauch, Josefin Engelke, Teresa Henning, Dirk Schulze Grachtrup, and Mathias Kraken for the nice talks, whenever we saw each other.

Finally, I would like to thank my family for their support during my studies and my PhD.